THE UNIVERSITY *of* EDINBURGH

Mechanochemical Processes in Energetic Materials: A Computational and Experimental Investigation

Adam Alexander Leon Michalchuk

Submitted for the Degree of Doctor of Philosophy

University of Edinburgh

August 2018

Abstract

Energetic materials (explosives, propellants and pyrotechnics; EMs) encompass a broad range of materials. These materials are used across a wide spectrum of applications, including civil and defence. For example, HMX, RDX and TNT are well known EMs with defence applications. Silver fulminate is instead used in house-hold Christmas crackers and ammonium nitrate is used for numerous industrial applications. Common to all EMs is their propensity to rapidly release energy upon external perturbation. The amount and type of energy that is required to initiate an EM can vary across orders of magnitude. Some materials (*e.g.* triaminotriperoxide, TATP) initiate with < 1 J of impact energy, while others (*e.g.* triaminotrinitrobenzene, TATB) cannot be initiated without > 100 J of impact energy. Understanding which materials can be handled safely is therefore of critical importance for maintaining the safe use of EMs across all sectors.

Current trends in EM research include a drive to develop new materials with decreased sensitivities. While it is relatively straightforward to selectively modify some properties (*e.g*. environmental impact), very little is understood about what constitutes a sensitive material. At present, a new EM must be synthesised and its sensitivity tested. However, with no *a priori* knowledge of the potential sensitivity of a novel EM, synthesis is accompanied by substantial hazard, as well as time and financial costs. It is therefore pressing to develop a fundamental understanding of what dictates a sensitive material, and hence develop a mechanism to predict these properties. A particularly promising model to explore impact sensitivity of EMs is based on vibrational up-pumping, *i.e.* the up-conversion of vibrational energy. This thesis explores the application of this model to a set of azide, organic molecular and polymorphic materials.

Azide-based EMs share the common N_3^- explosophore. The electronic structure of this anion was followed as a function of its normal modes of

vibration. It was found that excitation of the bending mode is sufficient to induce athermal electronic excitation of the molecule, and spontaneous decomposition. This is valid both in the gas and solid states. It is therefore suggested that this vibrational mode is largely responsible for decomposition of the azide materials. Based on calculations of the complete phonon dispersion curves, the various pathways to vibrational energy up-pumping were explored, namely *via* overtone and combination pathways. In particular, the relative rates of up-pumping into the N_3^- bending mode were investigated. Remarkable agreement is found between these up-pumping rates and the relative ordering of the impact sensitivity of these azides.

The calculated vibrational structures of organic molecular EMs were first compared with experimental inelastic neutron scattering spectra and found to provide accurate representation of the low temperature vibrational structure of these complex crystals. The decomposition pathways for organic EMs are not known and hence no target frequency could be unambiguously identified. Instead, the up-pumping model was developed for these materials by investigating the total rate of energy conversion into the internal vibrational manifold. A number of qualitative trends were identified, which may provide a mechanism for the rapid classification of EMs from limited vibrational information. The overtone pathways were found to offer a good agreement with experimental impact sensitivities of these compounds. However, the increased complexity of the vibrational structure of the organic EMs as compared to the azides required a more thorough treatment of the up-pumping mechanism to correctly reflect experimental sensitivities. The effects of temperature on up-pumping were also explored.

The sensitivity of organic EMs is known to differ across polymorphic forms. Most notable are the HMX polymorphs. The calculated vibrational structure of two HMX polymorphs was confirmed by inelastic neutron scattering spectroscopy. The up-pumping model developed for molecular organic EMs was therefore extended to a comparison of these two HMX polymorphs. The polymorphic forms of FOX-7 were also investigated under the premise of the

up-pumping model. Upon heating, FOX-7 undergoes two polymorphic transformations, which increases the layering of the materials. It therefore offered an opportunity to explore the widely-held hypothesis that layered materials are less sensitive than non-layered materials. The metastable γ-form was successfully recovered, and its experimental impact sensitivity investigated by BAM drop-hammer method. However, upon impact, the γ-polymorph appeared to convert to the α-form and initiate at the same input energy. Hence a considerable deficiency of experimental methods is identified when studying polymorphic materials. FOX-7 was therefore explored within the framework of the up-pumping model. The inelastic neutron scattering spectrum was collected for γ-FOX-7, which confirmed the calculated vibrational structure. It was shown that within the up-pumping model, the layered γ-polymorph is predicted to be less sensitive than the α-form, and results from a decrease in the maximum phonon-bath frequency. Hence a new mechanism is proposed to describe the insensitivity of layered compounds.

The work presented in this thesis explores the applications of vibrational up-pumping to rationalise and predict the relative impact sensitivities of a range of EMs. Despite the approximations employed in construction of the model, it leads to excellent correlation with experimental results in all cases. This work therefore opens the door to a new fully *ab initio* approach to designing new EMs based solely on knowledge of the solid-state structure.

Lay Summary

The term energetic material (EM) describe a range of compounds, which can be broadly classified as explosives, propellants and pyrotechnics. While it is most common to think of these materials as having military-based applications, their use is far more widespread. Christmas crackers contain a primary explosive known as silver fulminate, fireworks contain both pyrotechnics and propellants, and many automobile airbags are based on a range of EMs. Many industries are also dependent on the use of EMs, including the mining and oil industries. Common to all EMs is their propensity to explode when physically struck, heated or subjected to an electric shock. The amount of energy that is required depends strongly on the material. This is a critical physical parameter for ensuring the safe use of EMs across any sector.

With growing pressures to produce new EMs (*e.g.* for environmental purposes), effort is being placed on ensuring new EMs exhibit low sensitivities, *i.e.* are safer. It is relatively straightforward to design new materials with better environmental compatibility. For example, by removing lead or other heavy metals. However, there is no definitive understanding for what dictates the sensitivity of EMs. Any new EM must be fully synthesised in relatively large quantities, and tested. With no preceding knowledge of the physical properties of a new EM, this can be very dangerous. There is therefore considerable interest in developing computational methods to rationalise and predict the sensitivity of EMs.

When a material is struck by a physical blow, it introduces a large amount of energy into the material. Analogous to water, an impact leads to formation of waves, which dissipate through the medium. In a solid material, this translates into the vibrations of the molecules. This energy subsequently dissipates through the material and activates a chemical bond whose rupture leads to initiation and explosion. This thesis explores this mechanism as an underlying model for the rationalisation and prediction of impact (mechanical) sensitivity

of a range of EMs, include N_3^- -based materials and organic molecular materials.

The bond which ruptures in N_3^- -based materials is an N-N bond. A series of quantum mechanical calculations demonstrated that if the linear N_3^- molecule is bent, dissociation becomes favourable. Therefore, impact sensitivity of these materials was investigated by considering the rate of vibrational energy dissipation into the bending vibrational mode. This led to excellent correlation with experimental result. A similar approach was taken to investigate organic molecular EMs. However, given the complex molecular structures of these compounds, it was not possible to identify a single vibration that is responsible for dissociation. Instead, predictions were based on the total rate at which energy dissipates into the molecule. Again, excellent agreement is obtained with experimental results.

Many organic molecules can crystallise into different crystalline forms. Composed of the same molecule, these solid forms have different intermolecular interactions, which can lead to considerably different physical properties. Different polymorphic forms of EMs are also known to exhibit different sensitivities, most notably HMX. The vibrational energy transfer model was therefore applied to HMX polymorphs, and shown to offer successful differentiation of two polymorphic forms. The polymorphs of FOX-7 were therefore also investigated. It is typically accepted that crystals that contain layers of molecules (*e.g.* TATB) are very insensitive. On heating, the polymorphic forms of FOX-7 exhibit increased layering, and the high temperature form is therefore expected to be less sensitive. However, when the high temperature form was tested, it was found to convert to the ambient temperature form upon impact. Experiment is therefore not able to measure the sensitivities of these forms, and may in fact produce erroneous results for other polymorphic materials. The vibrational energy conversion model, however, does predict that the layered (high temperature) compound *should* be less sensitive than the ambient temperature (non-layered) form, and offers a new mechanism for rationalising why layered materials are insensitive.

The work in this thesis develops a new approach for understanding the mechanical impact sensitivity of a range of EMs. Based purely on computational methods, this work demonstrates that it may in fact be possible to predict the sensitivity properties of new EMs without the need for potentially dangerous synthetic procedures.

Declaration

I declare that this thesis was written by myself and that the work detailed in this thesis is my own, or I have contributed substantially to such work, except where specific reference is made to the work of another.

Adam A. L. Michalchuk

"I am just a child who has never grown up. I still keep asking these 'how' and 'why' questions… Occasionally, I find an answer"

-Prof. Stephen Hawking

Acknowledgements

There are very many people I must thank, without whom this would not have been possible.

First and foremost, to my supervisors Prof. Colin Pulham and Dr Carole Morrison. I could not have asked for a better team of mentors to guide me through my PhD. To Colin, who accepted my transfer into the School of Chemistry many years ago, sent me to Siberia time and again, gave me the opportunity to pursue my PhD and introduced me to the world of energetic materials. To Carole, for adopting me as her student when my project moved towards computational chemistry and for teaching me so much about the field. To you both for your enthusiasm and encouragement: thank you.

My sincerest thanks to all of the members of the Pulham group, past and present, for making the office feel like a family. To Dan, Emily, Hayleigh, Nisa, Oleg, Rowan, Stuart, Sumit, Xiaojiao– you have all made the last four years amazing, from laughs around the office to pub quizzes, games nights and a get-away to Arran. Special thanks to Karl, for our many cross-country (and indeed cross-continental!) synchrotron road trips, and for not getting too distracted by trains while driving. To Rowan, Hayleigh and Xiaojiao for welcoming me to the group four years ago. And thanks to Nilgun and Stuart for hilarious trips to the Cavendish Laboratory. My thanks also to Prof. Adam Cumming for his guidance. I am also very grateful for the friendship of the Boldyreva group (Novosibirsk, Russia) for their warm hospitality during my many stays in Novosibirsk. A special thanks to Prof Elena Boldyreva for her guidance and mentorship, to Academician Prof. Vladimir Boldyrev for many stimulating discussions and Prof Andrei Arzhannikov for his hospitality and friendship.

I must also thank the EPSRC Centre for Continuous Manufacturing and Crystallisation (CMAC) and an Edinburgh Global Research Scholarship for funding my PhD studies. Thank you to my fellow CMAC cohort (Alex, Alice, Antonia, Arabella, Bilal, Bruce, Carlotta, Lauren, Meifen, Ravi, Sara, Vaclav) and the rest of CMAC for making these years so enjoyable.

Further thanks to Dr. Svemir Rudić (STFC ISIS) for allowing me to put explosives on the TOSCA beamline, for his enthusiasm and for teaching me much about inelastic neutron scattering. Thanks to Dr Steven Hunter (University of Edinburgh) for helping me get started in computational chemistry. Additional thanks to Dr David Williamson (Cavendish Laboratory, University of Cambridge) for access to the BAM fall hammer.

Thank you to Dom for your friendship over the past four years, and for always being ready for a good laugh. To my fellow Canadian, Paul, thank you for your friendship and of course for the Canadian care packages. Darren, my sincerest thanks for putting up with my constant questions about Molpro, and for helping me so much with its use.

And to everyone else who has made my nine years in Edinburgh so unforgettable, my deepest thanks.

Finally, to my family back in Canada – this would not have been possible without you. Thank you.

- Adam

Abbreviations

ABT	1,1’-Azobistetrazole
BOA	Born-Oppenheimer Approximation
CASTEP	Cambridge Serial Total Energy Package
CI	Configurational Interaction
CL-20	Hexanitrohexaazaisowurtzitane (HNIW)
DFPT	Density Functional Perturbation Theory
DFT	Density Functional Theory
D2	Grimme’s D2 dispersion correction
EM	Energetic Material
FC	Frank-Condon
FOX-7	1,1-diaminio-2,2-dinitroethene (DADNE)
GGA	Generalised Gradient Approximation
G06	Grimme’s D2 dispersion correction
HBT	5,5’-Hydrazinebistetrazole
HF	Hartree-Fock
HK	Hohenberg-Kohn
HMX	1,3,5,7-Tetranitro-1,3,5,7-tetrazocane (Octagen)
HNB	Hexanitrobenzene
INS	Inelastic Neutron Scattering Spectroscopy
KS	Kohn-Sham
LBS	Localised Basis Set
LDA	Local Density Approximation
MP	Monkhorst-Pack
NTO	Nitrotriazolone
PETN	Pentaerythritoltetranitrate
PW	Plane Wave
pwDFT	Plane Wave Density Functional Theory
TATB	Triamino-trinitrobenzene
TATP	Triacetone-triperoxide
TNT	2,4,6-trinitrotoluene
TS	Tkachenko-Scheffler dispersion correction

Contents

Chapter 1

INTRODUCTION

1.1 Energetic Materials

1.1.1 Energetic Materials: A Brief History

Energetic materials (explosives, propellants and pyrotechnics; EMs) contain stored chemical energy which is rapidly released on initiation. EMs have proved to be of great value for industrial, commercial and military applications.[1] The origin of EMs is often ascribed to the accidental discovery of black powder (a mixture of KNO_3, S_8 and charcoal) *ca.* 220 BCE in China. Their development in Europe began much later, when the English monk Roger Bacon began further studies of black powder in 1249 CE, described in his letter *'On the Marvellous Power of Art and Nature and on the Nullity of Magic'*.[2] This led to the adoption by western nations of black powder for military applications by the end of the 13th century. Despite these early discoveries, EMs were not used industrially until some time later, with the first documented use of black powder in England in the 1670s.[3] Black powder quickly became notorious for its propensity to accidentally initiate, despite numerous attempts at desensitising the material using additives, including paraffin and starch. However, it remained the primary industrial EM until the 1870s.[3]

It was not until the late 19th century that substantial progress was made on EM technologies.[3,4] The Nobel family made enormous strides with the development of nitroglycerine (NG) based materials, including a variety of dynamite compositions.[5] A mixture of NG with clay (Guhr dynamite) proved sufficiently stable for industrial application, and mixtures of NG with nitrocellulose (NC) led to formation of gelatine dynamite. Both dynamite forms

remain in use today. The Nobel family also introduced mercury fulminate as an alternative detonator to replace black powder. Ammonium nitrate also became a popular additive to enhance explosive compositions.

Throughout the development of EMs, safety remained a top concern. Accidental, explosive-related casualties remained very high across industry, and it was finally recognised that government-regulated standards should be imposed to ensure explosives were fit for purpose. Both dynamite and black powder were barred from use, and ammonium nitrate-based compositions became favoured for industrial application.[3]

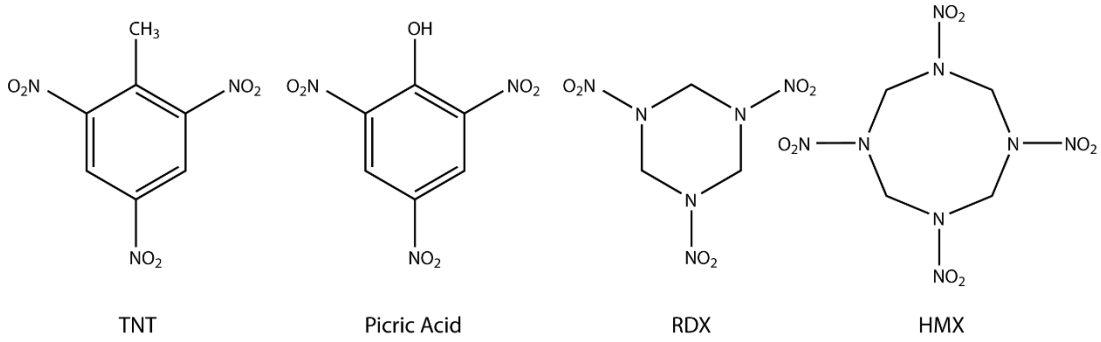

Figure 1.1: Chemical structure diagrams for common molecular energetic compounds.

Alongside the development of industrial EMs was the production of new military-grade materials. Picric acid, Figure 1.1, was an early favourite towards the end of the 19th century. However, when loaded into munitions, it had a tendency to react with the metallic shell walls, leading to highly sensitive metal salts.[6] This was largely overcome at the turn of the 20th century with the introduction of trinitrotoluene (TNT), Figure 1.1. This became a widely used explosive during the first World War. A number of other EMs were developed prior to the second World War, including pentaerythritoltetranitrate (PETN), 1,3,5,7-tetranitro-1,3,5,7-tetrazocane (Octogen or HMX) and 1,3,5-Trinitroperhydro-1,3,5-triazine (RDX). The latter two were favoured for military use due to their lower impact sensitivity, Figure 1.1.

The sensitivity of RDX and HMX remained a problem, and safety concerns persisted. Rather than developing new EMs, it was instead found that the

sensitivity of energetic crystals could be reduced by embedding into polymer matrices to produce polymer-bonded explosives (PBXs). Semtex is a well-known PBX containing PETN and RDX, although very many PBXs are known and used today.[7]

1.1.2 Insensitive Munitions

While the early development of EMs was slow, the latter half of the 20th century has seen rapid development of many new EMs. Generally, new molecules are desired that can be more safely handled and which exhibit more powerful energetics properties.[8,9] The need for safe EMs was finally recognised globally in the 1970s with the establishment of outlines for insensitive munitions (IMs).[10] An IM describes any EM that will not initiate under any condition other than its intended use, and has been made to include explosive formulations (*e.g.* PBXs) as well as insensitive explosive molecules. For example, HMX and RDX only meet IM regulations when formulated as PBXs. A variety of replacement EMs have been proposed, Figure 1.2. For example, hexanitrostilbene (HNS) and triaminotrinitrobenzene (TATB) are insensitive materials which exhibit high thermal stability. Nitro-1,2,4-triazol-3-one (NTO) is a high-energy, low-sensitivity material that has been suggested as a replacement for TNT and has found commercial applications (*e.g.* in automobile airbags). 1,1-diamino-2,2-dinitroethylene (FOX-7) has also become a popular EM, exhibiting excellent energetic properties and low sensitivity.

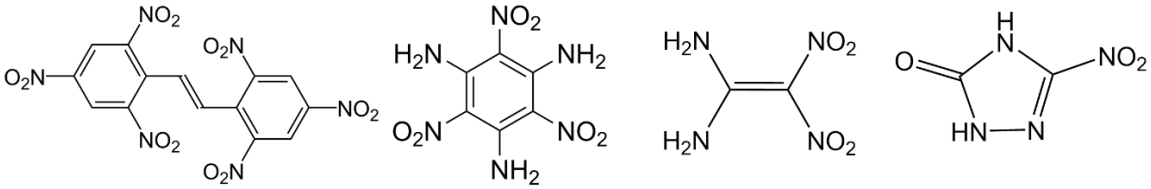

Figure 1.2: Molecular structure of new insensitive EMs.

An alternative to developing new molecules has been to generate multi-component materials: co-crystals and salts. The potential to tune EM properties by multi-component crystallisation was noted early by T. Brill, who,

while studying solvates of HMX, noted that '*the physical and chemical properties of HMX might be tailored systematically by such dopants*'.[11] Very many examples of multi-component EM crystals are now known (with both energetic and non-energetic co-formers), and in many cases exhibit drastically different sensitivity properties when compared to the pure EM.[12,13] Notable examples include co-crystals of TNT[14], including a co-crystal with the highly sensitive EM hexanitrohexaazaisowurtzitane (CL-20 or HNIW), CL-20●TNT.[14] This co-crystal exhibits substantially reduced impact sensitivity as compared to either pure EM. A number of co-crystals are also known based on HMX[15], including HMX●2-bromoaniline and HMX●2-pyrrolidone and 2CL-20●HMX.[16] All of these co-crystals exhibit notably different impact sensitivities than pure HMX. However, despite the possibility to develop new molecules and multi-component crystals, there remains very limited understanding of what constitutes a sensitive EM. Hence any new EM requires synthesis and thorough testing, at great cost and risk to safety.

Despite the enormous libraries of known explosive materials, safety and performance remain of utmost importance. The testing required to validate the safety and performance of new EMs is extensive. As such, very few of these new candidate molecules make their way into practical application. Instead, it has been more common to utilize EMs with well-characterised safety parameters, and vary the composition to which they are added.

1.1.3 Energetic Materials: Definitions and Classifications

Explosions caused by EMs are chemical explosions and are the result of a rapid chemical reaction that releases large amounts of energy and gas. The chemical transformation occurs so rapidly that gas products do not instantly expand out of the reaction zone. This leads to immense pressurisation within the material and formation of a shock wave.[17]

An EM can be any material that contains both a fuel and an oxidiser. These can be single component (*e.g.* TNT or HMX), or multi-component (*e.g.* black powder) systems. When the material ignites and reacts without the formation

of additional pressure (*i.e.* a slow burn), it is said to **combust**. If, however, pressure is generated in the material, the material is instead said to **deflagrate**. A deflagration is characterised by a sub-sonic burn rate. Under very particular circumstances – pressure build-up, confinement or very rapid reaction – deflagration can instead change to a **detonation**. This transition, known as the **deflagration-to-detonation (DDT)** transition, results from adiabatic heating, *i.e.* that that temperature increases with pressure. Hence, if sufficient pressure is accumulated within the material during its burn, or an intense shock is applied to the material, the propagation of the chemical reaction front accelerates due to increased temperature. In a detonation, the reaction front propagates at supersonic speeds, and is associated with the propagation of a shock front.

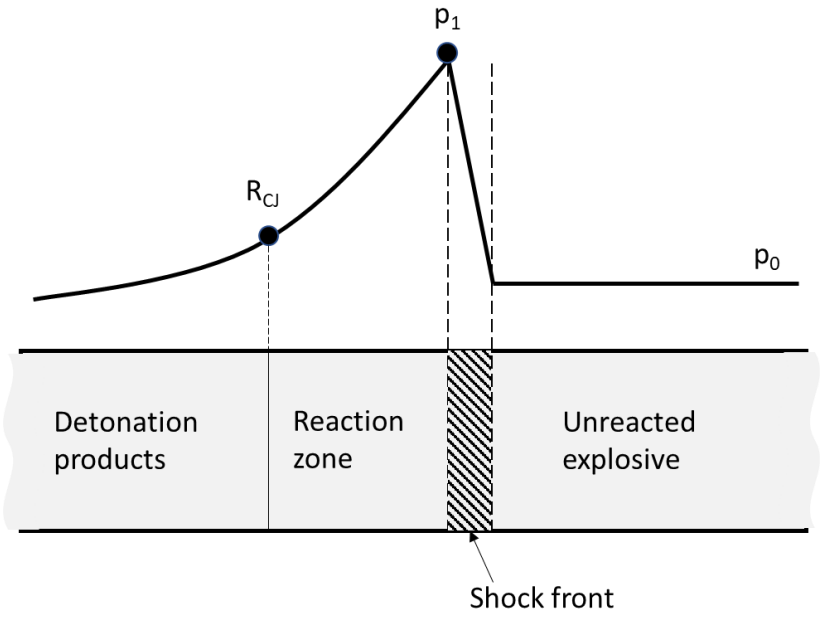

Figure 1.3: Schematic representation of the structure of a detonation front in an energetic material. Unreacted material has pressure of p_0, and the shock front is exposed to a pressure, p_1. The Chapman-Jouguet plane is indicated as R_{CJ}. Figure adapted from Ref. 4

During the propagation of a shock front into the unreacted material, a thin layer (*ca.* 10-100 Å)[18] of material is compressed, Figure 1.3. The pressure associated with the shock front leads to an increase in temperature of the material, and initiation of the reaction. As the shock front passes, the pressure

(and temperature) of the material behind the front decrease along the shock adiabat (Hugoniot adiabat). At a characteristic point, the **Chapman-Jouguet Point** (R_{CJ}), the chemical reaction reaches an equilibrium, the shock propagation reaches Mach 1 and the detonation process stops. The rate of shock propagation depends on the rate at which the chemical reaction can occur, with typical values of 1500-9000 ms^{-1}.[19] Hence, any model aimed at predicting this phenomenon must include processes no slower than this. The general scheme for explosion can therefore be summarised in Figure 1.4.

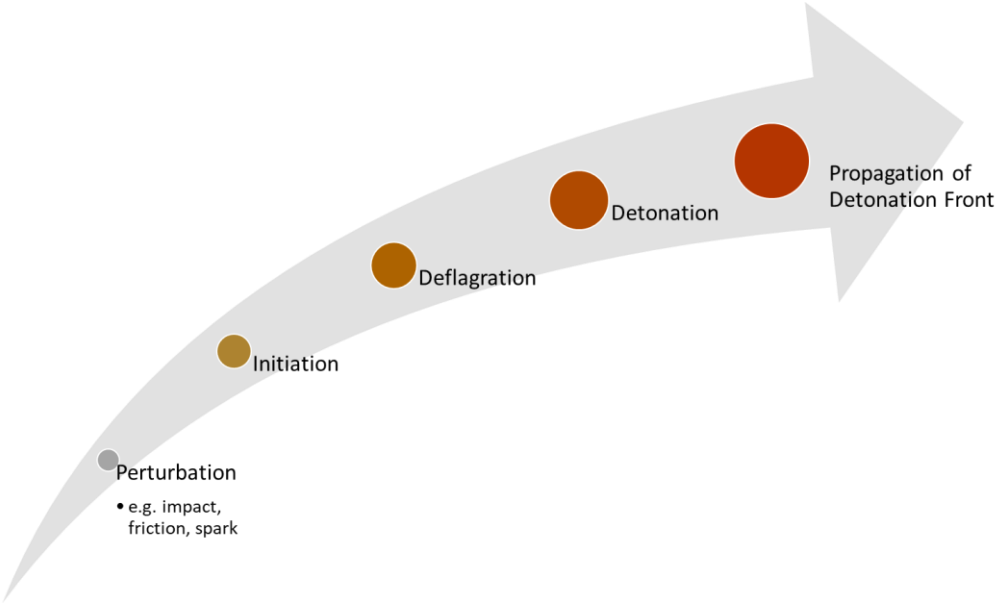

Figure 1.4: Stages of an explosion in an energetic material.

EMs can be classified based on either their structural type or their properties. In the first approach, molecules which are themselves classified as explosives contain chemical moieties with explosive properties, known as **explosophoric** groups. These explosophoric groups are then used to define the class of an EM. Plets[20] suggested structural groupings of explosives based on eight structure types, Table 1.1.

Table 1.1: Structural classifications of explosive compounds, according to Plets. [20]

Group	Explosive compounds
-O-O or -O-O-O	Inorganic and organic peroxides and ozonides
$-OClO_2$ and $-OClO_3$	Inorganic and organic chlorates and perchlorates
$-N-X_2$	Where X is a halogen
$-NO_2$ and $-ONO_2$	Inorganic and organic compounds
-N=N- or -N=N=N-	Inorganic and organic azides
-N=C	Fulminates
-C≡C-	Acetylene and metal acetylides
M-C	Molecules containing metal-carbon interactions

While these criteria can be useful in the design of new EMs, they do not provide much insight into their characteristic properties. In addition to discussion of their chemical properties, it is therefore common to classify EMs by their physical properties, Figure 1.5. At the highest level, a **high explosive** is taken as a material capable of detonating, while a **low explosive** cannot. Materials such as **propellants** and **pyrotechnics** burn, rather than explode. The classification of low explosive compounds generally depends on their applications. Broadly, propellants burn with timescales in the order of milliseconds, releasing a steady stream of gas and can therefore be used to generate thrust. Pyrotechnics burn with the intense emission of visible light.

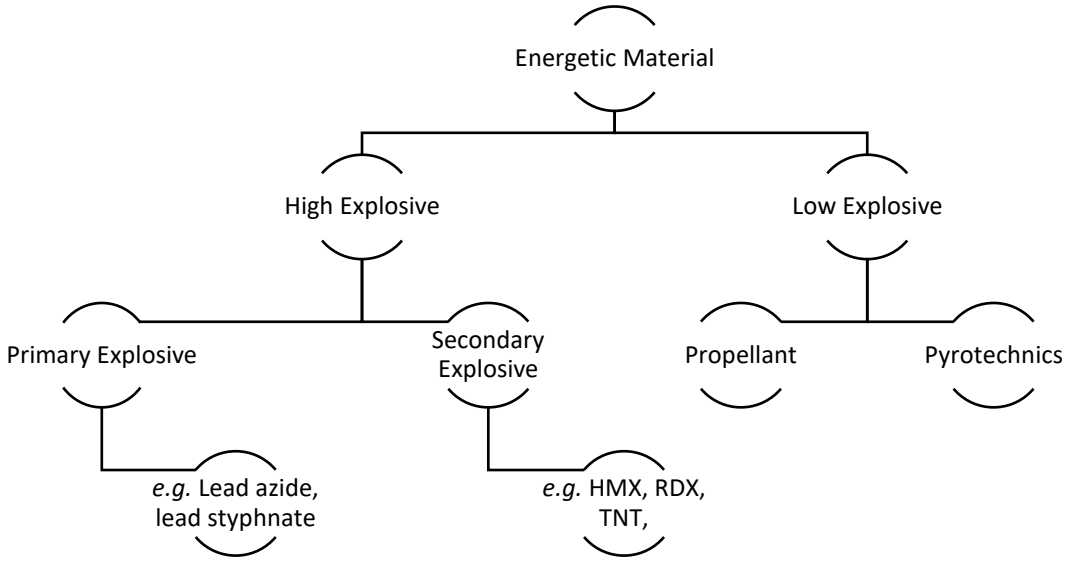

Figure 1.5: Classification of energetic materials.

Primary explosives undergo a very rapid transition from burning to detonation. The explosion products are accompanied with an enormous release of energy, which can in turn initiate a second, less sensitive EM. These materials will initiate under mild perturbations. **Secondary** explosives differ from primary explosives in that they cannot be readily detonated by heat, impact or friction. Initiation to detonation requires a shock produced by a primary explosive.

1.2 Initiation of Energetic Materials

1.2.1 Hot Spot Models

The general mode of events in an EM follows the sequence shown in Figure 1.6. The initial mechanical stimulus induces some macroscopic effect. This can include fracture, shear, plastic deformation, gas pressurisation or another similar phenomenon. This has the effect of producing microstructural defects within the material, and concentrates energy in these areas. These microstructural defects ultimately convert the mechanical energy into heat by some physicochemical mechanism, leading to a chemical reaction and further

heat generation. Finally, dissociated atoms recombine to propagate the reaction front, leading to release of gaseous products.[21]

The initiation step results from a large accumulation of energy at the molecular scale, leading to decomposition. This leads to a chain of reactions and self-sustaining combustion. The rate at which temperature rises begins to increase, and leads to deflagration and potentially detonation.

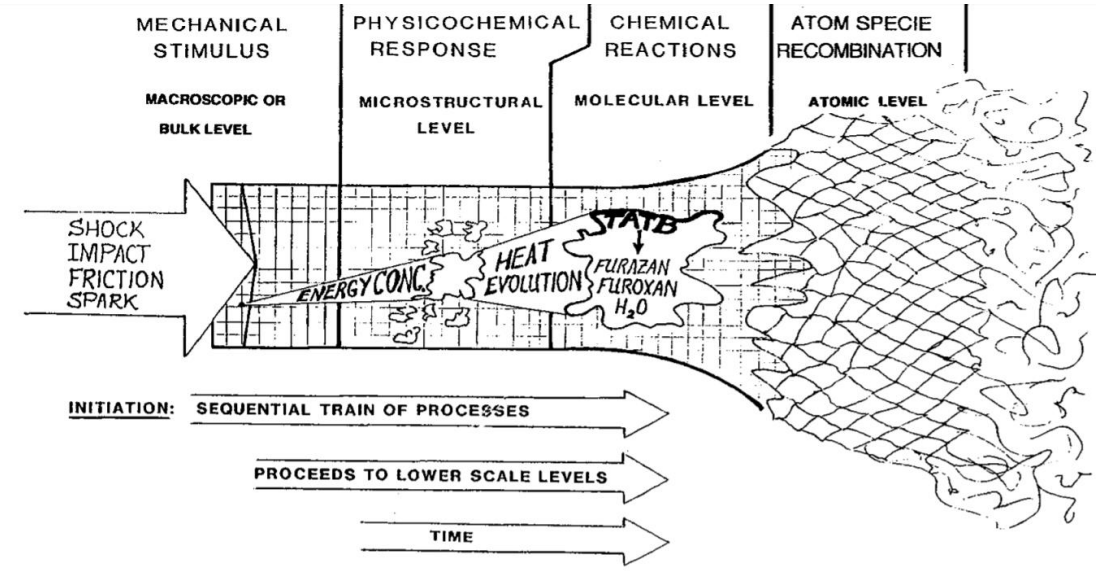

Figure 1.6: Progress of an explosion in a high explosive material. Reproduced from Ref 21.

Early work by Bowden and Yoffe[22,23] demonstrated that impacts known to induce initiation of explosives were associated with bulk heating too low to allow reaction. This led to the concept of 'hot spot' initiation, which remains popular today.[24] They demonstrated that over very small areas (0.1-10 μm), short mechanical pulses (< 1 ms) could lead to local temperatures of > 700 K. If hot-spots were outside these parameters, initiation could not occur.[22] Hot-spots with dimensions < *ca.* 0.1 μm or much lower temperatures may introduce some decomposition, but quench too rapidly for sustained reaction. Similar temperatures have also been recorded at the tip of propagating cracks during fracture. A variety of mechanisms have been proposed[25,26] for the formation of hot-spots, but the mechanism by which they occur depends critically on the

nature of the material. Some hot-spots (critical hot-spots) will lead to self-propagating initiation of an EM, while others (non-critical hot-spots) will lead to local heating, without initiation of the material. Hence, within the hot-spot theory for EM initiation, understanding the corresponding hot-spot mechanism is crucial. Field[26] studied the initiation events by high-speed photography, and concluded that there are only a few mechanisms that are responsible for critical hot-spot formation as a result of mechanical perturbation. In solids, these are adiabatic gas heating, friction, adiabatic shear and viscoplastic work.[26]

Within an explosive composition, gases trapped within defects (on the order of 0.1-10 μm) are adiabatically compressed from an initial pressure, P_i, to some final pressure, P_f. The temperature of this gas rises according to[23]

$$T_f = T_i \left(\frac{P_f}{P_i}\right)^{\gamma-1\,/\,\gamma}$$

Equation 1.1

where T_i is the initial temperature, T_f is the final temperature and γ represents the specific heat capacities of the phase. Numerical calculations have suggested hot-spot temperatures to rise in excess of 700-1000 K.[27]

Frictional heating, resulting from the interaction of explosive particles or with grit, has also been suggested as an important hot-spot forming mechanism. The maximum temperature is determined by the lowest melting component at the contact. In accordance with this effect, Bowden and Gurton[28] demonstrated a method to indirectly measure hot-spot temperatures due to friction by using grits with different melting temperatures. They determined 700 K to be the lowest hot-spot temperature required for initiation of PETN (the most sensitive secondary explosive in common use). The physical base for frictional heating remains largely debated, but has been suggested to result from accumulation of stress at the contact surfaces.[29] Frictional heating is largely an equilibrium phenomenon, however, and ignition temperatures tend to be much higher than the melting temperatures of typical explosive materials. Friction can therefore lead to melting and local decomposition.[30] In many cases it is therefore

believed that frictional heating acts in concert with other hotspot mechanisms.[25]

Solid compositions contain void space. As a mechanical force is imparted into a system, material is forced into these voids and are necessarily plastically deformed. This has been suggested as the principal mechanism for hot-spot formation in many materials.[31]

The final principal mechanism for hot-spot formation in solids is *via* localised adiabatic shear. This phenomenon stems from the anisotropic deformation of materials that are exposed to impact or shock. Plastic deformation can localize into bands, on the order of $> 1\mu m$. This is generally the case when thermal softening exceeds work hardening in a material. In such cases, deformation in a plane leads to further deformation in the same plane and thus a build-up of heat.[31] This phenomenon was first described by Recht for metals,[32] but was subsequently observed in inorganic explosives by Winter and Field[33] and later in organic explosives, PETN and HMX.[26]

A microscopic hot-spot model has also been suggested. This model is based on the concept of dislocation pile-ups.[29] Upon mechanical stimulation, the contact layer undergoes immense plastic deformation and generation of extended defects (dislocations) that extend into the bulk.[29] At any temperature $T > 0\,\mathrm{K}$, these defects rapidly migrate through the sample and collide (generally at existing defects), leading to local accumulations of energy within a crystallite. However, these pile-ups occur over length scales of 10s of nanometres.[34] Hence this mechanism does not produce sufficiently large hot-spots, and the accumulated energy quickly dissipates to the surrounding bulk. Hence dislocation pile-ups have been suggested as a non-critical hot-spot phenomenon.

1.2.2 Vibrational Up-Pumping

While the hot-spot mechanisms describe the generation of large amounts of energy in localised areas, they do not go so far as to describe localisation of this energy into a molecular response. An additional model, dubbed *vibrational*

up-pumping was therefore proposed by Coffey and Toton[35] in an attempt to describe the processes occurring immediately behind a shock front. This model was subsequently developed by Dlott and Fayer.[36]

The process of vibrational cooling was well established both experimentally and theoretically through the late 20th century.[37] This phenomenon describes the mechanism by which excess molecular vibrational energy relaxes within a crystal. However, when mechanical energy is inserted instead into the low frequency vibrational modes, the reverse process is observed.

Vibrational modes are inherently anharmonic, and the potential energy term of the Hamiltonian takes the form[36]

$$V = 1/2 \sum_{\varphi} \frac{\partial^2 V(\{\varphi\})}{\partial^2 \varphi} \varphi^2 + 1/3! \sum_{\varphi\varphi'\varphi''} \frac{\partial^3 V(\{\varphi\})}{\partial\, \varphi \partial\, \varphi' \partial\, \varphi''} \times \varphi\varphi'\varphi'' + \ldots$$

Equation 1.2

where $V(\varphi)$ is the potential energy surface of the solid, and $\{\varphi\}$ is a full set of normal coordinates, φ. Previous work demonstrated that in solids, where displacements are small compared to intermolecular distances, truncation of V after the cubic term is valid.[38] Hence, noting that mechanical perturbation directly excites phonon states in a crystal (mainly acoustic modes),[35] this model describes a process whereby the excited phonon state could transfer energy to an internal vibrational mode by coupling to a third normal mode with intermediate frequency: *vibrational up-pumping*.

The rate at which this up-pumping occurs between any set of three modes depends on the strength of their anharmonic coupling, *i.e.* the second term of V. Because the intermolecular potential is more anharmonic than the intramolecular potential, coupling processes that include higher numbers of external modes (q) are dominant over processes that contain higher numbers of internal modes (Q). Calculations on naphthalene[39] suggested the coupling to decrease by an order of magnitude with inclusion of Q terms, hence $q_1 q_2 q_3 > Q_1 q_2 q_3 > Q_1 Q_2 q_3$. It follows that upon mechanical perturbation, the phonon

bath becomes excited, and equilibrates quickly (in the order of ps).[36] This leads to the formation of a vibrationally 'hot' phonon bath and a vibrationally 'cold' internal molecular manifold. This state of quasi-equilibrium evolves, with energy flowing upwards at rates in the order of 10s of ps. Hence, this model suggests an ability for energy transfer and localisation immediately behind a shock front,[40] and is consistent with prevailing theories of deflagration and detonation. These theories require primary decomposition reactions to occur on the time scale of ps.[41]

In the initial model proposed by Coffey and Toton,[35] a direct phonon up-conversion mechanism was proposed for RDX. Using a complete quantum mechanical model, the rate of energy transfer from a shock-excited phonon bath into a select vibrational mode in RDX was calculated. It was demonstrated that the localisation of energy due to up-pumping was sufficient to overcome the bond dissociation limit from a mild shock. This result was a crucial step in understanding localisation of shock energy and hot-spot formation.

The subsequent models proposed by Dlott[36,37,39,40] and colleagues instead suggested an indirect phonon up-pumping mechanism. Using heat flow models, they calculated the rate of energy up-pumping into the internal vibrational region. The initial model of Dlott and Fayer[36] considered only the excitation of so-called *doorway modes* (*i.e.* modes with frequencies less than twice the highest phonon frequency). However, subsequent models later included the effects of doorway mode up-pumping.[39] In these models, it was found that up-pumping occurs in three stages: (1) equilibration of phonon modes within a time period of < 2 ps, (2) excitation of doorway modes, and (3) up-pumping of doorway modes only a few ps later. Hence, while the rate-limiting step is indeed excitation of the doorway modes, additional up-pumping occurs almost immediately afterwards. Additional work by Toton[42] and Bardo[43] also discussed the addition of shock pressure in models of nitromethane, where the pressure response of the vibrational density of states led to changes in reaction rates according to the up-pumping model.

Both Coffey[35] and Dlott[36,40] noted a particularly intriguing feature of this model. Defect sites within the crystalline lattice introduce points of extreme vibrational anharmonicity. Hence, the strength of anharmonic coupling in the vicinity of a defect is larger and the corresponding rate of up-pumping to these sites is greater, Figure 1.7. This offered a mechanism for the localisation of energy near defect sites, and thus the role of internal defects in generating hot-spots.[25,26] However, the exact anharmonic enhancement introduced by defect sites remains unknown.

Hence, with these early fundamental developments, vibrational up-pumping appeared to offer a complete mechanism for the introduction, propagation and localisation of energy, capable of describing initiation of EMs. The phenomenon has been validated both experimentally and based on theoretical molecular dynamics simulations.[44–47]

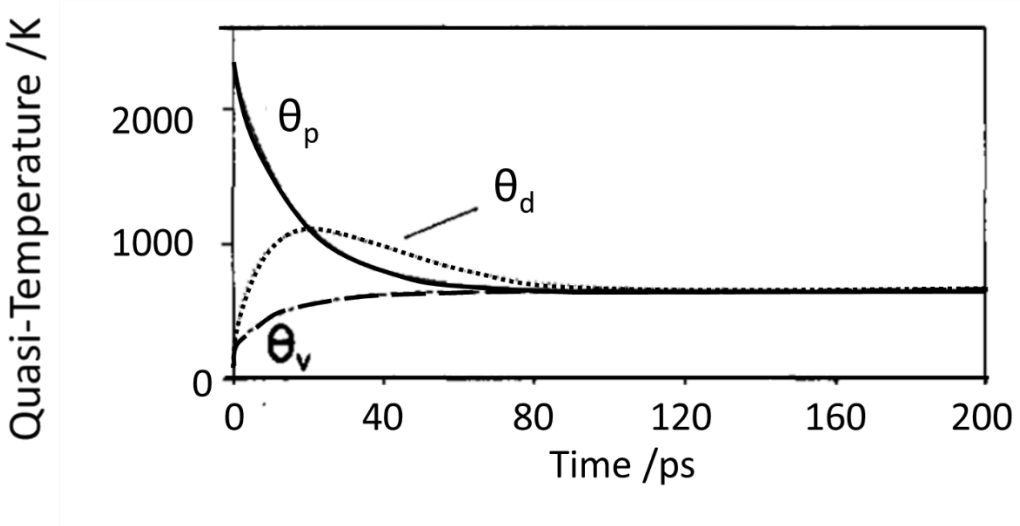

Figure 1.7: Time dependent vibrational quasi-temperatures for the phonon bath (θ_p), bulk vibrational manifold (θ_v) and defect sites (θ_d). Figure adapted from Ref. 36

1.3 Prediction and Rationalisation of Energetic Material Sensitivity

The initiation of energetic materials has been known for centuries. However, a consistent fundamental mechanism that underpins this phenomenon has not yet been established. Materials chemistry is now a well-developed field, with structure-property relations in many materials being thoroughly understood. Shock-wave physics is also well established. Hence, while tangential phenomena are largely understood, an understanding of the link between structure and detonation – *i.e*. initiation – remains elusive. A detailed understanding of the factors that govern the sensitivity of a material to the initiation of chemical reactions that occur under mechanical perturbation has yet to be obtained. More than most other criteria, the inability to target low-sensitivity compounds has placed one of the greatest limitations on the potential for selective and rational development of new energetic technologies.

This problem has attracted considerable attention in recent decades,[48–50] with much interest in discovering the single (or set of) physical parameters that can be used to rationalise and predict a potential material's sensitivity. This is a particularly challenging problem on account of the complex interplay of chemical and physical events spanning many scales of time and length,[51] as well as the poor consistency of experimentally reported impact sensitivities.[52] Correspondingly, many models have been developed to predict and rationalise the sensitivity properties of EMs. Broadly, these can be grouped into three approaches, based (1) on the properties of the isolated molecule, (2) on the properties of the solid state, and (3) on macroscopic descriptors. Typically, correlations are made against impact sensitivity data reported as the height at which a drop hammer test will induce initiation with 50% probability, dubbed h_{50}. For the purpose of the following, discussion will be limited to the main models that are aimed at predicting sensitivity to mechanical stimulation.

1.3.1 Isolated Molecule Methods

Much of the work that has attempted to rationalise the impact sensitivity of EMs is based on the study of isolated molecules. Initially, this was a consequence

of limited access to crystal structures of these compounds as well as limitations on computational methods. Numerous models were developed, and the relative simplicity of models based on isolated molecules keeps their development an ongoing area of research still today. Broadly, they can be classified into methods based on structural parameters and those based on quantum-mechanical properties.

1.3.1.1 Empirical Fitting of Molecular Descriptors

Many attempts have been made to develop fully empirical fits between molecular descriptors and sensitivities. These methods have been particularly popular for large-scale screening programmes, and indeed amongst the most powerful, although they offer no physical mechanism for their success. For example, Keshavarz[53] proposed a general equation based on chemical composition that was able to fit the impact sensitivities of EM compounds with formula $C_{a'}$ $H_{b'}$ $N_{c'}$ $O_{d'}$,

$$\log(h_{50}) = c_1 a' + c_2 b' + c_3 c' + c_4 d'$$

Equation 1.3

where $c_1 - c_4$ are adjustable fitting parameters. It was found that by adjusting the relative coefficients, a broad range of structural types could be analysed. However, this fitting remains limited to families of compounds. A variety of similar equations have also been proposed,[54–56] and have generally offered an excellent and rapid means to assess impact sensitivity of large libraries of materials.

In a similar fashion, empirical models based on molecular descriptors have become a popular approach, known as the Quantitative Structure-Property Relation (QSPR) methods. In these methods, a large number of molecular descriptors are chosen, including ionisation potentials, electrostatic potentials, oxygen balance, molecular orbital energies, bond lengths, and many others. Regression models are subsequently established on large databases and empirical equations established. Early QSPR-based models employed

structural descriptors, with Fayet[57,58] being amongst the first to employ quantum-mechanical descriptors for EMs.

Based on a series of 300 quantum-mechanical molecular descriptors, Fayet[58] investigated the impact sensitivity of a total of 161 nitro compounds, separated into three structural classes, using the QSPR approach. For each class of materials, this proved very promising, with $R^2 > 0.8$ in each case. The inability to produce stronger correlations was largely ascribed to poor experimental data.[58,59] A similar approach was also based on 61 non-quantum mechanical descriptors.[59] Other authors have employed considerably smaller numbers of descriptors. Badder and co-workers,[60] for example, built a QSPR model for 10 nitro compounds based on eight quantum-mechanical descriptors, with Shu[61] employing as few as two (nitro group charge and oxygen balance) descriptors. In both cases, reasonable models were obtained for the small test set of nitro-based compounds studied.

While these empirical methods are promising as screening tools, they offer no physical insight into sensitivity properties.

1.3.1.2 Oxygen Balance

Based on the assumption that structurally related compounds should undergo similar decomposition pathways, Kamlet[62] and subsequently Kamlet and Adolph[63] proposed a comparison of the impact sensitivity of a compound against its oxygen balance (OB). The OB was suggested to be relevant as it describes the ability of a molecule to oxidise itself. That is, compounds that contain sufficient oxygen to convert all nitrogen to NO_2, all carbon to CO_2 and all H to H_2O. For C-H-N-O molecules, this is defined as[63]

$$OB_{100} = \frac{100(2n_o - n_h - 2n_c - 2n_{coo})}{M_w}$$

Equation 1.4

Across a series of over 70 compounds,[62] a logarithmic correlation between the 50% impact heights (h_{50}) and OB. However, the compounds were found to

follow two different trends, depending on the structural features. For example, compounds with the same number and relative position of nitro groups followed trends, or compounds with/without α-C-H linkage followed their own trends (see Figure 1.8). This method has since been applied numerous times in the literature,[64] often with very good results. However, these methods are largely restricted to correlations within structural types, and cannot establish correlations between these series – even for structurally similar compounds like TNT and picric acid (see structures in Figure 1.1). If trend lines are mixed, TNT is predicted to be much more sensitive than Picric acid, Figure 1.8.

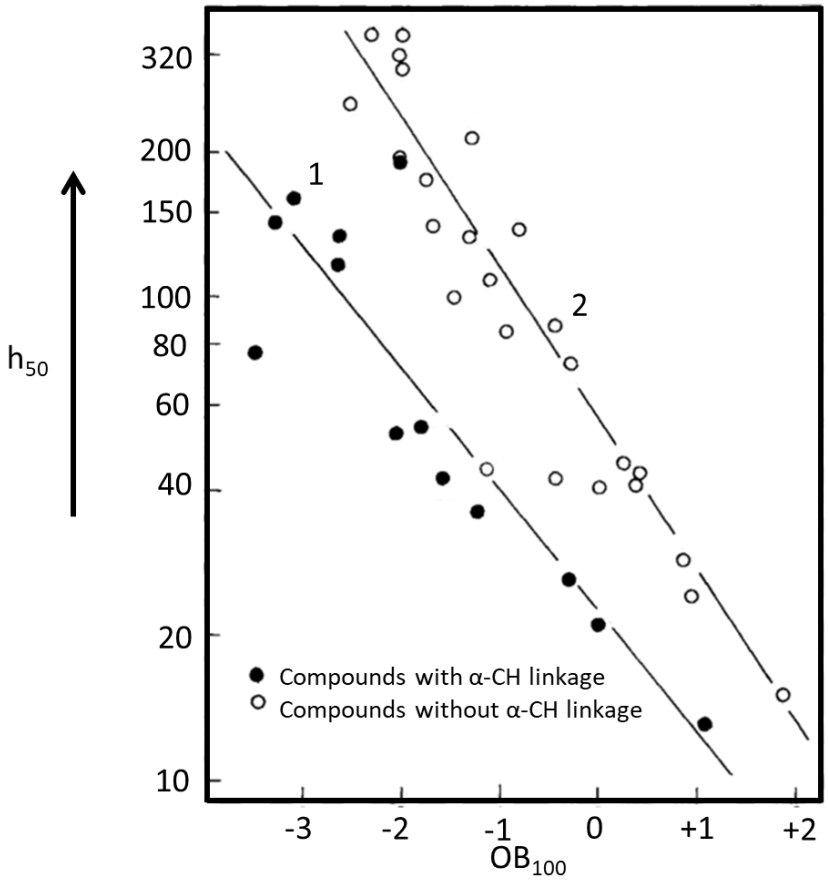

Figure 1.8: Correlation of impact sensitivity against OB_{100} for a series of polynitroaromiatic compounds. Closed circles are molecules with α-CH linkage (*e.g.* TNT, #1), and open circles do not (*e.g.* picric acid, #2). Figure adapted from Ref. 63

1.3.1.3 NMR Chemical Shift

The chemical shifts obtained in NMR are strongly dependent on the electronic structure of the molecule. It was therefore proposed that these chemical shifts should reflect the relative bond strength of a structural moiety to the molecule backbone, and thus give an indication of the stability of the structure. Correlations were initially made by Owens[65] between the ^{1}H NMR chemical shifts and the impact sensitivity of trinitroarene compounds. A similar model was subsequently extended based on ^{15}N and ^{13}C NMR chemical shifts by Zeman.[66–68] It has also been extended to the investigation of friction sensitivities.[69] While this has not yet become a widespread approach, it has demonstrated itself as a powerful method for predicting impact sensitivities of related compounds, Figure 1.9. However, it is evident that no reliable information can be obtained by this method if structurally unrelated compounds are compared.

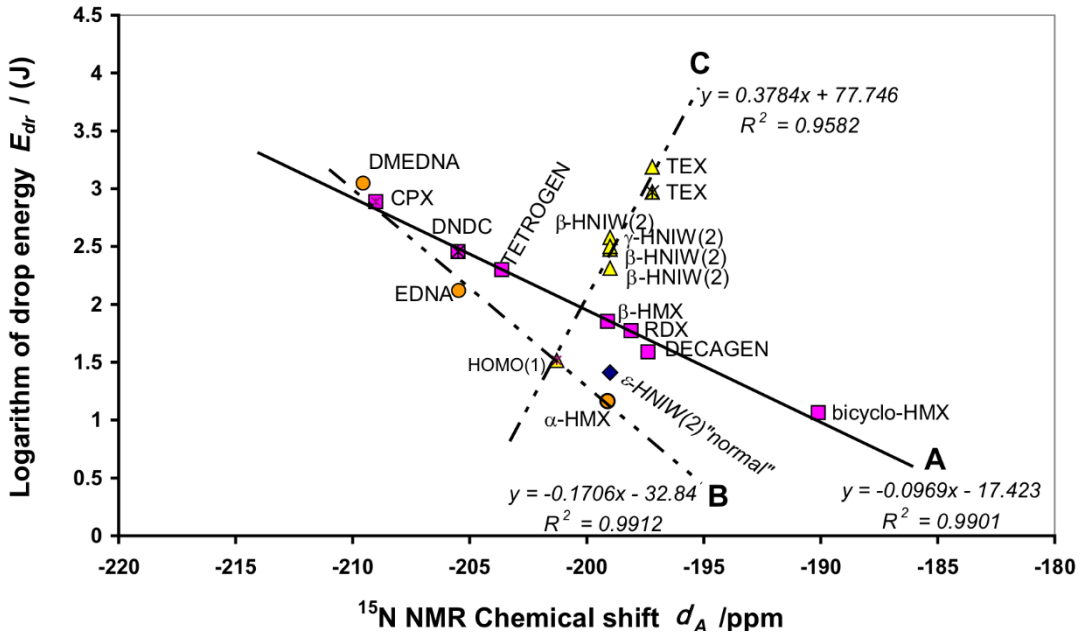

Figure 1.9: Comparison of impact drop energy (E_{dr}) against ^{15}N NMR chemical shifts of the aza nitrogen atoms to which -NO_2 groups are attached. These are chosen as they are believed to be involved in the initial step of initiation. Figure from Ref. 67

1.3.1.4 Bond Energies and Dissociation

A very popular method to investigate impact sensitivity (as well as thermal stability) of EMs has been based on the *ab initio* study of bond dissociation energies. The first *ab initio* results to this effect were performed at the Hartree-Fock level with a STO-3G basis set by Owens *et al.*[70] Owens demonstrated that the electronic density at the mid-point of the C-NO_2 bonds in a series of EMs correlated well with sensitivity, Figure 1.10A. Similar studies were performed by other groups, and the correlation substantiated further.[71] From this stemmed additional work in which these -NO_2 moieties were computationally cleaved, and the dissociation barriers hence calculated.[72] The first attempt at comparing these dissociation barriers to impact sensitivity was suggested by Rice and co-workers and gave promising results, Figure 1.10B.[73] This method continues to be a popular means to assess the stability and sensitivity of EMs. It has been applied to a variety of materials.[74,75] However, a thorough analysis by Mathieu has demonstrated that the correlation of bond dissociation energies against impact sensitivities only holds across families of structurally-related compounds.[76] Despite its widespread use, the investigation of bond dissociation, or the concept of the 'trigger linkage'[63] assumes a simple, single-step decomposition model. Such models have been widely debated, with both experimental[77] and theoretical results[77–80] for various molecular energetic materials suggesting more complex pathways are more likely. Often, decomposition may instead occur following a series of intramolecular isomerisation processes, such as C-NO_2 → C-O-NO.[77–80] In such cases, an understanding of the dissociation barriers of C-NO_2 may be limited in its use. Hence the physical basis for studying BDEs is limited, although its limits are not yet known.

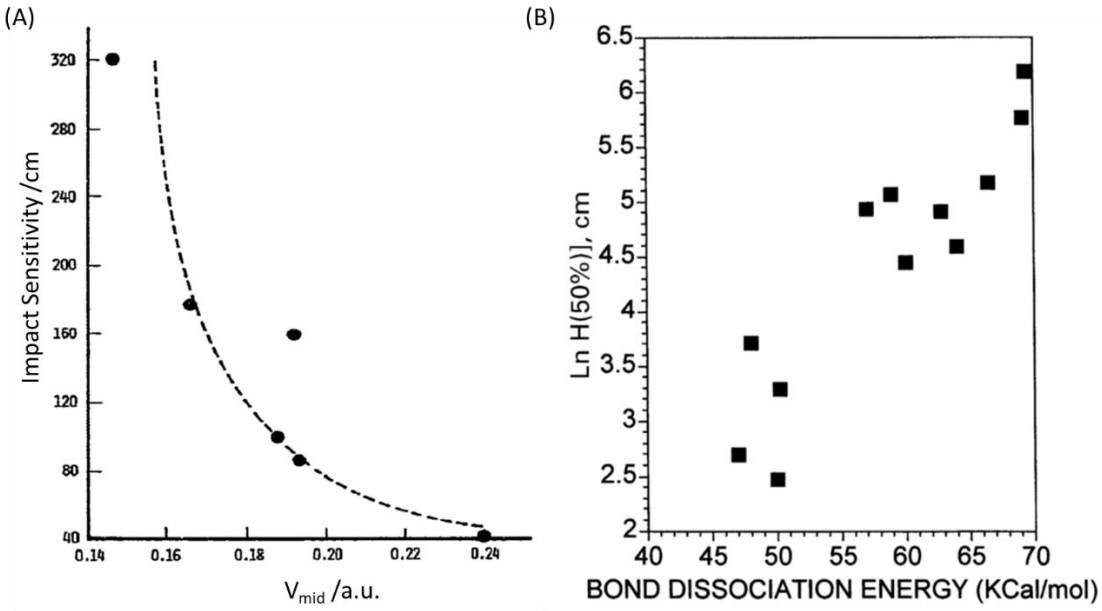

Figure 1.10: Correlations of C-NO_2 bond energies and impact sensitivity. (A) Correlation of the electron density at the C-NO_2 bond mid-point against sensitivity. From Ref 65 (B) Correlation of C-NO_2 bond dissociation energy and impact sensitivity. From Ref 73.

Largely based on the early findings by Owens *et al,*[70] it has been suggested that much of the information regarding bond dissociation energies can be obtained from a much simpler calculation: the electrostatic potential.[81] This methodology has been largely pioneered by Politzer and co-workers,[82] and has been applied to molecular and ionic energetic species.[83] Qualitative analysis of the electrostatic potential surfaces has been used to rank impact sensitivity, noting that molecules with more positive potentials tend to be more sensitive, Figure 1.11.[82,84] This can largely be rationalised by a lower electron density and hence decreased stabilisation of the molecule. However, Politzer suggested use of a set of descriptors – the first to describe the average deviation of the electrostatic potential across a bond, and a second to indicate the maximum value of the potential.[84] The former is taken to describe the charge separation, and hence the covalency of the bond, with the latter a measure of the maximum interaction strength, noting that the interaction energy is proportional to charge density.[85–87] Numerous studies have employed investigation of the electrostatic potential to rationalise impact sensitivities.[88–93] However, many of these investigations tend to conduct such

studies on small subsets of molecules, and therefore the wider applicability of this approach is unknown. However, it is reasonable to assume that it will also be limited to subsets of molecules that exhibit similar electronic structures.

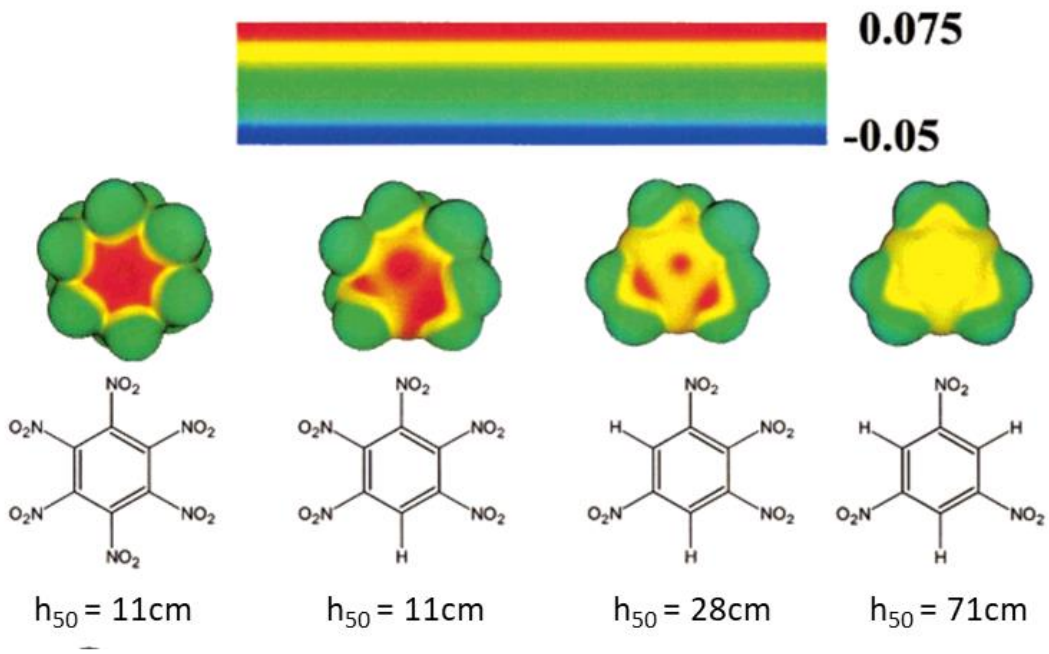

Figure 1.11: Electrostatic potential surfaces for polynitroaromatic molecules. Surfaces were calculated at B3LYP/6-31G* level and coloured according to the legend at the top of the figure. The experimental drop heights (h_{50}) are given below. Figure and values from Ref 88.

1.3.2 Solid State Methods

Despite the progress made in predicting properties of materials from isolated molecules, such models are limited. For example, description of the isolated molecule cannot rationalise the effects of polymorphism[16,94] or multi-component crystallisation[12] on sensitivity properties. This has led many researchers to move towards investigating mechanisms based on the crystalline state.

1.3.2.1 Crystal Packing and Non-Covalent Interactions

A number of authors have suggested structural arguments to rationalise impact sensitivity. The instantaneous, adiabatic compression of a solid leads to an increase in its final equilibrium temperature. The more compressible is the material, the higher the final temperature. Politzer and co-workers[95,96] therefore suggested that a simple trend for impact sensitivity could be sought in calculation of the free volume per molecule within the unit cell,

$$\Delta V = S/Z$$

Equation 1.5

where Z is the number of molecules and S is the free space

$$S = V_{cell}(1 - \text{packing coefficient})$$

Equation 1.6

Very simple in its approach, this method appeared to offer reasonable results, Figure 1.12. However, these results proved to be highly system dependent, with different types of EMs following considerably different trends.

The crystalline state is characterised by the type of intermolecular interactions it contains. This has led many authors to seek sensitivity arguments based on a study of these intermolecular interactions. Cartwright and Wilkinson[97] for example, suggested that compression of solids leads to formation of new intermolecular contacts, permitting bimolecular reactions to occur. Their investigation of a series of inorganic azides therefore focused on correlating impact sensitivity against the distance between nearest non-bonded nitrogen atoms. A number of authors have also attempted to correlate the type and strength of intermolecular interactions with sensitivity,[16,93,98,99] with findings that larger numbers of strong intermolecular interactions tend to reduce the sensitivity of EMs.

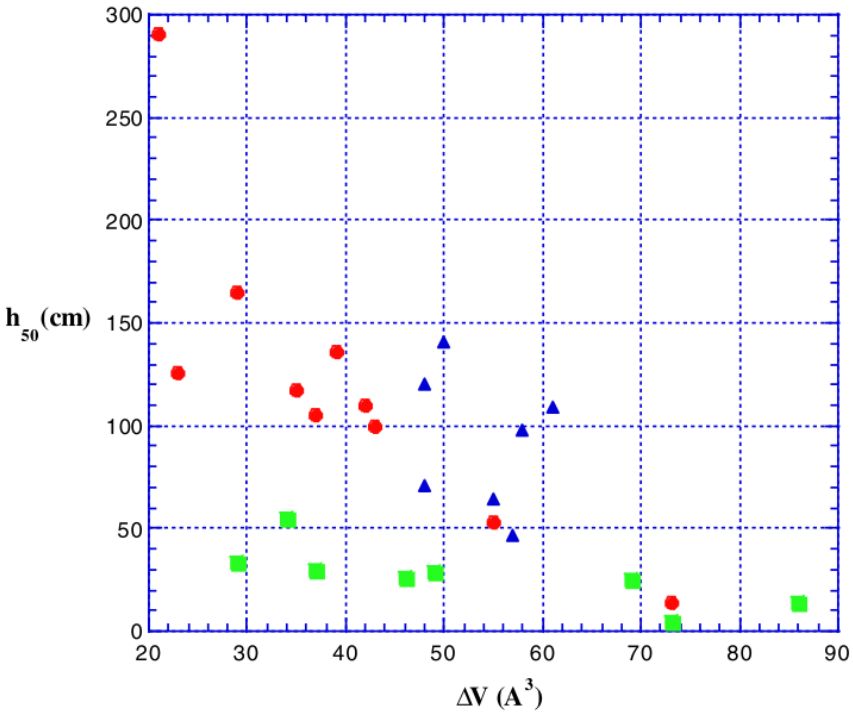

Figure 1.12: Experimental impact sensitivity (h_{50}) against free space per molecule in the unit cell, ΔV. Data are shown for (green) nitramines, (blue) nitroaromatics and (red) other EMs that do not fit these categories. Figure from Ref 95.

Analysis of the crystal packing arrangements in crystalline materials has been suggested as an alternative method to rationalise impact sensitivity. Early work by Coffey[100] suggested that the rate of plastic deformation in EMs could be linked to sensitivity. This was recently developed somewhat tangentially by Zhang,[101] as well as Shreeve and co-workers[92] who constructed a model based on the accumulation of energy due to mechanical strain. They suggested that studying the deformation potential associated with different lattice structures could therefore help to rationalise impact sensitivity. For a pair of multi-component crystals, it was found that packing which included non-layered components had substantially larger deformation potentials than the herringbone structure, Figure 1.13A. The material with larger deformation potential (and hence stored strain energy) was indeed found to be more sensitive. The same analysis was performed for RDX (a sensitive secondary

explosive) and compared to a layered compound, Figure 1.13B.[102] Again, it was shown that in the layered material, lower deformation potentials arose. Hence a structural mechanism for impact sensitivity was proposed. This has led to interest in studying the relative strengths of non-covalent interactions, primarily π … π and hydrogen bonding interactions, which contribute to these deformation potentials.[103,104] A recent study of PETN derivatives has also suggested that the deformability (*e.g.* shear or compression) does correlate well with impact sensitivity.[105] While these approaches have proved an intriguing direction for further research, it has not yet been thoroughly investigated against a broad range of EMs.

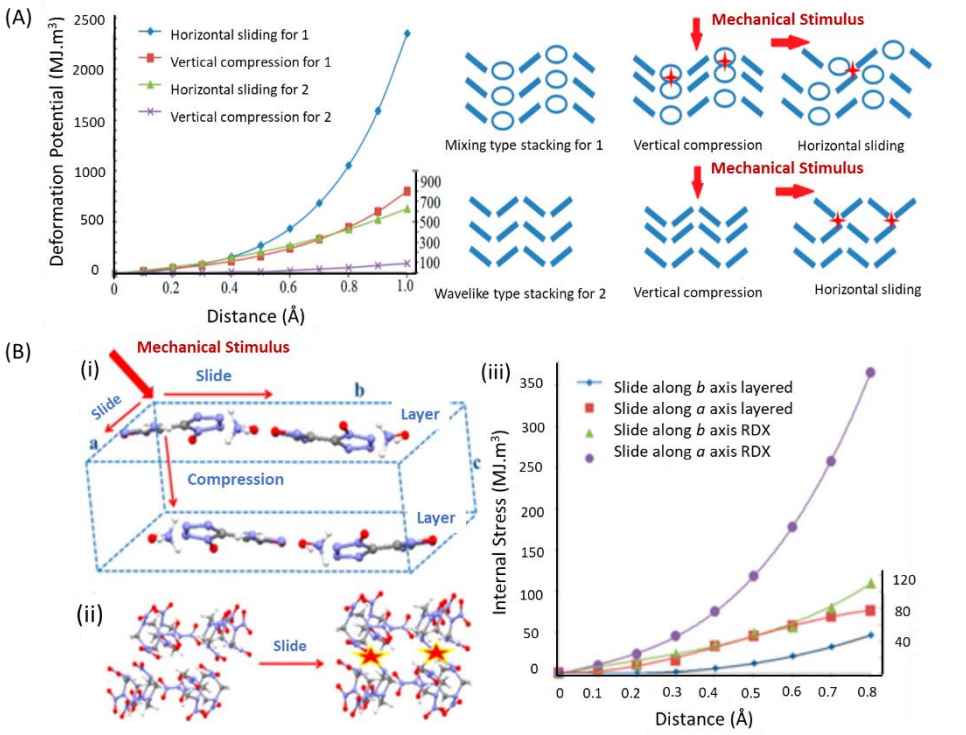

Figure 1.13: Correlation of deformation energy to impact sensitivity. (A) Comparison of deformation energies in two multi-component materials with different packing arrangements from Ref 92. (B) Comparison of deformation energies in layered vs non-layered materials, from Ref. 102

1.3.2.2 Electronic Band Gap Criterion and Band Gap Dynamics

Amongst the most popular solid state criteria for assessing impact sensitivity is the 'band-gap criterion'.[106,107] Noting that bond dissociation requires population of anti-bonding states, this simple analysis is based on consideration of the energy gap between the valence and conduction bands. Within this approach, materials with larger band gaps (*i.e.* those whose electronic transitions are less probable) are less sensitive. While extensive investigation of this band gap criterion is limited, it has been applied with varying success. Perhaps the largest drawback to this approach is the unreliable calculation of electronic band gaps within most commonly available computational methods,[108] and the lack of experimental band gap data.

Several authors have expanded this concept to dynamic phenomena. In a similar spirit to the work of Shreeve and co-workers,[92] Kuklja[109–111] investigated the electronic structure of both α-FOX-7 and TATB as a function of different lattice deformations. Rather than focussing on the deformation potential itself, Kuklja studied the resulting changes in the electronic band gap and bond dissociation energy at the interface between sheared planes, Figure 1.14A and 1.14B. Under sufficient shear the band gap of FOX-7 dropped to zero, and the dissociation energy of $-NO_2$ dropped considerably. In contrast, shear deformation had no notable influence on the dissociation energy of the $-NO_2$ moieties of TATB,[111] Figure 1.14B, although Manaa[112] did identify a large reduction (albeit not to metallisation) in its electronic band gap. This was suggested as a rationale for the different sensitivities of these compounds.

The effect of shear in α-FOX-7 is particularly noteworthy. The decomposition of FOX-7 is generally believed to pass *via* $-NO_2 \rightarrow -ONO$ isomerisation.[77] This renders comparison of $-NO_2$ dissociation energies largely irrelevant (Section 1.3.1.4). However, it was found[113] that under shear strain, direct $-NO_2$ scission at the interface of shear planes becomes more favourable than isomerisation. Hence, if shear deformation is considered, a comparison of $-NO_2$ dissociation energies again become important. This offers an excellent example of the complex interplay of physical and chemical phenomena in the initiation of EMs.

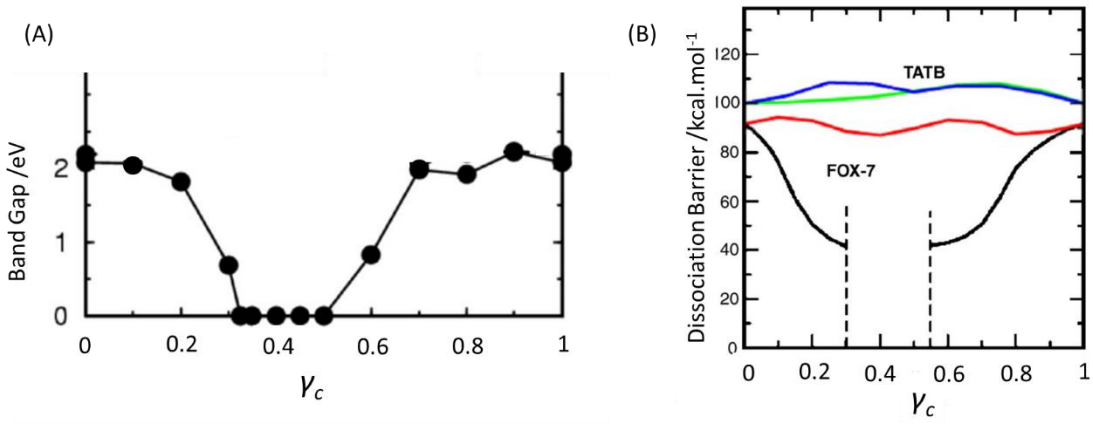

Figure 1.14: Effect of shear deformation on the electronic structure of α-FOX-7 and TATB. Figures adapted from Refs. 110 and 111.

The dynamic nature of electronic band gaps was recently re-examined by Bondarchuk.[114] Again, based on the need to induce electronic excitation, Bondarchuk investigated the propensity of organic materials to 'metallise' (*i.e.* reach a band gap of 0 eV) upon compression. Using a combination of particle shape, Ψ, melting temperature, T_m, the number of electrons per atom, N_F, the explosive energy content, E_c, and the metallization pressure, P_{trigg}, experimental impact sensitivity was fit to a so-called *sensitivity function*,

$$\Omega = \frac{\Psi T_m^2}{N_F^7} exp\left(P_{trigg}/1000\right) exp(E_c/1000)$$

Equation 1.7

This led to a relatively good correlation against experimental results (R^2=0.83). However, despite the seemingly good correlation, this method offers no real physical rationale for sensitivity.

1.3.3 Kinetic Models

A relatively new approach to the study of impact sensitivity is based on kinetic considerations. Pioneered by Mathieu,[76,115] these models assume that impact sensitivity is proportional to the rate of propagation of the initial decomposition step, *i.e.* X-NO_2 bond scission for nitro-containing compounds. If propagation

is too slow, localised energy dissipates away from the reactive sites, and self-sustained decomposition does not occur. This model states that the impact sensitivity (h_{50}) is given by[116,117]

$$h_{50} = \left(\mathrm{k_c}/k_{pr}\right)^n$$

Equation 1.8

where k_{pr} is the rate constant for the propagation of the primary decomposition pathway, k_c is a fitted parameter, and *n* is the order of the reaction and must be > 0. The rate constant is subsequently constructed as a function of the number of atoms in a molecule N_A, bond dissociation energies, D_i, the energy released due to decomposition of the first molecule, E_c, and a set of scaling parameters, *c* and Z_i. This yields

$$k_{pr} = N_A^{-1} \sum_i Z_i \, exp\left(\frac{-cD_iN_A}{E_c}\right)$$

Equation 1.9

where the sum is over all possible X-NO_2 scission pathways, *i*, with additional summation terms required for each identify of X (*i.e.* O-NO_2 vs C-NO_2).[116] Based on a limited set of input parameters, a QSPR-type regression is subsequently performed to obtain values of *c* and Z_i. Despite the mathematical similarity to QSPR methods, the physical basis used in developing this model has allowed a reduction in the number of required parameters (from hundreds to only three), and better correlations to large datasets.[118]

Excellent correlations have been obtained using this approach, with $R^2 > 0.8$ based on diverse datasets of 93 nitroaliphatic compounds.[118] This could be extended to a larger dataset (156 compounds) including nitroaromatic compounds with the addition of one extra fitted parameter to reflect an additional bond type, Figure 1.15.[116]

Based on a physical model of impact-induced reactions, these semi-empirical methods have proved very powerful for the rationalisation and prediction of impact sensitivities.

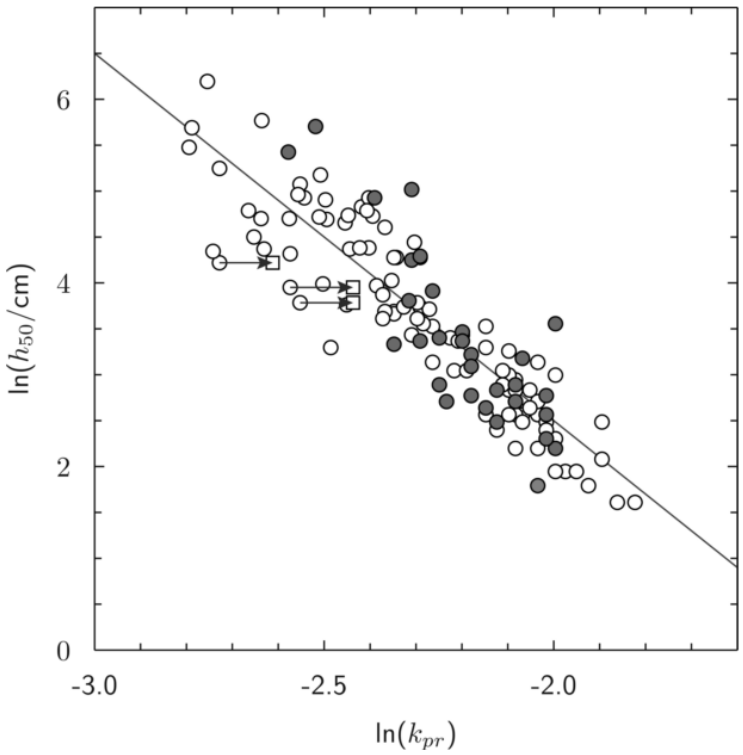

Figure 1.15: Correlation of experimental sensitivity against k_{pr}. Test set includes a diverse range of molecules with -NO_2 based explosophores. Grey circles include carbonyl moieties. Figure from Ref 116

1.3.4 Vibrational Up-pumping: A Tool for Prediction

While many of the models discussed above describe decomposition processes, none are based on the relative rates of energy localisation and subsequent formation of hot-spots in EMs. To this end, models based on vibrational up-pumping (Section 1.2.2) have been considered.

Since its conceptual development in the 1980/90s,[36,39,40] and experimental validation[44] of the up-pumping phenomenon by Dlott and colleagues, there

have been a number of attempts at employing up-pumping models to predicting impact sensitivity. The initial numerical analyses by Dlott and co-workers[36] were based on rigorous heat-flow models and set out a detailed understanding of the phenomenon of vibrational up-pumping. These concepts formed the base for simplified models capable of spanning a range of materials.

Perhaps the first attempt at rationalising sensitivities using an up-pumping model was that by Fried and Ruggiero.[119] In their early model, the vibrational density of states of a set of energetic materials was generated from inelastic neutron scattering spectra, Figure 1.16A. A kinetic model for the up-conversion of energy was developed based on the two-phonon density of states and the temperature-dependent populations. Despite the very limited quality of data (limited both by data resolution and the maximum measurable energy transfer), the resulting trend in predicted sensitivities was very promising, Figure 1.16B. Importantly, vibrational energy transfer was not considered above 600 cm^{-1}, although this was primarily the result of the experimental limitations at the time. A similar approach was taken by Koshi more recently, which included lattice dynamics calculations of phonon density of states.[120]

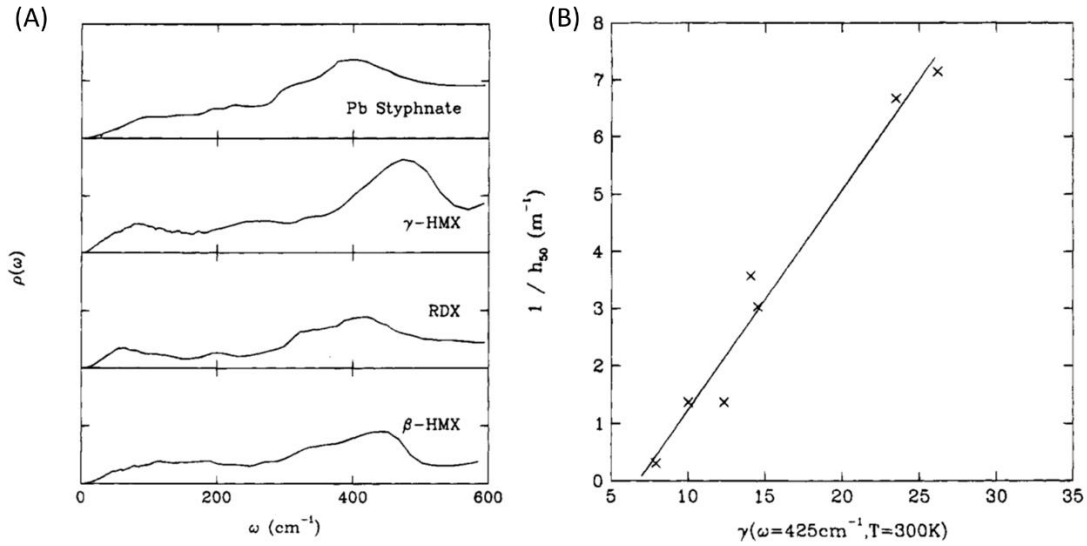

Figure 1.16: Vibrational up-pumping model of Fried and Ruggiero. (A) Phonon density of states derived from inelastic neutron spectra. (B) Predicted sensitivity ordering based on up-conversion rates into a select vibrational mode ($\omega = 425$ cm^{-1}) at 300 K. Figures adapted from Ref 119.

McNesby and Coffey[121] subsequently built a model based on experimental Raman spectroscopy. In their model, the assumption was made that the rate-determining step in vibrational up-pumping is the transfer of energy from the phonon manifold to the doorway region, consistent with prevailing theory. The phonon bath was arbitrarily defined as modes with $\omega < 250\,\text{cm}^{-1}$. Following on from the work by Fried and Ruggiero,[119] all up-pumping into the region with $\omega < 700\,\text{cm}^{-1}$ was considered, based on a kinetic analysis of the harmonic overtones. Following from Fermi's Golden Rule, overtone modes that were off-resonance with a doorway mode scattered more slowly. Despite the assumptions made, this proved promising in predicting the relative ordering of impact sensitivities, Figure 1.17.

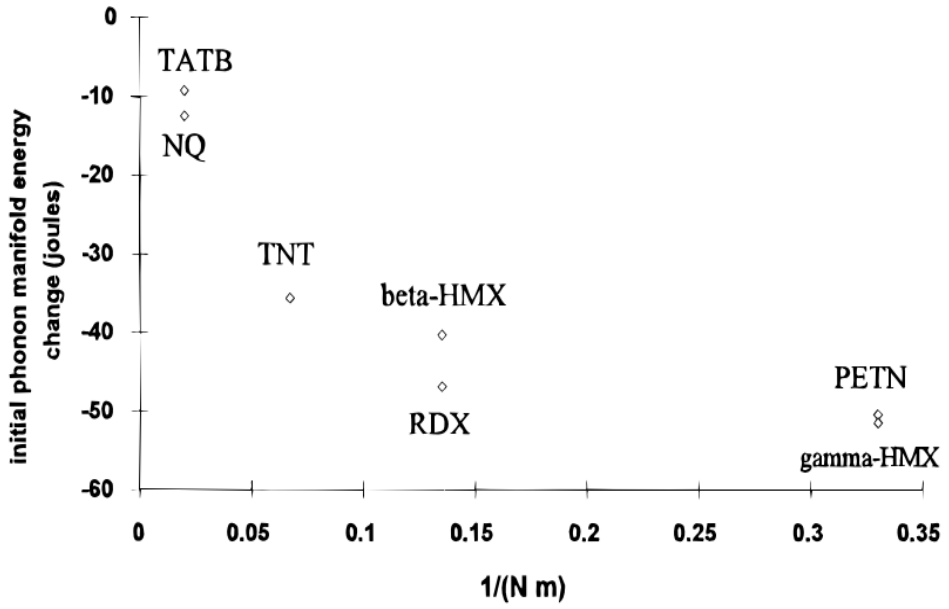

Figure 1.17: Relative rate of energy up-conversion to the doorway region for a series of energetic materials. Note the exponential trend. Figure from Ref 121

Koshi[122] was subsequently first to employ an approach based on *ab initio* quantum mechanical calculations, and on a rate equation proposed by Dlott,[36]

$$\kappa = \frac{j\hbar\Omega}{\tau_1(0)\theta_e}$$

Equation 1.10

Here, j is the number of doorway modes with frequency Ω and 0 K lifetime τ_1. θ_e describes a temperature equivalence term, which describes the temperature at which the rate of transfer *into* a doorway mode is the same as the low temperature rate at which it transfers *out* of this same doorway mode by two-phonon emission

$$n_{\Omega/2}(\theta_e) - n_{\Omega}(\theta_e) = 1$$

Equation 1.11

Noting that Ω/θ_e is constant, and noting that $\tau_1(0)$ is approximately constant for organic EMs (*ca.* 2-6 ps),[40] Koshi argued that the rate of energy transfer therefore depends *only* on the number of doorway modes. Noting the discrepancy in the upper limit of the doorway region in earlier studies, the doorway region was varied with $2\Omega_{max}$ set at 500, 600 and 700 cm^{-1} and the number of doorway modes counted in each material. The gas-phase frequencies were calculated, and the number of doorway modes correlated well with experimental impact sensitivities Figure 1.18.

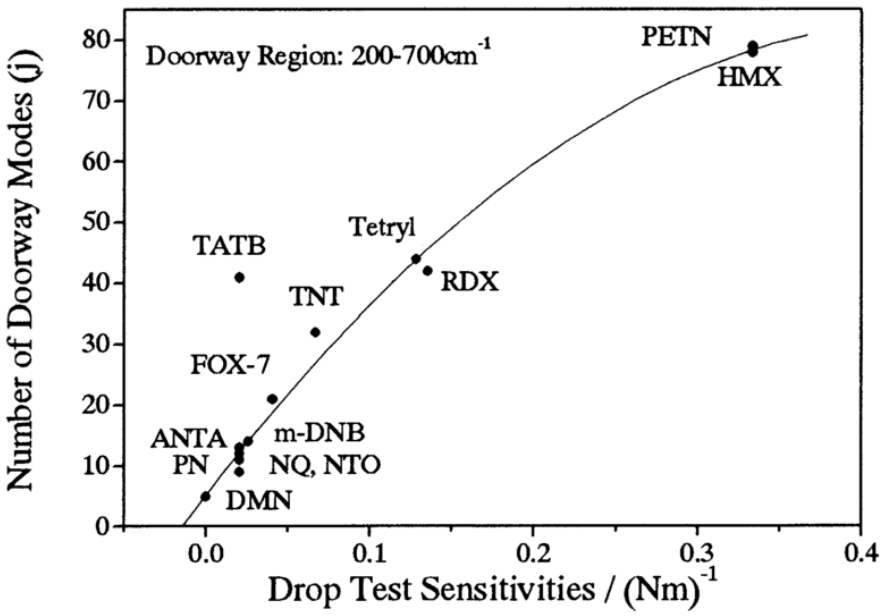

Figure 1.18: Comparison of the number of doorway modes in a series of EMs and experimental impact sensitivities. Doorway mode frequencies were based on *ab initio* calculations. Figure from Ref.122

Very recently, Bernstein[123] has expanded on this method. The frequencies of crystalline materials were calculated by *ab initio* methods, and the harmonic overtones extrapolate. Bernstein subsequently correlated the number of overtone frequencies that were 'near resonant' (*i.e.* $\omega \pm 10$) with fundamental doorway modes in the region $200 < \omega < 700$ cm^{-1}. Again, this led to good correlation with experiment.

The major drawback to these studies has been an inability to directly calculate the anharmonic coupling constants, which depend on the material and associated vibrational frequencies. While it is in principle possible to calculate these from *ab initio* methods, computational approaches are currently too intensive. Most studies have assumed these to be constant for all materials, while some have attempted to approximate them based on simple force-field potentials.[120] Most recently, McGrane[124,125] considered vibrational up-pumping in HMX, TATB and PETN by extracting the anharmonic potentials from high resolution Raman spectra. All three materials were found to exhibit similar average anharmonicities, and therefore lends validation to previous models in which this term is neglected.

These models have proved very promising. The rather limited application of these models in the last 20 years can only be ascribed to their difficulty. Calculation of the vibrational structure is a long, arduous task that has only recently become computationally feasible. Furthermore, the quality of spectroscopic data, and in particular inelastic neutron scattering data, has only reached sufficiently high resolution in recent years.[126] Moreover, previous models have varied largely in their assumptions and no thorough analysis has yet been undertaken. It is therefore very timely to re-examine this model as a physical basis from which to understand mechanically-induced reactions in EMs.

1.4 Research Concept and Aims

The development of new EMs is an active area of fundamental research. Amongst the main target characteristics of new EMs, ensuring low sensitivity to mechanical perturbation is simultaneously a top priority and notoriously difficult. This difficulty is largely due to the fact that no underlying mechanism for EM sensitivity is yet known.

It is generally accepted that initiation of an EM requires localisation of energy within the material. This localisation can be described by hot-spots. The origin of these hot-spots remains widely debated, although a number of mechanisms (Section 1.2) have been proposed. Some theories suggest hot-spots to be rooted in equilibrium temperature increases, while others describe non-equilibrium, athermal processes.

Many models (Section 1.3) have been proposed in an attempt to identify a set of physical parameters to understand and describe the impact sensitivity of EMs. The 'band gap criterion' remains the most popular amongst solid state models. While many models are promising, they often lack a physical basis and are restricted to subsets of energetic materials. A particularly promising physical model is rooted in the so-called *up-pumping* of vibrational energy (Section 1.2.2). This model describes the transfer of energy from an initial mechanical impulse, and the mechanism by which it transitions into localised molecular energy. Importantly, the up-pumping model is not isolated from previous hot-spot models, as the initial energy can originate *via* any phenomenon, including adiabatic compression, fracture, plastic deformation, contact stresses, amongst others. Hence, it offers a physical basis for converting hot-spot generation mechanisms into a chemical reaction. Considerable experimental work has validated the up-pumping phenomenon, and numerical modelling has been used to rationalise many of its general features. However, only very limited work has focused on applying these concepts to test sets of EMs for the prediction of impact sensitivity. Those that have done so have been based on low resolution inelastic neutron scattering

spectra,[119,120] or very limited consideration of vibrational structure from calculation,[123,124] or on Raman spectroscopy.[121] The models employed in these studies have been limited to very simple (and often different) energy-transfer models and typically require the inclusion of additional experimental data. Before a model based on up-pumping based model can therefore be employed to predict impact sensitivity, a fully *ab initio* model must be developed.

This work therefore conducted with the following aims:

- *Investigate the vibrational properties of a range of energetic materials.*
- *Consider possible target vibrational modes for simple EMs.*
- *Consider the 'band-gap criterion' for a range of EMs.*
- *Investigate the development and use of an up-pumping based ab initio model to predict the relative impact sensitivities of a range of energetic materials.*
- *Validate potential models against available experimental impact sensitivities.*
- *Unify previously proposed predictive up-pumping models into a single model.*

1.5 References

(1) Agrawal, J. P. *High Energy Materials*; Agrawal, J. P., Ed.; Wiley-VCH: Weinheim, 2010.

(2) Davis, T. L. Roger Bacon's Gunpowder and His Secret Wisdom. *Ind. Eng. Chem.* **1928**, *20* (7), 772–774.

(3) Akhavan, J. *The Chemistry of Explosives*, 3rd ed.; Akhavan, J., Ed.; Royal Society of Chemistry: Cambridge, UK, 2011.

(4) Klapötke, T. M. *Chemistry of High-Energy Materials*, 2nd ed.; Klapötke, T. M., Ed.; De Gruyter: Berlin, 2012.

(5) Nobel, A. Alfred Nobel, Inventor of Dynamite. *J. Chem. Educ.* **1928**, *5* (11), 1480.

(6) Medard, L. A. *Accidental Explosions Volume 2: Types of Explosive Substances*; Medard, L., Ed.; Wiley & Sons, Ltd.: New York, USA, 1989.

(7) Elbeih, A.; Jungová, M.; Zeman, S.; Vávra, P.; Akštein, Z. Explosive Strength and Impact Sensitivity of Several PBXs Based on Attractive Cyclic Nitramines. *Propellants, Explos. Pyrotech.* **2012**, *37* (3), 329–334.

(8) Cumming, A. S. New Trends in Advanced High Energy Materials. *J. Aerosp. Technol. Manag.* **2009**, *1* (2), 161–166.

(9) Doherty, R. M. Emerging Trends in Energetic Materials. In *Insensitive Munitions & Energetic Materials Technology Symposium (IMEMTS)*; Miami, Fl. USA, 2007.

(10) Powell, I. J. Insensitive Munitions – Design Principles and Technology Developments. *Propellants, Explos. Pyrotech.* **2016**, *41* (3), 409–413.

(11) Haller, T. M.; Rheingold, A. L.; Brill, T. B. Structure of the 1/1 Complex between HMX and NMP. *Acta. Cryst.* **1985**, *C41*, 963–965.

(12) Kennedy, S. R.; Pulham, C. R. Co-Crystallization of Energetic Materials. In *Co-crystals: Preparation, Characterization and Applications*; Aakeröy, C. B., Sinha, A. S., Eds.; Royal Society of Chemistry: Cambridge, UK, 2018; pp 231–266.

(13) Zhang, J.; Shreeve, J. M. Time for Pairing: Cocrystals as Advanced Energetic Materials. *CrystEngComm* **2016**, *18* (33), 6124–6133.

(14) Landenberger, K. B.; Matzger, A. J. Cocrystal Engineering of a Prototype Energetic Material: Supramolecular Chemistry of 2,4,6-Trinitrotoluene. *Cryst. Growth Des.* **2010**, *10* (12), 5341–5347.

(15) Landenberger, K. B.; Matzger, A. J. Cocrystals of 1,3,5,7-Tetranitro-1,3,5,7-Tetrazacyclooctane (HMX). *Cryst. Growth Des.* **2012**, *12* (7), 3603–3609.

(16) Bolton, O.; Simke, L. R.; Pagoria, P. F.; Matzger, A. J. High Power Explosive with Good Sensitivity: A 2:1 Cocrystal of CL-20:HMX. *Cryst. Growth Des.* **2012**, *12* (9), 4311–4314.

(17) *Chemistry and Physics of Energetic Materials*; Bulusu, S. N., Ed.; Kluwer Academic Publishers: Netherlands, 1990.

(18) Harris, P.; Presles, H. N. The Shock Induced Electrical Polarization of Water. *J. Chem. Phys.* **1982**, *77* (10), 5157–5164.

(19) Meyer, R.; Köhler, J.; Homburg, A. *Explosives*, 6th ed.; Meyer, R., Köhler, J., Homburg, A., Eds.; Wiley-VCH: Weinheim, 2007.

(20) Plets, V. *Zh. Obs. Khim.* **1953**, *5*, 173.

(21) Shackelford, S. A. A General Concept Concerning Energetic Material Sensitivity and Initiation. *J. Phys. IV* **1995**, *5* (C4), 485–499.

(22) Bowden, F. P.; Yoffe, A. D. *Initiation and Growth of Explosion in Liquids and Solids*; Cambridge University Press: Cambridge, UK, 1952.

(23) Bowden, F. P.; Yoffe, A. Hot Spots and the Initiation of Explosion. *Symp. Combust. Flame Explos. Phenom.* **1949**, *3* (1), 551–560.

(24) Balaz, P. Mechanochemistry and Nanoscience. In *Mechanochemistry in Nanoscience and Minerals Engineering*; Balaz, P., Ed.; Springer-Verlag: Berling Heidelberg, 2008; pp 1–102.

(25) Field, J. E.; Bourne, N. K.; Palmer, S. J. P.; Walley, S. M.; Sharma, J.; Beard, B. C. Hot-Spot Ignition Mechanisms for Explosives and Propellants. *Philos. Trans. R. Soc. A Math. Phys. Eng. Sci.* **1992**, *339* (1654), 269–283.

(26) Field, E. J. Hot Spot Ignition Mechanisms for Explosives. *Acc. Chem. Res.* **1992**, *25* (11), 489–496.

(27) Mader, C. L. Shock and Hot Spot Initiation of Homogeneous Explosives. *Phys. Fluids* **1963**, *6* (3), 375–381.

(28) Bowden, F. P.; Gurton, O. A. Birth and Growth of Explosion in Liquids and Solids Initiated by Impact and Friction. *Proc. R. Soc. London. Ser. A Math. Phys. Sci.* **1949**, *198* (1054), 350.

(29) Heinicke, G.; Sigrist, K. Heinicke, G. *Z. Chem.* **1971**, *11*, 226.

(30) Dickson, P. M.; Parker, G. R.; Smilowitz, L. B.; Zucker, J. M.; Asay, B. W. Frictional Heating and Ignition of Energetic Materials. *AIP Conf. Proc.* **2006**, *845 II*, 1057–1060.

(31) Frey, R. B. *The Initiation of Explosive Charges by Rapid Shear*; Aberdeen Proving Ground, MD, 1980.

(32) Recht, R. F. Catastrophic Thermoplastic Shear. *J. Appl. Mech.* **1964**, *31* (2), 189.

(33) Winter, R. E.; Field, J. E. The Role of Localized Plastic Flow in the Impact Initiation of Explosives. *Proc. R. Soc. London, Ser. A. Math. Eng. Phys. Sci.* **1975**, *343* (1634), 399–413.

(34) Mohan, V. .; Bhasu, V. C. J.; Field, J. E. Role of Adiabatic Shear Bands in Initiation of Explosives by Drop-Weight Impact. In *Ninth Symposium on Detonatino*; Portland, OR., 1989; pp 1276–1283.

(35) Coffey, C. S.; Toton, E. T. A Microscopic Theory of Compressive Wave-Induced Reactions in Solid Explosives. *J. Chem. Phys.* **1982**, *76* (2), 949–954.

(36) Dlott, D. D.; Fayer, M. D. Shocked Molecular Solids: Vibrational up Pumping, Defect Hot Spot Formation, and the Onset of Chemistry. *J. Chem. Phys.* **1990**, *92* (6), 3798–3812.

(37) Dlott, D. D. Ultrafast Vibrational Energy Transfer in the Real World: Laser Ablation, Energetic Solids, and Hemeproteins. *J. Opt. Soc. Am. B* **1990**, *7* (8), 1638.

(38) Hill, J. R.; Chronister, E. L.; Chang, T. C.; Kim, H.; Postlewaite, J. C.; Dlott, D. D. Vibrational Relaxation of Guest and Host in Mixed Molecular Crystals. *J. Chem. Phys.* **1988**, *88* (4), 2361–2371.

(39) Kim, H.; Dlott, D. D. Theory of Ultrahot Molecular Solids: Vibrational Cooling and Shock-Induced Multiphonon up Pumping in Crystalline Naphthalene. *J. Chem. Phys.* **1990**, *93* (3), 1695–1709.

(40) Tokmakoff, A.; Fayer, M. D.; Dlott, D. D. Chemical Reaction Initiation and Hot-Spot Formation in Shocked Energetic Molecular Materials. *J. Phys. Chem.* **1993**, *97* (9), 1901–1913.

(41) Walker, F. E. Physical Kinetics. *J. Appl. Phys.* **1988**, *63* (11), 5548–5554.

(42) Zerilli, F. J.; Toton, E. T. Shock-Induced Molecular Excitation in Solids. *Phys. Rev. B* **1984**, *29* (10), 5891–5902.

(43) Bardo, R. D. Theoretical Calculations of Rate-Determining Steps for Ignition of Shocked, Condensed Nitromethane. *Int. J. Quantum Chem.* **1986**, *30* (20 S), 455–469.

(44) Chen, S.; Tolbert, W. A.; Dlott, D. D. Direct Measurement of Ultrafast Multiphonon Up-Pumping in High Explosives. *J. Phys. Chem.* **1994**, *98* (32), 7759–7766.

(45) Joshi, K.; Losada, M.; Chaudhuri, S. Intermolecular Energy Transfer Dynamics at a Hot-Spot Interface in RDX Crystals. *J. Phys. Chem. A* **2016**, *120* (4), 477–489.

(46) Kraczek, B.; Chung, P. W. Investigation of Direct and Indirect Phonon-Mediated Bond Excitation in α-RDX. *J. Chem. Phys.* **2013**, *138* (7).

(47) Dlott, D. D. Multi-Phonon up-Pumpng in Energetic Materials. In *Overview of Recent Research on Energetic Materials*; Shaw, R. W., Brill, T. B., Thompson, D. L., Eds.; World Scientific, 2005; pp 303–333.

(48) Tsyshevsky, R. V.; Sharia, O.; Kuklja, M. M. Molecular Theory of Detonation Initiation: Insight from First Principles Modeling of the Decomposition Mechanisms of Organic Nitro Energetic Materials. *Molecules* **2016**, *21* (2).

(49) Zeman, S.; JungovÃ¡, M. Sensitivity and Performance of Energetic Materials. *Propellants, Explos. Pyrotech.* **2016**, *41* (3), 426–451.

(50) Yan, Q.-L.; Zeman, S. Theoretical Evaluation of Sensitivity and Thermal Stability for High Explosives Based on Quantum Chemistry Methods: A Brief Review. *Int. J. Quantum Chem.* **2013**, *113* (8), 1049–1061.

(51) Rice, B. M. A Perspective on Modeling the Multiscale Response of Energetic Materials. *AIP Conf. Proc.* **2017**, *1793*.

(52) Storm, C. B.; Stine, J. R.; Kramer, J. F. Sensitivity Relationships in Energetic Materials. In *Chemistry and Physics of Energetic Materials*; Bulusu, S. N., Ed.; Springer, Dordrecht, 1990; pp 605–639.

(53) Keshavarz, M. H.; Pouretedal, H. R. Simple Empirical Method for Prediction of Impact Sensitivity of Selected Class of Explosives. *J. Hazard. Mater.* **2005**, *124* (1–3), 27–33.

(54) Keshavarz, M. H.; Zali, A.; Shokrolahi, A. A Simple Approach for Predicting Impact Sensitivity of Polynitroheteroarenes. *J. Hazard. Mater.* **2009**, *166* (2–3), 1115–1119.

(55) Keshavarz, M. H. A New General Correlation for Predicting Impact Sensitivity of Energetic Compounds. *Propellants, Explos. Pyrotech.* **2013**, *38* (6), 754–760.

(56) Keshavarz, M. H. Simple Relationship for Predicting Impact Sensitivity of Nitroaromatics, Nitramines, and Nitroaliphatics. *Propellants, Explos. Pyrotech.* **2010**, *35* (2), 175–181.

(57) Fayet, G.; Rotureau, P.; Joubert, L.; Adamo, C. Predicting Explosibility Properties of Chemicals from Quantitative Structure-Property Relationships. *Process Saf. Prog.* **2010**, *29* (4), 359–371.

(58) Fayet, G.; Rotureau, P.; Prana, V.; Adamo, C. Global and Local QSPR Models to Predict the Impact Sensitivity of Nitro Compounds. *Glob. Congr. Process Saf. 2012 - Top. Conf. 2012 AIChE Spring Meet. 8th Glob. Congr. Process Saf.* **2012**, *1* (April), 254–270.

(59) Fayet, G.; Rotureau, P. Development of Simple QSPR Models for the Impact Sensitivity of Nitramines. *J. Loss Prev. Process Ind.* **2014**, *30* (1), 1–8.

(60) Badders, N. R.; Wei, C.; Aldeeb, A. A.; Rogers, W. J.; Mannan, M. S. Predicting the Impact Sensitivities of Polynitro Compounds Using Quantum Chemical Descriptors. *J. Energ. Mater.* **2006**, *24* (1), 17–33.

(61) Shuo, G. A QSPR Model for Prediction of the Impact Sensitivities of Some Nitro Compounds.

Adv. Mater. Res. **2013**, *641–642*, 109–112.

(62) Sixth Symposium on Detonation; Edwards, D. J., Jacobs, S. ., Eds.; Office of Naval Research-Department of the Navy: Coronado, California, 1976.

(63) Kamlet, M. J.; Adolph, H. G. The Relationship of Impact Sensitivity with Structure of Organic High Explosives. II. Polynitroaromatic Explosives. *Propellants, Explos. Pyrotech.* **1979**, *4* (2), 30–34.

(64) Skare, D.; Suceska, M. Study of Detonation Parameters of Polynitroadamantanes , Potential New Explosives . I . Molecular Mass / Density and Oxygen Content / Sensitivity Relationships . *Croat. Chem. Acta* **1998**, *71* (3), 765–776.

(65) Owens, F. J. Relationship between Impact Induced Reactivity of Trinitroaromatic Molecules and Their Molecular Structure. *J. Mol. Struct. THEOCHEM* **1985**, *22* (1–5), 213–220.

(66) Zeman, S. Relationship between Detonation Characteristics and 15n Nmr Chemical Shifts of Nitramines. *J. Energ. Mater.* **1999**, *17* (4), 305–329.

(67) Jungová, M.; zeman, S.; yan, Q.-L. Recent Advances in the Study of the Initiation of Nitramines by Impact Using Their ^{15}N NMR Chemical Shifts. *Cent. Eur. J. Energ. Mater.* **2014**, *11* (3), 383–393.

(68) Zeman, S. A Study of Chemical Micromechanism of the Organic Polynitro Compounds Initiation. In *Theoretical and Computational Chemistry, Energetic Materials. Part 2: Detonation, Combustion.*; Politzer, P., Murray, J. S., Eds.; Elsevier B.V.: Amsterdam, 2003; pp 25–52.

(69) Keshavarz, M. H.; Hayati, M.; Ghariban-Lavasani, S.; Zohari, N. A New Method for Predicting the Friction Sensitivity of Nitramines. *Cent. Eur. J. Energ. Mater.* **2015**, *12* (2), 215–227.

(70) Owens, F. J.; Jayasuriya, K.; Abrahmsen, L.; Politzer, P. Computational Analysis of Some Properties Associated With the Nitro Groups in Polynitroaromatic Molecules. *Chem. Phys. Lett.* **1985**, *116* (5), 434.

(71) Murray, J. S.; Politzer, P. Structure-Sensitivity Relationships in Energetic Compounds. In *Chemistry and Physics of Energetic Materials*; Bulusu, S. N., Ed.; Kluwer Academic Publishers: Netherlands, 1990; pp 157–158.

(72) Owens, F. J. Some Energetic Molecules. *J. Mol. Struct.* **1996**, *370*, 11–16.

(73) Rice, B. M.; Sahu, S.; Owens, F. J. Density Functional Calculations of Bond Dissociation Energies for NO 2 Scission in Some Nitroaromatic Molecules. *J. Mol. Struct. THEOCHEM* **2002**, *583* (1), 69–72.

(74) Li, J. Relationships for the Impact Sensitivities of Energetic C-Nitro Compounds Based on Bond Dissociation Energy. *J. Phys. Chem. B* **2010**, *114* (6), 2198–2202.

(75) Li, X.-H.; Han, D.-F.; Zhang, X.-Z. Investigation of Correlation between Impact Sensitivities and Bond Dissociation Energies in Benzenoid Nitro Compounds. *J. Struct. Chem.* **2013**, *54* (3), 499–504.

(76) Mathieu, D. Toward a Physically Based Quantitative Modeling of Impact Sensitivities. *J. Phys. Chem. A* **2013**, *117* (10), 2253–2259.

(77) Yuan, B.; Yu, Z.; Bernstein, E. R. Initial Decomposition Mechanism for the Energy Release from Electronically Excited Energetic Materials: FOX-7 (1,1-Diamino-2,2-Dinitroethene, C2H4N4O4). *J. Chem. Phys.* **2014**, *140* (7).

(78) Booth, R. S.; Butler, L. J. Thermal Decomposition Pathways for 1,1-Diamino-2,2-Dinitroethene (FOX-7). *J. Chem. Phys.* **2014**, *141* (13).

(79) Chakraborty, D.; Muller, R. P.; Dasgupta, S.; Goddard, W. A. Mechanism for Unimolecular Decomposition of HMX (1,3,5,7-Tetranitro-1,3,5,7-Tetrazocine), an Ab Initio Study. *J. Phys. Chem. A* **2001**, *105* (8), 1302–1314.

(80) Cohen, R.; Zeiri, Y.; Wurzberg, E.; Kosloff, R. Mechanism of Thermal Unimolecular Decomposition of TNT (2,4,6- Trinitrotoluene): A DFT Study. *J. Phys. Chem. A* **2007**, *111* (43), 11074–11083.

(81) Politzer, P.; Murray, J. S. Relationships between Dissociation Energies and Electrostatic Potentials of C-NO2 Bonds: Applications to Impact Sensitivities. *J. Mol. Struct.* **1996**, *376* (1–3), 419–424.

(82) Murray, J. S.; Concha, M. C.; Politzer, P. Links between Surface Electrostatic Potentials of Energetic Molecules, Impact Sensitivities and C-NO2/N-NO2bond Dissociation Energies. *Mol. Phys.* **2009**, *107* (1), 89–97.

(83) Politzer, P.; Lane, P.; Murray, J. S. Sensitivities of Ionic Explosives. *Mol. Phys.* **2017**, *115* (5), 497–509.

(84) Murray, J. S.; Lane, P.; Politzer, P. Relationships between Impact Sensitivities and Molecular Surface Electrostatic Potentials of Nitroaramatic and Nitroheterocyclic Molecules. *Mol. Phys.* **1995**, *85* (1), 1–8.

(85) Bankiewicz, B.; Matczak, P.; Palusiak, M. Electron Density Characteristics in Bond Critical Point (QTAIM) versus Interaction Energy Components (SAPT): The Case of Charge-Assisted Hydrogen Bonding. *J. Phys. Chem. A* **2012**, *116* (1), 452–459.

(86) Espinosa, E.; Souhassou, M.; Lachekar, H.; Lecomte, C. Topological Analysis of the Electron Density in Hydrogen Bonds. *Acta Crystallogr. Sect. B Struct. Sci.* **1999**, *55* (4), 563–572.

(87) Grabowski, S. J. Hydrogen Bonding Strength—measures Based on Geometric and Topological Parameters. *J. Phys. Org. Chem.* **2004**, *17* (1), 18–31.

(88) Rice, B. M.; Hare, J. J. A Quantum Mechanical Investigation of the Relation between Impact Sensitivity and the Charge Distribution in Energetic Molecules. *J. Phys. Chem. A* **2002**, *106* (9), 1770–1783.

(89) Hammerl, A.; Klapötke, T. M.; Nöth, H.; Warchhold, M.; Holl, G. Synthesis, Structure, Molecular Orbital and Valence Bond Calculations for Tetrazole Azide, CHN7. *Propellants, Explos. Pyrotech.* **2003**, *28* (4), 165–173.

(90) Gökçinar, E.; Klapötke, T. M.; Bellamy, A. J. Computational Study on 2,6-Diamino-3,5-Dinitropyrazine and Its 1-Oxide and 1,4-Dioxide Derivatives. *J. Mol. Struct. THEOCHEM* **2010**, *953* (1–3), 18–23.

(91) Politzer, P.; Lane, P.; Murray, J. S. Tricyclic Polyazine N-Oxides as Proposed Energetic Compounds. *Cent. Eur. J. Energ. Mater.* **2013**, *10* (3), 305–324.

(92) Zhang, J.; Zhang, Q.; Vo, T. T.; Parrish, D. A.; Shreeve, J. M. Energetic Salts with Stacking and Hydrogen-Bonding Interactions Lead the Way to Future Energetic Materials. *J. Am. Chem. Soc.* **2015**, *137* (4), 1697–1704.

(93) Ma, Y.; Meng, L.; Li, H.; Zhang, C. Enhancing Intermolecular Interactions and Their Anisotropy to Build Low-Impact-Sensitivity Energetic Crystals. *CrystEngComm* **2017**, *19* (23), 3145–3155.

(94) Asay, B. W.; Henson, B. F.; Smilowitz, L. B.; Dickson, P. M. On the Difference in Impact Sensitivity of Beta and Delta Hmx. *J. Energ. Mater.* **2003**, *21* (4), 223–235.

(95) Politzer, P.; Murray, J. S. Impact Sensitivity and Crystal Lattice Compressibility/Free Space. *J. Mol. Model.* **2014**, *20* (5).

(96) Pospisil, M.; Vavra, P.; Concha, M. C.; Murray, J. S.; Politzer, P. A Possible Crystal Volume Factor in the Impact Sensitivities of Some Energetic Compounds. *J. Mol. Model.* **2010**, *16* (5), 895–901.

(97) Cartwright, M.; Wilkinson, J. Correlation of Structure and Sensitivity in Inorganic Azides i Effect of Non-Bonded Nitrogen Nitrogen Distances. *Propellants, Explos. Pyrotech.* **2010**, *35* (4), 326–332.

(98) Taylor, D. E. Prediction of the Impact Sensitivity of Energetic Molecules Using Symmetry Adapted Perturbation Theory. **2011**.

(99) Jones, T. E. Role of Inter- and Intramolecular Bonding on Impact Sensitivity. *J. Phys. Chem. A* **2012**, *116* (45), 11008–11014.

(100) Coffey, C. S.; Sharma, J. Plastic Deformation, Energy Dissipation, and Initiation of Crystalline Explosives. *Phys. Rev. B - Condens. Matter Mater. Phys.* **1999**, *60* (13), 9365–9371.

(101) Zhang, C.; Wang, X.; Huang, H. π-Stacked Interactions in Explosive Crystals: Buffers against External Mechanical Stimuli. *J. Am. Chem. Soc.* **2008**, *130* (26), 8359–8365.

(102) Zhang, J.; Mitchell, L. A.; Parrish, D. A.; Shreeve, J. M. Enforced Layer-by-Layer Stacking of Energetic Salts towards High-Performance Insensitive Energetic Materials. *J. Am. Chem. Soc.* **2015**, *137* (33), 10532–10535.

(103) Ma, Y.; Zhang, A.; Zhang, C.; Jiang, D.; Zhu, Y.; Zhang, C. Crystal Packing of Low-Sensitivity and High-Energy Explosives. *Cryst. Growth Des.* **2014**, *14* (9), 4703–4713.

(104) Tian, B.; Xiong, Y.; Chen, L.; Zhang, C. Relationship between the Crystal Packing and Impact Sensitivity of Energetic Materials. *CrystEngComm* **2018**, *20* (6), 837–848.

(105) Manner, V. W.; Cawkwell, M. J.; Kober, E. M.; Myers, T. W.; Brown, G. W.; Tian, H.; Snyder, C. J.; Perriot, R.; Preston, D. N. Examining the Chemical and Structural Properties That Influence the Sensitivity of Energetic Nitrate Esters. *Chem. Sci.* **2018**, *9* (15), 3649–3663.

(106) Zhu, W.; Xiao, H. First-Principles Band Gap Criterion for Impact Sensitivity of Energetic Crystals: A Review. *Struct. Chem.* **2010**, *21* (3), 657–665.

(107) Zhang, H.; Cheung, F.; Zhao, F.; Cheng, X. Band Gaps and the Possible Effect on Impact Sensitivity for Some Nitro Aromatic Explosive Materials. *Int. J. Quantum Chem.* **2009**, *109*, 1547–1552.

(108) Crowley, J. M.; Tahir-Kheli, J.; Goddard, W. A. Resolution of the Band Gap Prediction Problem for Materials Design. *J. Phys. Chem. Lett.* **2016**, *7* (7), 1198–1203.

(109) Kuklja, M. M.; Rashkeev, S. N.; Zerilli, F. J. Shear-Strain Induced Decomposition of 1,1-Diamino-2,2-Dinitroethylene. *Appl. Phys. Lett.* **2006**, *89* (7), 2004–2007.

(110) Kuklja, M. M.; Rashkeev, S. N. Shear-Strain-Induced Structural and Electronic Modifications of the Molecular Crystal 1,1-Diamino-2,2-Dinitroethylene: Slip-Plane Flow and Band Gap Relaxation. *Phys. Rev. B - Condens. Matter Mater. Phys.* **2007**, *75* (10), 1–10.

(111) Kuklja, M. M.; Rashkeev, S. N. Shear-Strain-Induced Chemical Reactivity of Layered Molecular

Crystals. *Appl. Phys. Lett.* **2007**, *90* (15).

(112) Manaa, M. R. Shear-Induced Metallization of Triamino-Trinitrobenzene Crystals. *Appl. Phys. Lett.* **2003**, *83* (7), 1352–1354.

(113) Kuklja, M. M.; Rashkeev, S. N. Interplay of Decomposition Mechanisms at Shear-Strain Interface. *J. Phys. Chem. C* **2009**, *113* (1), 17–20.

(114) Bondarchuk, S. V. Quantification of Impact Sensitivity Based on Solid-State Derived Criteria. *J. Phys. Chem. A* **2018**, *122*, 5455–5463.

(115) Mathieu, D. Theoretical Shock Sensitivity Index for Explosives. *J. Phys. Chem. A* **2012**, *116* (7), 1794–1800.

(116) Mathieu, D.; Alaime, T. Predicting Impact Sensitivities of Nitro Compounds on the Basis of a Semi-Empirical Rate Constant. *J. Phys. Chem. A* **2014**, *118* (41), 9720–9726.

(117) Mathieu, D.; Alaime, T. Impact Sensitivities of Energetic Materials: Exploring the Limitations of a Model Based Only on Structural Formulas. *J. Mol. Graph. Model.* **2015**, *62* (2), 81–86.

(118) Mathieu, D. Physics-Based Modeling of Chemical Hazards in a Regulatory Framework: Comparison with Quantitative Structure-Property Relationship (QSPR) Methods for Impact Sensitivities. *Ind. Eng. Chem. Res.* **2016**, *55* (27), 7569–7577.

(119) Fried, L. E.; Ruggiero, a J. Energy-Transfer Rates in Primary, Secondary, and Insensitive Explosives. *J. Phys. Chem.* **1994**, *98* (39), 9786–9791.

(120) Ye; Koshi, M. Theoretical Studies of Energy Transfer Rates of Secondary Explosives. *J. Phys. Chem. B* **2006**, *110* (37), 18515–18520.

(121) McNesby, K. L.; Coffey, C. S. Spectroscopic Determination of Impact Sensitivities of Explosives. *J. Phys. Chem. B* **1997**, *101* (16), 3097–3104.

(122) Ye, S.; Tonokura, K.; Koshi, M. Energy Transfer Rates and Impact Sensitivities of Crystalline Explosives. *Combust. Flame* **2003**, *132* (1–2), 240–246.

(123) Bernstein, J. *Ab Initio* Study of Energy Transfer Rates and Impact Sensitivities of Crystalline Explosives. *J. Chem. Phys.* **2018**, *148* (8), 084502.

(124) McGrane, S. D.; Barber, J.; Quenneville, J. Anharmonic Vibrational Properties of Explosives from Temperature-Dependent Raman. *J. Phys. Chem. A* **2005**, *109* (44), 9919–9927.

(125) Piryatinski, A.; Tretiak, S.; Sewell, T. D.; McGrane, S. D. Vibrational Spectroscopy of Polyatomic Materials: Semiempirical Calculations of Anharmonic Couplings and Infrared and Raman Linewidths in Naphthalene and PETN Crystals. *Phys. Rev. B - Condens. Matter Mater. Phys.* **2007**, *75* (21), 1–9.

(126) Colognesi, D.; Celli, M.; Cilloco, F.; Newport, R. J.; Parker, S. F.; Rossi-Albertini, V.; Sacchetti, F.; Tomkinson, J.; Zoppi, M. TOSCA Neutron Spectrometer: The Final Configuration. *Appl. Phys. A Mater. Sci. Process.* **2002**, *74* , 64–66.

Chapter 2

Experimental and Computational Methods

2.1 Computational Methods

2.1.1 The Schrödinger Equation

The ultimate goal of common quantum chemical approaches is to reach a (approximate) solution of the time independent, non-relativistic Schrödinger equation,[1,2]

$$\widehat{H}\Psi(\overrightarrow{x_1},\overrightarrow{x_2},\dots\overrightarrow{x_N},\overrightarrow{R_1},\overrightarrow{R_2},\dots\overrightarrow{R_M}) = E\Psi(\overrightarrow{x_1},\overrightarrow{x_2},\dots\overrightarrow{x_N},\overrightarrow{R_1},\overrightarrow{R_2},\dots\overrightarrow{R_M})$$

Equation 2.1

for a system of *M* nuclei and *N* electrons, where $\widehat{H}$ is the Hamilton operator (or Hamiltonian) and Ψ is the wavefunction that describes the system. Note that Equation 2.1 combines the electron spatial coordinate ($\vec{r}$, *xyz*) and spin coordinate (s_i, either α or β) into a single term ($\vec{x}$), and the nuclear spatial coordinates are denoted $\vec{R}$. The Hamiltonian (here defined in atomic units) is a differential operator that describes the total energy,

$$\widehat{H} = -\frac{1}{2}\sum_{i=1}^{N}\nabla_i^2 - \frac{1}{2}\sum_{A=1}^{M}\frac{1}{M_A}\nabla_i^2 - \sum_{i=1}^{N}\sum_{A=1}^{M}\frac{Z_A}{r_{iA}} + \sum_{i=1}^{N}\sum_{j>i}^{N}\frac{1}{r_{ij}} + \sum_{A=1}^{M}\sum_{B>1}^{M}\frac{Z_A Z_B}{R_{AB}}$$

Equation 2.2

In Equation 2.2, the terms *i* and *j* are electron indices, and run over all *N* electrons, *A* and *B* are the nuclear indices, running over all *M* nuclei with charge *Z* and mass M_A. The five terms in Equation 2.2 thus describe:

1. Electron kinetic energy
2. Nuclear kinetic energy
3. Attractive electron-nucleus electrostatic interaction
4. Repulsive electron-electron electrostatic interaction
5. Repulsive nuclear-nuclear electrostatic interaction

Terms 3-5 depend on the spatial separation between electron and nuclear spatial coordinates $\vec{r_i}$ and $\overrightarrow{R_A}$, respectively; hence $r_{iA} = \left|\vec{r_i} - \overrightarrow{R_A}\right|$.

The Schrödinger equation therefore 'simply' states that using the mathematical formulation of the Hamiltonian, the energy of a system can be extracted from its wavefunction. Unfortunately, due to the infamous many-body problem, the Schrödinger equation cannot be solved exactly for multi-electron systems, and a variety of approximations must be made.

Arguably the most important approximation in quantum chemistry is the Born-Oppenheimer approximation (BOA).[3] Within the BOA, the significant difference in mass between a nucleus and an electron is considered (*ca.* 1800 times greater in ^{1}H, and > 20000 times greater in ^{14}C). The electrons can therefore be taken as moving in a field of fixed nuclear geometry, hence term 2 of Equation 2.2 disappears and term 5 becomes a constant described by Coulomb's law. The Hamiltonian (and wavefunction) can therefore be split into electronic and nuclear components, to be solved independently. The electronic Hamiltonian, $\hat{H}_{elec}$ becomes,

$$\hat{H}_{elec} = -\frac{1}{2}\sum_{i=1}^{N}\nabla_i^2 - \sum_{i=1}^{N}\sum_{A=1}^{M}\frac{Z_A}{r_{iA}} + \sum_{i=1}^{N}\sum_{j>i}^{N}\frac{1}{r_{ij}} = \hat{T} + \hat{V}_{Ne} + \hat{V}_{ee}$$

Equation 2.3

The total energy therefore comes from the sum of electronic energy, E_{elec} and the constant nuclear repulsion term $E_{tot} = E_{elec} + E_{nucl}$, where

$$E_{nucl} = \sum_{A=1}^{M} \sum_{B>1}^{M} \frac{Z_A Z_B}{R_{AB}}$$

Equation 2.4

This includes all of the energy of the system under fixed nuclear geometry.

Despite the great simplifications obtained *via* the BOA, no solution to the many-body problem is achieved. The third term of Equation 2.3, $\hat{V}_{ee}$, cannot be solved explicitly for multi-electron systems, and elements of terms one and two are beyond reach. Methods designed to deal with this issue using a variety of approximations have been developed and are widely employed in the field of Computational Chemistry.

2.1.2 Hartree-Fock Theory

The simplest *ab initio* method is the Hartree-Fock (HF) scheme. The HF method forms the base for nearly all wavefunction based theories. Noting that the solution of the complete *N*-electron wavefunction cannot be solved exactly, HF theory approximates the wavefunction by an antisymmetrised product[1] of *N* one-electron wavefunctions, $\chi_i(\vec{x}_i)$, known as spin orbitals, their exact description depends on the basis set used (Section 2.1.3). This product is known as the *Slater determinant,*[4] Φ_{SD}

$$\Psi \approx \Phi_{SD} = \frac{1}{\sqrt{N!}} \begin{vmatrix} \chi_1(\vec{x}_1) & \chi_2(\vec{x}_1) & \dots & \chi_N(\vec{x}_1) \\ \chi_1(\vec{x}_2) & \chi_2(\vec{x}_2) & \dots & \chi_N(\vec{x}_2) \\ \vdots & \vdots & \ddots & \vdots \\ \chi_1(\vec{x}_N) & \chi_2(\vec{x}_N) & \dots & \chi_N(\vec{x}_N) \end{vmatrix}$$

Equation 2.5

where the pre-factor ensures the normalization condition that $\int |\Psi|^2 d\tau = 1$. Due to the use of the antisymmetrised wavefunction in this way, HF theory is

[1] Antisymmetrisation is the result of Pauli's exclusion principle, which dictates that interchange of any two fermions (*e.g.* electrons) must result in a change in sign. Hence $\Psi(\vec{x}_1, \vec{x}_2, \dots \vec{x}_i, \vec{x}_j, \dots, \vec{x}_N) = -\Psi(\vec{x}_1, \vec{x}_2, \dots \vec{x}_j, \vec{x}_i, \dots, \vec{x}_N)$

said to include *exact exchange*. For example, the Slater determinant of a two-electron system can be formulated according to

$$\Psi(\vec{x}_1, \vec{x}_2) = \frac{1}{\sqrt{(2)}}\left(\chi_1(\vec{x}_1)\chi_2(\vec{x}_2) - \chi_2(\vec{x}_1)\chi_1(\vec{x}_2)\right)$$

Equation 2.6

Hence, the two electrons are indistinguishable, and cannot exist in the same spin-orbital.

Derivation of the HF equations are outside the scope of this work, but introductory texts can be found in Reference 5. However, it is useful to briefly introduce the results here, which lead to definitions of *electron exchange* and *electron correlation*.

The energy of the one-electron wavefunction can be found using the *Fock* operator, $\hat{f}$; one electron wavefunctions are found to reduce to,

$$\hat{f}\chi_i = \epsilon_i\chi_i$$

Equation 2.7

where ϵ_i describes the orbital energy of spin-orbital *i* and

$$\hat{f_i} = -\frac{1}{2}\nabla_i^2 - \sum_{i=1}^{M}\frac{Z_A}{r_{iA}} + V_{HF}(i)$$

Equation 2.8

The Fock operator hence represents the kinetic energy and the electrostatic interaction between nuclei and electrons. The third term in Equation 2.8, $V_{HF}(i)$ is known as the *Hartree-Fock potential.* This term describes the average repulsive potential felt by electron *i* due to interaction with the other $N-1$ electrons. Hence, the two-electron repulsive operator (term 3 of Equation 2.3) is reduced to a simple electron operator $V_{HF}(i)$, in which the electron-electron repulsion is only accounted for in an *average* way. HF theory thus introduces

so-called *average electron correlation*[2]. To see this better, it is worth considering the Hartree-Fock potential in further detail,

$$V_{HF}(\vec{x}_1) = \sum_{j}^{N} (\hat{J}_j(\vec{x}_1) - \hat{K}_j(\vec{x}_1))$$

Equation 2.9

The term $\hat{J}$, the Coulomb operator, is defined as

$$\hat{J}_j(\vec{x}_1) = \int \left|\chi_j(\vec{x}_2)\right|^2 \frac{1}{r_{12}} d\vec{x}_2$$

Equation 2.10

This operator describes the repulsive potential experienced by an electron at position $\vec{x}_1$ due to the *average* charge distribution of another electron in a second spin orbital χ_j.[3]

The second term in Equation 2.9, $\hat{K}_j$ describes the exchange contribution of the HF potential. This term has no classical interpretation, and is due entirely to the interaction of spin orbitals,

$$\hat{K}_j(\vec{x}_1)\chi_i(\vec{x}_1) = \int \chi_j^*(\vec{x}_2) \frac{1}{r_{12}} \chi_i(\vec{x}_2) d\vec{x}_2 \chi_j(\vec{x}_1)$$

Equation 2.11

This term only exists for electrons of like spin, and results from the antisymmetry of the Slater determinant. Hence, this term is computed without approximation in HF theory.

[2] Electron correlation within HF is taken as the difference in energy between the real system and the HF-derived energy, $E_c^{HF} = E_0 - E_{HF}$. Under normal bonding conditions, this difference is mainly due to the short-range instantaneous repulsion that occur between electrons (dynamic correlation). In HF, this potential is treated only as an average, and hence is underestimated. Typically, correlation energies are quite small (*ca.* 0.04 E_h in H_2).

[3] Note that the Borne interpretation of the wavefunction states that $\left|\chi_j(\vec{x}_2)\right|^2 d\vec{x}_2$ describes the probability of finding the electron within volume $d\vec{x}_2$.

HF theory therefore offers an approach for approximating the solution of the Schrödinger equation for an *N*-electron system, by assuming *N* non-interacting particles that move in an effective potential, V_{HF},

$$\hat{H}_{HF}\Phi_{SD} = E^0_{HF}\Phi_{SD} = \sum_i^N \hat{f}_i\Phi_{SD} = \sum_i^N \varepsilon_i\Phi_{SD}$$

Equation 2.12

Despite its simplifications, HF is able to reproduce overall system energies to within *ca.* 10% of the most accurate computational approaches (*i.e.* couple cluster methods). However, the approximations made by neglect of correlation can lead to issues surrounding calculation of system properties. Numerous post-HF methods (*e.g.* Møller-Plesset Perturbation theory) have been developed, alongside other theories (*e.g.* Density Functional Theory) in an attempt to better model the complex electron behaviour.

2.1.3 Multi-Reference Methods

A particular drawback to the neglect of correlation in HF comes in the form of non-dynamic (or static) correlation – the fact that in some cases a single-reference wavefunction cannot describe a given electronic state.[6] For example, for the H_2 molecule, HF provides a reasonable estimate for the geometry around the equilibrium geometry. However, if the bond is elongated, the Slater determinant generates a wavefunction which can be represented as

$$(H^{\alpha} \ldots H^{\beta}) + (H^{\beta} \ldots H^{\alpha}) + (H^{-\,\alpha\beta} \ldots H^{+}) + (H^{+} \ldots H^{-\,\alpha\beta})$$

Equation 2.13

Thus the HF scheme builds a wavefunction including equal weightings of two ionic states. This leads to considerable issues in reproducing the asymptotic limit of H_2 dissociation.[5]

These problems, amongst others, have been approached using configurational interaction (CI) methods.[7] The full theory of these methods is extensive and can be found in many textbooks, including Reference 5 and 8.

In CI methods, the ansatz wavefunction is taken as a linear combination of determinants (derived from HF), and are weighted by an appropriate coefficient,

$$\Psi_{CI} = c_1\phi_1 + c_2\phi_2 \ldots$$

Equation 2.14

To expand beyond the HF method, CI methods introduce excited determinants, in which an electron is permitted to occupy a valence HF orbital. This introduces extra flexibility to the electrons within the calculation, and reflects the fact that excited state orbital structures become important at large perturbations away from equilibrium, and when considering electronic excitations. This addition therefore offers a means to treat non-dynamic correlation. Hence, Equation 2.14 can be re-written in terms of the number excited determinants used and their excitation level, here denoted S (single) and D (double) excitations (higher order excitations can be used),

$$\Psi_{CI} = c_1\phi_{HF} + \sum_S c_s\phi_s + \sum_D c_D\phi_D \ \ldots = \sum_{i=0} c_i\phi_i$$

Equation 2.15

To understand how non-dynamical correlation improves the description of H_2 dissociation, the nature of the frontier orbitals must first be considered, Figure 2.1.

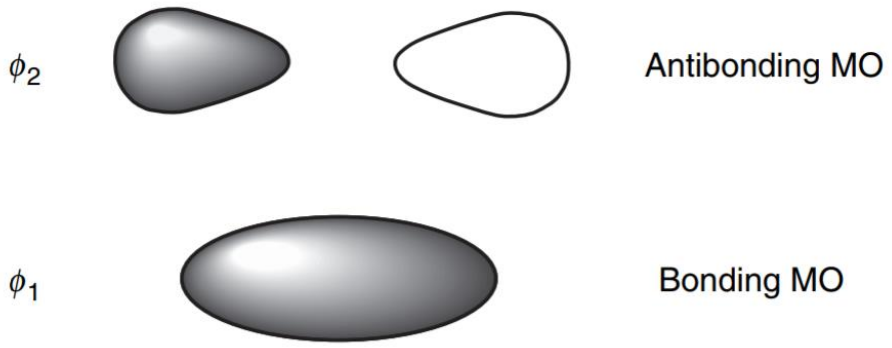

Figure 2.1: Schematic representation of the frontier orbitals of molecular H_2. Figure from Ref. 5

The HF method constricts both electrons to the *bonding* (ϕ_1) orbital, whereas inclusion of the ϕ_2 antibonding orbital in the CI-based approach permits these electrons to occupy different sides of the nodal plane. Hence, on dissociation, CI methods have the flexibility to employ a large weighting to the ϕ_2 orbital on dissociation, and to suppress the contribution of the ϕ_1 ion states. This therefore eliminates the so-called 'left-right' correlation that hindered the HF approach.

Truncations of Equation 2.15 formed the base for early CI approaches, such as CIS and CID. As these methods lead to large imbalance of electron correlation to the minimal excitations used, they are rarely used today. It is instead common to employ a multi-configurational approach, such as the complete active space, CASSCF. In these methods, *all* excitations are permitted within a defined 'active' space, which includes occupied and un-occupied HF orbitals. For each excitation, the orbitals are re-optimised. If an appropriate active space is selected, this limits bias in the correlation energy. Hence, these methods allow for flexibility in electron energies as a result of changing the electronic configuration. It follows that multi-reference methods are particularly adept at treating excited states.

While many multi-reference methods do an excellent job at treating non-dynamic correlation (*e.g.* CASSCF), treatment of dynamic correlation remains limited. The multi-reference configurational interaction (MRCI) method, however, employ a series of multi-reference wave functions, on which additional CI calculations are performed (and orbitals optimized).[9] This is amongst the best approaches for including dynamic correlation effects.

In this work, the electronic structure of isolated molecules was monitored as a function of bond perturbations. Hence non-dynamic correlation can prove problematic. Further, this work was interested in monitoring the relative energies of the excited states along these perturbations. Thus, it was particularly appropriate to employ multi-reference CI methods. Given the small size of the systems studied here, it was possible to perform full MRCI

calculations. Hence, both dynamic and non-dynamic correlation was accounted for. This was done using the Molpro 2012 software[10] in this work.

2.1.4 Density Functional Theory

An alternative approach to handling the Schrödinger equation is Density Functional Theory (DFT). In contrast to HF-based methods, DFT is not based on explicit calculation of Ψ. Rather, the energy is extracted directly from the electron density, ρ. This is a particularly attractive approach, since the electron density is experimentally observable, while a wavefunction is not. An excellent introduction to DFT can be found in Reference 11 and 12, and more detailed derivations can be found in dedicated texts.[5]

2.1.4.1 Hohenberg-Kohn Theorems

Rooted in the BOA Hamiltonian, Equation 2.3, the development of DFT began with the seminal theories proposed by Hohenberg and Kohn: the Hohenberg-Kohn Theorems (HK). According to the HK theorems:[13]

1. *The external potential, $\boldsymbol{V_{ext}}(\vec{\boldsymbol{r}})$ is uniquely defined by $\boldsymbol{\rho}(\vec{\boldsymbol{r}})$*

Since the Hamiltonian is fixed by this term, Equation 2.3, this suggests that the energy of the system is uniquely defined by $\rho(\vec{r})$. In addition, this posits that the *3N* spatial coordinates required to define a system in the HF equations can be reduced to only 3 spatial coordinates.

Conceptually, this theorem stems from the fact that the electron density (whose integral is the total number of electrons in the system) depends on the number, charge and position of nuclei. It can be shown[14] that because the total energy is a function of the electron density, so too must its components, and thus Equation 2.3 can be recast as,

$$E_0[\rho_0] = T[\rho_0] + E_{ee}[\rho_0] + E_{Ne}[\rho_0]$$

Equation 2.16

This equation is conveniently separated into the system-dependent term ($E_{Ne}[\rho_0] = \int \rho_0(\vec{r}) V_{Ne}\, d\vec{r}$) and the terms which are universal, (*i.e.* their form is independent of *N, R_A* and *Z_A*),

$$F_{HK}[\rho] = T[\rho] + E_{ee}[\rho] = T[\rho] + J[\rho] + E_{ncl}[\rho]$$

Equation 2.17

where the electron-electron energy is decomposed into the Coulombic component (*J*) and a non-classical component, E_{ncl}, which includes correlation and exchange effects. And thus the total energy is defined by

$$E_0[\rho_0] = F_{HK}[\rho] \; + \int \rho_0(\vec{r}) V_{Ne}\, d\vec{r}$$

Equation 2.18

Hence, it appears that the first HK theorem offers a direct link between density and energy. Despite the immense simplicity of these equations, the problem again arises that, due to the effects of electron correlation and exchange, no explicit form for $T[\rho]$ or $E_{ee}[\rho]$ are known.

2. Variational Principle

This theorem states that the functional that returns the ground state energy of a system will deliver the lowest energy *only* if the input electron density is the true ground state density. Hence, there should exist a universal function, $\hat{E}[\rho(\boldsymbol{r})]$, that could be used to obtain the exact ground state density and energy. The only problem is that its actual form is not known.

2.1.4.2 Kohn-Sham Equations

Whilst the theories proposed by Hohenberg and Kohn suggest the existence of a universal functional, they offer no means to determine what form this functional should take. Following from Equation 2.18, Kohn and Sham[15] made further developments to render a more tractable form of DFT which enjoys widespread use today.

Kohn and Sham suggested that as much of Equation 2.18 that *could* be calculated explicitly, *should* be. Hence, they proposed that the kinetic and potential energy terms should instead be treated in a similar way to that of HF theory. It was posited that a good first approximation would be to set-up a non-interacting reference system based on a Slater determinant wavefunction and an effective local potential, $V_s(\vec{r})$,

$$\hat{H}_S = -\frac{1}{2}\sum_i^N \nabla_i^2 + \sum_i^N \mathrm{V}_S(\vec{r}_i)$$

Equation 2.19

The Slater determinant, spin orbitals and one-electron operators are analogous to the HF cases in Equations 2.5, 2.7 and 2.8, respectively, the only difference being that the orbitals within the Kohn-Sham approach (the KS orbitals, φ_i) are largely artificial. The value of V_s must be chosen such that KS orbitals reproduce the electron density of the real interacting system.[4] As was the case with HF theory, the kinetic energy of the *non-interacting system* can therefore be written as

$$T_s = -\frac{1}{2}\sum_i^N \langle \varphi_i | \nabla^2 | \varphi_i \rangle$$

Equation 2.20

This term allows calculation of a large subset of the kinetic energy, but will not be the same as that of the true, interacting system, even for the same electron density. Hence, the functional $F[\rho]$ is separated,

$$F[\rho(\vec{r})] = T_S[\rho(\vec{r})] + J[\rho(\vec{r})] + E_{XC}[\rho(\vec{r})]$$

Equation 2.21

[4] $\sum_i^N \sum_s |\varphi_i(\vec{r}, s)|^2 = \rho_o(\vec{r})$

where the term E_{XC} contains all of the non-classical (interacting) terms that are neglected in solving for a non-interacting system. This is known as the *exchange-correlation* energy,

$$E_{XC}[\rho] = (T[\rho] - T_S[\rho]) + (E_{ee}[\rho] - J[\rho])$$

Equation 2.22

Hence, the *exchange-correlation* energy contains all parts of the total energy equation that are unknown, including effects of self-interaction, exchange, correlation and components of the kinetic energy. The total energy therefore becomes

$$E[\rho(\vec{r})] = T_S[\rho] + J[\rho] + E_{XC}[\rho] + E_{Ne}[\rho]$$

Equation 2.23

The final difficulty was therefore to establish a means to define a unique set of KS orbitals that represent the non-interacting system. It turns out that this can be done by application of the variational principle,[5] and leads to the so-called (one-electron) *Kohn-Sham* equation,

$$\left(-\frac{1}{2}\nabla^2 + \left[\int \frac{\rho(\vec{r}_2)}{r_{12}} d\vec{r}_2 + V_{XC}(\vec{r}_1) - \sum_A^M \frac{Z_A}{r_{1A}} \right] \right) \varphi_i$$
$$= \left(-\frac{1}{2}\nabla^2 + V_{eff}(\vec{r}_1) \right) \varphi_i = \varepsilon_i \varphi_i \, .$$

Equation 2.24

Similar to the HF one-electron equations, this must be solved iteratively. It is also worth noting the similarity of the Kohn-Sham equation with the HF equation (Equation 2.8), with the main difference being the nature of the spin-orbitals and the exchange-correlation terms. In Equation 2.24, the only term that remains unknown is V_{XC} (the exchange-correlation potential), which is defined as,

$$V_{XC} = \frac{\delta E_{XC}}{\delta \rho}$$

Equation 2.25

Thus, if the form of V_{XC} were known, the KS approach would lead to an exact solution of the Schrödinger equation.

2.1.4.3 Exchange-Correlation Functionals

The most active area of research in DFT development surrounds developing approximate forms for V_{XC}. A number of approaches have been made, with varying complexities. A full discussion of these approaches is outside the scope of this thesis, but an excellent introduction is provided in Reference 16 and 17. The most basic form of V_{XC} is based on the work of Thomas and Fermi[18,19] and known as the Local Density Approximation (LDA).[15] It makes the assumption that the electron density can be treated as a uniform electron gas and thus the exchange-correlation at a point $\boldsymbol{r}$ with density $\rho(\boldsymbol{r})$ should be the same as that of a uniform gas of the same density.[20] Physically, this is similar to the electronic structure of solid metals, for which LDA works quite well. However, when molecular solids are considered, this approximation becomes rather poor. Electrons in such systems are not delocalised, but are confined to the spaces occupied by the molecules. Therefore, for molecular systems like those studied in this thesis, the Generalised Gradient Approximation (GGA) becomes more appropriate. The GGA approximation[21,22] accounts for rapidly changing properties of the electron density by considering both the charge density at a point, and the gradient of the charge density to account for local deviations. The most common GGA functionals are the PBE[23] (Perdew, Burke and Ernzerhof), PW91[24,25] (Perdew and Wang) and BLYP (Beck 88 exchange functional[26] with the correlation functional of Lee, Yang and Parr[27]). PBE is particularly popular for modelling of molecular crystals, and has been previously demonstrated to perform well for structural and vibrational properties of molecular energetic materials.[28–31] It has therefore been used in this thesis.

In contrast to HF theory, DFT does not treat exchange explicitly, but rather approximates both correlation and exchange. To rectify this, hybrid DFT functionals are used. These functionals work by introducing a component of exact HF exchange into the functional. The amount of HF that is included is based on substantial paramaterisation against experimental data, and many hybrid DFT functionals are developed 'for purpose', and on a specific class of compounds. The most common hybrid functional, B3LYP,[11] is obtained by adding gradient corrections to the LDA method, the exchange of Becke and the correlation function of Lee, Yang and Parr. Generally, hybrid functionals perform very well and are less computationally demanding than wavefunction methods, particularly for larger systems.

DFT exchange-correlation functionals are inherently local and they therefore are not capable of accounting for the long-range dynamic correlation that results in van der Waals interactions. These interactions are vital to the correct description of molecular materials, such as those studied in this thesis. As such, a number of empirical and semi-empirical corrections have been developed. Most notable are those by Tkatchenko and Scheffler (TS)[32] and Grimme.[33,34] In the popular D2 scheme (Grimme G06[33]), the dispersion correction takes the form,

$$E_{disp} = -\frac{1}{2}\sum_{i=1}^{N}\sum_{j=1}^{N}\sum_{L}\frac{C_{6ij}}{r_{ij,L}^{6}} f_{d,6}(r_{ij,L})$$

Equation 2.26

where N is the number of atoms and L is a unit cell translation. For $L = 0$, $i \neq j$. C_{6ij} is the dispersion coefficient for atom pair ij, and $r_{ij,L}$ is the distance between this pair at translation L.The final term, $f_{d,6}(r_{ij,L})$ works to scale the dispersion correction force-field such to minimize the term when atoms are within typical bonding distances. In the common D2 scheme, the C_6 term is empirical, and hence the dispersion is not sensitive to an atom being in a particular chemical environment. The TS scheme, however, accounts in part for chemical environment by accounting for changes in an atoms' charge

density. Other DFT functionals have also been developed which attempt to include non-local correlation explicitly within the *ab initio* calculation. A particularly promising non-local correlation functional is rVV10,[35] which has proven to perform very well for structural and vibrational calculations of molecular materials. Unfortunately, due to the complexity of the non-local correlation functionals, they become increasingly expensive with the size of the unit cell.[36]

A second issue surrounding the intrinsic localised nature of DFT correlation is that DFT functionals tend to over delocalise electrons due to their intrinsic self-interaction. [5] This introduces problems with calculation of electronic band gaps, where typical GGA functionals tend to grossly underestimate these gaps.[37] While there is some improvement with the introduction of HF exchange in the hybrid functionals, there remain problematic effects with long-range HF exchange, although cancellation of errors in hybrid methods can solve many of these problems.[38] Development of so-called screened hybrid DFT functionals has therefore appeared. These methods separate the Coulomb operator within the HF exchange into short- and long-range effects. The definition of the range (and thus the length-scale of HF exchange) is varied with an empirically fit parameter. The HSE06[39] (Heyd, Scuseria and Ernzerhof) functional is one such screened hybrid functional, and has proved particularly promising for the calculation of electronic band gaps. It was therefore selected for this purpose in this thesis.

2.1.5 Basis Sets

Solution of the Schrödinger equation, Equation 2.2, requires two components, the Hamiltonian (*i.e. how* to evaluate the energy) and the wavefunction (*i.e.* what to evaluate the energy *of*). The former is considered within the theories of HF and DFT, while the latter depends on the so-called *basis set*.[5] The basis set is a set of functions whose linear combination represents a wavefunction. Generally, the larger the basis set, the more accurately the wavefunction will be described. While it is therefore tempting to use large basis sets, a larger

number of functions greatly increases the computational cost. Compromises must therefore be made.

There are two main types of basis sets: localised and delocalised.[8] The former is typically used in the study of isolated molecules, while the latter is more commonly used for periodic (*e.g.* crystalline) materials. Both have been utilised in this thesis.

2.1.5.1 Localised Basis Set – Isolated Molecules

Modelling the electronic structure of an isolated molecule is typically done using localised functions that are centred on the individual atoms. These functions form the atomic orbitals, and their linear combination forms the linear combination of atomic orbitals, molecular orbital method. Early methods employed Slater-type functions[40] (STOs) as they have a similar form to the hydrogen atom eigenfunctions. However, these functions could not be handled efficiently by algorithms, and instead Gaussian-type orbitals (GTO) became popular. While Gaussian functions are more easily handled, they do not have the necessary cusp at the nucleus, and they decay too rapidly.[5,41] As such, in practice a contraction of Gaussian primitive functions $g_j(\boldsymbol{r})$, each with an appropriate weighting coefficient (d) is used. As such, a contracted GTO (CGTO) containing *L* primitive functions takes the form

$$\chi_i(r) = \sum_{j=1}^{L} d_j g_j(r)$$

Equation 2.27

The larger the number of CGTOs and primitives used to construct a CGTO, the more accurate will be the model, and the more computationally demanding will be the calculation. Noting that chemistry typically involves only the valence electrons, split-valence basis sets are common, where the number of CGTOs used to model the core orbitals differs from that used for the valence orbitals. The Pople[42] basis set 6-31G, for example, states that six gaussian primitives are summed to a single CGTO to model the core shells, while two CGTOs are employed to model the valence region, one composed of three primitives and

one of a single primitive function. This offers additional flexibility to the valence electrons and permits more accurate representation of perturbations to these electron orbitals. Additional functions can be added to further enhance the flexibility of these valence states: polarisation and diffuse functions. The former describes addition of higher angular momentum functions onto an atom (*e.g.* a *p*-orbital onto an *s*-orbital), and assists in capturing changes in the shape of electron density on bonding. Diffuse functions add higher principle quantum number orbitals (*e.g.* a larger orbital of the same angular momentum). Polarisation functions are crucial for accurate capture of anions, polarizable atoms, excited states and long range interactions. A number of different families of GTOs exist, and differ mainly in their optimization of the primitive Gaussian exponents. The most common families[5] are the Dunning[43] and Pople[42] basis sets.

In this thesis, GTOs are used to study bond elongation and excited state potential energy surfaces of anions. This requires accurate modelling of the atom-atom bonding interactions, as well as permitting sufficient flexibility to capture the excited state. Hence in this work both polarization and diffuse functions are incorporated. However, due to the computational expense of the calculation, only a limited number of these functions could be used.

2.1.5.2 Condensed Matter, Delocalised Basis Sets and Bloch Theorem

Treating electrons in a solid, which is essentially an infinite array of periodic unit cells, brings the additional challenge of solving the Schrödinger equation for an infinite number of electrons. This problem can be solved by considering Bloch's theorem, which states that due to the periodicity of a crystalline material, it is necessary to consider only the electrons that reside within the primitive unit cell. Bloch's theorem states that the wavefunction of an electron within a perfectly periodic potential can be written as[44]

$$\psi_{j,\boldsymbol{k}}(\boldsymbol{r}) = u_{j,\boldsymbol{k}}(\boldsymbol{r})e^{i\boldsymbol{k}.\mathrm{r}}$$

Equation 2.28

In this equation, $u_j(\boldsymbol{r})$ describes a function with the periodicity of the potential, such that $u_j(\boldsymbol{r}+\boldsymbol{g}) = u_j(\boldsymbol{r})$, where $\boldsymbol{g}$ is the translational length of the crystal. The term j describes the band index, and $\boldsymbol{k}$ a wave vector within the first Brillouin zone. In a typical calculation, $\boldsymbol{k}$ is sampled at a discrete number of points. This is often done using a Monkhorst-Pack grid,[45] which is an unbiased means of selecting a subset of $\boldsymbol{k}$ points to sample based on a rectangular grid of points, spaced evenly throughout the Brillouin zone. Appropriate dimensions for this grid require convergence testing on a system-by-system basis,[46] and depends on complexities in the underlying electronic structure.

As u_j of Equation 2.28 is periodic, it can be expressed as a Fourier series,

$$u_{j,k}(\boldsymbol{r}) = \sum_{G} c_{j,\boldsymbol{G}} exp(i\boldsymbol{G}\cdot\boldsymbol{r})$$

Equation 2.29

where $\boldsymbol{G}$ is a reciprocal lattice vector and $c_{j,\boldsymbol{G}}$ are expansion coefficients for each plane wave. It follows that the electron wavefunctions can be constructed as a linear combination of these plane waves,

$$u_{j,k}(\boldsymbol{r}) = \sum_{\boldsymbol{G}} c_{j,\boldsymbol{k}+\boldsymbol{G}} exp(i(\boldsymbol{k}+\boldsymbol{G})\cdot\boldsymbol{r}$$

Equation 2.30

Similar to the GTO, a DFT calculation therefore aims to minimize the energy of this function by optimizing the expansion coefficients through self-consistent field cycles.

Electronic wavefunctions represented by plane waves are fast to compute, and further, the set of plane waves is universal and does not depend on the position or type of atoms in the unit cell.[5] Hence, in contrast to localised basis sets, all systems can be treated with the same set of functions. In principle, the plane wave series is infinite. However, this is clearly not computationally tractable, and a truncation must be made. This is done by setting an upper energy limit

for the plane wave kinetic energies (and thus electron kinetic energies) to be incorporated in the wavefunction, E_{cut},

$$E_{cut} = \frac{\hbar^2}{2m}|\boldsymbol{k} + \boldsymbol{G}|^2$$

Equation 2.31

In contrast to GTOs, plane wave basis sets are therefore readily improved, simply by the addition of more plane waves (*i.e.* increasing E_{cut}). An appropriate E_{cut} must be optimised for each system studied, and depends intimately on the pseudopotential (described below) and type of atom being investigated. The ability of plane waves to correctly model atomic structure is shown in Figure 2.2.

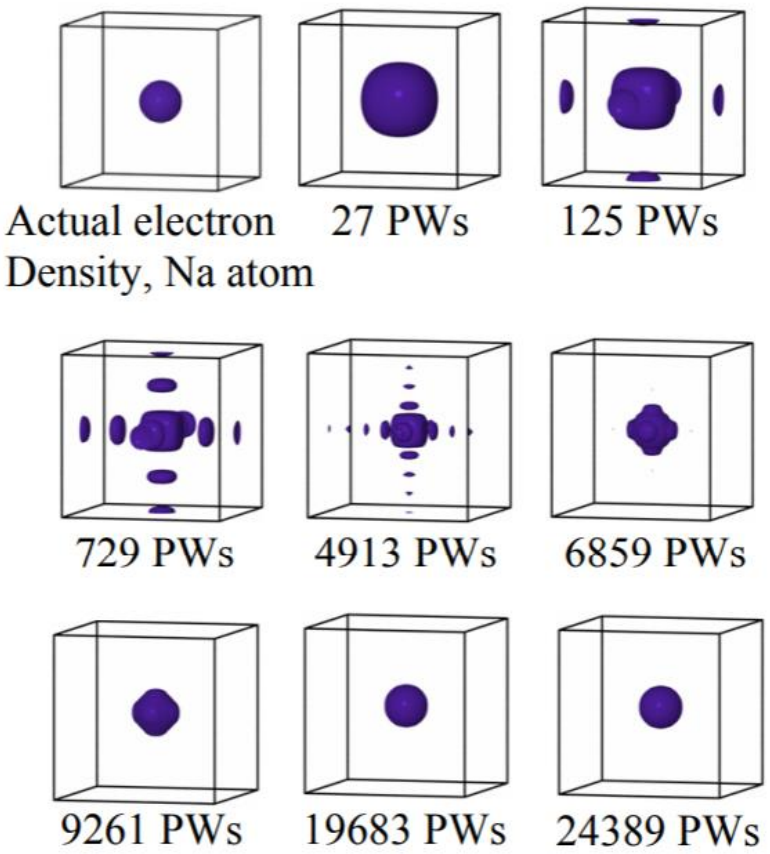

Figure 2.2: The effect of increase the number of plane waves (PW) on the modelled electron density of a Na atom. From Ref 47.

It is also possible (albeit less common) to build Bloch functions of Equation 2.28 based on GTOs. For an *N*-electron system, this is done by expanding the unknown crystalline orbitals, *i,* as a set of *m* Bloch functions that are constructed from local atom-centred Gaussian functions, χ,[48]

$$\psi_{\boldsymbol{k}i}(\boldsymbol{r}) = N\sum_{j=1}^{m} a_{ji}(\boldsymbol{k})\left(\sum_{\boldsymbol{G}} \chi_{\boldsymbol{G},i}(\boldsymbol{r})exp(i\boldsymbol{k}\cdot\boldsymbol{G})\right)$$

Equation 2.32

where ***G*** is again a reciprocal lattice vector, and terms a_{ji} are the scaling coefficients. The main advantage of using GTOs for periodic systems comes in the study of the electron density, which is more carefully reproduced by GTOs. Further, the use of GTOs greatly reduces the number of basis functions used to describe the system and hence are favoured for use with hybrid functionals, which have explicit consideration of the Fock matrix (and which scales directly with the number of basis functions employed). Hence the electronic band structures calculated in this work were performed almost exclusively using periodic Gaussian-type Bloch functions, along with the screened hybrid DFT functional, HSE06. The major disadvantage is that there is no systematic and unique approach to enhancing the basis set quality as there is with plane waves, and hence the basis sets used in this work were obtained from previous works in which they were successfully employed in similar systems.

2.1.5.3 Pseudopotentials

The Pauli exclusion principle[2] dictates that higher electronic states are orthogonal with all states of lower energy. It follows that the electronic wavefunction becomes highly oscillating in the core region. The expansion of the electronic wavefunction in a plane wave basis set requires very large numbers of plane waves to capture this feature. Fortunately, the core electrons of an atom are only negligibly affected by the chemical environment, and can be treated as being frozen. It is therefore possible to replace the ionic potential with a weaker pseudopotential that mimics the screening effect of the core

electrons, and which yields the same valence electron wavefunction outside of the core region, $r > r_c$.[49,50] This has the effect of removing the Kohn-Sham orbitals of the core states, as well as removing all nodes from the valence pseudo wavefunction for $r < r_c$. Hence, the use of pseudopotentials greatly reduces the number of plane waves required to reproduce it, Figure 2.3. Potentials that place r_c higher are considered 'softer' potentials and require fewer plane waves to model. However, softer potentials also tend to be less transferrable.

The choice of pseudopotential is not unique, and many approaches exist. However, all pseudopotentials must obey the simple criteria including:

1. The core charge of the pseudo-wavefunction must be identical to that of the atomic wavefunction.
2. The eigenvalues of the pseudo-electrons must be the same as in the atomic wavefunction.
3. The pseudo-wavefunction and its first and second derivatives must be continuous at $\boldsymbol{r_c}$

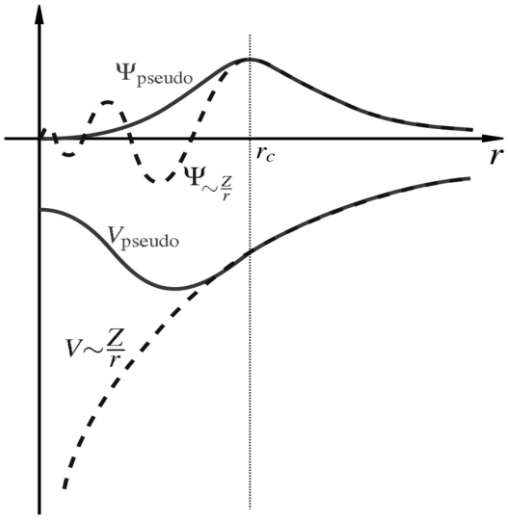

Figure 2.3: The structure of the valence wavefunction as a function of its distance, *r*, from the nucleus. Modification of the ionic potential Z/r by use of a pseudopotential V_{pseudo} in the region $r < r_c$ leads to a smooth pseudo-wavefunction, Ψ_{pseudo} as compared to the original wavefunction $\Psi_{Z/r}$. Figure adapted from Ref. 51

A variety of pseudopotential types have been developed that satisfy these conditions. The most commonly employed pseudopotentials are the ultra-soft pseudopotentials (USPP). These were introduced by Vanderbilt[52] to allow the lowest possible cut-off energies for plane-wave basis sets.

In addition to the above criteria, norm-conserving pseudopotentials[53] (NCPP) can be generated such that the pseudo- and all-electron wavefunctions yield the same charge density.[5] This is done by generating a pseudopotential that maintains

$$\int_0^{r_c} \boldsymbol{\varphi}_{AE}^*(\boldsymbol{r})\boldsymbol{\varphi}_{AE}(\boldsymbol{r})\boldsymbol{dr} = \int_0^{r_c} \boldsymbol{\varphi}_{ps}^*(\boldsymbol{r})\boldsymbol{\varphi}_{ps}(\boldsymbol{r})\boldsymbol{dr}$$

Equation 2.33

where $\varphi_{AE}(r)$ and $\varphi_{ps}(r)$ are the all-electron and pseudopotential wavefunctions, respectively. This ensures equality of electronic charge both inside and outside the core region. Because of this, NCPPs ensure accurate reproduction of the scattering properties of ions and are most easily developed into DFT (this is particularly true for density functional perturbation theory, DFPT) codes. The work presented in this thesis therefore employs norm-conserving pseudopotentials throughout all lattice dynamics calculations. All pseudopotentials were taken from databases available within the quantum chemical software: CASTEP (00PBE_OP for C,H,N and O atoms).

2.1.6 Phonon Calculations

There are two approaches to calculating vibrational properties within DFT: the linear response (also known as density functional perturbation theory, DFPT) and the finite differences approach. Only DFPT is used in this thesis and will therefore be discussed briefly here. An extensive review on the subject can be found in Reference 54 and an excellent introduction to the field in Reference 55. The use of DFPT over finite differences methods in this thesis is due to the fact that the latter requires use of supercells to calculate the frequencies at wave vectors away from zone centre. This very quickly becomes

computationally intractable for larger, low symmetry systems such as those used in this work.

It is convenient to begin by considering the total energy of a unit cell composed of *N* atoms, with indices l. Each atom has three degrees of freedom, denoted as α, and can describe displacement along the *x,y and z* axes. DFPT is based on a Taylor (*i.e.* derivative) series of small perturbations, u, of the atoms (l) in the direction α (*i.e.* x, y and z), such that,

$$E = E_0 + \sum_{l,\alpha} \frac{\partial E}{\partial \boldsymbol{u}_{l,\alpha}} . \boldsymbol{u}_{l,\alpha} + \frac{1}{2} \sum_{l,\alpha,l\prime,\alpha\prime} \frac{\partial^2 E}{\partial \boldsymbol{u}_{l,\alpha} \partial \boldsymbol{u}_{l\prime,\alpha\prime}} . \boldsymbol{u}_{l,\alpha} . \boldsymbol{u}_{l\prime,\alpha\prime} + \ldots$$

Equation 2.33

Where E_0 is a constant (referring to the energy of the equilibrium structure) and is not considered further. At equilibrium geometry, the forces on all atoms are zero, and hence the first derivative summation disappears. Within the harmonic approximation, all terms above the second term are ignored. Hence only the second summation remains. Note that this is akin to Hooke's classical law, $U = {}^1/_2\, kx^2$. It is convenient to define the force constant matrix,

$$\Phi^{l,l\prime}_{\alpha,\alpha\prime} = \frac{\partial^2 E}{\partial \boldsymbol{u}_{l,\alpha} \partial \boldsymbol{u}_{l\prime,\alpha\prime}}$$

Equation 2.34

It is worth noting here that because phonon calculations are based on Equation 2.33, atomic forces must be converged as close to zero as possible such that the above approximation holds. This requires geometry optimisation of the structure prior to phonon calculations. Furthermore, as will be discussed below because the energy is defined by the wavefunction, a well-optimised wavefunction is also required.

Assuming periodic boundary conditions (*i.e.* that $u(\boldsymbol{R} + N\boldsymbol{a}) = u(\boldsymbol{R})$ where $N\boldsymbol{a}$ is an integer translational vector in the crystal), the displacement $\boldsymbol{u}$ of Equations 2.33 and 2.34 can be written as a plane waves,

$$u_{l,\alpha} = \boldsymbol{\epsilon}_{\mathbf{q}} exp(i(\mathbf{q} \cdot \boldsymbol{R} - \omega t)$$

Equation 2.35

Here, $\boldsymbol{\epsilon}$ is the polarisation vector, which determines the direction in which ions move, and $\mathbf{q}$ is the associated phonon wave vector. Inserting Equation 2.35 into the classical equation of motion gives

$$\mathrm{D}^{l,l'}_{\alpha,\alpha'}(\boldsymbol{q})\boldsymbol{\epsilon}_{\boldsymbol{q},\alpha,l} = \omega^2 \boldsymbol{\epsilon}_{\boldsymbol{q},\alpha,l}$$

Equation 2.36

This is an eigenvalue equation that links the vibrational frequencies, ω to the *dynamical matrix*, defined as

$$\mathrm{D}^{l,l'}_{\alpha,\alpha'}(\boldsymbol{q}) = \frac{1}{\sqrt{M_l M_{l'}}} \sum_{\alpha} \mathrm{C}^{l,l'}_{\alpha,\alpha'}(\boldsymbol{q}) = \frac{1}{\sqrt{M_l M_{l'}}} \sum_{\alpha} \Phi^{l,l'}_{\alpha,\alpha'} e^{-i\boldsymbol{q}\cdot\boldsymbol{r}_{\boldsymbol{\alpha}}}$$

Equation 2.37

where M_l is the mass of atom l. That is to say that the dynamical matrix is the mass-reduced Fourier transform of the real-space force constant matrix.

The base of *ab initio* lattice dynamics therefore is to obtain the force constant, $\Phi^{l,l'}_{\alpha,\alpha'}$, which, according to Equation 2.34, are the second derivatives of the total energy. Thus, $\Phi^{l,l'}_{\alpha,\alpha'}$ describes a Hessian matrix.

The forces acting on atoms can be determined according to the Hellmann-Feynman theorem.[56,57] This is a central theorem in both geometry optimisation and phonon calculations. In bra-ket notation the Hellmann-Feynman theorem relates the derivative of the total energy with respect to a perturbation, λ, to the expectation value of the Hamiltonian to that same perturbation,[54]

$$\frac{\partial E_\lambda}{\partial \lambda} = \left\langle \varphi_\lambda \middle| \frac{\partial \hat{H}}{\partial \lambda} \middle| \varphi_\lambda \right\rangle$$

Equation 2.38

It follows from Equation 2.38 that for displacement of the *i*th nucleus, $\boldsymbol{R_i}$,

$$F_A = -\frac{\partial E}{\partial \boldsymbol{R}_A} = \left\langle \varphi \left| \frac{\partial \hat{H}}{\partial \boldsymbol{R}_A} \right| \varphi \right\rangle$$

Equation 2.39

Equation 2.39 is known as the electrostatic force theorem, and is used to minimise ionic positions during geometry optimisation (hence the need for a good approximation of the wavefunction). For phonon calculations, however, it is the Hessian of the Born-Oppenheimer energy surface that is required. This comes from differentiating the Hellmann-Feynman forces (Equation 2.39) with respect to nuclear coordinates and noting that from the BOA Hamiltonian in Equation 2.4 the Hamiltonian depends on nuclear coordinates *via* the electron-ion interactions ($V_{\boldsymbol{R}}(\boldsymbol{r})$) and the charge density, $n(\boldsymbol{r})$. Hence,[54]

$$\frac{\partial^2 E(\boldsymbol{R})}{\partial R_i \partial R_j} = -\frac{\partial \mathbf{F_i}}{\partial \mathbf{R_j}} = \int \frac{\partial n_R(\boldsymbol{r})}{\partial \mathbf{R_j}} \frac{\partial V_R(\boldsymbol{r})}{\partial \mathbf{R_I}} d\boldsymbol{r} + \int n_{\boldsymbol{R}}(\boldsymbol{r}) \frac{\partial^2 V_R(\boldsymbol{r})}{\partial \mathbf{R_I} \partial \mathbf{R_J}} d\boldsymbol{r} + \frac{\partial^2 E_N(\boldsymbol{R})}{\partial \mathbf{R_I} \partial \mathbf{R_J}}$$

Equation 2.40

and the Hessian matrix of the Born-Oppenheimer energy depends on the ground state electron density, $n_{\boldsymbol{R}}(\boldsymbol{r})$, and its *linear response* to nuclear perturbation, $\partial n_R(r) / \partial \boldsymbol{R}_I$. The final term in Equation 2.40 describes the second force imposed by one nucleus on another as a function of the perturbation (*i.e.* the second derivative of the nuclear-nuclear interaction energy).

In a DFPT (or linear response) calculation, the Hessian matrix is generated according to Equation 2.40 for a select subset of wave vectors and the dynamical matrix attained *via* Equation 2.37. These can be subsequently Fourier interpolated onto other wave vectors, and hence a small number of explicitly calculated dynamical matrices can yield a complete dispersion curve. This allows access not only to dispersion relations along high symmetry lines, but also to generation of phonon density of states, which require consideration of a large number of wave vectors for accurate production. This assumes that the calculated wave vectors capture the nature of the force constant along the

wave vector that is being interpolated. In an attempt to ensure unbiased sampling of wave vectors in the initial case, wave vector sampling is often done using a Monkhorst Pack grid.

2.2 Experimental Methods

2.2.1 X-ray Diffraction

The most definitive way to analyse the structure of a solid is *via* diffraction-based techniques. Most commonly, diffraction techniques use X-ray radiation, although neutron- and electron-based techniques are also well-known. An excellent introduction to the field of X-ray diffraction and crystallography can be found in Reference 58.

X-rays are a form of electromagnetic radiation, with wavelength ~ 0.1 to 100 Å. Their interaction with matter results from interactions with the electrons of the material, and the intensity of their scattering is therefore proportional to the electron density. While X-rays are less sensitive to atom type (and insensitive to isotopes), they scatter more strongly than neutrons. Thus, for most purposes, X-ray diffraction tends to be favoured due to faster collection times and higher quality data as compared to neutron diffraction.

An additional benefit to X-ray diffraction is its availability, with laboratory X-ray sources now commonplace. In a laboratory source, X-rays are generated by accelerating an electron into an anode of a characteristic material. Upon collision, the kinetic energy of the electron is sufficient to eject a core-level electron from the anode, leaving an unstable vacant core state. An electron in a higher energy orbital therefore drops into the vacant state, and the excess energy emitted as an X-ray. Due to the quantized structure of atomic orbitals, the X-ray energy is characteristic of a particular anode. Most common laboratory sources use a Cu anode (K_α=1.54056 Å), although others can be used. All diffraction data reported in this work is based on monochromatic Cu

radiation using a Bruker D2 phase diffractometer (flat plate geometry) in the School of Chemistry, University of Edinburgh.

The “discovery” of X-rays is often accredited to German physicist Wilhelm Röntgen in 1895.[59] It was not until 1912 that von Laue first theorised that due to the similar size of X-ray wavelengths and inter-atomic spacings, that X-rays could scatter from the periodic arrays presented by crystals.[60–63] William and Lawrence Bragg subsequently simplified the models proposed by von Laue and developed the now famous Bragg’s Law.[61,64] This led the Father and Son to demonstrate the capabilities of X-ray diffraction in 1913 with the structural solution of NaCl, KCl, KBr and KI,[64] and crystallography was born.

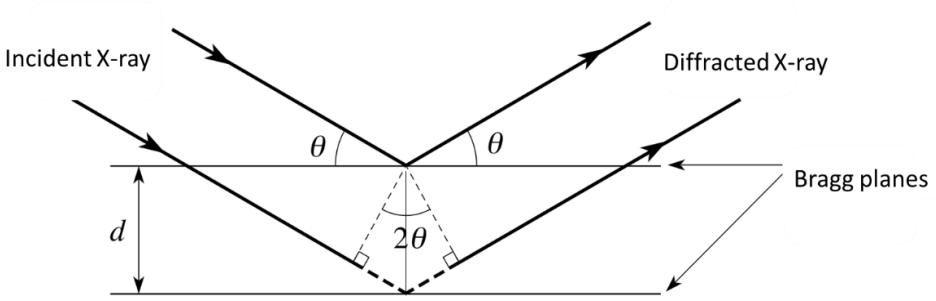

Figure 2.4: Schematic representation of Bragg’s Equation. Figure adapted from Ref 58

The model proposed by the Braggs is best represented pictorially, Figure 2.4. Diffraction is taken to occur from a set of theoretical planes, with interplanar spacing *d*, that run through the real space primitive cell. In order to observe diffraction, scattered X-rays must interfere constructively, and hence must possess a wavelength, λ, with half integer values of *d.* For a given λ, this condition can be met by varying the angle of incidence, θ. This leads to the Bragg equation,

$$n\lambda = 2d\sin\theta$$

Equation 2.41

An additional term, *n,* is observed in Equation 2.41. This term results from the fact that coherent scattering can occur from higher order reflections in reciprocal space (wave vectors). It is the convention for this term to be

absorbed into *d*, and to describe sets of planes using the real space Miller indices, (*hkl*). These indices describe the number of times a set of planes intersect with the crystallographic *a*, *b* and *c* axes, respectively. Due to the intimate relation between *d* and θ, the positions of the peaks in the diffraction pattern is indicative of the structure of the unit cell, and hence the crystallographic parameters that describe the size and shape of the crystallographic unit cell: *a, b, c* α, β and γ. Coupled to knowledge of the quantity of electron density located along each plane (by the intensity of diffraction), X-ray scattering therefore contains the required information to determine the relative positions of the atoms, and to identify them, within a crystalline material

2.2.1.1 X-ray Powder Diffraction

If a single crystal scatters monochromatic X-rays, a set of well-defined diffraction spots are observed according to[58]

$$F(hkl) = \int \mathrm{dV}\ \rho(\mathrm{xyz})\exp(2\pi\mathrm{i}(\mathrm{hx} + \mathrm{ky} + \mathrm{lz})$$

$$I(hkl) \propto |F(hkl)|^2$$

Equation 2.42

Thus, the angle of scattering for a set of Miller indices depends on Braggs law, Equation 2.41, and their intensities on the relative position of atoms in real space (electron density, $\rho(xyz)$), with respect to that set of diffracting planes.

In powder diffraction techniques, however, monochromatic radiation is incident on a bulk sample, containing many, randomly oriented crystals. This has the effect of smearing the single diffraction spots into concentric cones, known as the Debye-Scherrer cones, Figure 2.5.

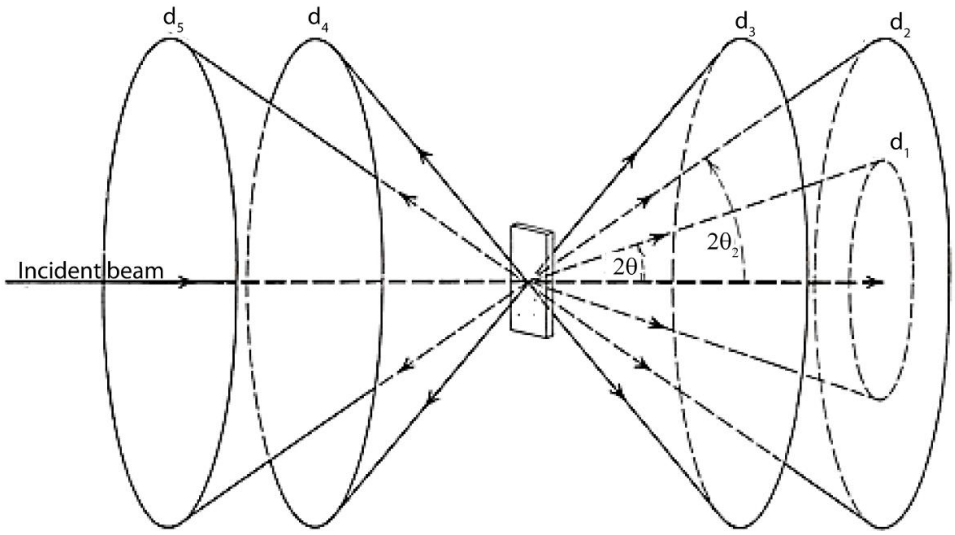

Figure 2.5: Schematic representation of the Debye-Scherrer cones. Adapted from Ref.65

It is common to collect the complete set of cones (*e.g.* on a 2D area detector), or simply a small subsection of them (*e.g.* a point detector). The collected cones are integrated, and a one-dimensional pattern produced, Figure 2.6. In accordance with Bragg's law, Equation 2.41, unit cells of different dimensions will give rise to a set of peaks at different 2θ positions. Hence, a qualitative comparison of powder diffraction patterns can be used to assess polymorphic modifications. In principle, Equation 2.42 suggests that peak intensities correspond to the relative position of atoms within the diffracting structure. Peak intensities from powder diffraction experiments can be misleading, however. If crystallite morphology favours a particular orientation of powder particles, not all lattice planes will be equally represented within the powder mixture, a phenomenon known as texturing or preferred orientation. This is particularly problematic when powder samples are analysed on a flat plate as is commonly done on the Bruker D2 phaser used in this work. If reliable peak intensities are required, it is more common to collect diffraction data from powder samples held within a capillary.

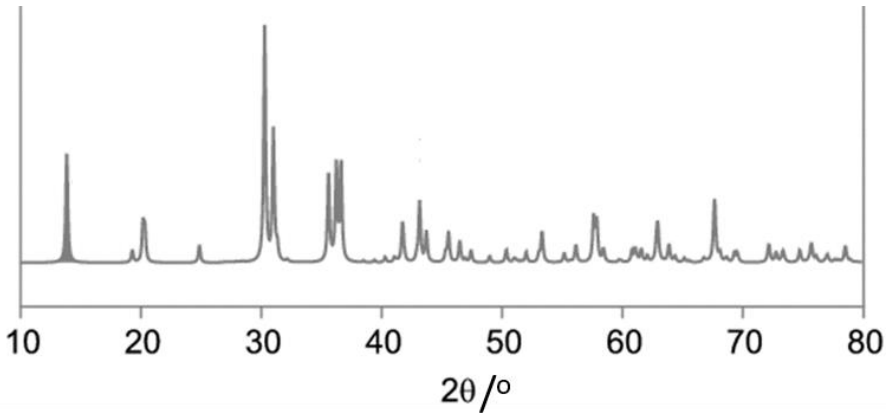

Figure 2.6: Example integrated powder diffraction pattern.

2.2.2 Inelastic Neutron Scattering Spectroscopy

Inelastic neutron scattering spectroscopy (INS) is used for studying the vibrational properties of molecules and materials. An excellent text on its theory and applications can be found in Reference 66 and 67. In INS spectroscopy, a beam of neutrons is incident on a sample. These neutrons scatter from the nuclei within the sample and exchange energy, hence measurement of vibrational frequencies, (ω) and momentum ($\boldsymbol{q}$) with the sample. The INS experiment is often compared to the optical spectroscopies: Raman and infrared spectroscopy.[68] While there are many similarities between INS and optical probes, the nature of INS possesses several distinct advantages, including:

1. *Ease of modelling.*

The scattering function is purely dynamical (Section 2.2.2.2) and as such is easily calculated within the framework of classical and quantum mechanics.

2. *Broad spectral range.*

Typical INS spectrometers (*e.g.* TOSCA) extend from 0 to > 4000 cm^{-1}.[69] This is much broader than typical optical spectrometers, which often miss the far infrared region 10 – 400 cm^{-1}, and thus omit the lattice, or external, modes of vibration which are critical in this work.

3. *Sensitivity to normal modes involving hydrogen atoms.*

Optical probes are dominated by heavy atoms due in part to higher electron densities. INS intensities are proportional to neutron cross sections (σ), and that of hydrogen is particularly high.[5]

4. *Lack of selection rules.*

Unlike optical probes, all vibrational modes (including fundamental, overtone and combination modes) are in principle observed in INS spectroscopy. Group theory selection rules, which limit the observation of modes in Raman and infrared spectra, do not apply to INS spectroscopy.

5. *Weak interactions with matter.*

INS therefore is inherently weighted towards measurement of the bulk properties of a sample, whereas optical methods are weighted towards surface properties.

However, these advantages are accompanied by a number of complicating factors, including:

1. *Momentum transfer.*

INS does *not* measure scattering from the centre of the Brillouin zone. While this does not tend to be a large effect for internal molecular modes, it can lead to some changes in frequency as compared to optical probes, which only detect the Brillouin zone centre (*i.e.* long-range order) vibrations.

2. *Neutrons interact weaker with matter than protons.*

INS requires much larger sample size, and longer collection times to obtain vibrational spectra as compared to optical techniques.

[5] No theoretical method is available to calculated neutron scattering cross sections σ, and all tabulated values are directly obtained from experiment. Molecular vibrations are dominated by incoherent neutron scattering, with σ_{inch} for common nuclei ^{1}H, ^{2}D, ^{12}C, ^{13}C, ^{14}N and ^{16}O are; 80.27, 2.05, 0, 0.034, 0.5 and 0 barn,[83] respectively. σ_{inch} of ^{1}H clearly dominates.

3. *Availability*

INS is only possible at dedicated beamlines, located at neutron sources.

4. *Temperature Range*

Neutron scattering is much more sensitive to temperature than optical probes. Typical INS spectra are therefore obtained at *ca.* 10 K.

2.2.2.1 Generation of Neutrons

Neutrons can be produced from a variety of nuclear reactions:[67] fusion, photofission, fission, and spallation. The latter two are most common for scattering experiments. In a fission reactor (such as the ILL in Grenoble), neutrons are produced by thermal fission of fissionable isotopes, typically ^{235}U. Thermal fission of this ^{235}U generates a continuous stream of high energy neutrons, which can be moderated to produce thermal neutrons. At a spallation source, high energy protons are generated using a synchrotron. These protons bombard a metal target (*e.g.* tungsten or tantalum), which triggers emission of a cascade of high energy neutrons. As the protons are generated in pulses, so too are the neutrons at a spallation source. All of the INS spectra used in this thesis were obtained at a spallation source: the ISIS Neutron and Muon Facility, STFC Rutherford Appleton Laboratory, UK. Hence this process will be considered further.

At the ISIS Neutron Facility, high energy protons are generated using a synchrotron, and are directed at a tantalum coated tungsten target (at Target Station 1, where the INS beamline is located). These protons have immense energy (*ca.* 800 MeV), which excites nuclei in the target. This induces an intranuclear cascade, which in turn leads to emission of high energy neutrons (approximately 15 per proton) Hence, an intense neutron pulse is generated. The neutrons that result from this process have energies on the order of ~ 2 MeV, termed epithermal neutrons. However, these are too energetic for most practical applications. To reduce the energy of these neutrons, they are

therefore passed through a moderator. For the TOSCA beamline, this is ambient temperature (300 K) water.[70] The neutrons undergo numerous inelastic collisions with the water molecules, and their energy is therefore subdued. The resulting neutrons (known as thermal neutrons) adhere to a Maxwell-Boltzmann distribution of energies, about a peak flux that is characteristic of the moderator. For water, the peak flux is approximately 200 cm^{-1}. It is these thermal neutrons that are finally passed to the instrument and used for INS.

2.2.2.2 The TOSCA Instrument

The TOSCA instrument was used for collection of INS spectra in this work.[69–71] TOSCA is an indirect geometry time-of-flight (ToF) neutron spectrometer with resolution $\Delta\omega/\omega \approx 2 - 3\%$. As an indirect instrument, the experiment works by fixing the final energy of the detected neutrons that are scattered from the sample, and scans the incident energies. As described above, the incident neutron beam contains a distribution of neutron energies (*i.e.* it is a white beam), which are characterised by their kinetic energy and hence the rate at which they reach the sample. To maximise signal, TOSCA utilises both forward and backward scattering detectors. Only the neutrons which scatter at fixed angles (45° or 135°) will impinge on the analyser crystals (the (002) plane of pyrolytic graphite). It follows from Bragg's law, Equation 2.41 that since the scattering Bragg plane is fixed, only a single wavelength (and its higher orders) of neutron will be passed from the analyser crystal to the detector. All remaining neutrons will pass through the analyser crystal and are absorbed by the spectrometer shield. The neutrons that are scattered by the analyser are passed through a beryllium filter, scattering away neutrons with multiples of the fundamental wavelength. Finally the remaining neutrons are detected by a bank of ^{3}He filled detector tubes. The result of using both the graphite analyser in parallel with the beryllium filters is to create a narrow band-pass filter.

Because neutrons can be treated as both particle and wave, it is possible to define the kinetic energy of a neutron based on its velocity, *v*, and its mass, m_n,

$$E = \frac{1}{2} m_n \boldsymbol{v}^2 \Longrightarrow \boldsymbol{v} = \sqrt{\left(\frac{2E}{m_n}\right)}$$

Equation 2.43

The energy that is transferred between the incident neutron and the sample, E_{tr}, is defined by the difference in energy of the initial (E_i) and final (E_f) neutron energies. For a ToF instrument, the total time, t_{tot}, travelled by the neutron is defined as the time taken to travel from moderator to sample (distance l_1, time t_1), and the time taken for the scattered neutron to travel from the sample to the detector (distance l_f, time t_2). It therefore follows that

$$t_{tot} = \frac{l_1}{v_1} + \frac{l_2}{v_2} = \frac{l_1}{\sqrt{\frac{2E_i}{m_n}}} + \frac{l_2}{\sqrt{\frac{2E_f}{m_n}}}$$

Equation 2.44

In Equation 2.44, E_f, l_1 and l_2 are all fixed by the geometry of the instrument. Hence, the time taken to travel to the detector uniquely defines the incident energy of the neutron, and correspondingly, E_{tr}.

2.2.2.3 Neutron Scattering

In a neutron scattering experiment, an incident beam of neutrons (neutral subatomic particles with mass, m_n, approximately equal to that of a proton) is scattered from a sample. This scattering can be the result of magnetic interactions, or due to nuclear interactions. Scattering due to magnetic interactions is outside the scope of this work, and will not be discussed here; an introduction can be found in Ref 72.

The total nuclear scattering is defined by the differential scattering cross section,

$$\frac{d\sigma}{d\Omega} = b^2 = \frac{\sigma_t}{4\pi}$$

Equation 2.45

which describes the amount of total scattering, σ_t into the elementary scattering cone of solid angle $d\Omega$ per unit time. This depends on the nuclear scattering length, b. The scattering according to Equation 2.45 forms the base for diffraction experiments.

As was discussed Section 2.2.1.2, INS is an inelastic process, and the detected neutrons depend both on the solid angle at which they are scattered, and also on their energy. This is captured in the partial differential cross-section for a system of N atoms, which must therefore be considered as,

$$\frac{d^2\sigma}{d\Omega dE_f} = b^2 \frac{k_f}{k_i} NS(\boldsymbol{Q}, \omega)$$

Equation 2.46

where $k = \frac{2\pi}{\lambda}$ is the wave vector for the incident (k_i) and final (k_f) neutron.

The term $S(\boldsymbol{Q}, \omega)$ is the scattering function, and describes the probability that the scattering process will change the energy of the system by an amount ω, and its momentum by $\hbar\boldsymbol{Q} = \hbar\Delta\boldsymbol{k}$**.** Because both the energy and angle of the final scattered neutron are fixed on TOSCA, this also fixes $\boldsymbol{k}_f$. The value of $\boldsymbol{Q}$ is therefore dependent on E_{tr}, and TOSCA probes a narrow stripe in ($\boldsymbol{Q}$,ω) of kinematic space.[70]

The scattering described in Equations 2.45 and 2.46 account for the elastic and inelastic scattering processes. However, due to nuclear effects (isotope and spin effects), the scattering cross section in both cases requires consideration of *coherent* and *incoherent* processes. The former describes the in-phase scattering and results in interference effects. Hence, coherent scattering is required for diffraction and vibrational spectroscopy of collective motions (*e.g.* phonon dispersion). The incoherent scattering describes motion

of single particles, in which no correlation exists between different molecules or atoms. These motions are particularly important for studying internal molecular vibrations. In an INS spectrum, both coherent and incoherent scattering processes are observed, and the dominating scattering mechanism depends largely on the scattering cross-sections of the atoms involved. Incoherent scattering dominates in hydrogen-containing compounds.

The absolute intensity of an INS spectrum is difficult to interpret, and so only the relative spectral intensities are considered. The calculated relative intensity (the scaled scattering factor, $S^*(\boldsymbol{Q}, \omega_i)$) of the i^{th} vibrational mode with momentum transfer $\boldsymbol{Q}$ and neutron energy loss $E_{tr} = \omega_i$ is defined as[73]

$$S^*(\boldsymbol{Q}, \omega_i)_m^n = y\sigma_m \frac{\left[\left(\boldsymbol{Q} \cdot {}^i\boldsymbol{u}_m\right)^2\right]^n}{n!} exp\left(-\left(\boldsymbol{Q} \cdot \sum_i {}^i u_m\right)^2\right)$$

Equation 2.47

In Equation 2.47, ${}^i\boldsymbol{u}_m$ is the displacement vector for atom *m* of mode *i, y* is a linear factor (units barn cm), which acts to convert the actual units of $S^*(\boldsymbol{Q}, \omega_i)$) into scaled dimensionless units. The final variable, *n*, indicates the final state of the excited mode. So, an elastic process has *n=0*, a fundamental *n=1*, the first overtone *n=2*, etc. The pre-exponential term of Equation 2.47 increases with increasing momentum transfer and vibrational amplitude. The exponential term (known as the Debye-Waller factor), however, decreases more rapidly with $\boldsymbol{Q}^2\boldsymbol{u}^2$. Hence, there is an overall decrease in vibrational amplitude with increasing temperature. As such, it is typical to collect INS spectra at cryogenic temperatures, although (as done in this thesis) higher temperature measurements are still possible.

Equation 2.47 is surprisingly simple, and depends on the momentum transferred, the scattering cross section and the magnitude of the atomic displacement. Hence, the observed INS intensity is purely dynamic and can be easily calculated: frequencies are obtained from normal mode eigenvalues

and the displacements from the eigenvectors. Thus INS is an excellent technique against which to validate calculated vibrational spectra.[31,74].

2.2.3 BAM fall Hammer

A number of tests have been developed to measure the impact sensitivity of energetic materials (EMs). These include the Picatinnany Arsenal apparatus, the Bureau of Mines Machine, the Rotter Impact Machine, and the BAM fall hammer.[75,76] The standard procedures and device depend largely on geography.[77] Some devices, such as the Rotter Impact Machine, define a successful initiation based on the production of gas products. For other methods, such as in the BAM fall hammer, a successful initiation is determined by the user, and is generally based on sound or visual inspection of the sample. It follows that the reported impact sensitivities that result from different testing methods can vary substantially.[78] Further difficulties in the experimental validation of impact sensitivity stems from sample and environmental factors,[79] which include particle size, crystallinity, purity, temperature, and humidity, amongst others. These factors are not regularly controlled, and their effects on impact sensitivity are poorly understood. These all contribute to the extreme variability in reported impact sensitivities for materials.

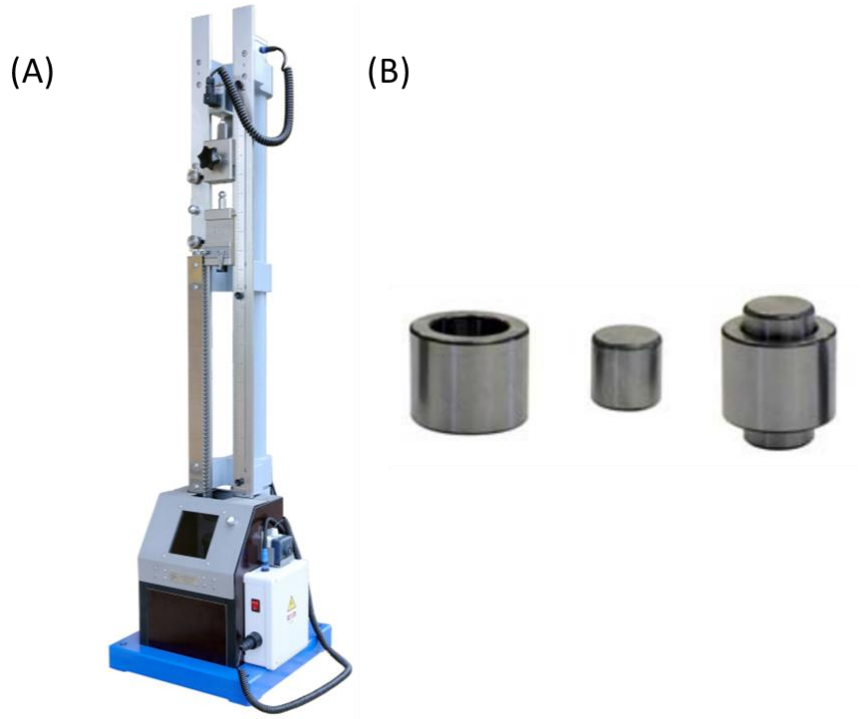

Figure 2.7: BAM fall hammer device used for impact sensitivity testing. (A) The BAM BFH-12 apparatus. (B) Sample anvil. Figure adapted from Ref. 80

This work makes use of the BAM fall hammer (BFH-12), based at the Cavendish Laboratories, University of Cambridge, Figure 2.7A. This device has been accepted as the NATO qualification testing method, described in the United Nations recommendations for the Transport of Dangerous Goods.[76] The BFH procedure requires a sample of 40 mm^3 to be enclosed in an anvil setup, composed of two coaxial steel cylinders and a guide ring, Figure 2.7B. To apply the impact, a load mass of 10, 5, 2, 1 or 0.5 kg is dropped onto a sample, from heights ranging 20 – 100 cm. The energy is therefore calculated as, *e.g.* 1 kg from 50 cm = 5 J.

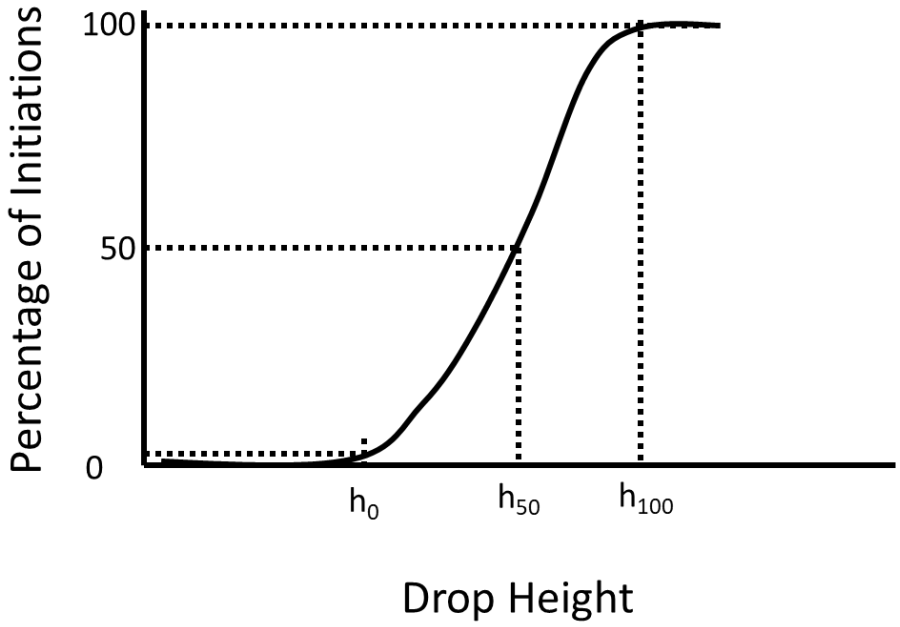

Figure 2.8: Probability of initiation of energetic materials to impact. Figure from Ref. 81

There are two testing protocols typically used for assessing the impact sensitivity of EMs. The Limiting Impact Energy Test (known also as the 1-in-6 method) is outlined in the United Nations testing requirements for the transport of explosives.[76] According to this method, the impact energy is lowered step-wise until an impact energy is reached at which six consecutive trials result in a 'No Go' (that is, no explosion, discolouration, flash or loud noise is observed upon impact). This is taken as the highest drop height at which impact will *not* induce initiation of the sample, h_0, Figure 2.8. This method is good for assessing the safe handling of materials, and for testing small sample sizes.

The Bruceton up-down method also leads to measurement of a sample's h_{50} value, Figure 2.8 (*i.e.* the drop height at which 50% of tested samples will initiate). It has a corresponding energy denoted E_{50}. In this method, the drop height is varied depending on the outcome of a previous measurement. If the sample initiates at a particular energy, the subsequent test is performed at a lower stimulus energy. Instead if the sample does not initiate, the new test is performed at higher energy. This method assumes a normal response to input energy and has been criticised,[82] although it remains widely used.

Both methods are indicative of the impact sensitivity of a material. However, their values are clearly not directly comparable. Moreover, the fall hammer method used is often not described in the literature alongside the numerical data, and this further contributes to the large discrepancy of sensitivity reported in literature. Where possible, this work seeks to compare its models against reported h_{50} values, unless otherwise stated.

2.3 References

(1) Schrödinger, E. An Undulatory Theory of the Mechanics of Atoms and Molecules. *Phys. Rev.* **1926**, *28* (6), 1049–1070.

(2) Atkins, P.; Friedman, R. *Molecular Quantum Mechanics*, 4th editio.; Oxford University Press: New York, 2005.

(3) Born, M.; Oppenheimer, R. Zur Quantentheorie Der Molekeln. *Ann. Phys.* **1927**, *389* (20), 457–484.

(4) Slater, J. C. The Theory of Complex Spectra. *Phys. Rev.* **1929**, *34* (10), 1293.

(5) Jensen, F. *Introduction to Computatinoal Chemistry*, 2nd ed.; John Wiley & Sons, Ltd: Chichester, UK, 2007.

(6) Dawes, R.; Ndengué, S. A. Single- and Multireference Electronic Structure Calculations for Constructing Potential Energy Surfaces. *Int. Rev. Phys. Chem.* **2016**, *35* (3), 441–478.

(7) Bartlett, R. J. To Multireference or Not to Multireference: That Is the Question? *Int. J. Mol. Sci.* **2002**, *3* (6), 579–603.

(8) Namboori, K.; Ramachandran, K. I.; Deepa, G. *Computational Chemistry and Molecular Modeling*; Springer-Verlag: Berling Heidelberg, 2008.

(9) Werner, H. J.; Knowles, P. J. *Molpro: Getting Started with Molpro V 2015.1*; 2015.

(10) Werner, H. J.; Knowles, P. J.; Knizia, G.; Manby, F. R.; Schütz, M. Molpro: A General-Purpose Quantum Chemistry Program Package. *Wiley Interdiscip. Rev. Comput. Mol. Sci.* **2012**, *2* (2), 242–253.

(11) Burke, K. Perspective on Density Functional Theory. *J. Chem. Phys.* **2012**, *136* (15), 150901.

(12) Baseden, K. A.; Tye, J. W. Introduction to Density Functional Theory: Calculations by Hand on the Helium Atom. *J. Chem. Educ.* **2014**, *91* (12), 2116–2123.

(13) Hohenberg, P.; Kohn, W. Inhomogeneous Electron Gas. *Phys. Rev.* **1964**, *136* (3B), 864.

(14) Koch, W.; Holthausen, M. C. *A Chemist's Guide to Density Functional Theory*, 2nd ed.; Wiley-VCH: Weinheim, 2001.

(15) Kohn, W.; Sham, L. J. Self-Consistent Equations Including Exchange and Correlation Effects. *Phys. Rev.* **1965**, *140* (4A), 1133–1138.

(16) Perdew, J. P. Jacob's Ladder of Density Functional Approximations for the Exchange-Correlation Energy. *AIP Conf. Proc.* **2001**, *577* (2001), 1–20.

(17) Peverati, R.; Truhlar, D. G. Quest for a Universal Density Functional : The Accuracy of Density Functionals across a Broad Spectrum of Databases in Chemistry and Physics. *Phil. Trans. R. Soc A.* **2014**, *372*, 20120476.

(18) Thomas, L. H. The Calculation of Atomic Fields. *Math. Proc. Cambridge Philos. Soc.* **1927**, *23*, 542–548.

(19) Fermi, E. Eine Statistische Methode Zur Bestimmung Einiger Eigenschaften Des Atoms Und Ihre Anwendung Auf Die Theorie Des Periodischen Systems Der Elemente. *Z. Phys. A Hadron. Nucl.* **1928**, *48*, 73–79.

(20) Becke, A. D. Density-Functional Thermochemistry. III. The Role of Exact Exchange. *J. Chem. Phys.* **1993**, *98* (7), 5648–5652.

(21) Langreth, D. C.; Mehl, M. J. Beyond the Local-Density Approximation in Calculations of Ground-State Electronic Properties. *Phys. Rev. B* **1983**, *28* (4), 1809–1834.

(22) Perdew, J. P. Accurate Density Functional for the Energy: Real-Space Cutoff of the Gradient Expansion for the Exchange Hole. *Phys. Rev. Lett.* **1985**, *55* (16), 1665–1668.

(23) Perdew, J. P.; Burke, K.; Ernzerhof, M. Generalized Gradient Approximation Made Simple. *Phys. Rev. Lett.* **1996**, *77* (18), 3865–3868.

(24) Burke, K.; Perdew, J. P.; Wang, Y. Derivation of a Generalized Gradient Approximation: The PW91 Density Functional. In *Electronic Density Functional Theory*; Dobson, J. F., Vignale, G., Das, M. P., Eds.; Springer-Verlag: Boston, 1998; pp 81–111.

(25) Perdew, J.; Chevary, J.; Vosko, S.; Jackson, K.; Pederson, M.; Singh, D.; Fiolhais, C. Atoms, Molecules, Solids, and Surfaces: Applications of the Generalized Gradient Approximation for Exchange and Correlation. *Phys. Rev. B* **1992**, *46* (11), 6671–6687.

(26) Becke, A. D. Density-Functional Exchange-Energy Approximation with Correct Asymptotic Behavior. *Phys. Rev. A* **1988**, *38* (6), 3098–3100.

(27) Lee, C.; Yang, W.; Parr, R. G. Development of the Colle-Salvetti Correlation-Energy Formula into a Functional of the Electron Density. *Phys. Rev. B* **1988**, *37* (2), 785–789.

(28) Campbell, R.; Konar, S.; Hunter, S.; Pulham, C.; Portius, P. Labile Low-Valent Tin Azides: Syntheses, Structural Characterization, and Thermal Properties. *Inorg. Chem.* **2018**, *57*, 400–411.

(29) Hunter, S.; Davidson, A. J.; Morrison, C. A.; Pulham, C. R.; Richardson, P.; Farrow, M. J.; Marshall, W. G.; Lennie, A. R.; Gould, P. J. Combined Experimental and Computational Hydrostatic Compression Study of Crystalline Ammonium Perchlorate. *J. Phys. Chem. C* **2011**, *115* (38), 18782–18788.

(30) Hunter, S.; Coster, P. L.; Davidson, A. J.; Millar, D. I. A.; Parker, S. F.; Marshall, W. G.; Smith, R. I.; Morrison, C. A.; Pulham, C. R. High-Pressure Experimental and DFT-D Structural Studies of the Energetic Material FOX-7. *J. Phys. Chem. C* **2015**, *119* (5), 2322–2334.

(31) Hunter, S.; Sutinen, T.; Parker, S. F.; Morrison, C. A.; Williamson, D. M.; Thompson, S.; Gould, P. J.; Pulham, C. R. Experimental and DFT-D Studies of the Molecular Organic Energetic Material RDX. *J. Phys. Chem. C* **2013**, *117* (16), 8062–8071.

(32) Tkatchenko, A.; Scheffler, M. Accurate Molecular van Der Waals Interactions from Ground-State Electron Density and Free-Atom Reference Data. *Phys. Rev. Lett.* **2009**, *102* (7), 6–9.

(33) Grimme, S. Semiempirical GGA-Type Density Functional Constructed with a Long-Range Dispersion Correction. *J. Comput. Chem.* **2006**, *27*, 1787–1799.

(34) Grimme, S.; Antony, J.; Ehrlich, S.; Krieg, H. A Consistent and Accurate Ab Initio Parametrization of Density Functional Dispersion Correction (DFT-D) for the 94 Elements H-Pu. *J. Chem. Phys.* **2010**, *132* (15), 154104.

(35) Mardirossian, N.; Ruiz Pestana, L.; Womack, J. C.; Skylaris, C. K.; Head-Gordon, T.; Head-Gordon, M. Use of the RVV10 Nonlocal Correlation Functional in the B97M-V Density Functional: Defining B97M-RV and Related Functionals. *J. Phys. Chem. Lett.* **2017**, *8* (1), 35–40.

(36) Sabatini, R.; Küçükbenli, E.; Pham, C. H.; De Gironcoli, S. Phonons in Nonlocal van Der Waals Density Functional Theory. *Phys. Rev. B* **2016**, *93* (23), 1–7.

(37) Crowley, J. M.; Tahir-Kheli, J.; Goddard, W. A. Resolution of the Band Gap Prediction Problem for Materials Design. *J. Phys. Chem. Lett.* **2016**, *7* (7), 1198–1203.

(38) Benjamin G. Janesko, Thomas M. Henderson, and G. E. S. Screened Hybrid Density Functionals for Solid-State Chemistry and Physics. *Phys. Chem. Chem. Phys.* **2009**, *11* (3), 443–454.

(39) Heyd, J.; Peralta, J. E.; Scuseria, G. E.; Martin, R. L. Energy Band Gaps and Lattice Parameters Evaluated with the Heyd-Scuseria-Ernzerhof Screened Hybrid Functional. *J. Chem. Phys.* **2005**, *123* (17), 174101.

(40) Slater, J. C. Atomic Shielding Constants. *Phys. Rev.* **1930**, *36* (1), 57–64.

(41) Magalhães, A. L. Gaussian-Type Orbitals versus Slater-Type Orbitals: A Comparison. *J. Chem. Educ.* **2014**, *91* (12), 2124–2127.

(42) Hehre, W. J.; Stewart, R. F.; Pople, J. A. Self-Consistent Molecular-Orbital Methods. I. Use of Gaussian Expansions of Slater-Type Atomic Orbitals. *J. Chem. Phys.* **1969**, *51* (6), 2657–2664.

(43) Dunning, T. H. Gaussian Basis Sets for Use in Correlated Molecular Calculations. I. The Atoms Boron through Neon and Hydrogen. *J. Chem. Phys.* **1989**, *90* (2), 1007–1023.

(44) Martin, R. M. *Electronic Structure: Basic Theory and Practical Methods, by Richard M. Martin*; Cambridge University Press: Cambridge, UK, 2004.

(45) Pack, J. D.; Monkhorst, H. J. Special Points for Brillouin-Zone Integrations. *Phys. Rev. B* **1976**, *13* (12), 5188–5192.

(46) Binns, J.; Healy, M. R.; Parsons, S.; Morrison, C. A. Assessing the Performance of Density Functional Theory in Optimizing Molecular Crystal Structure Parameters. *Acta Crystallogr. Sect. B Struct. Sci. Cryst. Eng. Mater.*

2014, *70* (2), 259–267.

(47) Kochman, M. Private Communication. University of Edinburgh.

(48) Towler, M. D.; Zupan, A.; Causà, M. Density Functional Theory in Periodic Systems Using Local Gaussian Basis Sets. *Comput. Phys. Commun.* **1996**, *98* (1–2), 181–205.

(49) Heine, V. The Pseudopotential Concept. *Solid State Phys. - Adv. Res. Appl.* **1970**, *24* (C), 1–36.

(50) Schwerdtfeger, P. The Pseudopotential Approximation in Electronic Structure Theory. *ChemPhysChem* **2011**, *12* (17), 3143–3155.

(51) *Castep Guide*; San Diego, USA, 2014.

(52) Vanderbilt, D. Soft Self-Consistent Pseudopotentials in a Generalized Eigenvalue Formalism. *Phys. Rev. B* **1990**, *41* (11), 7892–7895.

(53) Kleinman, L.; Bylander, D. M. Efficacious Form of Model Pseudopotentials. *Phys. Rev. Lett.* **1982**, *48* (20), 1425–1428.

(54) Baroni, S.; De Gironcoli, S.; Dal Corso, A.; Giannozzi, P. Phonons and Related Crystal Properties from Density-Functional Perturbation Theory. *Rev. Mod. Phys.* **2001**, *73* (2), 515–562.

(55) Dove, M. T. *Introduction to Lattice Dynamics*; Cambridge University Press: Cambridge, UK, 1993.

(56) Hellmann, H. Einführung in Die Quantenchemie. *Angew. Chemie* **1937**, *54* (11), 156.

(57) Feynman, R. P. Forces in Molecules. *Phys. Rev.* **1939**, *56* (4), 340–343.

(58) Hammond, C. *The Basics of Crystallography and Diffraction.*, 4th ed.; Oxford University Press: Oxford, UK, 2015.

(59) Rontgen, W. C. A New Kind of Rays. *Nature* **1896**, *53*, 1369.

(60) Laue, M. X-Rays. *Sitz. ber Bayer. Akad. D. Wiss.* **1912**, *8*, 363–373.

(61) Thomas, J. M. William Lawrence Bragg: The Pioneer of X-Ray Crystallography and His Pervasive Influence. *Angew. Chemie - Int. Ed.* **2012**, *51* (52), 12946.

(62) Friedrich, W.; Knipping, P.; Laue, M. Interferenzerscheinungen Bei Rontgenstrahlen. *Ann. Phys.* **1913**, *346* (10), 971–988.

(63) Laue, M.; Friedrich, W.; Knipping, P. Xrays. *Sitz. ber Bayer. Akad. D. Wiss.* **1912**, *88*, 303–322.

(64) Bragg, P. W. H.; Bragg, W. L. The Structure of Some Crystals as Indicated by Their Diffraction. *Proceeds R. Soc.* **1913**, *17*, 428–438.

(65) Klug, H. P.; Alexander, L. E. *X-Ray Diffraction Procedures for Polycrystalline and Amorphous Materials*; John Wiley & Sons, Ltd: New York-Sydney-Toronto, 1974.

(66) Mitchell, P. C.; Parker, S. F.; Ramirez-Cuesta, A. J.; Tomkinson, J. *Vibrational Spectroscopy with Neutrons*; World Scientific, 2005.

(67) Willis, B. T. M.; Carlile, C. J. *Experimental Neutron Scattering*; Oxford University Press: Oxford, UK, 2009.

(68) Luczynska, K.; Druzbicki, K.; Lyczko, K.; Starosta, W. Complementary Optical and Neutron Vibrational Spectroscopy Study of Bromanilic Acid: 2,3,5,6-Tetramethylpyrazine (1:1) Cocrystal. *Vib. Spectrosc.* **2014**, *75*, 26–38.

(69) Parker, S. F.; Fernandez-Alonso, F.; Ramirez-Cuesta, A. J.; Tomkinson, J.; Rudic, S.; Pinna, R. S.; Gorini, G.; Fernández Castañon, J. Recent and Future Developments on TOSCA at ISIS. *J. Phys. Conf. Ser.* **2014**, *554* (1), 012003.

(70) Colognesi, D.; Celli, M.; Cilloco, F.; Newport, R. J.; Parker, S. F.; Rossi-Albertini, V.; Sacchetti, F.; Tomkinson, J.; Zoppi, M. TOSCA Neutron Spectrometer: The Final Configuration. *Appl. Phys. A Mater. Sci. Process.* **2002**, *74*, 64–66.

(71) Pinna, R. S.; Rudić, S.; Parker, S. F.; Armstrong, J.; Zanetti, M.; Škoro, G.; Waller, S. P.; Zacek, D.; Smith, C. A.; Capstick, M. J.; et al. The Neutron Guide Upgrade of the TOSCA Spectrometer. *Nucl. Instruments Methods Phys. Res. Sect. A Accel. Spectrometers, Detect. Assoc. Equip.* **2018**, *896*, 68–74.

(72) Zaliznyak, I. A.; Lee, S.-H. Magnetic Neutron Scattering and Recent Developments in the Triple Axis Spectrometer. In *Magnetic Neutron Scattering*; Brookhaven National Laboratory, 2004.

(73) Mitchell, P. C.; Parker, S. F.; Ramirez-Cuesta, A. J.; Tomkinson, J. The Theory of Inelastic Neutron Scattering Spectroscopy. In *Vibrational Spectroscopy with Neutrons*; World Scientific, 2005; pp 13–65.

(74) Parker, S. F.; Refson, K.; Williams, K. P. J.; Braden, D. a; Hudson, B. S.; Yvon, K. Spectroscopic and Ab Initio Characterization of the [ReH9]2- Ion. *Inorg. Chem.* **2006**, *45* (26), 10951–10957.

(75) *Test Method Standard Safety and Performance Tests for the Qualification of Explosives (High Explosives, Propellants and Pyrotechnics)*; Indian Head, MD., 1999.

(76) *Recommendations on the Transport of Dangerous Goods. Manual of Tests and Criteria*, 5th ed.; United Nations: New York & Geneva, 2009; Vol. 39.

(77) Eriksen, J. H. *Manual of Data Requirements and Tests for the Qualification of Explosive Materials for Military Use*; 2003.

(78) Meyer, R.; Köhler, J.; Homburg, A. *Explosives*, 6th ed.; Meyer, R., Köhler, J., Homburg, A., Eds.; Wiley-VCH: Weinheim, 2007.

(79) Matyáš, R.; Pachman, J. *Primary Explosives*; Springer-Verlag: Berlin, 2013.

(80) OZM. *BAM Fall Hammer*; Hrochuv Tynec.

(81) Suceska, M. *Test Methods for Explosives*; Springer-Verlag: New York, 1995.

(82) Preston, D. N.; Brown, G. W.; Skidmore, C. B.; Reardon, B. L.; Parkinson, D. A. Small-Scale Explosives Sensitivity Saftey Testing: A Departure from Bruceton. *AIP Conf. Proc.* **2012**, *1426*, 713–716.

(83) Munter, A. Neutron scattering lengths and cross sections https://www.ncnr.nist.gov/resources/n-lengths/ (accessed Aug 1, 2018).

Chapter 3

VIBRATIONAL UP-PUMPING: PREDICTING IMPACT SENSITIVITY OF SOME ENERGETIC AZIDES

This chapter published as Michalchuk *et al* (2018), *J. Phys. Chem. C.* 122 (34) 19395-19408 and Michalchuk *et al* (2018*), Phys. Chem. Chem. Phys*., 20, 29061-29069

3.1 Introduction

To a simple approximation, a mechanical impact can be taken to induce two main effects: (1) the material being impacted is compressed, and (2) if the impact energy exceeds a threshold energy, fracture of the impacted body.[1] In the first, a compressive pressure wave passes through the material, akin to an acoustic wave. The propagation of this pressure wave through the material has been suggested to induce vibrational excitation of the lattice by a two-fold mechanism.[2] The pressure associated with the impact leads to a shift in the vibrational frequencies of the material. These vibrations are subsequently populated by the sudden increase in energy of the lattice. For the adiabatic compression of a solid,[3]

$$\left(\frac{T}{T_o}\right) = \left(\frac{V}{V_o}\right)^{-\Gamma}$$

Equation 3.1

where Γ is the Grüneisen parameter describing the vibrational anharmonicity of the lattice, V/V_0 describes the change in volume on compression, and T/T_0 is the change in temperature of the bulk material on compression. The exact temperature that can be achieved depends largely on the heat capacity of the material.[4] It follows that the magnitude of the excitation that results from an

impact is proportional to the magnitude of the impact pressure, and the response of the material to this pressure.[5–7]

Previous work found that for the model organic material naphthalene, a modest impact (4 GPa) is associated with a total increase in internal energy, ΔU, of 37 000 cm^{-1} per molecule.[4] However, as $\Delta U = H + W$, the increase in internal energy will distribute between heat (H) and work (W). The proportion of ΔU that converts to H follows from Equation 3.1, and therefore increase with the anharmonicity of the material through Γ. For naphthalene, V/V_o = 0.793 at 4 GPa, while for α-NaN_3 this value is *ca.* 0.860,[8] and *ca.* 0.915 for AgN_3.[9] Thus the values of $\Gamma(NaN_3)$[10] $\approx \Gamma(AgN_3)$[11], whilst Γ(naphthalene) is nearly 2.5-fold higher.[4] The proportion of impact energy that is converted to heat is therefore expected to be lower for the inorganic azide materials. The energy that is introduced into the material affects only the lattice vibrations, which equilibrate very rapidly. This leads to a highly excited phonon region, or *bath*.[5,6,12] Noting that the heat capacity of the phonon bath is much lower than for the bulk material, it was found that the phonon quasi-temperatures reach approximately 2300 K, corresponding to *ca.* 1.2 eV per molecule in napthalene.[4]

In addition to the impact-induced heating of the material, a second process, fracture, can occur.[1] Within the contact surface, stresses build beyond the elastic limit of the material. This leads to plastic deformation in the form of dislocations or fracture.[13] Analogous to the rupture of a loaded spring, the sudden rupture of non-covalent (or covalent) interactions along a fracture surface leads to rapid excitation of lattice vibrations associated with the ruptured interaction.[14] Rapid equilibration again leads to formation of a ‘hot’ phonon bath.

The hot phonon bath produced by both mechanisms is bound by a maximum frequency, defined as Ω_{max}, Figure 3.1.[15–17] Vibrational modes that sit above the phonon bath are not directly excited by the impact, and remain vibrationally ‘cold’. The excess vibrational energy of the phonon bath can either dissipate outwards, or upwards; the latter is substantially faster and hence vibrational

energy continues to scatter upwards. The general process of up-conversion occurs in two stages:[15]

1. Scattering of the phonon bath modes leads to excitation of intermediate librational modes, known as *doorway modes*.

2. The 'hot' doorway mode subsequently scatters with additional phonon bath modes.

This process ultimately allows up-conversion of energy from the initially excited phonon region into the localised molecular modes, Figure 3.1. Experiment has found such energy conversion processes to occur on the order of picoseconds,[16] and occur more rapidly around defects.[4,18] These processes therefore occur considerably faster than the thermally-induced chemical decomposition in energetic materials (EM).[12] The rate of vibrational energy transfer is on the same time scale as the primary events associated with an explosion,[6] and has prompted interest in this model to explain mechanically-induced initiation of EMs.[19,20]

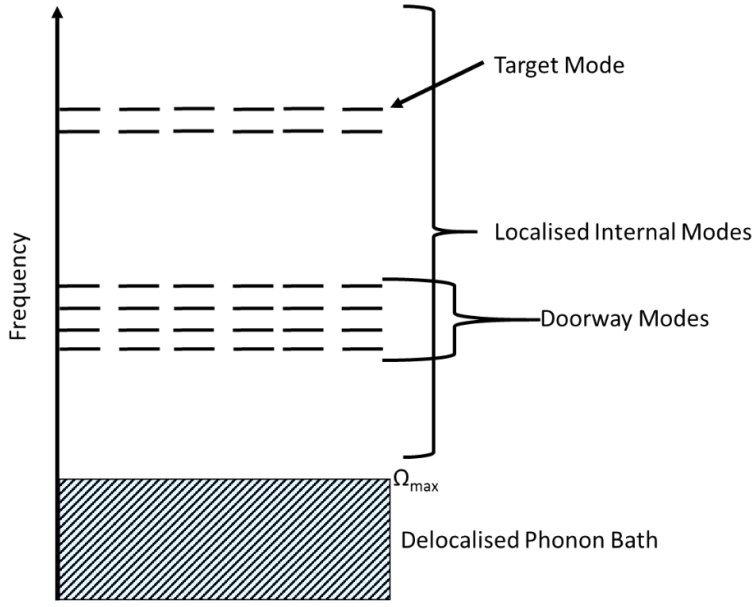

Figure 3.1: Schematic representation of the vibrational energy ladder traversed by mechanical (shock) impact energy. Injected energy begins in the delocalised phonon bath, up-converting to the localised molecular-based target modes *via* intermediate doorway modes. Figure adapted from Ref. 21.

The initial stage of a chemical explosion involves the rupture of a covalent bond. Within the proposed vibrational energy transfer model,[21,22] it follows that the vibrational energy must ultimately localise into a particular molecular vibration, the *target mode*, Q_T. When this target mode is sufficiently populated, distortion along its eigenvector reduces the energy separation of the frontier orbitals, and athermal bond rupture ensues.[23–25]

The apparent structural simplicity of azide-based EMs, where only a single covalent bond (N-N bond) exists for initiation, offer a particularly interesting challenge for understanding impact sensitivity. Azides have been known for over a century,[27] and their initiation mechanism has been the subject of research for nearly three-quarters of a century.[28] Despite this apparent simplicity, the sensitivity of these materials span orders of magnitude. For example, NaN_3 is completely insensitive to impact, while $Pb(N_3)_2$ is a common primary explosive used in detonators.[13] Broadly, the azide materials can be classified into three structural types: ionic, polymeric and molecular.[29] The ionic materials have been reported to be less sensitive than the polymeric or molecular materials.[30] The existence of covalent bonds in the latter two material types has been used to rationalise a decrease in N-N bond strengths and hence increase sensitivity, although the change in N-N dissociation energies typically varies only slightly.[29] This rationale is therefore insufficient to explain the range of sensitivities observed, both within and between structural classifications, or between polymorphic forms.[31]

The breadth of physical and chemical characteristics displayed by azide-based EMs is vast, which in conjunction with the relative simplicity of azide-based chemistry,[32] continues to keep the development of azide-based materials an active area of research.[32–35] However, without a means to predict the relative sensitivity of new materials *a priori*, the preparation of new azide materials remains very hazardous.

3.2 Aims

Simple inorganic azide energetic materials display a huge variation in impact sensitivity behaviour, and development of new azide-based materials is of high interest to the energetics community. A physical basis for their initiation has not yet been elucidated, although some qualitative trends, including bond lengths, cation ionization potentials and symmetry breaking of azide vibrational modes with energetic behaviour have been noted.[36,37] More physical models have also been proposed, noting that crack propagation rates may be linked to sensitivity,[13] based on formation of hot-spots at crack tips or deformation pile-ups. However, no unified mechanism has yet been proposed to explain the sensitivity relationships observed for these compounds. The sensitivity of energetic materials is a complex phenomenon, and the underlying mechanism can differ. For example, initiation may occur due to hot-spot formation in a bulk composition, or at extended defects within single crystallites (Chapter 1.2). Which mechanism dominates (and thus the type and magnitude of hot-spot that forms) depends on the nature of the prepared sample and is largely irreproducible. Regardless of the mechanism by which the energy is generated, its localisation can be sought in terms of the vibrational up-pumping mechanism (Chapter 1.2.2). At the most fundamental level is the intrinsic sensitivity of a material. This describes the propensity of the ideal material (*i.e.* defect-free) to react under mechanical perturbation and will form the basis for the work presented here.

This chapter aims to build a model for ideal crystalline materials, based on a vibrational up-pumping approach, in order to rationalise and predict the relative sensitivity ordering of a test set of azide-based EMs. To that end, the work presented here sought to:

1. Identify a vibrational mode (target mode, $\boldsymbol{Q_T}$) that is responsible for the initial decomposition of the explosophoric azido anion.
2. Investigate the pathways to vibrational up-pumping.
3. Correlate the relative rate of vibrational up-pumping to impact sensitivity.

3.3 Test Set of Energetic Azides

The model presented here is constructed from a selected series of crystalline energetic azides, Table 3.1 and Figure 3.2, selected to cover a range of reported experimental sensitivities and cover the three main structural types. Of the ionic species selected, two are based on molecular cations: triaminoguananidinium azide (TAGZ) and ammonium azide (NH_4N_3). The experimental measurement of EM sensitivity is highly unreliable, with many conflicting reports in the literature.[38] In many cases, conflicting reports are due to crystal size, purity, defect concentration, as well as both environmental and experimental conditions.[39–41]

Literature discrepancies are particularly prevalent across the azide materials, most notably for the ordering of the more sensitive materials. Due to these large discrepancies, exact values are not quoted in developing the model in this chapter, but instead the relative ordering is considered. The sensitivity classifications given in Table 3.1 are based on the following:

1. $Ba(N_3)_2$, is quoted by some as being more sensitive than AgN_3,[36] and by others as less sensitive.[36,42] Its impact sensitivity has been measured to be between 4-10 J and shown to be highly dependent on temperature, particle size and impurities.[30,43,44]

2. AgN_3 is generally accepted to be somewhat less sensitive than $Pb(N_3)_2$.[44]

3. $Zn(N_3)_2$ in its pure form remains poorly characterized. Unquantified reports indicate that it explodes on minimal mechanical provocation,[34] with mixtures of zinc with $Pb(N_3)_2$ forming dangerously sensitive azide products.[45] Literature reports that state “zinc azide” to be insensitive are likely inadvertently discussing the sensitivity of hydrated form, given the extreme hygroscopicity of the anhydrous form.[46,47,30]

4. LiN_3 has been measured to have an impact sensitivity of *ca.* 22 J,[30] with some sources stating it to be completely insensitive.[36]

5. $Sn(N_3)_2$ is believed to have a similar sensitivity as its structural homologue, $Pb(N_3)_2$.[33] (*ca.* 1.7 J [44]).

6. NaN_3 and NH_4N_3 are known to exhibit very low sensitivity.[48] However, recent work has suggested that impacts of *ca.* 25 J can induce chemical decomposition in NaN_3 without the visible burn that is typically used as the main criterion for experimental impact sensitivity testing.[49]

7. TAGZ has been found to have impact sensitivity of *ca.* 34 J.[50]

8. Both liquid and gaseous HN_3 are known to be highly sensitive,[30] although no sensitivity studies on crystalline[51] HN_3 are known.

The work presented in this chapter therefore compare against a general experimental ordering of NaN_3 ≈ TAGZ ≈ NH_4N_3 < LiN_3 < $Ba(N_3)_2$< AgN_3 < $Sn(N_3)_2$, with the exact positions of HN_3 and $Zn(N_3)_2$ remaining unknown.

Table 3.1: Test set of energetic azides used in this work, listed in approximate order of increasing sensitivity.

Material	Sensitivity Class*	Bond Type#	Ref.
NaN_3	I	I	42
TAGZ	LS	I	50
NH_4N_3	LS	I	48
LiN_3	LS	I	30
HN_3	S	M	30
$Ba(N_3)_2$	S	P	30,42,43
AgN_3	S	P	31
$Zn(N_3)_2$	S	P	34
$Sn(N_3)_2$	S	P	33

**Experimental sensitivity class according to indicated references. Sensitivity reported as insensitive (I), low sensitivity (LS), sensitive (S). #Classification of bonding type: molecular (M), ionic (I) or polymeric (P)*

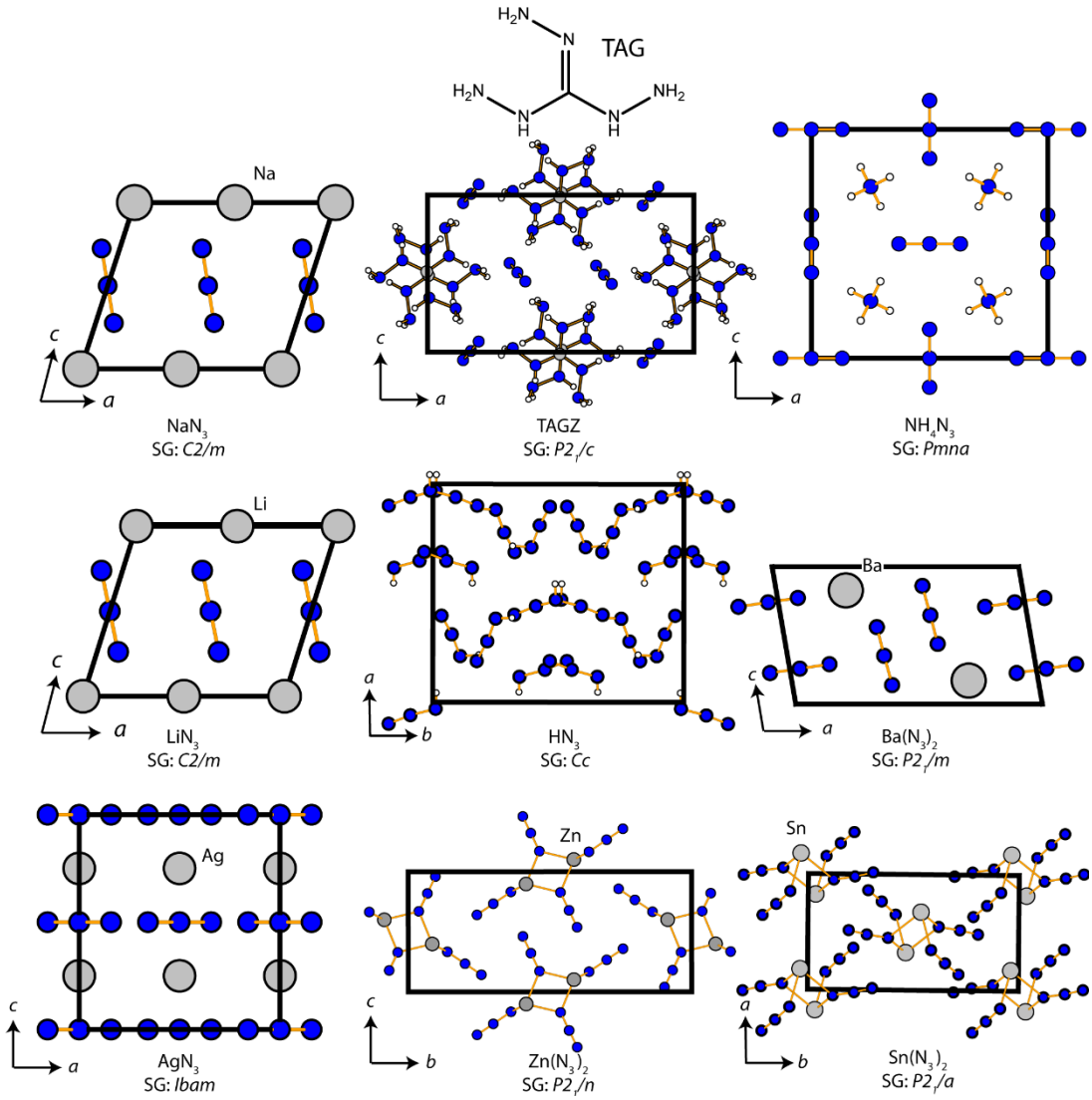

Figure 3.2: Conventional crystallographic cells of the energetic azides used in this work. The space group (SG) is given for each cell, along with an indication of the crystallographic axes. The azides are given in approximate order of impact sensitivity according to literature reports. In all cases, atoms are coloured as: blue- N; grey- metal; white- hydrogen; black- carbon. The structure of the triaminoguanidinium (TAG) cation is shown above its unit cell.

3.4 Methods

Gas phase calculations. Calculations of isolated molecules were performed *in vacuo* using Molpro 2012.[52] Geometry optimisation and subsequent vibrational frequency calculation was performed to ensure equilibrium geometry was obtained. The electronic structure was built upon a CAS(8,8)/6-31+G* calculation, on which a MRCI calculation was added for the same active space

and basis set. The highest atomic orbital was chosen to ensure inclusion of frontier bonding orbitals, while also ensuring that the orbital occupation of the highest unoccupied orbital was no more than 0.02.[53]

Condensed Matter Calculations: Input unit cell geometries were taken from the experimentally determined structures deposited in the Inorganic Crystal Structural Database (ICSD, FIZ Karlsruhe), Table 3.2. Geometry optimisation was performed using plane wave Density Functional Theory (PW-DFT) as implemented in CASTEP v16.[54] Where appropriate pseudopotentials were not available in CASTEP, calculations were performed using the QuantumEspresso v6.1 software. For CASTEP calculations, the GGA functional of Perdew-Burke-Ernzerhof (PBE)[55] was applied, while QuantumEspresso calculations used the rVV10 non-local functional, which performs very similarly to the PBE+D scheme.[56] For CASTEP calculations, dispersion correction leading to the best structural agreement with experiment was chosen: Grimme's D2[57] dispersion correction, PBE-D2, or that of Tkatchenko-Scheffler (TS), PBE-TS.[58] The use of PBE + dispersion has previously performed well for these materials.[33,59] Convergence criteria for electronic structure calculations are given in Table 3.2. In all cases, the electronic structure was sampled on a Monkhorst-Pack *k*-point grid[60] with spacing no greater than 0.05 $Å^{-1}$. Note that tighter convergence was required for the Zn structure to remove imaginary phonon frequencies. Norm-conserving pseudopotentials were used throughout. The optimised structural parameters are given in Table 3.3.

Phonon calculations were performed on the optimised structures, using the same computational packages as for structural optimisation, within the framework of linear response theory. Dynamical matrices were initially calculated on a regular grid of *q*-points and subsequently Fourier interpolated onto a finer grid. Phonon dispersion curves were generated along the high symmetry paths as suggested by SeeKPath[61].The dynamical matrix was subsequently calculated across a regular set of *q*-points. Density of states (DoS, $g(\omega)$) were generated using Gaussian line broadening of 10 cm^{-1}.

Phonon density of states were normalised to *3N*, where *N* is the number of atoms, such that the resulting curves represent the number of available coupling pathways within each unit cell. Note that phonon dispersion curves were generated for the primitive cells in all cases except for AgN_3, for which imaginary frequencies could only be removed by use of the conventional cell. This does not affect the structure of $g(\omega)$, but only the factor of $3N$, which can be accounted for by re-normalisation.

Band structures were generated along high symmetry paths. As GGA based band gaps are known to provide poor agreement with experiment, further band structures were generated in CRYSTAL17[63] using the HSE06[64] hybrid DFT functional (with localised basis sets available from the CRYSTAL17 database: N- N_m-6-311G(d)_Heyd_2005[65]; Na, Li, C; H-TZVP[65]; Ba-HAYWSC-3111(2d)G [66]; Ag-From Ref 67; and Sn- DURAND-21G*[68]) which has been demonstrated to offer reasonable agreement with experimental band gaps for a broad range of materials.[69] Those presented here can therefore be regarded as accurate to within a reasonable level of confidence. The wavefunction was converged to $< 10^{-8}$, and convergence criteria TOLINTEG 7 7 7 19 30, as recommended for this functional and basis set[65]. The electronic structure was calculated at 172 *k*-points across a 7 x 7 x 7 Monkhorst-Pack grid.[60] Analysis of the crystal overlap Hamilton populations (COHP) were performed using the *properties* code, as implemented in the CRYSTAL17 suite. A minimal basis set (STO-6G) was used to avoid spurious overlap of basis functions, which were found to contaminate the calculation. COHP were calculated for directly bonded N atoms in the azido anion.

Inelastic Neutron Scattering Spectroscopy. All spectra were collected on the TOSCA spectrometer at the ISIS Neutron and Muon source.[94-96] A sample of NaN_3 (*ca.* 1.5) was placed in an aluminium sample holder and cooled to *ca.* 10 K. Data were collected for a total of *ca.* 400 μAh. Both forward and back-scattered data were summed and corrected for scattering from the sample holder and background. All data processing was done using Mantid.[72] Simulated spectrum was generated using ABINS,[97] as implemented in Mantid.

Table 3.2: Optimisation criteria for the energetic azides. The quantum chemical code (QuantumEspresso; Q, or Castep; C), is shown alongside the applied exchange correlation scheme (XC).

Azide	ICSD Code	Code	XC	ΔE /eV.atom^{-1}	Max. Force / eV Å^{-1}	Max. Atomic Disp. /Å	Max. Stress/ GPa	E_{cut} /eV
NaN_3	29370	C	PBE + D2	$2x10^{-6}$	0.001	0.001	0.005	1800
NH_4N_3	2236	C	PBE +TS	$2x10^{-6}$	0.001	0.001	0.005	1800
TAGZ	Ref [62]	C	PBE + TS	$2x10^{-6}$	0.001	0.001	0.005	1800
HN_3	261955	C	PBE + TS	$2x10^{-6}$	0.001	0.001	0.005	1800
LiN_3	34675	Q	rVV10	$1x10^{-9}$	1.0 x 10^{-8} Ry/Bohr	0.0001	$5x10^{-6}$	2312
$Zn(N_3)_2$	430428	C	PBE+D2	$2x10^{-9}$	0.0005	0.0005	0.0005	1800
$Ba(N_3)_2$	26202	Q	rVV10	$1x10^{-9}$	1.0 x 10^{-8} Ry/Bohr	0.0001	$5x10^{-6}$	2312
AgN_3	88335	Q	rVV10	$1x10^{-9}$	1.0 x 10^{-8} Ry/Bohr	0.0001	$5x10^{-6}$	1768
$Sn(N_3)_2$	433812	C	PBE + TS	$2x10^{-6}$	0.001	0.001	0.005	1800

Table 3.3: Comparison of experimental (exp) and computed (calc) unit cell geometries. Low temperature experimental data are used where available

Azide	a	b	c	α	β	γ	V	ΔV /%
AgN_3 (Exp)	5.60	5.98	5.99	90.00	90.00	90.00	200.86	+1.5
AgN_3 (Calc)	5.71	5.96	5.98	90.00	90.00	90.00	203.81	
BaN_3 (Exp)	9.59	4.39	5.42	90.00	99.75	90.00	224.89	+6
BaN_3 (Calc)	9.83	4.44	5.53	90.00	99.14	90.00	238.50	
HN_3 (Exp)	8.21	8.21	6.78	110.42	110.42	90.01	397.42	+5.9
HN_3 (Calc)	8.38	8.38	6.90	110.51	110.51	90.00	421.18	
NH_4N_3 (Exp)	8.93	3.81	8.66	90.00	90.00	90.00	294.62	+0.1
NH_4N_3 (Calc)	9.02	3.81	8.57	90.00	90.00	90.00	294.80	
LiN_3 (Exp)	5.63	3.32	4.98	90.00	107.40	90.00	88.73	-0.5
LiN_3 (Calc)	5.59	3.32	4.91	90.00	104.80	90.00	88.25	
NaN_3 (Exp)	3.61	3.61	5.41	105.36	105.36	60.96	57.30	+1.1
NaN_3 (Calc)	3.59	3.59	5.20	101.81	101.82	61.76	57.94	
SnN_3 (Exp)	6.78	11.06	6.23	90.00	94.67	90.00	465.51	+0.7
SnN_3 (Calc)	6.69	11.80	5.95	90.00	91.41	90.00	468.93	
TAGZ (Exp)	6.68	7.72	13.14	90.00	95.44	13.14	674.80	+0.5
TAGZ (Calc)	6.69	7.74	13.16	90.00	95.76	90.00	678.39	
ZnN_3 (Exp)	3.46	16.26	6.93	90.0	95.90	90.0	387.80	+1.5
ZnN_3 (Calc)	3.44	16.47	6.99	90.0	96.42	90.0	393.84	

3.5 Results and Discussion

3.5.1 Bond Rupture of Explosophoric N_3^-

The initiation of an energetic material involves rapid release of chemical potential energy. This process must therefore involve rupture of a covalent bond within the explosophoric moiety of the material. Within the azide materials, this is rupture of an N-N bond. In their ground state structures, the azide materials contain a closed-shell N_3^- molecule. It is therefore necessary to understand the reactivity of this molecule. Due to the delocalised nature of electronic states in solids, however, there is an intimate interaction between the electronic states of the counter-ion and the azido anion. Further, with the unavoidable presence of intrinsic defects (*e.g.* vacancies), the electronic band structures will likely include some additional states within the band gap that may influence sensitivity.[70,71] A variety of pathways are therefore available for the reduction or oxidation of the azido anion species within the solid state. Only those in the ideal crystal are considered through this chapter.

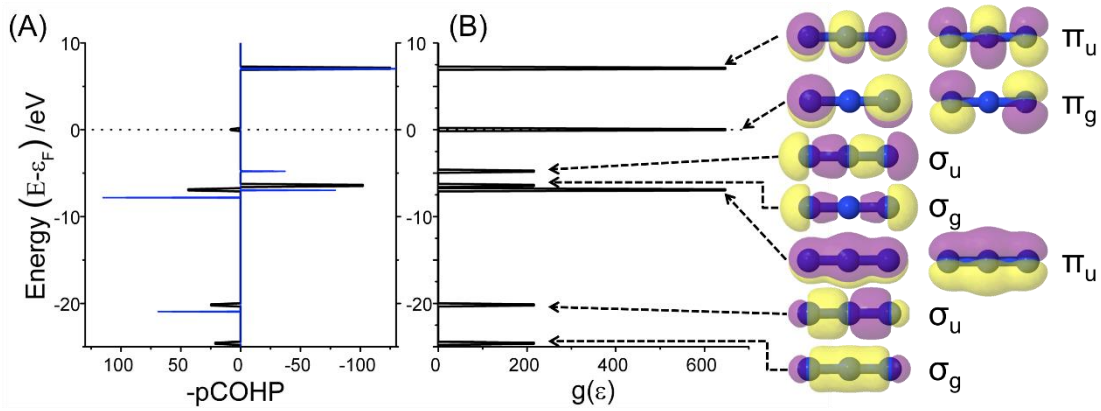

Figure 3.3: Electronic structure of the azido anion by HSE06 in a periodic box, N_3^-. (A) Projected Crystal Overlap Hamilton population (pCOHP) for a TZVP (blue) and STO-6G (black) basis set. A high-level basis set leads to spurious results,[72] hence use of a minimal basis set (B) The 'density of states' for the azido anion, alongside visualisation of the associated molecular orbitals. Figure from Ref. 21

The electronic structure of the azido anion, present in all the energetic azides studied here, is given in Figure 3.3. The Projected Crystal Overlap Hamilton

Population (pCOHP) weights each orbital by the overlap matrix component associated with neighbouring N atoms. Hence, it identifies orbitals in which directly bonded N atoms are stabilised or not. The first excited state associated with the azido anion involves excitation of an electron from a non-bonding π_g orbital (*i.e.* –pCOHP close to zero) to an antibonding π_u molecular orbital (*i.e.* –pCOHP is negative). Hence excitation should yield considerable weakening of the N-N covalent bonds. Analysis of the crystalline band structures in Figure 3.4 suggests that for all azides, the top of the conduction band and bottom of the valence bands are both primarily azide in character. This suggests that direct excitation of the N_3^- molecule is the dominant transition mechanism.

This concept has led to the 'band gap criterion' for predicting impact sensitivity in some materials Chapter 1.3.2.2).[73] Despite interest in the energetic azides, no data on the experimental band gaps could be found. As such, band gaps presented here are compared against literature calculated values, where possible, Table 3.4. The electronic band structure was calculated for each of the nine crystalline azide materials listed in Figure 3.1 using the PBE and HSE06 (Shown in Figure 3.4) DFT functionals. It is first worth noting that all of the crystalline materials have smaller band gaps than the isolated molecule.[74] This is expected and due to the periodicity of the former. It is generally found that the ionic azide materials (NaN_3, TAGZ, NH_4N_3, LiN_3 and BaN_6) exhibit larger band gaps than the polymeric (SnN_6, AgN_3, ZnN_6) or molecular (HN_3) systems. Noting that the ionic azide materials are typically less sensitive to mechanically-induced initiation than the polymeric and molecular systems (Section 3.3), the trend in PBE band gaps generally agree with the band gap criterion. However, it is worth noting a discrepancy in this trend, where the sensitivity of BaN_6 >> NaN_3 despite their band gaps being similar.

As expected, the magnitude of the band gap for each of the materials increases on moving to the screened hybrid HSE06 functional, Table 3.4. Comparison to previously calculated band gaps, based on various functionals, for some of the azide materials agree well with the HSE06 values. A notable exception is NH_4N_3, for which earlier works have suggested a direct band gap

of *ca.* 0.7 eV lower than that calculated here.[75] Other theoretical studies support the present findings that NH_4N_3 is an indirect band gap material.[76] Experimental validation is therefore required. The band gap of $Ba(N_3)_2$ is also considerably larger by HSE06 than previously reported based on PW91 GGA DFT calculations. Despite this GGA functional performing relatively well for other azides, it appears to fail in the case of $Ba(N_3)_2$. Instead, the PW91 result for $Ba(N_3)_2$ is much closer to the PBE band gap.

Table 3.4: Calculated band gaps for the crystalline azide materials by PBE (PBE and LBS) and HSE06 (LBS). The band gaps are labelled as being direct (D) or indirect (ID). Comparison of energies are shown with literature and discrepancy in momentum conservation is shown.

Material	PBE	HSE06	D/ID	Literature
N_3^-	5.64	7.06	--	--
α-NaN_3	4.02	5.34	D	$5.38^{\neq a}$; $5.03^{V b}$
TAGZ	4.48	5.82	ID	--
NH_4N_3	4.36	5.75	ID	5.08 (D) $^{\neq b}$
LiN_3	3.56	4.75	D	$4.98^{\neq a}$; $4.68^{V b}$
HN_3	3.78	5.20	ID	--
$Ba(N_3)_2$	4.12	5.32	D	$3.65^{V c}$
AgN_3	1.57	2.77	D	$1.72^{\tau a}$; $2.5^{V a}$
$Zn(N_3)_2$	3.41	4.78	ID	--
$Sn(N_3)_2$	0.66	1.51	ID	--

$^{\neq}$ TB-mBJ band gaps from (a) Ref. 59 (b) Ref. 75 ; $^{\tau}$ PBE band gap from (a) Ref 77 ; ^{V}PW91 band gap from (a) Ref 78 (b) Ref 79 (c) Ref 80

Interestingly, while the band gap criterion holds relatively well across the PBE-based band gaps, it is less prominent for the higher-level functional HSE06. Noting that the latter is expected to be much more accurate, this suggests that the correlation with the lower level functional was largely fortuitous. Some earlier works also show discrepancy between sensitivity and band gap.[81] No obvious trend is seen between the sensitivity and a material having a direct or indirect electronic band gap.

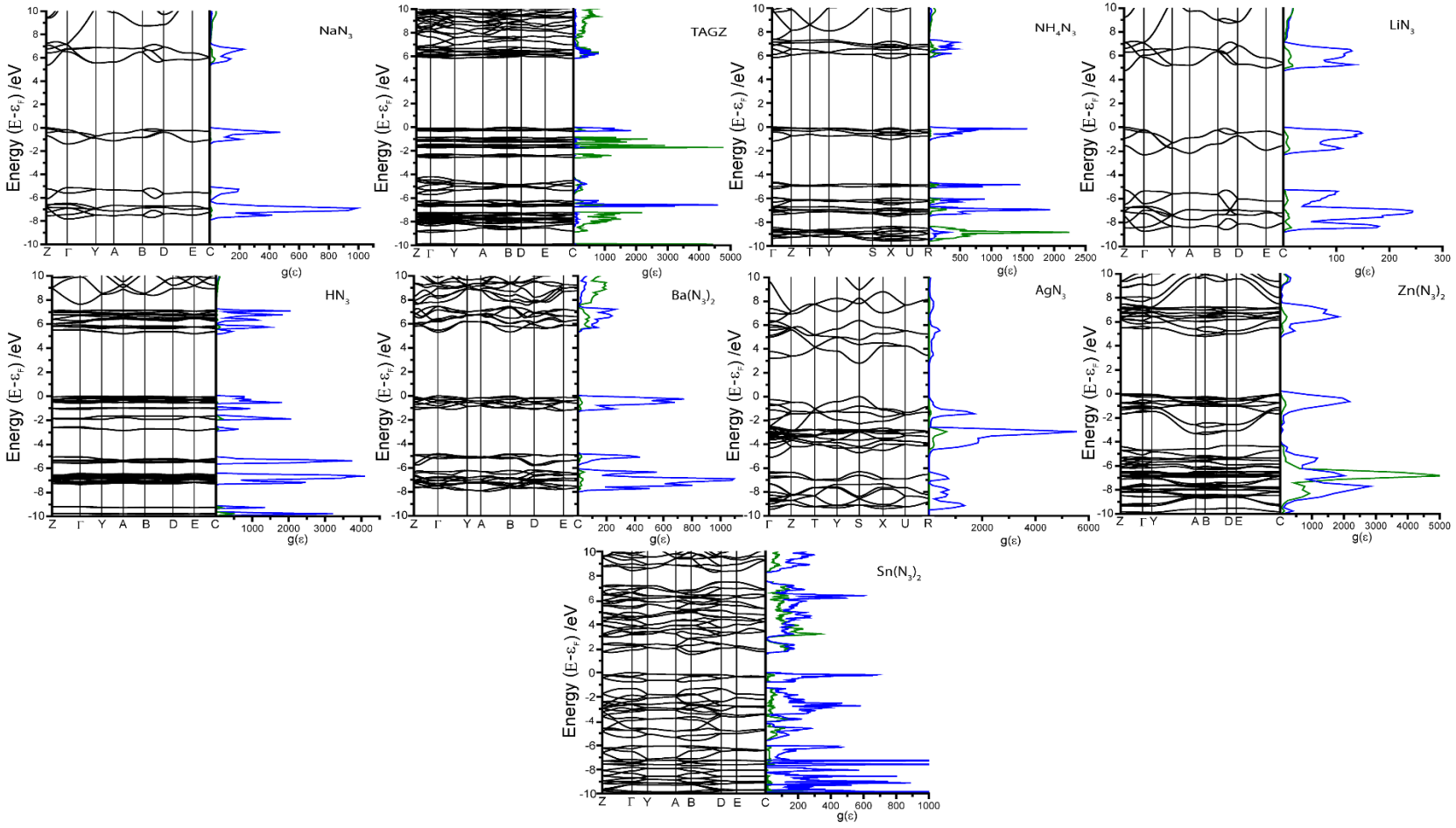

Figure 3.4: Electronic band structures (HSE06) for the energetic azides. Band dispersions are plotted along high symmetry lines. The partial density of states are plotted for each, decomposed as (blue) N_3^- channel and (green) cation channel.

3.5.1.1 Dissociation of N_3^-

Throughout the following discussion, the symmetric N-N bonds are denoted R_1 and R_2, with the electronic state given as a preceding superscript. The S_o bond length of R_1 is thus denoted ${}^{S_o}R_1$.

In the closed-shell ground state of the N_3^- anion, the optimised geometry (CAS(8,8)/6-31+G*) of the molecule shows two equivalent N-N bonds (${}^{S_0}R_1 = {}^{S_0}R_2 = 1.1865$ Å), with the bond angle $\theta_{NNN} = 180^o$. This value is in very good agreement with the experimentally-observed gas-phase equilibrium bond length of 1.188 Å, as obtained from rotational spectroscopy.[82] If the optimisation is performed with a full valence active space, CAS(16,12), the N-N bonds elongate, with ${}^{S_0}R_1 = {}^{S_0}R_2 = 1.2002$ Å. This is only slightly longer than the experimental bond length in the gas phase molecule, and for the molecule in the ionic azide materials (*ca*. 1.17-1.18 Å). Optimisation of the first triplet state, T_1, leads to an increase in the N-N bond lengths, with ${}^{T_1}R_1 = {}^{T_1}R_2 =$ 1.2607 Å using a CAS(8,8) active space, increasing to 1.2855 Å when optimised at CAS(16,12). The T_1 state remains linear in all cases. Similarly, the bond lengths of the first singlet state, S_1, expand from 1.2243 Å to 1.2475 Å when moving from a CAS(8,8) to CAS(16,12) calculation.

Importantly, when the active space is increased, the relative energies of the equilibrium structures change only slightly with $E_{S1} - E_{S0}$ < -0.3 eV, $E_{T1} - E_{S0}$, < +0.03 eV. The same holds for comparison of structures with $R_2 = 2.5$ Å, *i.e.* beyond the dissociation limit of the azido anion. The effect of increasing the active space is therefore small relative to the additional computational costs, and as such the smaller active space was used for the remainder of this work. To assess the effect of vibrational normal coordinates on the relative stabilities of the electronic states of N_3^-, all excitations were performed as Frank-Condon (FC) transitions from perturbations to the ground state (S_0) optimised geometry. Hence, rupture of bond R_2 along the excited state PESs are investigated based on R_1 fixed at the optimised length of the S_1 state.

Elongation of R_2 leads to bond dissociation at $^{S_0}R_2$ > 2 Å, with a dissociation energy of *ca.* 4.52 eV, Figure 3.5A. The $|S_0, V_0\rangle$ $|S_1, V_0\rangle$ transition requires *ca.* 5.1 eV energy, with the FC transition requiring 5.22 eV. In contrast to the dissociation energy of the ground state, N-N dissociation in the S_1 state has an energy barrier of only *ca*. 1 eV. This occurs with $^{S_1}R_2 > 1.75$ Å. Importantly, once this energy barrier is surpassed, dissociation is spontaneous, with $\Delta E(\,^{S_1}R_{2,diss} - \,^{S_1}R_{2,eqm}) \approx -0.4$ eV. The $|S_0, V_0\rangle|T_1, V_0\rangle$ transition occurs at notably lower energy, 4.21 eV, with the FC transition occurring at 4.46 eV. In the T_1 state, bond dissociation is met with a similar energy barrier to the S_1 state (*ca.* 1 eV when $^{T_1}R_2$> 1.65 Å). Again, once this energetic barrier has been surpassed, bond dissociation is spontaneous, with $\Delta E(^{T1}R_{2,diss} - \,^{T1}R_{2,eqm}) \approx$ -1.05 eV. The dissociation product of the T_1 state sits *ca.* 1.2 eV below that of the S_0 and S_1 states. The same general trend is observed for all higher excited states. It therefore follows that excitation of the azido anion into any of the excited states favours bond dissociation.

Based on energetic considerations, the T_1 state appears the most likely candidate for bond dissociation given its low dissociation barrier. However, at equilibrium geometry, the energies required to reach any of the excited states greatly exceeds k_BT. As described in Section 3.1, impact induced initiation results from mechanical perturbation of the impacted material. This leads to excitation of the lattice modes, and eventual localisation of this energy into vibrational modes.[4] The amount of energy localised in this way can be greatly in excess of the energy achievable by bulk temperatures, and sufficient to induce bond rupture.[12] Hence, it is necessary to consider the effects of the vibrational normal coordinates on the electronic structure of N_3^-. For the isolated anion, these include two degenerate bending modes ($\delta\theta_{NNN}$), a single symmetric stretch (δR_S), and an asymmetric stretching mode (δR_A). Variations in the electronic structure of N_3^- were studied as a function of these normal modes, Figure 3.5B-D.

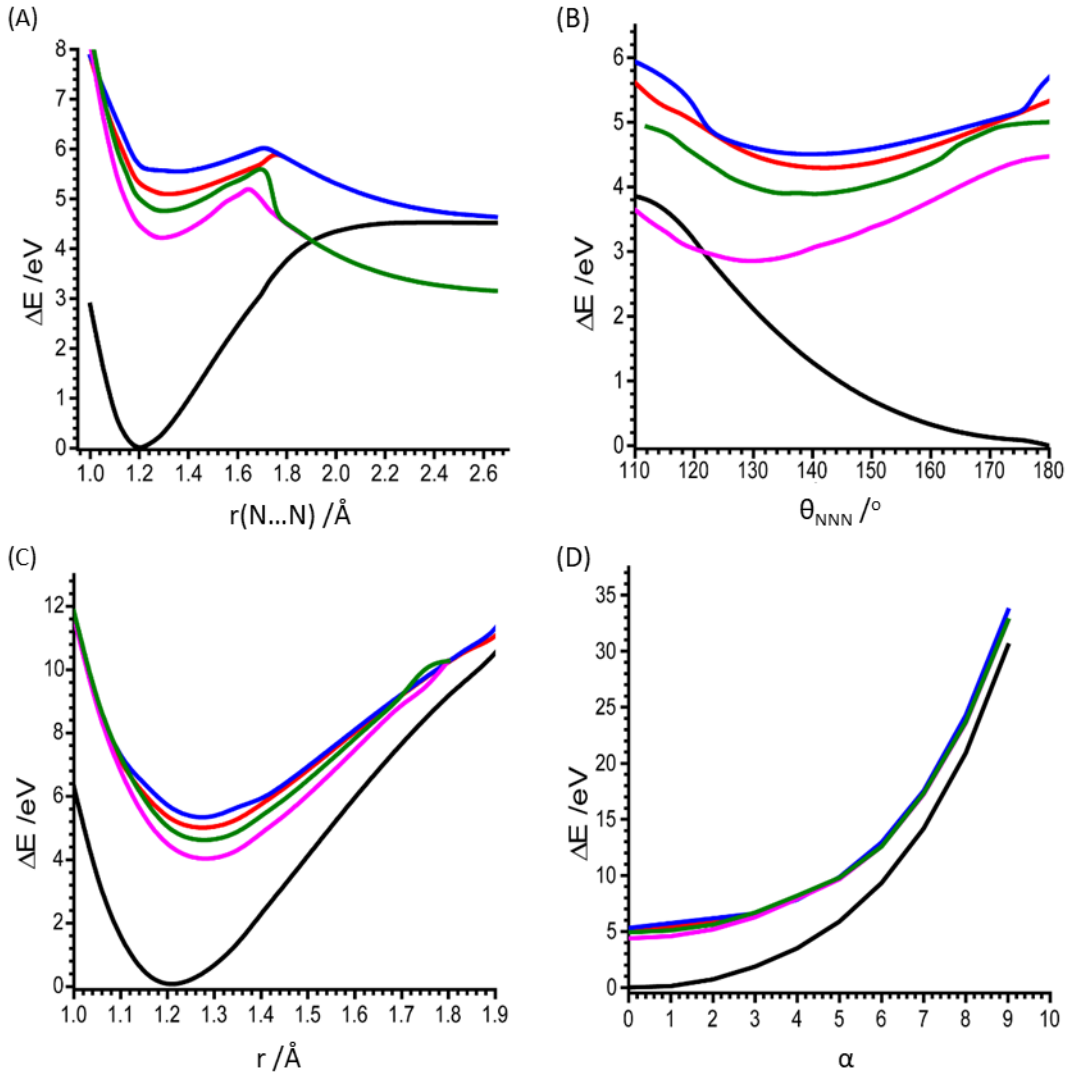

Figure 3.5 Potential energy surfaces (PES) associated with the N_3^- anion. PES are shown for (A) elongation of a single N…N covalent bond, and the three symmetry independent normal modes: (B) $\delta\theta_{NNN}$, (C) δR_S, and (D) δR_A; $r_1=(r_{eqm} + \alpha/10)$, $r_2=(r_{eqm} - \alpha/10)$, where r_{eqm} is the equilibrium bond distance. In each case the potential energy surface for S_0 (black), S_1 (red), S_2 (blue), T_1 (pink) and T_2 (green) are given. All energies are normalized to the S_0 equilibrium energies. Figure adapted from Ref. 21

At the lowest frequency, $\delta\theta_{NNN}$ is most responsive to mechanical perturbation. As the anion bending angle θ_{NNN} deviates from 180^o, the energy of the ground state species increases until an apparent plateau is achieved at *ca.* 110^o, Figure 3.5B. At this plateau, an overall increase in the internal energy, ΔU, of 3.9 eV is observed. In contrast, as θ_{NNN} decreases, the energy of the S_1 state

decreases, reaching its minimum energy at approximately 140^o, with ${}^{S1}E(\theta_{NNN} = 180^o) - {}^{S1}E(\theta_{NNN} = 140^o) \approx 1.1$ eV. At this angle, the energy separation between the S_0 and S_1 state decreases from *ca.* 5.3 eV to only *ca*. 3.0 eV. This energy gap decreases further as θ_{NNN} continues to decrease, reaching a minimum energy separation of 1.5 eV at 115^o.

The energy of T_1 also decreases with θ_{NNN}. An energetic minimum is observed at *ca.* $\theta_{NNN} = 130^0$, where ${}^{T1}E(\theta_{NNN} = 180^o) - {}^{T1}E(\theta_{NNN} = 130^o) \approx 1.7$ eV. At this angle, the energy separation between S_0 and T_1 reduces from 4.2 eV to only 0.7 eV. This energy is less than the energy associated with the second overtone of δR_A. As θ_{NNN} is compressed further, a conical intersection (CI) is reached, with an S_0/T_1 crossing at $\theta_{NNN} \approx 120^0$. The T_1 state remains more energetically favourable than S_0 over a small range of θ_{NNN} in this region, Figure 3.5B. Thus, the bending mode of N_3^- appears to offer a mechanism for the athermal electronic excitation of the molecule.

Discussion of the PES associated with δR_S is done with respect to the symmetric N-N bond lengths, Figure 3.5C. Across the eigenvector of this mode, the T_1 state remains lowest in energy amongst the excited states. In contrast to the bending mode, however, extending the eigenvectors of this mode does not lead to a CI, even up to a bond stretch of 2.0 Å and an associated $\Delta U \approx 11$ eV. Similarly, discussion of the PES of δR_A requires definition of a distortion parameter α. This dimensionless value represents the degree to which the eigenvector is perturbed, with $R_1 = R_{eqm} + \alpha/10$ and $R_2 = R_{eqm} - \alpha/10$ in Figure 3.5D. Due to contraction of R_2 as the eigenvector is imposed on equilibrium geometries, the energy is found to rise considerably faster than for the symmetric mode. Again, no CI is observed below $\Delta U \approx 30$ eV along this eigenvector.

It follows from the above that a CI is only attainable through the bending motion of N_3^-. However, the geometry of a real molecule results from the time-dependent superposition of all vibrational normal modes. The combination of $\delta\theta_{NNN}$ with δR_S and δR_A are therefore of interest. At relatively low energies,

the excitation energies between the S_o and excited states decreases substantially further in δR_S as compared to δR_A, Figure 3.5. Hence, only the combination of $\delta\theta_{NNN} + \delta R_S$ is considered here. At $\theta_{NNN} = 150^0$ ($\Delta U \approx 0.7$ eV according to Figure 3.5B), the PES of δR_S is found to deviate from that observed in the linear molecule, Figure 3.6A in comparison to Figure 3.5C. Most notably, with only a small distortion of θ_{NNN}, the T_1/S_0 CI becomes accessible *via* δR_S, with the CI observed at $R_S \approx 1.65$ Å. However, this pathway is clearly not most energetically favourable. The total ΔU (*i.e.* $\Delta U(\delta\theta_{NNN}) + \Delta U(\delta R_S)$) associated with this CI is over twice that required to achieve the CI by bending alone. As θ_{NNN} is decrease to 130° ($\Delta U \approx 2$ eV according to Figure 3.5B), it is instead possible to access the CI along the δR_S eigenvector (at $R_S \approx 1.5$ Å) with a total $\Delta U \approx 4$ eV, Figure 3.6B. The total energy required to achieve the CI by this pathway is therefore comparable to that required to access it by bending alone, but requires a smaller distortion of the molecule within the confinements of a crystal lattice.

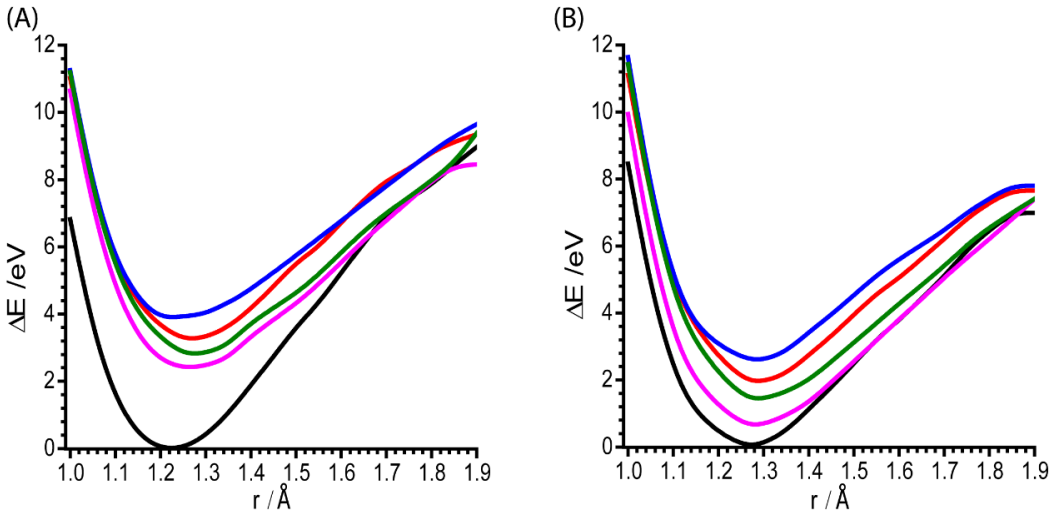

Figure 3.6: The PES for the symmetric stretch at (A) $\theta_{NNN} = 150^0$ and (B) $\theta_{NNN} = 130^0$. In each case the potential energy surface for S_0 (black), S_1 (red), S_2 (blue), T_1 (pink) and T_2 (green) are given.

The T_1 state is accessible by extending the normal modes of the N_3^- molecule. For the linear geometry in this state, the N_3^- dissociation barrier was found to be *ca.* 1 eV. When θ_{NNN} is bent to 150^o, the S_0 dissociation energy decreases from 4.5 to 3.6 eV, with the dissociation barrier on the T_1 PES decreasing to 0.67 eV, Figure 3.7A. As compared to the linear geometry, however, the

energetic drive to dissociation at this angle decreases considerably, and is only -0.2 eV at this angle. At $\theta_{NNN} = 150^0$, the dissociation barrier on the S_1 PES also decreases, albeit minimally (from 1 eV to 0.88 eV). However, at this angle, dissociation on the S_1 surface is no longer energetically favourable. If θ_{NNN} is reduced further to 120^0 (*i.e.* the geometry of the CI), the barrier to dissociation on the T_1 PES remains approximately the same as at $\theta_{NNN} = 150^0$, 0.69 eV, although that on the S_0 surface drops drastically, from 3.6 eV to 1.6 eV, Figure 3.7b. The dissociation barrier on the T_1 PES decreases to 0.34 eV at $\theta_{NNN} = 110^0$, and is completely absent at $\theta_{NNN} = 100^0$. At both $\theta_{NNN} = 110^0$ and $\theta_{NNN} = 100^0$, dissociation on the T_1 PES is overall exothermic, Figure 3.7c-d. It follows that, near the T_1/S_0 CI, dissociation of N_3^- is more accessible than under equilibrium, linear geometry.

The energies required to reach the CI for the pure azido anion are larger than are generally considered attainable by measurement of temperatures under mild impacts (typically < 3000 K). However, this energy translates into orders of 1.5 eV/molecule, increasing with stronger impacts.[15] Furthermore, it has been shown that localisation of up-pumped energy in the region of defects can be substantially higher,[4] and sufficient to overcome bond dissociation barriers.[12] It is also worth mentioning that the periodicity of the crystalline state leads to a reduction in the energy separation between ground and excited states, particularly in the sensitive azide materials. Thus, smaller energies will be required to achieve this excitation in these materials. The interaction of cations with the azido anion in polymeric and molecular systems also reduces the frequency of the bending vibrational mode. The ΔU associated with these bends therefore decrease further. Critically, it is evident that electronic excitation of the azido anion can be achieved by a purely mechanical route, *via* the bending motion of the molecule.

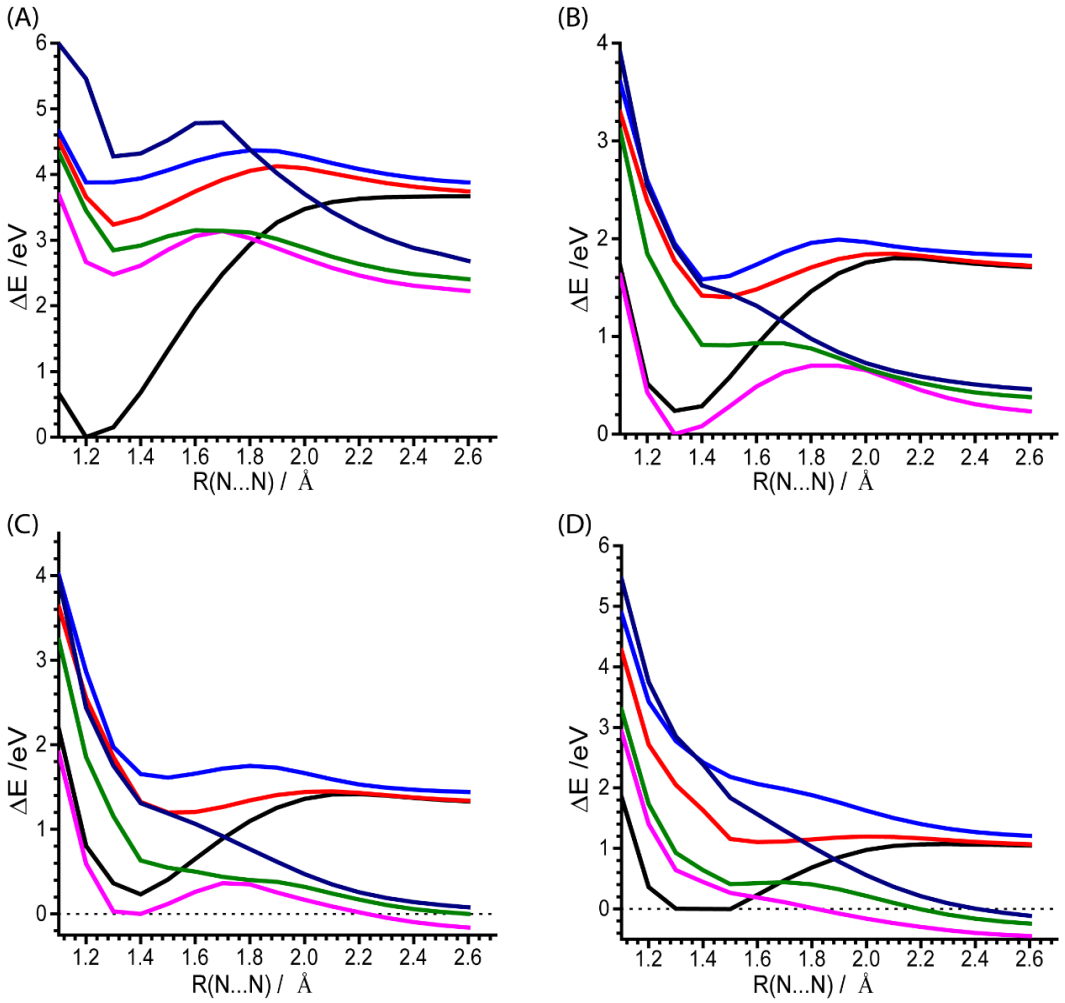

Figure 3.7: Elongation of R_2 for N_3^- with (A) $\theta_{NNN} = 150^0$, (B) $\theta_{NNN} = 120^0$, (C) $\theta_{NNN} = 110^0$ and (D) $\theta_{NNN} = 100^0$. In each case the potential energy surface for S_0 (black), S_1 (red), S_2 (blue), T_1 (pink) and T_2 (green) are given.

3.5.2 Metallisation in the Azides: Case Study of α-NaN_3

To assess the validity of the gas phase calculations within the solid state, the band structure was followed as a function of the normal mode eigenvectors using an example energetic azide, α-NaN_3. With discussion of external vibrational modes, it is non-trivial to define the eigenvector as a function of an internal coordinate. Instead, it is convenient to define a perturbative term associated with 'walking' along each eigenvector,

$$T_i = \alpha \epsilon_i R_{eqm}$$

Equation 3.2

where ϵ_i describes the normalised eigenvector of mode *i* that perturb the equilibrium atomic position $\boldsymbol{R_{eqm}}$ by a factor of α. Perturbations of the eigenvectors were placed on the conventional cell, as it allows a more direct calculation of the perturbation of neighbouring unit cells. The conventional cell is the result of doubling the primitive cell, and hence halving the Brillouin zone. As such, the conventional cell contains twice the number of vibrational frequencies as the primitive cell, Table 3.5. The additional set of 12 modes correspond to the edge of the primitive Brillouin zone and hence to neighbouring primitive cells being directly out of phase. This is often the maximum energy state of these vibrational bands.

Table 3.5: Calculated vibrational frequencies (ω) for the primitive and conventional unit cells of α-NaN_3 using PBE-D2.

Mode	ω Primitive	ω Conventional	Assignment
M_4	--	84.78	Lattice
M_5	--	88.61	Lattice
M_6	150.97	151.41	Lattice
M_7	--	154.47	Lattice
M_8	--	157.09	Lattice
M_9	177.99	184.34	Lattice
M_{10}	202.21	206.42	Lattice
M_{11}	214.51	219.05	Lattice
M_{12}	220.22	221.37	Lattice
M_{13}	--	221.54	Lattice
M_{14}	--	226.97	Lattice
M_{15}	--	230.22	Lattice
M_{16}	--	236.87	Lattice
M_{17}	606.27	610.35	In phase $\delta\theta_{NNN}$
M_{18}	609.71	614.72	In phase $\delta\theta_{NNN}$
M_{19}	--	617.49	Out of phase $\delta\theta_{NNN}$
M_{20}	--	618.24	Out of phase $\delta\theta_{NNN}$
M_{21}	--	1247.99	Out of phase δR_S
M_{22}	1250.43	1250.25	In phase δR_S
M_{23}	--	1929.65	Out of phase δR_A
M_{24}	1959.81	1964.65	In phase δR_A

Experimental data regarding the lowest frequency modes (*i.e.* lattice modes) is sparse. To explore the validity of DFT to model lattice modes in ionic azides, the inelastic neutron scattering spectrum (INS) of α-NaN_3 was obtained, Figure 3.8. Unlike Raman and infrared spectroscopy, INS is not limited by quantum selection rules, and therefore all vibrational modes are in principle visible. The INS spectrum reveals the five lattice modes, the three highest with observed frequencies ~220 cm^{-1}, 210 cm^{-1} and 196 cm^{-1}. The calculated frequencies agree well with these experimental values, occurring at 220 cm^{-1}, 214 cm^{-1} and 202 cm^{-1}. Two additional features are observed at ~160 cm^{-1} and 130 cm^{-1} in the INS spectrum, which appear to be somewhat lower in frequency than the calculated frequencies of 177 cm^{-1} and 150 cm^{-1} using the D2 dispersion correction. Low frequency vibrations are extremely sensitive to the weak underlying potential of the surrounding crystal. The zone-centre vibrational modes were therefore re-calculated using a second common dispersion correction scheme, TS, which is somewhat less empirical than the D2 scheme.

The optimised primitive unit cell obtained under the DFT-TS scheme had a volume *ca.* 1.2% below the experimental volume (as compared to DFT-D2, which overestimated the volume by 1.1%). The frequencies that result from the DFT-TS scheme show poorer agreement with the higher frequency lattice modes (226 cm^{-1}, 189 cm^{-1} and 187 cm^{-1}), although it did lead to slight improvements of the lowest frequency lattice modes (127 cm^{-1} and 174 cm^{-1}). The DFT-D2 scheme was therefore selected for further use. The internal vibrational modes are modelled less accurately. The bending frequency (DFT-D2) is calculated to be ~606/610 cm^{-1}, *ca.* 4.5% lower than the measured INS frequency of 639 cm^{-1}. The symmetric stretching mode is modelled even more poorly at 1250 cm^{-1}, *ca.* 8% lower than the INS value of 1358 cm^{-1}. However, the calculated δR_S frequency does agree well with previous simulations and suggests an inherent inability of the PBE scheme to capture this mode.[59] Note that the band corresponding to δR_{as} was not observed in the INS spectrum likely due to the low scattering cross section of ^{14}N and the low amplitude of the asymmetric stretching mode. The calculated $\nu(\delta R_{as})$ can therefore be compared to literature Raman spectra.[83] The frequency of δR_{as} is better

reproduced by the PBE-D2 than δR_s, simulated to occur at 2037 cm^{-1} (1959.98 cm^{-1} without LO-TO correction) and the experimental Raman[83] frequency at 2043 cm^{-1}, a 0.2% underestimation). Overall, it therefore appears that the PBE-D2 based scheme leads to a good correlation with experimental frequencies in the external mode region and $\delta\theta_{NNN}$. The latter is particularly important as it is the target frequency identified in Section 3.5.1.1

Despite the agreement between zone-centre simulated low-frequency bands and the INS spectrum, there are two striking differences:

- A well-defined band is observed at *ca.* 100 cm^{-1} in the INS spectrum
- The experimental intensities are poorly reproduced by simulation.

Both effects can be explained by noting that the TOSCA spectrometer does not probe the Brillouin zone centre, Chapter 2.2.2.2, but spans a broad range of momentum transfer.[84] As scattering from both N and Na are dominated by coherent scattering, vibration dispersion through the Brillouin zone becomes important.

Despite the high frequency associated with the top external bands near $\boldsymbol{k} = 0$, these frequencies represent only a small subset of the Brillouin zone, Figure 3.9. By comparison with the simulated INS spectra in Figure 3.8, it can be inferred that these frequencies are diluted (*e.g.* by powder averaging[85]) as they are not observed when simulated scattering from the full Brillouin zone is considered. Instead, the highest feature observed in the simulated INS band occurs at *ca.* 240 cm^{-1}, consistent with the average frequency of these external bands. This is only slightly higher than the experimentally observed highest frequency (*ca.* 230 cm^{-1}). This explains why the zone-centre calculation of α-NaN_3 without LO-TO correction offered a good starting point in Figure 3.8. In fact, inclusion of the LO-TO correction for the zone centre calculation leads to gross overestimation of the INS frequencies of the external modes.

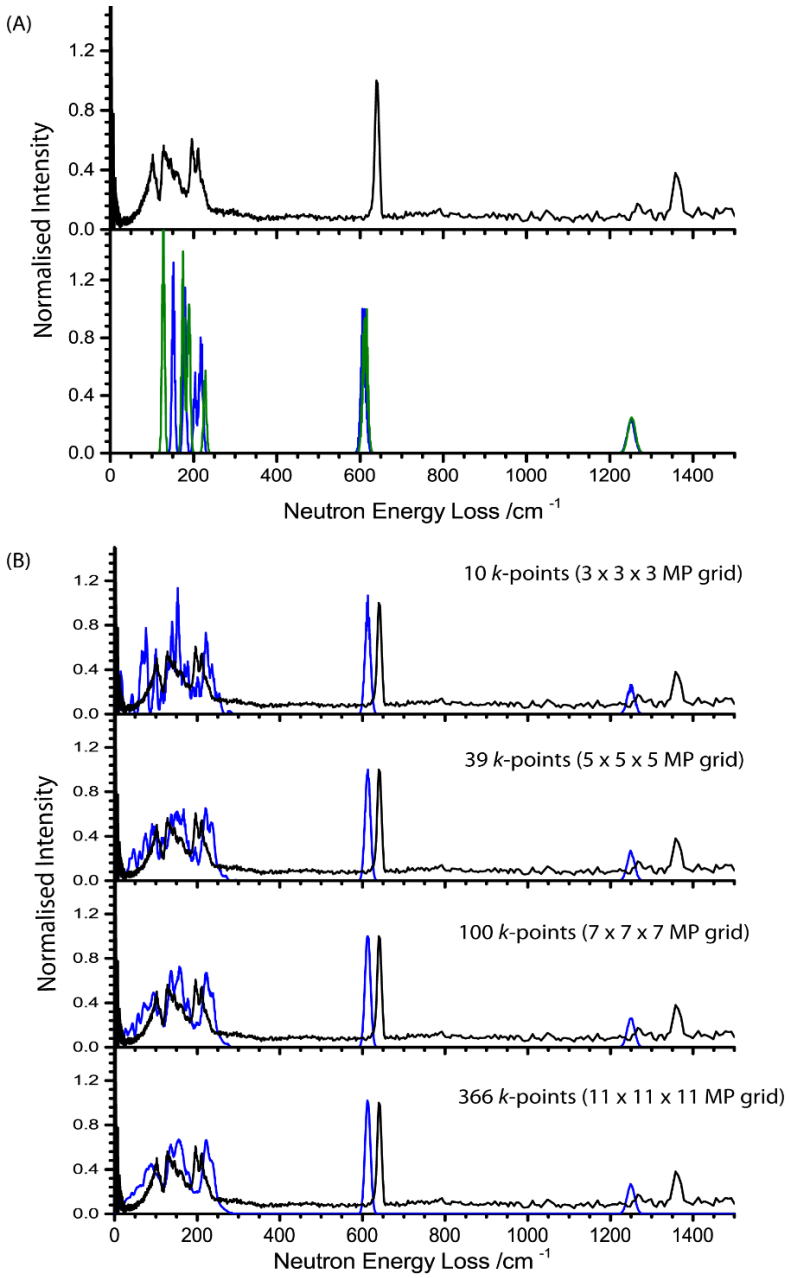

Figure 3.8: Inelastic neutron spectra of α-NaN_3 at 10 K obtained on the TOSCA spectrometer. (A) The experimental spectrum (top) is shown alongside the simulated INS spectra (bottom) using PBE-D2 (blue) and PBE-TS (green) methods. The INS spectrum is truncated at 1500 cm^{-1}, as no bands are observed above this frequency. No LO-TO correction is included in the simulated spectra and only first order quantum events are included. (B) Modelling of the INS spectrum based on the primitive cell, DFT-D2 phonon dispersion curve using different *q*-point sampling densities.

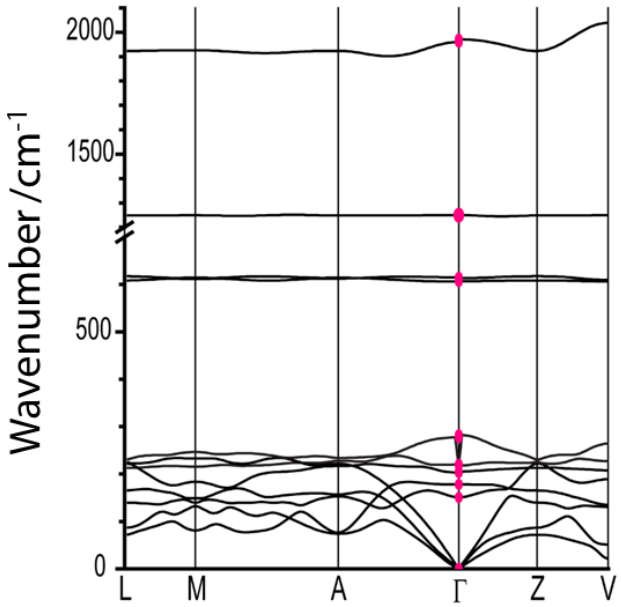

Figure 3.9: Phonon dispersion curve calculated using PBE-D2 for the primitive cell of α-NaN_3. The zone centre frequencies calculated with LO-TO correction are highlighted as pink dots.

3.5.2.1 Band gap dependence on external lattice modes in α-NaN_3

The DFT-D2 scheme leads to reliable calculation of the external vibrational modes and hence can be used for further investigation. It is convenient to begin with discussion of the external vibrational modes that contain no Na character, M_6, M_8, M_9 and M_{16} (Table 3.5). These four modes correspond to tilting of the N_3^- molecules. In the first, azide molecules tilt in phase, polarized primarily along the crystallographic *b*-axis. The second corresponds to a tilt along this same axis, with each of the azido anions tilting out of phase with one another. Hence, these modes correspond to the zone centre and primitive Brillouin zone edge, respectively. Modes M_9 and M_{16} describe the same motion polarized primarily along the crystallographic *a*-axis.

As M_6 and M_8 are followed, the band gap is found to decrease dramatically (*i.e.* towards metallisation), Figure 3.10A and 3.10B. However, this appears to be an artefact of the rectilinear nature of the imposed eigenvectors. Indeed, if N-N bond lengths are corrected to the equilibrium bond lengths, this trend towards metallisation is lost. Only a small reduction in the bad gap is observed at very large perturbations from the equilibrium geometry. The large difference

observed between rectilinear and corrected distortions clearly shows that the addition of internal molecular modes may be promising to induce metallisation.

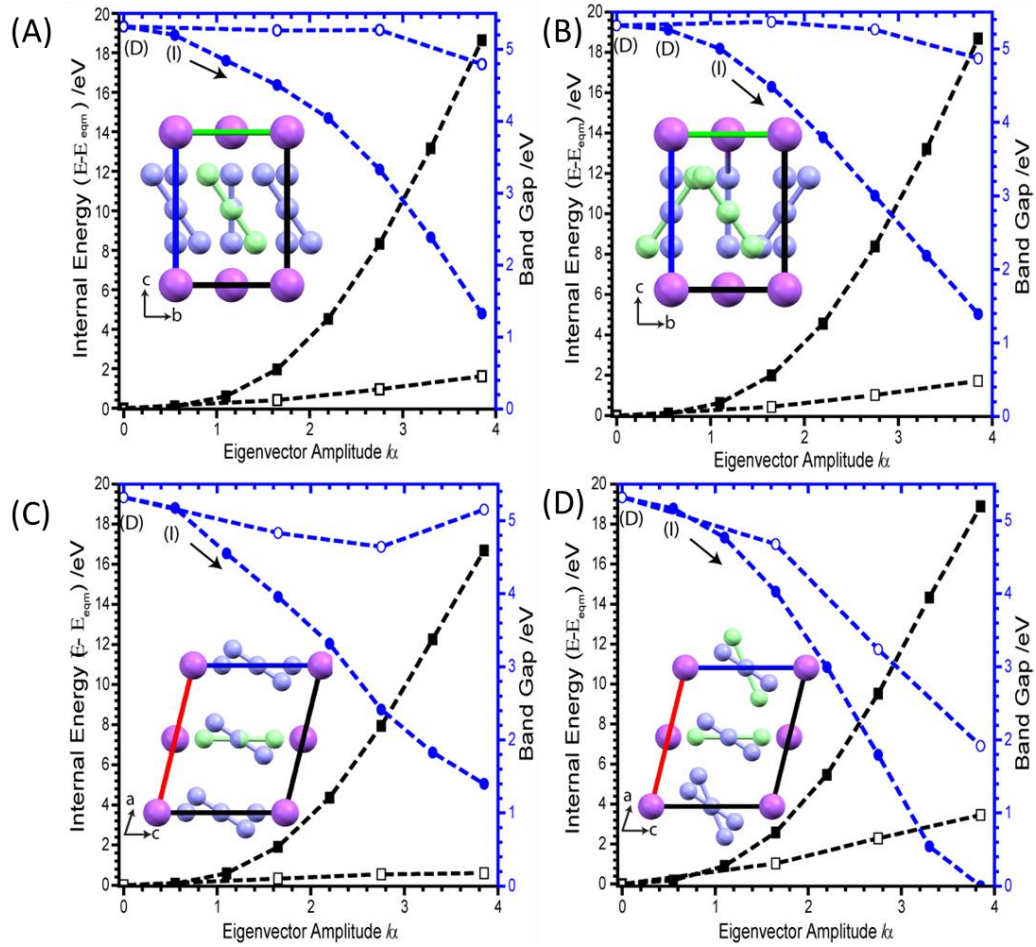

Figure 3.10: Tilting of the azido anion molecule showing (A) M_6 (B) M_8, (C) M_9 and (D) M_{16}. Closed symbols are derived from rectilinear application of eigenvectors, and open symbols result from correction to the N-N bond lengths. The band gap is initially a direct band gap (D), but becomes indirect (I) on perturbation. Inset graphics show the distortion (green molecule) with respect to the unperturbed (purple) molecular position. Band gap based on HSE06 calculation.

Along M_9, the band gap is seen to decrease very slightly before returning towards its equilibrium band gap at higher distortions, Figure 3.10C. In stark contrast, however, the band gap decreases markedly along M_{16}, Figure 3.10D. Imposing very large perturbations along this eigenvector (to a factor of 8) decreases the band gap asymptotically to *ca.* 0.15 eV, but does not reach metallisation, Figure 3.11. This is associated with $\Delta U \approx 5.6$ eV.

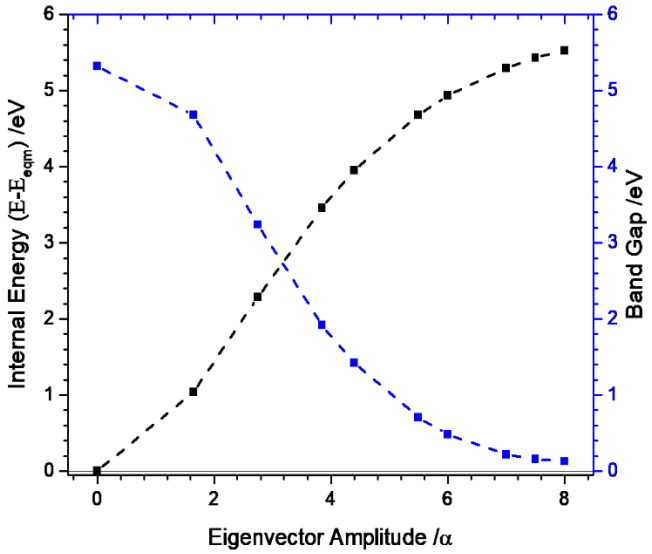

Figure 3.11: Calculated band gap for M_{16} extended to large perturbation. Band gap based on HSE06 calculation.

On further analysis of the band structure, it is found that this band gap narrowing does not result from a closing of the N_3^- band gap, but rather from a closing of the N…Na band gap, Figure 3.12. A comparison of the absolute energies of the valence bands suggests that this results from an increase in the N valence band energies by approximately 3.5 eV, which occurs as the occupied non-bonding π_g orbitals of the azido anions are forced together. While band gap narrowing in this manner would not permit excitation of the N_3^- molecule, it may permit transient oxidation of $N_3^- \rightarrow N^{\cdot}{}_3 + e^-$. The process[77]

$$2N_3^- + 2Na^+ \rightarrow 2N_3^{\cdot} + Na$$
$$2N_3^{\cdot} \rightarrow 3N_2$$

has been suggested as a possible thermal decomposition mechanism of the azides. Band gap narrowing by M_{16}, however, results in an indirect band gap. The rate of excitation across such band gap transitions are very slow.[86] Moreover, given that the narrow band gap exists across only a small subset of *k*-space, Figure 3.12, very few potential excitation channels are available. With the impact-induced vibrational energy transfer processes occurring on the sub-nanosecond (picosecond for phonon-phonon dissipation), it is reasonable to

suggest that electronic excitation along eigenvector M_{16} are simply too slow to be considered here. However, this does suggest a potential mechanism for the thermally induced decomposition of these materials, with long-duration excitation of the lattice. While the exact rationale governing the inactivity of M_{16} requires further investigation, experiment has demonstrated that α-NaN_3 is not reactive to impact initiation.[30] It therefore follows that M_{16} in unlikely to be responsible for impact-induced initiation.

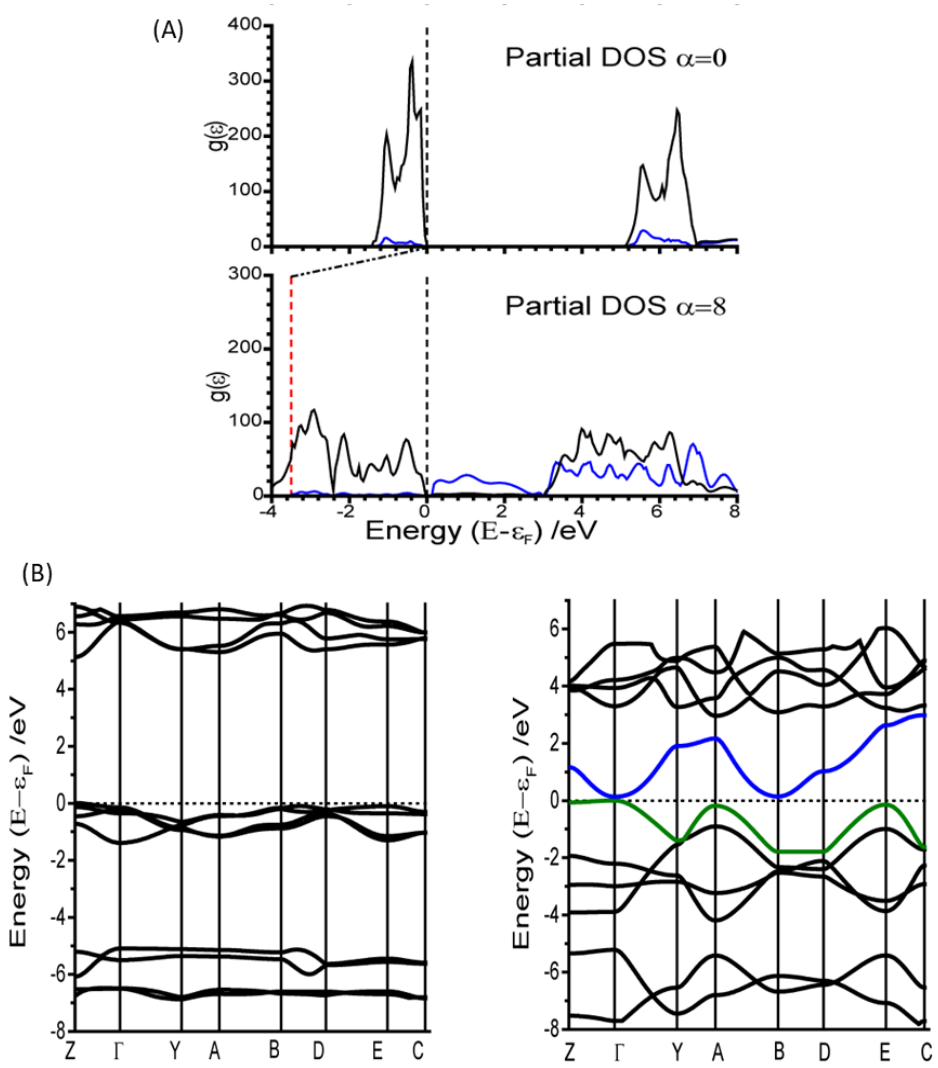

Figure 3.12: Comparison of the electronic band gap under equilibrium and after imposing an $\alpha = 8$ fold perturbation of M_{16}. (A) The partial DOS is given for (black) N and (blue) Na species. The vertical dotted line on (A) is given to indicate the Fermi surface (ϵ_F), and the red vertical line shows the energy of ϵ_F relative to the unperturbed structure. (B) The electronic band structure plotted along high symmetry lines in the Brillouin zone for (left) unperturbed and (right) $\alpha = 8$ structures.

The remaining nine external modes all exhibit a mixture of N and Na displacement. It is reassuring to find that none of these modes lead to any notable decrease in the band gap, Figure 3.13. There is typically no more than a *ca*. 1 eV decrease in the band gap along any of these eigenvectors, with M_{12} (the out of phase translation of Na and N_3^- species along the crystallographic *c*-axis), leading to an overall increase in the band gap. The only exception is M_{15}, which leads to rapid decrease in band gap energies at large α. However, it must be noted that this is associated with a 60 eV increase in energy, which arises due to the eigenvector contracting the distance between neighbouring Na^+ ions.

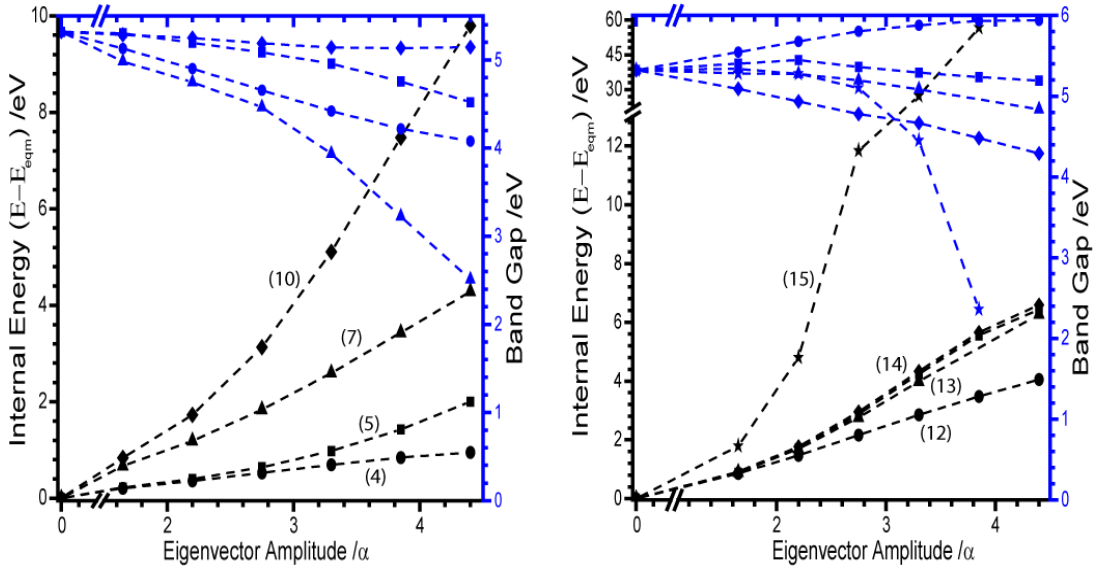

Figure 3.13: Effect of external vibration normal coordinates on the energies and band gap of αNaN_3. Mode numbers are indicated in brackets in each plot. Modes are identified as, (Left) M_4 (-●-), M_5 (-■-), M_7 (-▲-), M_{10} (-◆-), (Right) M_{11} (-■-), M_{12} (-●-), M_{13} (-▲-), M_{14} (-◆-), M_{15} (-★-).

3.5.2.2 Band gap dependence on internal vibrational modes in α-NaN_3

The subsequent four vibrational modes (M_{17} - M_{20}) correspond to the $\delta\theta_{NNN}$ modes. M_{17} and M_{18} are the zone-centre (*i.e.* in phase) modes, perpendicular to and along the crystallographic *b*-axis, respectively. M_{19} and M_{20} are their corresponding out-of-phase modes.

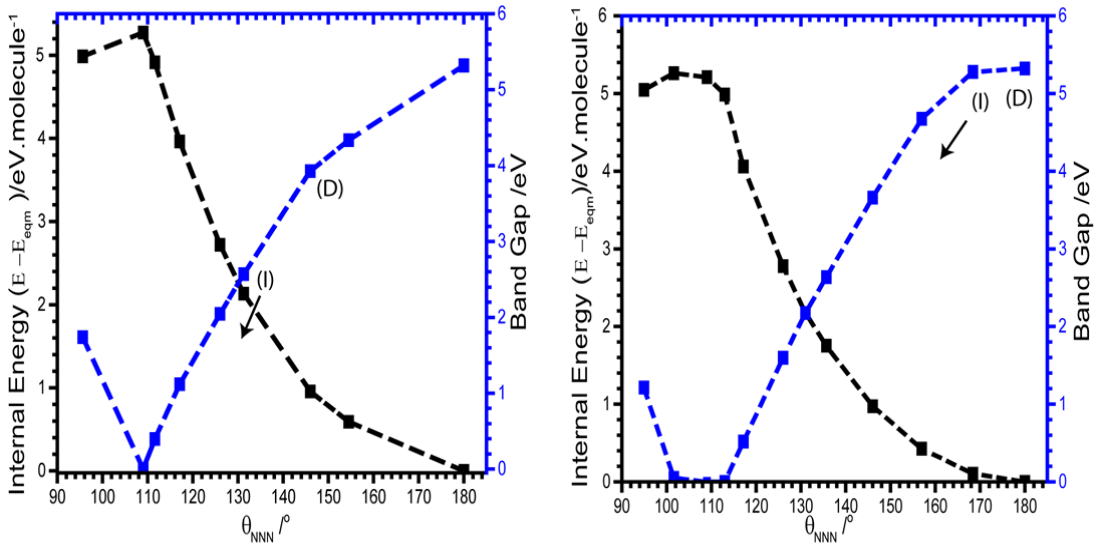

Figure 3.14: Effect of M_{17} (left) and M_{19} (right) on the band gaps and energies of α-NaN_3. Band gap momentum conservation is indicated as direct (D) or indirect (I). The arrow indicates continuation of an indirect band gap. Band gaps from HSE06 calculation. To reflect perturbation of two azido anions (in the conventional cell), energy is given per molecule.

To follow the band gaps associated with M_{17} - M_{20}, the rectilinear perturbation was applied according to Equation 3.2, and the N-N bond lengths were restored to equilibrium lengths. This was done to ensure only the isolated normal coordinates were investigated. As the azido anion was perturbed along the bending mode, $\delta\theta_{NNN}$, the band gap was found to decrease steadily with angle. The band gap reaches approximately half of its original value at $\theta_{NNN} \approx 130^{o}$, and continues to decrease on further bending. By 110^{o}, the band gap drops to 0 eV, and the material is found to have metallised, Figure 3.14. This metallisation is of particular interest as it corresponds to a crossing of the S_0/S_1 PES, which was not observed in the isolated gas-phase molecule. This can be suggested to result from the band gap narrowing that occurs when a molecule is introduced into a periodic crystal.[74] Note as the calculations performed here were single-reference ground state, closed shell simulations, the triplet states observed in the multi-references CI calculations (Section 3.5.1.1) were not considered here. However, given that the multi-reference calculations suggest that the T_1 state should exist ca. 1 eV lower in energy than the S_1 state, it is reasonable to propose that the T_1/S_0 CI may be accessible in the crystalline

lattice model at $\theta_{NNN} \approx 115 - 120^0$, and $\Delta U \approx$ 4-4.5 eV.molecule^{-1}. As both the in- and out-of-phase modes exhibit the same behaviour modes M_{18} and M_{20} are not reported here.

Unlike for M_{16}, the metallisation that is observed along $M_{17} - M_{20}$ is not the result of a decreasing N…Na band gap. Instead, it occurs by a decrease in the N_3^- conduction/valence band gap. While comparison of the absolute energies does suggest partial increase in the energy of the valence band as a function of this bend, the major effect results from a lowering in the conduction band energies, Figure 3.15. While the band gap is again indirect, it is worth noting how flat the band gap is compared to Figure 3.12 and therefore the existence of many more available transition channels. Thus, a potential S_0/S_1 CI exists in the solid state and again permits excitation of the azido anion. The lowering of the conduction band to such considerable degrees also offers a role for local electronic defects within these structures (*e.g.* holes or dopant states), which sit within the band gap of the pure crystalline material. These defects have previously been suggested as being crucial for the initiation of energetic compounds, although no mechanism for their athermal influence has been proposed.[71,87] It can be suggested that their interaction with the electronic structure, and its dynamics as a result of normal mode perturbation, may be crucial to understanding their mechanism of action.

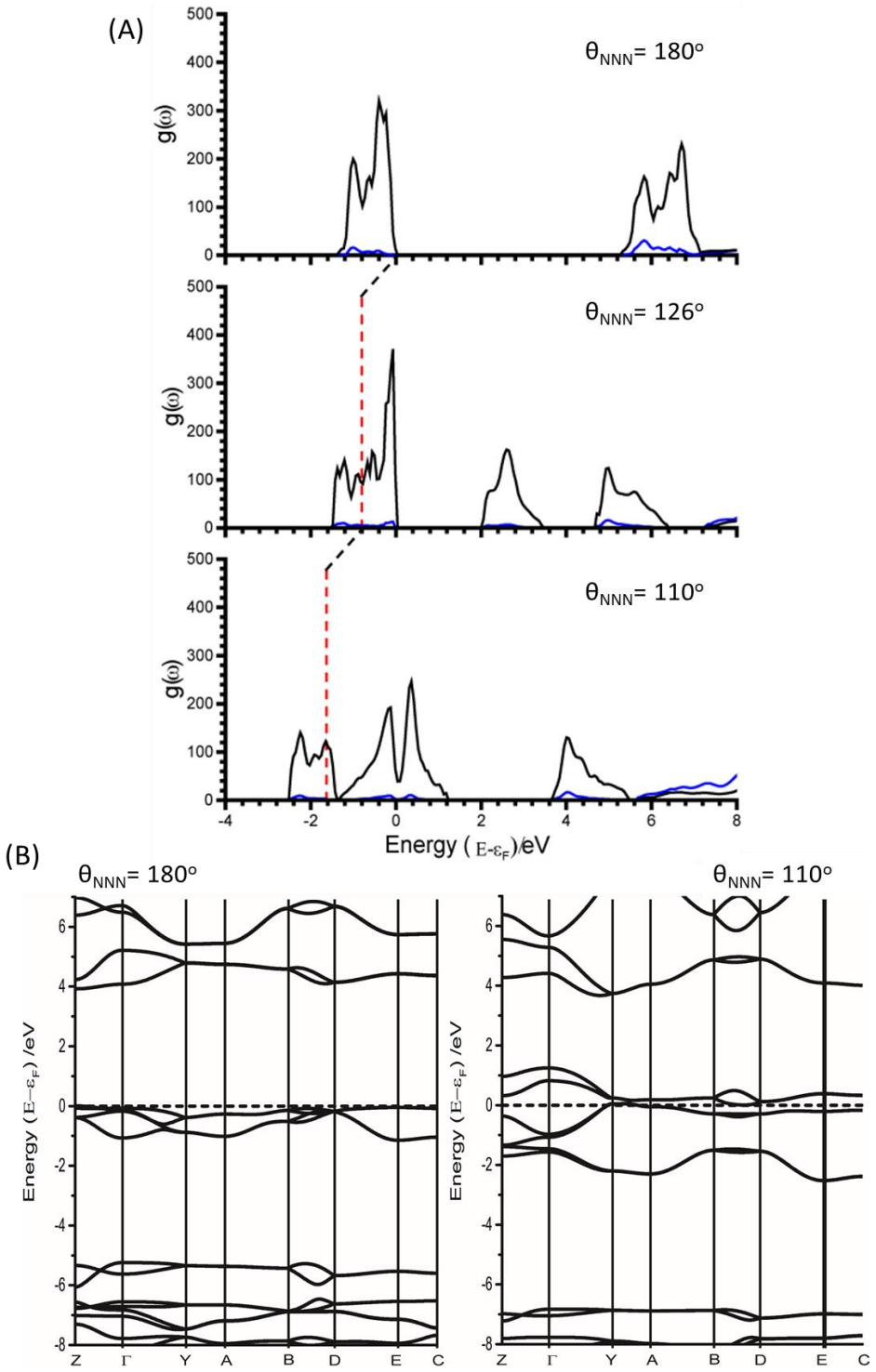

Figure 3.15: (A) Partial electronic density of states as a function of M_{17}, with contributions from N_3^- (black) and Na^+ (blue). The relative energy of ϵ_F at θ_{NNN}=180° is shown as a red vertical line in the perturbed structures. (B) Electronic band structures for NaN_3 with $\theta_{NNN} = 180^o$ and $\theta_{NNN} = 110^o$. ϵ_F is marked with a dotted line.

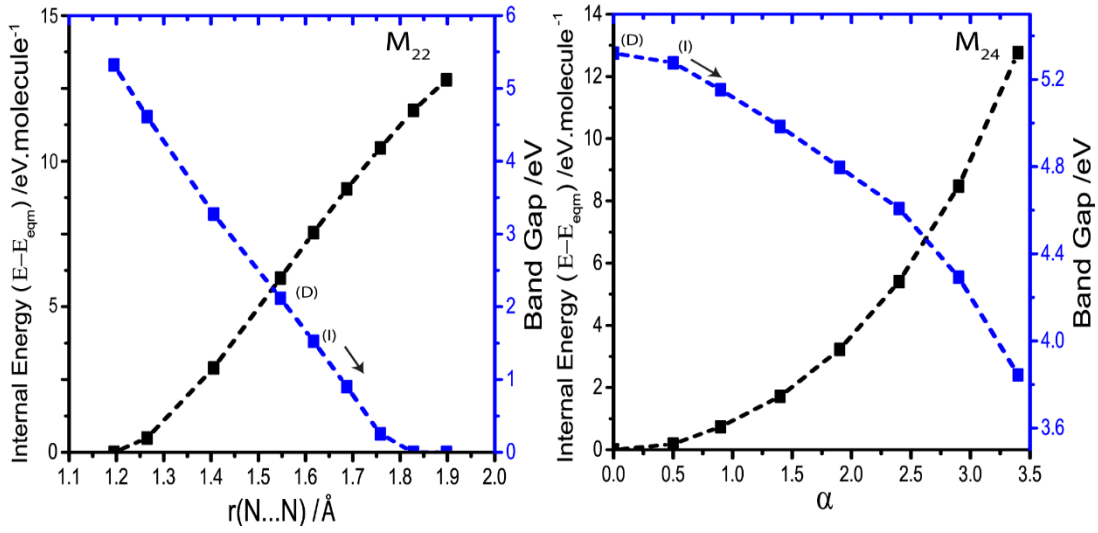

Figure 3.16: Effect of M_{22} and M_{24} (*i.e.* δR_s and δR_{as}, respectively) on the electronic band gap. The latter is plotted as α, defined as in Figure 3.5. Band gaps are defined as direct (D) or indirect (I) and the arrow indicates that the indirect band gap continues. To reflect perturbation of two azido anions (in the conventional cell), energy is given per molecule

M_{21} is the out of phase δR_S mode. Due to the contraction of one set of N-N bonds over this normal coordinate, it was not possible to follow this mode beyond a N-N stretch of 1.4 Å. By this limit, the band gap was found to decrease only slightly, from *ca.* 5.2 to 3.3 eV. It is therefore unlikely that this mode provides a route to metallisation. The in-phase (zone centre) δR_S is expressed as M_{22}. By the same ΔU (*ca.* 5 eV.molecule^{-1}) at which the bending modes led to metallisation, the band gap from δR_S reduces to only *ca.* 2 eV. Further extension of this normal coordinate unsurprisingly leads to metallisation as the N-N bonds are ruptured. However, this occurs at $\Delta U > 12$ eV.molecule^{-1}. The final two normal coordinates, M_{23} and M_{24}, are the in- and out-of-phase δR_{as}, respectively, and behave the same. For the reason described for M_{21}, there is a physical limitation on the maximum T_i that can be applied to these modes. This limit was reached with an energy penalty of *ca.* 13 eV.molecule^{-1}, by which point the band gap was found to reduce to only 3.8 eV. Thus, metallisation can only be attained *via* the bending normal coordinate, consistent with findings for the gas phase N_3^- molecule. The solid state, however, introduces the availability of a S_1/S_0 CI, which is not apparently available in the gas phase.

Thus to summarise, two sets of modes have been identified that lead to a narrowing of the band gap in α-NaN_3. The first is a phonon mode, M_{16} which suggests that a route to $N_3^- \rightarrow N_3$ might be possible under the application of a long-duration vibrational excitation but does not occur under mechanical impact. Modes $M_{17} - M_{20}$ support the gas-phase calculations, identifying the bending mode as being a probable target mode for initiation of explosions in azide materials.

3.5.3 Up-Pumping and Impact Sensitivity

Note the phonon dispersion curves for $Sn(N_3)_2$, NH_4N_3, TAGZ and HN_3 were calculated by Dr. Carole Morrison (School of Chemistry, University of Edinburgh)

The discussions presented in Sections 3.5.1 and 3.5.2 suggest that vibronic processes may be responsible for the spontaneous electronic excitation of the explosophoric N_3^- species. These processes are driven by the normal coordinate eigenvector of $\delta\theta_{NNN}$, but require perturbations that are larger than are typical under thermal equilibrium. Hence, to reach the CIs that appear along the PES of N_3^-, the molecule must be promoted to a highly excited vibrational state. This can be achieved by phonon up-pumping. This process is given in Equation 3.3, which describes the vibrational lifetime of a mode with branch index *j* and wave vector, $\boldsymbol{q}$,[88]

$$\gamma_{\mathbf{q},\mathrm{j}} = \frac{\pi}{\hbar^2 N_q} \sum_{\boldsymbol{q}',j',j''} \left| V^{(3)}_{\boldsymbol{q}j,\boldsymbol{q}'j',\boldsymbol{q}''j''} \right|^2 \times \left[\left(1 + n_{\boldsymbol{q}'j'} + n_{\boldsymbol{q}''j''}\right) \delta\left(\omega_{\boldsymbol{q}j} - \omega_{\boldsymbol{q}'j'} - \omega_{\boldsymbol{q}''j''}\right) + 2\left(n_{\boldsymbol{q}'j'} - n_{\boldsymbol{q}''j''}\right) \delta\left(\omega_{\boldsymbol{q}j} + \omega_{\boldsymbol{q}'j'} - \omega_{\boldsymbol{q}''j''}\right) \right]$$

Equation 3.3

Equation 3.3 restricts discussion to within the first anharmonic approximation. This is a reasonable restriction as higher order terms occur too slowly in most cases.[4] The phonon lifetime can be understood by two sets of scattering processes, which are displayed in the square brackets. The first term describes the *down-conversion* process, where vibration $\omega_{\boldsymbol{q}j}$ decomposes into two lower-frequency modes, $\omega_{\boldsymbol{q}'j'}$ and $\omega_{\boldsymbol{q}''j''}$. The second term describes the

combination of two phonons, $\omega_{\boldsymbol{q}j}$ and $\omega_{\boldsymbol{q}'j'}$, to create a third, $\omega_{\boldsymbol{q}''j''}$. Where $\omega_{\boldsymbol{q}''j''} > \omega_{\boldsymbol{q}j}$, this process is known as *up-conversion*. At finite temperature, the scattering processes described in each event depend on the Bose-Einstein statistical occupations ($n_{\boldsymbol{q},j}$), Equation 3.4, and a third-order anharmonic coupling constant, $V^{(3)}$. The magnitude of the latter term depends on the relative polarisation and anharmonic character of the three coupling phonon modes. As both up- and down-conversion processes are possible, excess energy is rapidly equilibrated through the molecule *via* the available vibrational relaxation mechanisms. Thus, to achieve a highly excited state of a target mode ($\delta\theta_{\mathrm{NNN}}$ in the case of the azides) it is important to achieve rapid conversion *into* the corresponding branch, *j*. The slower the conversion into the branch, the more the required input energy to achieve sufficient excitation.

$$\mathrm{n}_{\omega} = \left[e^{(\hbar\omega/k_{\mathrm{B}}T)} - 1\right]^{-1}$$

Equation 3.4

It follows from Equations 3.3 and 3.4 that energy transfer rates will be faster when including low frequency modes, which at temperature, T, will exhibit higher populations, and are typically more anharmonic.[4] As described in Section 3.1, a mechanical impact can be treated as instantaneous heating of the lowest frequency vibrational modes.[12] This therefore leads to highly populated phonon states, which rapidly reach a quasi-equilibrium state. For simplicity, the model employed here chooses this initial equilibrated phonon bath as a starting point.

At this starting point, it is convenient to construct a temperature-independent model, by extending Equation 3.3 to the low temperature limit of $\mathrm{T} = 0\ \mathrm{K}$. Under this limit,

$$\gamma_{\mathbf{q},\mathrm{j}} = \frac{\pi}{\hbar^2 N_q} \sum_{\boldsymbol{q}',j',j''} \left|V^{(3)}_{\boldsymbol{q}j,\boldsymbol{q}'j',\boldsymbol{q}''j''}\right|^2 \times \left[\delta\left(\omega_{\boldsymbol{q}j} - \omega_{\boldsymbol{q}'j'} - \omega_{\boldsymbol{q}''j''}\right)\right]$$

Equation 3.5

Here the bracketed term represents the two-phonon density of states, $\Omega^{(2)}$. In the absence of temperature considerations, microscopic reversibility dictates that the number of down-conversion pathways must equal the number of up-conversion pathways. Hence, Equation 3.5 describes the total number of scattering pathways that can transfer energy into mode $\omega_{\boldsymbol{q}j}$. In this form, $\omega_{\boldsymbol{q}j}$ is defined as the target frequency (herein labelled $\omega_{\boldsymbol{T}}$, the N_3^- $\delta\theta_{NNN}$ mode), with $\omega_{\boldsymbol{q}'j'}$ and $\omega_{\boldsymbol{q}''j''}$ denoting lower frequency modes. The Dirac δ ensures conservation of energy, and momentum is conserved by setting $\boldsymbol{q} = -\boldsymbol{q}' - \boldsymbol{q}''$. Energy transfer to $\omega_{\boldsymbol{T}}$ is then largely dependent on the number of pathways defined by $\Omega^{(2)}$.

By imposing the Einstein approximation (that ω is $\mathbf{q}$-independent) for the internal vibrational modes, it is possible to consider only the phonon density of states (PDOS), rather than the full phonon dispersion curves. The latter are shown in Figure 3.17. This is based on the following:

1. To a good approximation, there is a continuum of vibrational states within the phonon bath.
2. For phonon-phonon coupling involving two phonons with the same branch index, $j_1 = j_2$, momentum conservation and phase matching dictate that $\boldsymbol{q_1} = -\boldsymbol{q_2}$, such that $\omega_{j,\mathbf{q}} + \omega_{j,-\mathbf{q}} = \omega_{T,\boldsymbol{q}=0}$. Thus, ω_T is only accessible at the zone centre and only the absolute frequency of the low frequency modes is important.
3. For phonon-phonon coupling involving two phonons with different branch index, $j_1 \neq j_2$, the $\mathbf{q}$-independence of ω_T imposes that for any combination of $(\omega_{\boldsymbol{q}j}, \omega_T)$, there will be a $\omega_{\boldsymbol{q}'j'}$ at the appropriate momentum and frequency to satisfy Equation 3.5. The same holds under the assumption that one of the phonon modes is a doorway mode, regardless of its $\mathbf{q}$-dependence.
4. In the absence of explicit consideration of $V^{(3)}$, coupling between all sets of phonons can be taken to be approximately the same, provided they comprise distortion of the same set of interacting atoms (*i.e.* are of the same molecule or strongly bonding intermolecular atoms).[89,90]

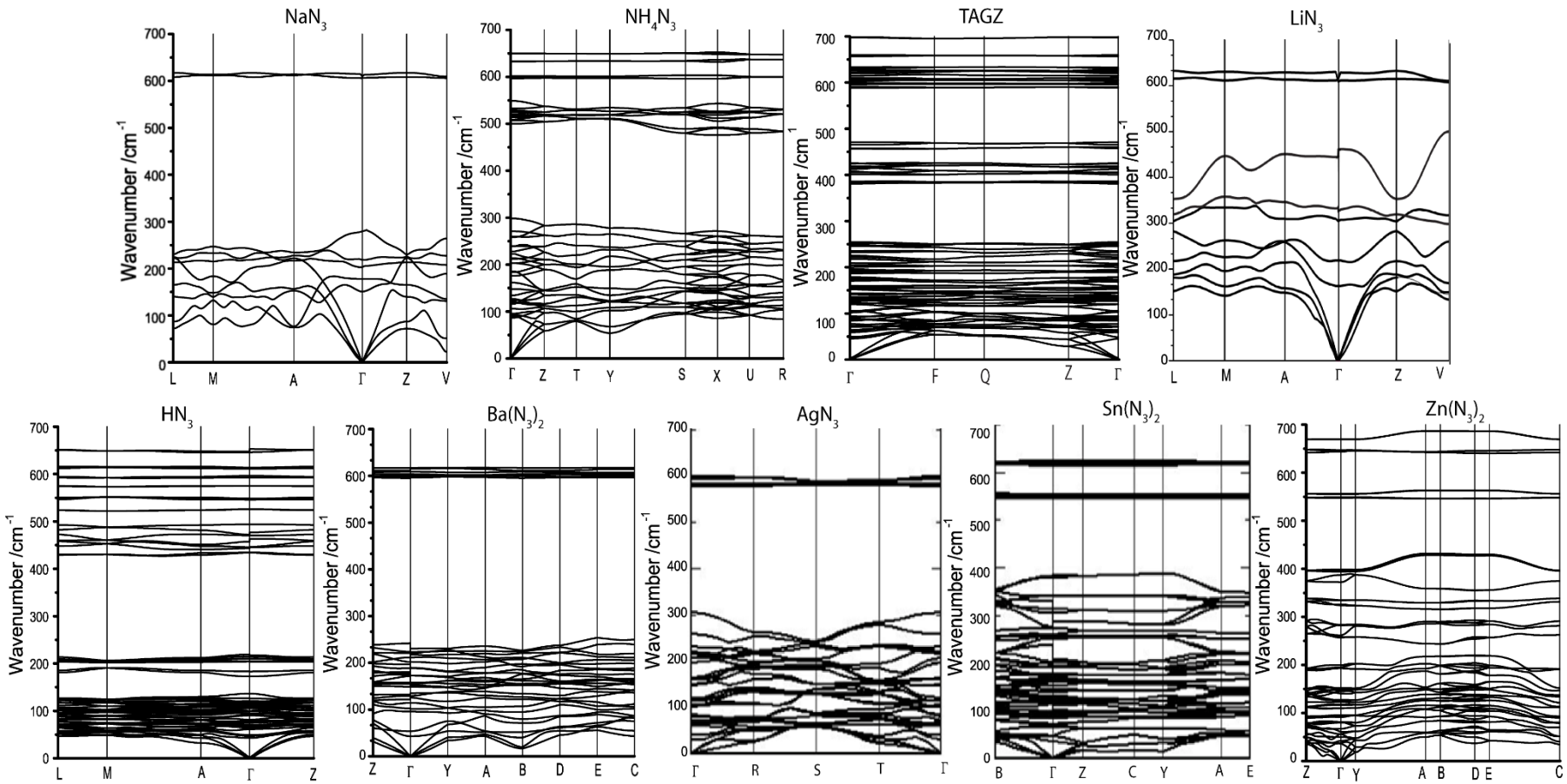

Figure 3.17: Phonon dispersion curves for the energetic azides. All are given for the primitive cell except AgN_3.

3.5.3.1 Partitioning of the Vibrational Structure

Following from the three terms contained in $\Omega^{(2)}$ of Equation 3.5, the PDOS can be segmented into a series of physically meaningful regions, Figure 3.18.[16] The first mode, $\omega_{\boldsymbol{q}'j'}$, generally exhibits lattice character, and is held within the phonon bath, which has an upper limit defined by $\Omega_{\max}$. While this value is not rigorously defined, it can be qualitatively described as the highest lattice-based mode. Due to the high anharmonicity of these lattice modes, and the high density of vibrational states, the thermalisation of vibrational energy occurs very rapidly in this region. This imposes a crude definition of Ω_{max} as being the first point in which the phonon density of states drops to zero. The second frequency, $\omega_{\boldsymbol{q}''j''}$, generally sits somewhere between Ω_{max} and $2\Omega_{max}$, and is termed the 'doorway mode'. The upper limit of $2\Omega_{max}$ is significant as it defines the highest frequency attainable by coupling of two phonon bath modes. The third mode, ω_T is the target vibrational frequency. It must fall within $3\Omega_{max}$ to be accessed by coupling of a phonon mode with a doorway mode. The identity of ω_T was determined in Section 3.5.1 as being $\delta\theta_{NNN}$. Within the Einstein approximation, the frequency of $\delta\theta_{NNN}$ can be identified from the Γ-point eigenvectors. This was done by artificially extending the eigenvectors of each zone-centre normal coordinate and led to easy identification of ω_T, Figure 3.19. Note that due to factor group splitting and symmetry independent azido anions, multiple distinct $\delta\theta_{NNN}$ frequencies can exist in the same crystal. The covalent compounds exhibit a more extensive spread in $\delta\theta_{NNN}$ frequencies. While a cluster of $\delta\theta_{\mathrm{NNN}}$ exists around 600 cm^{-1} in all of the azides (with the exception of HN_3), the covalent (more sensitive) compounds exhibit additional $\delta\theta_{\mathrm{NNN}}$ at lower frequency. Within the framework of the up-pumping model of impact initiation, this may be indicative of their higher sensitivity and offer a design target for novel materials.

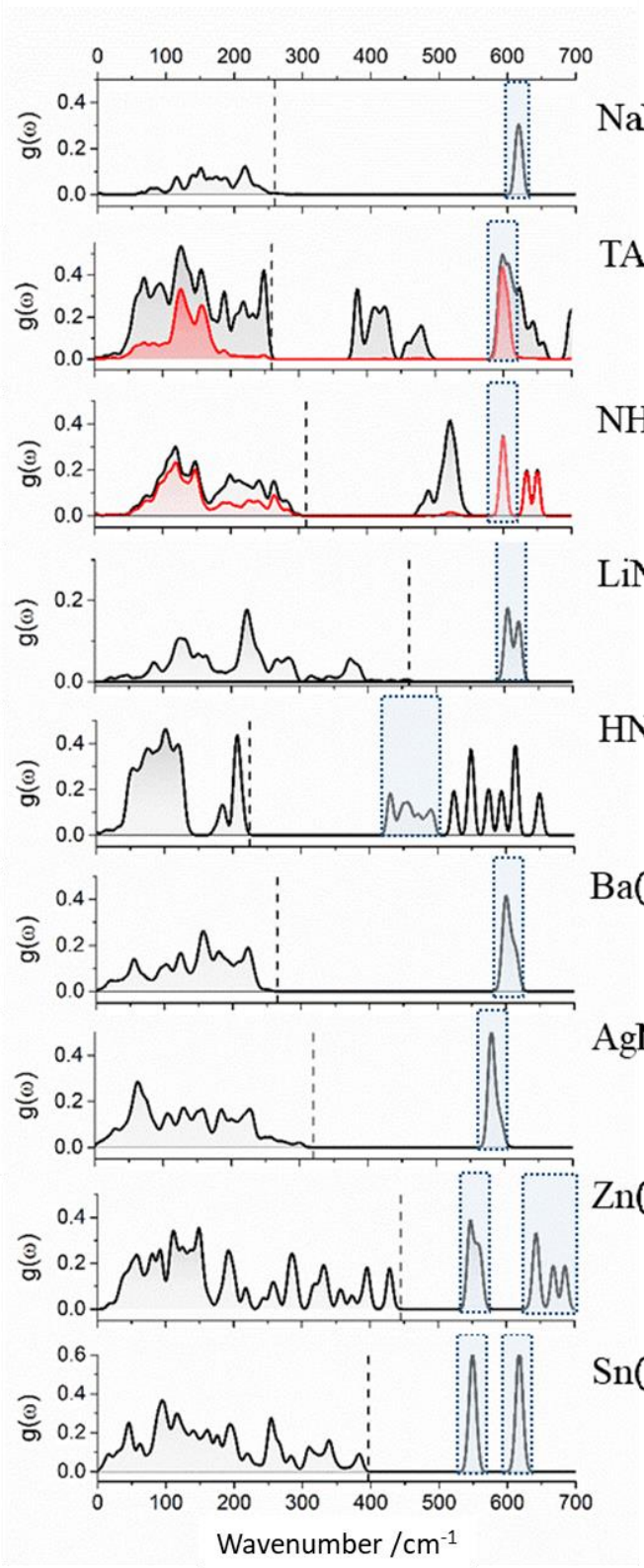

Figure 3.18: The phonon density of states for the crystalline azide materials studied here. The vertical dotted line indicates $\Omega_{\max}$, and the blue rectangle highlights the position of ω_{T}. Red indicates azido anion partial DOS Figure is adapted from Ref 21.

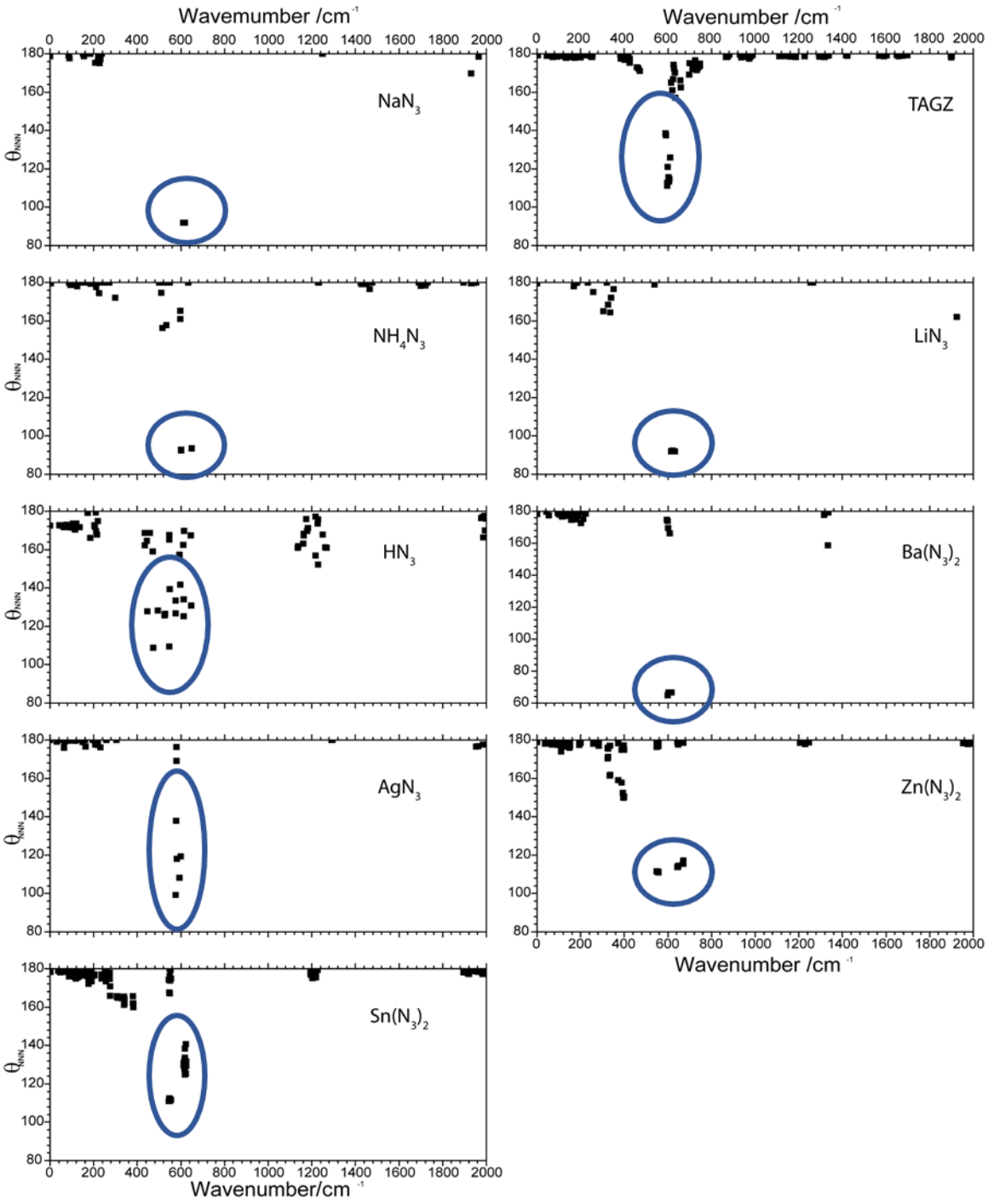

Figure 3.19: Identification of target modes. The azide bend at each Γ-point normal mode is highlighted.

The position of Ω_{max} is important as the anharmonicity of $\omega < \Omega_{max}$ leads to a rapid equilibration of the population of these modes in accordance with both up- and down-conversion processes of Equation 3.3.[4] Experimental work has

suggested that this equilibration occurs at least an order of magnitude faster than any up-conversion beyond Ω_{max}.[4] The up-conversion of this energy then occurs in two stages:

1. coupling of two modes with $\omega_j < \Omega_{max}$ to excite a mode with $\Omega_{max} < \omega < 2\Omega_{max}$, and
2. further up-pumping to modes with $2\Omega_{max} < \omega < 3\Omega_{max}$.[17]

It is from this sequence that vibrational modes with $\Omega_{max} < \omega < 2\Omega_{max}$ derive their name: *doorway modes*. While step (1) is first, step (2) occurs only picoseconds afterwards[17] and hence these processes may become important. This sequence of steps also limits primary up-pumping steps to a maximum of $3\Omega_{max}$.

The probability ($\wp$) of phonon-phonon coupling processes is governed by Fermi's Golden rule,[91]

$$\wp(i \to f) \propto \left|\langle \varphi_f | H_3 | \varphi_i \rangle\right|^2 D_f(E)$$

Equation 3.6

where $\mathrm{D_f(E)}$ is the density of final states and $\mathrm{H_3}$ is the third order anharmonic Hamiltonian. Thus, the probability of scattering is a maximum when the initial and final scattering states, $|\varphi_i\rangle$ and $|\varphi_f\rangle$, respectively, are coherent.[14] Qualitatively, it follows that the greater the total change in the PDOS, the less probable the transition will be. Within the nomenclature introduced above, it might therefore be expected that energy transfer to ω_T will occur more quickly given a smaller $\Delta\omega = \omega_T - \Omega_{max}$. This is because more combinations of phonon modes will be resonant with ω_T as $\Delta\omega \to 0$. Generally, more sensitive materials are found to exhibit higher Ω_{max} values, and analysis of $\Delta\omega$ does suggest some merit to this qualitative approach, Table 3.6, although discrepancies do arise. This is most notable with LiN_3 and $Ba(N_3)_2$, which appear in different sensitivity classifications according to this method.

Table 3.6: Characteristic frequencies for the azide materials. The Γ-point based target frequency (ω_T), top of the phonon bath (Ω_{max}) and $\Delta\omega = \omega_T - \Omega_{max}$.

Material	ω_T(Γ) /cm^{-1}	Ω_{max} /cm^{-1}	$\Delta\omega$ /cm^{-1}
NaN_3	615	250	365
TAGZ	595	260	335
NH_4N_3	605	310	295
LiN_3	605, 620	460	145, 160
HN_3	435-500	225	210-275
$Ba(N_3)_2$	600, 615	265	335, 350
AgN_3	581, 594	320	261, 274
$Zn(N_3)_2$	547, 630, 670, 685	445	102, 185, 225, 240
$Sn(N_3)_2$	550, 615	395	155, 220

3.5.3.2 Coupling Pathways and Impact Sensitivity

Within the first anharmonic approximation, only two phonons ($\omega_{j'}$ and $\omega_{j''}$) may scatter to form a third (ω_T). This leads to two different scattering mechanisms:

1. $\omega_{j'}$ and $\omega_{j''}$ share the same branch index and frequency, *i.e.* $\omega_{j'} = \omega_{j''}$, imposing the restriction that **q**($\omega_{j'}$) = - $\boldsymbol{q}(\omega_{j''})$, and **q**($\omega_T$) = Γ.
2. $\omega_{j'} \neq \omega_{j''}$ such that **q**(ω_T) = $\boldsymbol{q}(\omega_{j'})$+ $\boldsymbol{q}(\omega_{j''})$

These two scattering mechanisms are analogous to spectroscopic processes of (1) overtone and (2) combination bands. This terminology will therefore be adopted for ease of the following discussion.

While explicit solution of Equation 3.5 requires the calculation of $V^{(3)}$, its calculation is intractable for large, low symmetry systems.[88] Previous attempts at deriving values of this term have suggested that structurally similar materials exhibit minimal difference in the average value of $V^{(3)}$, and that its neglect is generally sufficient.[19,20,89] However, it follows from the definition of this term that vibrational eigenvectors that do not comprise the same atoms will not couple with any notable efficiency. This is an important consideration for NH_4N_3 and TAGZ, where large portions of the vibrational structure contain no

N_3^- character. For these systems, coupling pathways are therefore considered only for the azide-channel PDOS, Figure 3.18.

Overtone Pathways

In accordance with Equation 3.5, overtone pathways can be expected to occur more efficiently.[17] This assumption formed the base for previous work at understanding impact sensitivity.[14,19] However, the number of overtone pathways is far fewer than the pathways available by the combination mechanism. Further, only the first overtone pathway can be considered within the first anharmonic approximation. Higher order overtones become increasingly improbable, making these pathways less likely for materials in which $\omega_T > 2\Omega_{max}$. This restriction affects NaN_3, TAGZ, and BaN_3. However, due to the high anharmonicity of phonon modes, it has been suggested that quartic terms can occur with sufficient speed for further consideration. [93] This extends the restriction to $3\Omega_{\max}$.

To describe the overtone pathways, the PDOS, *g(ω)* is scaled by *N*, the overtone number,

$$g^N(\omega) = \frac{g(\omega)}{N}\,;\, \omega^N = \omega N$$

Equation 3.7

Within this model, the number of pathways through which energy can transfer can then be taken as an integration of $g^N(\omega)$ at each ω_T, Figure 3.19**.** To account for the existence of resonant vibrational states, a sampling window of $\omega_T \pm 10$ cm^{-1} was used. This reflects the magnitude of Gaussian smearing that was applied during generation of the PDOS.

The number of overtone pathways present in each material does appear to correlate loosely with the relative sensitivities, Figure 3.19B. As expected, modes in which $\omega_T > 2\Omega_{\max}$ have $g^2(\omega_T)$=0. The total $g^N(\omega_T)$ observed for the insensitive materials is consistently less than for the sensitive materials, with a sensitivity ordering following TAGZ < HN_3 < NaN_3 ≈ NH_4N_3 < $Ba(N_3)_2$ < AgN_3 < $Sn(N_3)_2$ < $Zn(N_3)_2$ for the first two overtones (*i.e.* quartic coupling).

While many of the materials are correctly ordered, the overtone pathways alone are clearly incapable of fully describing the sensitivity ordering of these materials. This deficiency is particularly notable for the low sensitivity materials and HN_3. However, in developing the up-pumping model, interest rests in the localisation of energy. Hence, it is worth recasting these values based on the number of molecules present in the unit cell (this also has the effect of correcting for the use of conventional cells in some cases), Figure 3.19C. Renormalisation in this manner highlights even further the deficiencies of considering only overtone pathways in the up-pumping model, with HN_3 in particular being substantially underestimated in its sensitivity. The general trend remains with sensitive compounds exhibiting higher integrated overtone densities than the less sensitive compounds.

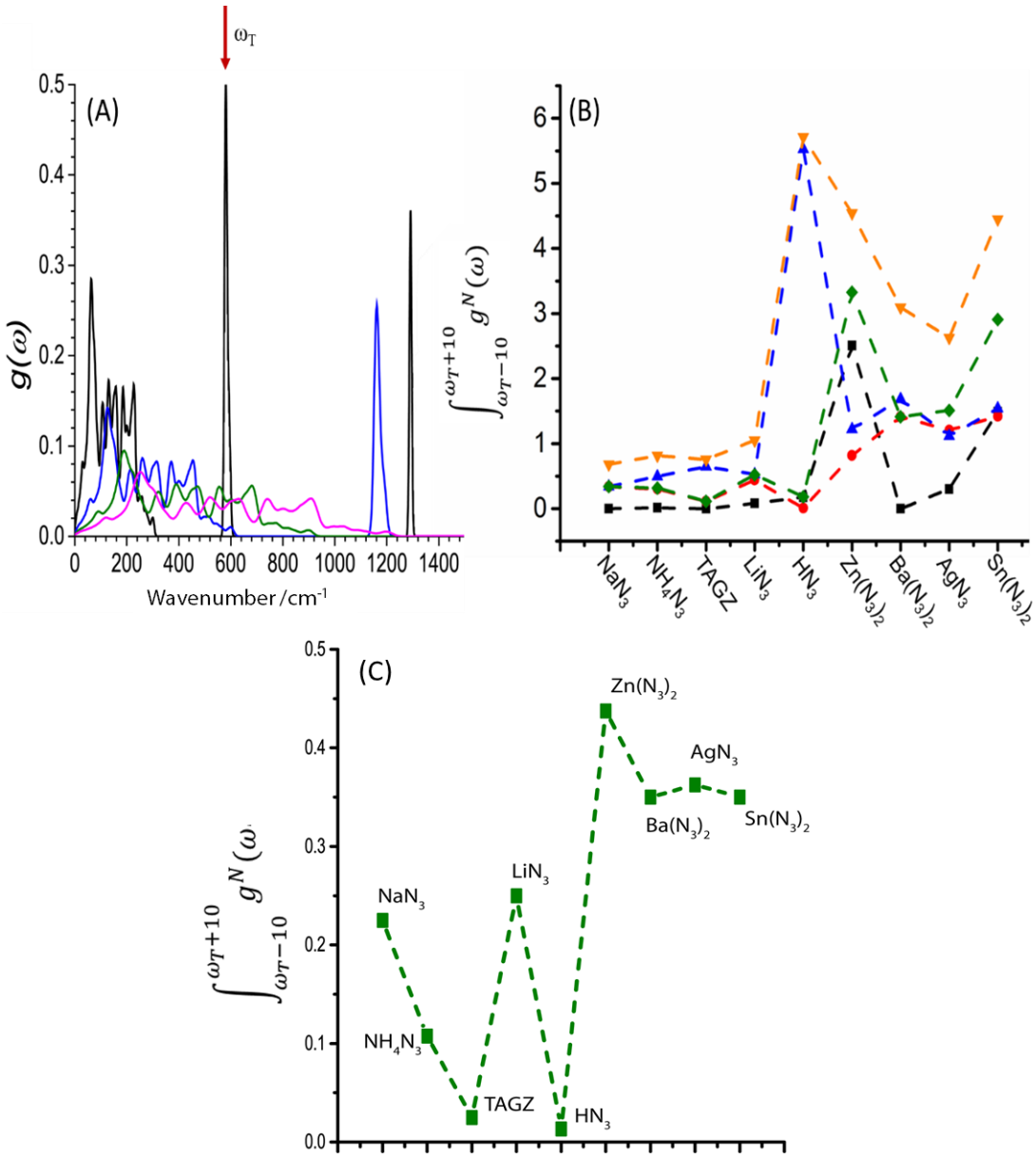

Figure 3.19: Overtone pathways for phonon up-pumping. (A) Example of overtone coupling in AgN_3, showing the (black) PDOS, (blue) N=2 overtone, (green) N=3 overtone and (pink) N=4 overtone. (B) Integration over $\omega_T \pm 10$ cm^{-1} for the overtone pathways available in the crystalline azide materials, arranged in approximate order of increasing sensitivity. Values are given as sums across all target modes. Overtones N=2 (black), N=3 (red) and N=4 (blue) are shown, alongside N2+N3 (green), as well as N2+N3+N4 (orange). (C) Renormalisation of the N2+N3 overtone curve by the number of N_3^- molecules in the unit cell.

Multiphonon Density of States: Combination pathways

Given the deficiency of the overtone pathways alone, it was necessary to consider also the combination pathways. This was done by generation of $\Omega^{(2)}$ for each of the materials under investigation, Figure 3.20. By Equation 3.5, only up-conversion processes are accounted for, ensuring $\omega_{\boldsymbol{q}'j'}$ and $\omega_{\boldsymbol{q}''j''} < \omega_{\boldsymbol{T}}$. To further adhere to the model proposed in Section 3.5.3, further constraints are imposed on generation of $\Omega^{(2)}$, ensuring that $\omega_{\boldsymbol{q}'j'}$ and $\omega_{\boldsymbol{q}''j''} < 2\Omega^{(2)}$ and $\omega_{\boldsymbol{q}'j'} < \Omega_{max}$. This ensures that all values of $\Omega^{(2)} < 3\Omega_{\max}$ must include at least one phonon mode. It is generally found, however, that this restriction has little effect on the structure of $\Omega^{(2)}(\omega_{\boldsymbol{T}})$, Figure 3.20. Generally, it is found that $\omega_{\boldsymbol{T}}$ falls within the region of this restricted $\Omega^{(2)}$for the sensitive materials, with little to no $\Omega^{(2)}$ density found at $\omega_{\boldsymbol{T}}$ for insensitive materials. The magnitude of $\Omega^{(2)}$ is seen to increase notably with increasing sensitivity. Only one exception ($Ba(N_3)_2$) is found to this trend. Despite its similarity to the PDOS of AgN_3, the lower value of $\Omega_{\max}$ for $Ba(N_3)_2$ means that the ω_T sits just beyond the doorway region. Thus, the magnitude of $\Omega^{(2)}$ in the restricted case is necessarily zero, given no doorway modes are present. The calculated Γ-point Ω_{max} of $Ba(N_3)_2$ agrees well with experimental measurements (230-240cm^{-1})[92] and suggests minimal error in the selection of the phonon bath for this material.

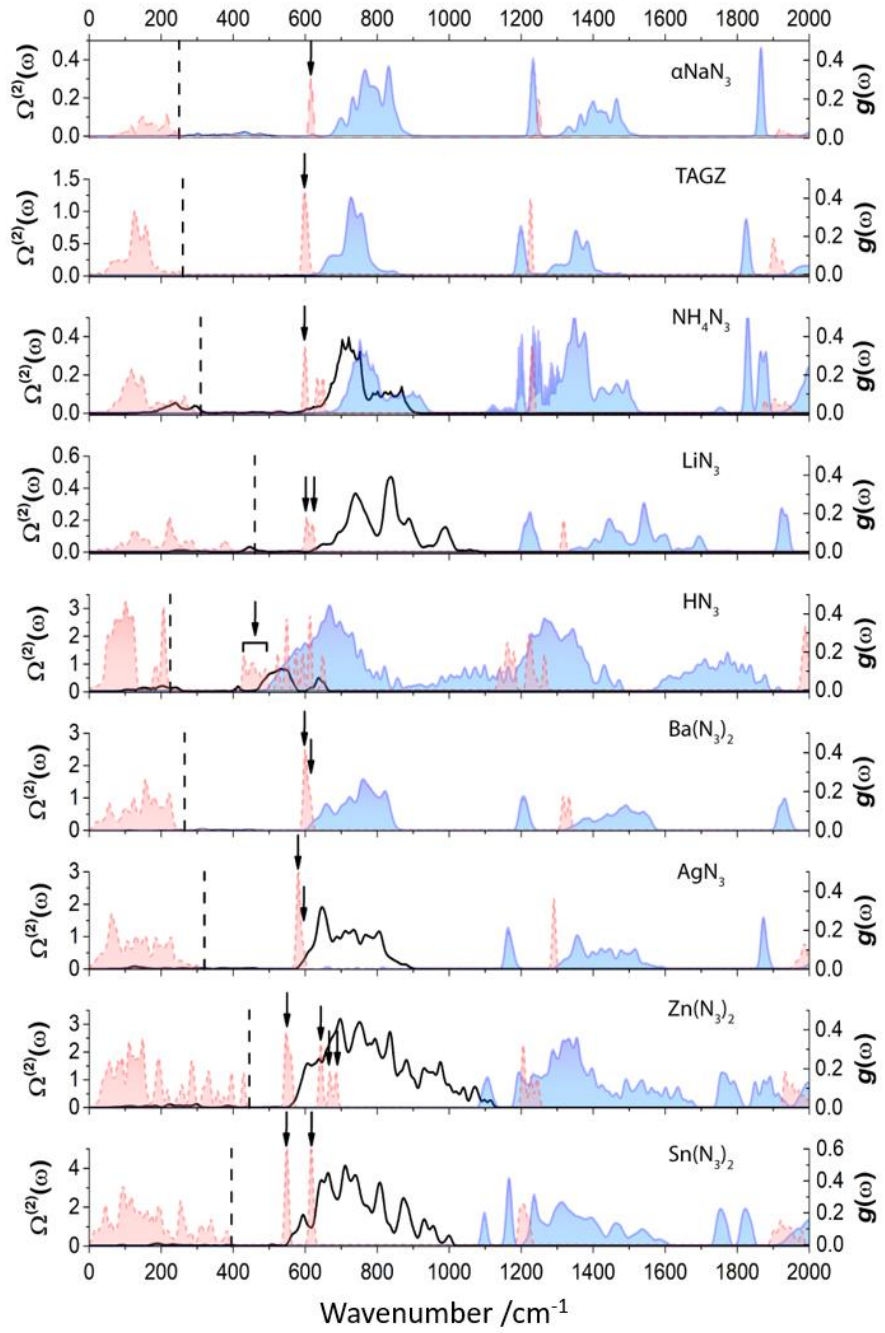

Figure 3.20: Two phonon density of states (2PDOS; $\Omega^{(2)}$) for the azides, calculated by enforcing both $\omega_{\boldsymbol{q}'j'}$ and $\omega_{\boldsymbol{q}''j''} < 2\Omega_{max}$ (black). The difference between this restricted 2PDOS and that produced by considering *all* combination modes is also shown (blue). The PDOS is given in red. Ω_{max} is given as a vertical dotted line, and $\omega_{\boldsymbol{T}}$ is indicated with an arrow.

Prediction of Impact Sensitivity

By imposing the approximation that ω_T is flat (*i.e.* $\boldsymbol{q}$-invariant), the total value of $\Omega^{(2)}(\omega_T)$ is indicative of the number of coupling pathways capable of up-converting energy into this mode. Based on Equation 3.5, it follows that the faster energy can transfer into ω_T, the lower the dissipation of this energy and the more sensitive will be the compound.

A clear correlation is observed between $\Omega^{(2)}(\omega_T)$ and the experimental impact sensitivity for each compound, Figure 3.21. The insensitive materials exhibit $\Omega^{(2)}(\omega_T) \approx 0$. This suggests that within the ideal crystal, direct transfer of energy into ω_T is not possible, and therefore that they cannot be easily initiated by impact. The calculated value of $\Omega^{(2)}(\omega_T)$ increases with increasing experimental impact sensitivity. However, by enforcing $\omega_{\boldsymbol{q}'j'}$ and $\omega_{\boldsymbol{q}''j''} < 2\Omega_{max}$ and $\omega_{\boldsymbol{q}'j'} < \Omega_{max}$, $Ba(N_3)_2$ appears to be as insensitive as α-NaN_3, Figure 3.21A. If this restriction is lifted and consideration is therefore given to all combination modes ($\omega_{\boldsymbol{q}'j'}$ and $\omega_{\boldsymbol{q}''j''} < \omega_{\boldsymbol{T}}$), the predicted sensitivity of $Ba(N_3)_2$ increases in line with the sensitive materials, Figure 3.21B. It is worth mentioning that the slope of $\Omega^{(2)}$ for $Ba(N_3)_2$ is very steep; small changes in the target frequency or integration window can therefore have considerable influence on the resulting sensitivity prediction. The same is not true for the other azide materials investigated here. In the frame of experimental consideration, this suggests that the presence of defects, or the compression that is associated with a shock wave, may drastically alter the sensitivity above the 0 K levels predicted here. Similar phenomena are known.[43]

Unfortunately, despite yielding excellent correlation with experiment, it is not sensible to lift the restriction of $\omega_{\boldsymbol{q}'j'}$, $\omega_{\boldsymbol{q}''j''} < 2\Omega_{max}$ and $\omega_{\boldsymbol{q}'j'} < \Omega_{max}$ based on the model outlined in Section 3.5.3. This poses a problem for the relative sensitivity of $Ba(N_3)_2$, which must abide by the same physics as the remaining materials. As a final step it is therefore worth reintroducing the possible energy coupling pathways available through overtones, with the second overtone (*N=3*) being taken as the highest contributing overtone pathway, as discussed

above. If these pathways are considered, the predicted ordering becomes very promising, Figure 3.21C-D. In the final ordering, $Ba(N_3)_2$ is predicted to be slightly less sensitive than AgN_3. LiN_3 is found to sit at the interface between the low and high sensitivity compounds. Both of these predicted orderings are in agreement with experiment. Based on the results in Figure 3.21C, the predicted sensitivity ordering of the azides follows as $NaN_3 \approx TAGZ < NH_4N_3 < LiN_3 < Ba(N_3)_2 < AgN_3 < HN_3 < Sn(N_3)_2 < Zn(N_3)_2$. This appears to be consistent with experimental reports.

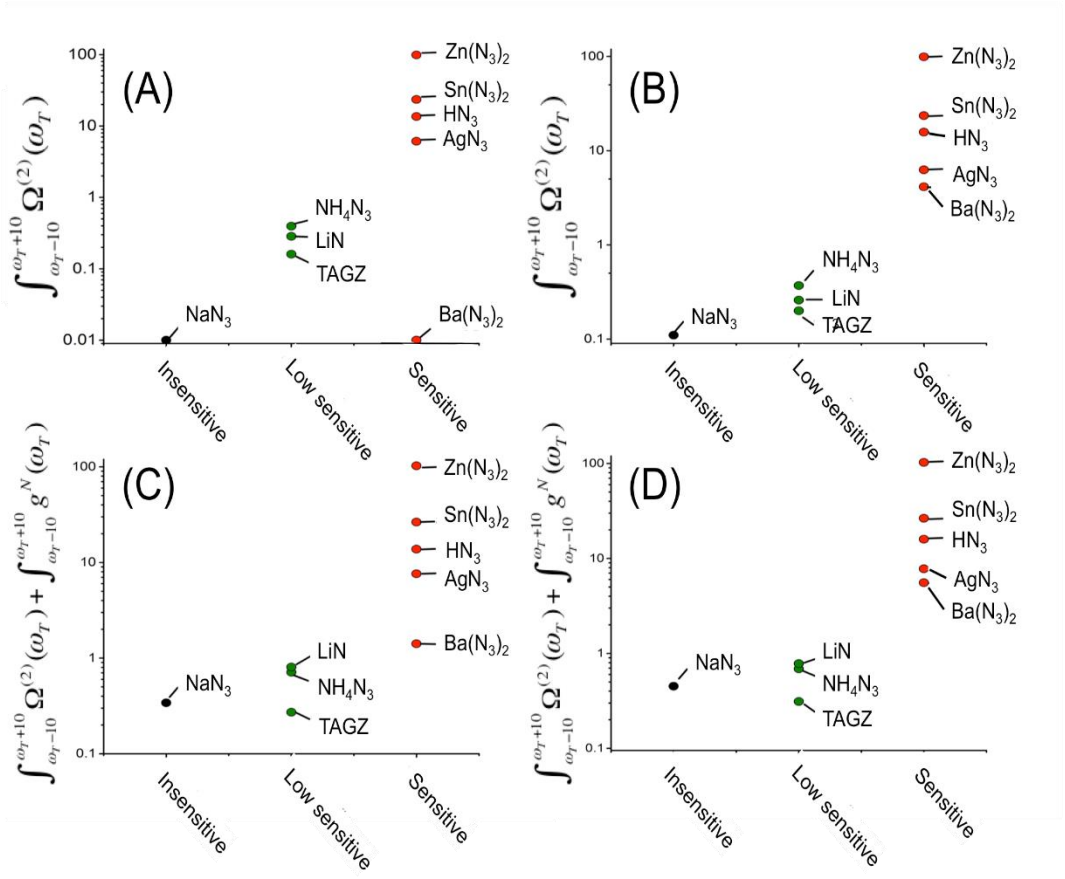

Figure 3.21: Integrated $\Omega^{(2)}(\omega_T)$ for the azides. (A) Based on $\Omega^{(2)}$ generated under the restriction of $\omega_{\boldsymbol{q}'j'}$ and $\omega_{\boldsymbol{q}''j''} < 2\Omega_{max}$ and $\omega_{\boldsymbol{q}'j'} < \Omega_{max}$. (B) Based on $\Omega^{(2)}$ with $\omega_{\boldsymbol{q}'j'}$ and $\omega_{\boldsymbol{q}''j''} < \omega_{\boldsymbol{T}}$. (C) Recasting of (A) with addition of $g^N(\omega_T)$ for N=2,3; and (D) recasting of (B) with addition of $g^N(\omega_T)$ for N=2,3.

As with overtone modelling, it becomes necessary to consider localisation of this energy per molecule, Figure 3.22. When this is done, the same general trend is observed as in Figure 3.21C, although the scale is recast. Only a change in the ordering of HN_3 and AgN_3 is observed. Based on the molecule-normalised up-pumping rates in Figure 3.22B, the final ordering is therefore predicted as $NaN_3 \approx TAGZ < NH_4N_3 < LiN_3 < Ba(N_3)_2 < HN_3 \approx AgN_3 < Sn(N_3)_2 < Zn(N_3)_2$.

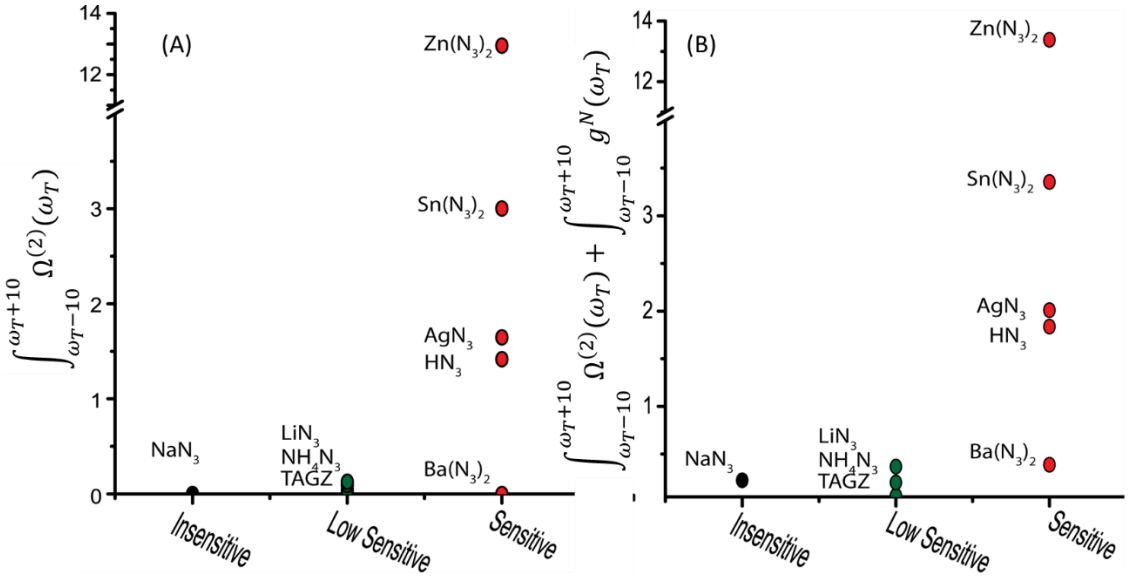

Figure 3.22: Recasting of Figure 3.21 (C-D) normalising by the number of azido anions in the unit cell.

As highlighted in Section 3.3, the ordering of impact sensitivities of the energetic azides is widely debated in literature. For example, the relative ordering of $Ba(N_3)_2$ and AgN_3 is contested, with most recent reports suggesting $AgN_3 > Ba(N_3)_2$.[36] The sensitivity of $Zn(N_3)_2$ is also inconsistently reported in literature, with some reports stating that is more sensitive than $Pb(N_3)_2$, acting as a sensitizer.[45] It is likely that these discrepancies result from variations in experimental conditions (particle size, crystallinity, impurities, etc). However, the model presented here does appear to correlate well with the majority of literature reports. This model may therefore be helpful in clarifying the ordering

of azide materials, or highlight areas for deeper experimental investigation, where reports are drastically different.

3.6 Conclusions

Azides represent a broad class of energetic compounds, covering a wide range of structural chemistry and impact sensitivity. To understand the initiation of a chemical explosion, it is necessary to understand the decomposition of the explosophoric moiety. For the simple azides, this is rupture of an N-N covalent bond. The electronic structure of the N_3^- molecule was therefore investigated. Bond dissociation was found to be possible *via* an athermal mechanism, provided sufficient excitation of the bending vibrational mode of N_3^-. At sufficient perturbation of the nuclear geometry, a conical intersection (CI) was observed between the S_0 and T_1 electronic states. The potential energy surface of the latter readily facilitates N-N bond dissociation. The existence of this CI was verified in the solid state.

Noting that mechanical impact leads to rapid excitation of lattice vibrations, the up-pumping model was explored as a mechanism for impact initiation. Based on the electronic structure calculations, the bending motion was selected as the target vibration into which vibrational energy must up-convert to initiate an explosion. Considering both overtone and combination up-conversion pathways, it was found that the relative rate of up-pumping into this target vibration led to excellent correlation with experimental impact sensitivities. Thus, the work presented in this chapter demonstrates the first fully *ab initio* approach to the prediction of the relative impact sensitivities of energetic azide materials, without the need for any empirical correlations.

The rate of up-conversion was found to be largely dependent on two key vibrational frequencies: 1) the maximum phonon frequency, Ω_{max}, and 2) the frequency of the N_3^- bending mode, $\omega_{\boldsymbol{T}}$. This therefore offers targets and rationales for the design of novel materials:

1. Ω_{max}. This value depends on the nature of the external lattice modes and crystal packing. As such, a model based on vibrational energy transfer includes potential for understanding the different sensitivities of polymorphic and multi-component materials (co-crystals and salts). Stronger bonding of the N_3^- anion within the lattice (*i.e.* polymeric or molecular structures) was found to correlate with higher Ω_{max}. It also follows that more compressible materials will exhibit a higher Ω_{max} when subject to a mechanical perturbation. As such, materials based on weaker non-covalent interactions between energetic molecules may be more sensitive
2. ω_T. This value depends on the bonding nature of the N_3^- anion within the crystal lattice. Higher covalent character leads to a decrease in ω_T, and thus enhanced sensitivity. The increased covalent character between the N_3^- molecule and a cation also appear to weaken the N-N bond. Initiation may therefore be easier.

A particular strength of the model presented in this chapter is the fact that it encompasses many aspects of earlier models reported in the literature. For example, within the framework of this chapter, there are clear rationales for a correlation of band gap and bond dissociation energy with impact sensitivity. Further, effects such as packing density and crystal packing can all find a physical basis within this model, *via* compressibility and the capability of molecules to undergo necessary geometric perturbations. This work therefore makes strides towards an overarching understanding of initiation in energetic materials.

Despite its promise, the present model is based on idealised crystalline structures, which do not exist in reality. The model therefore only offers insight into the intrinsic potential of a material to initiate under mechanical perturbation. Further work will be required to introduce non-ideal features, such as defects and surfaces. Further, while the model here can justify the relative sensitivity of energetic materials, it is not yet able to determine whether a material will be energetic in the first place. This is to say, the model describes the *propensity*

of a material to react under mechanical perturbation, but it does not determine what that reaction will be. That aside, the present contribution offers a powerful platform from which novel materials can be designed *in silico* and offers novel insight into the structure-property relationships of common energetic materials.

3.7 Suggestions for Future Work

The material presented in this chapter clearly identifies the *up-pumping* model as a powerful tool to understanding the impact sensitivity of the crystalline energetic azides. This offers a starting point for numerous follow-up investigations.

- The decomposition pathway of the azido anion within the crystal structure would offer important validation of this model. While the CI was identified in the α-NaN_3 lattice, it would be interesting to investigate how this translates across the azides. In particular, how the PES associated with the bending mode changes as the covalent bond character of the metal-anion increases. It will also be important to further investigate the role of lattice-based eigenvectors in the reactivity of these materials. As was demonstrated for α-NaN_3, the highest frequency lattice mode does permit formation of a reactive $N_3^{\cdot}$ species. However, this pathway is unlikely to be responsible for impact-induced initiation, given that α-NaN_3 is well known to be insensitive to this form of mechanical stimulation.
- A lattice mode in α-NaN_3 was found to be sufficient to induce metallisation at large eigenvector displacement. However, α-NaN_3 is not known to be sensitive to impact. Further insight into *why* this vibrational mode does not lead to impact-induced initiation is therefore required.
- Investigating the initial stages of lattice excitation by dynamics simulations would offer considerable insight into the up-pumping model. In particular, understanding how the initial energy is inserted into the crystalline material, and how this initial excitation varies as a function of material structural type.

- The model employed in the present contribution is based on T=0 K. Hence, it does not offer a mechanism for understanding the temperature dependence of impact sensitivity. The introduction of temperature by means of thermal populations into the scattering equations would offer a new direction for the application of this model.
- Many initiation models suggest that local defects are crucial to the process. It would therefore be of interest to introduce computationally tractable models for defects. Initially, this could be done by introduction of electronic defects into the band structure calculations.
- It is clear that the dissociation energy cannot be neglected in a complete model of initiation. Introducing a correlation term between the relative dissociation energy of the azido anion and the quantity of up-pumped vibrational energy at $\Omega_{\max}$ would offer an important step forward in generalization of this model.

3.8 References

(1) Heinicke, G. *Tribochemistry*; Akademic-Verlag: Berlin, GDR, 1984.

(2) Dlott, D. D. Ultrafast Vibrational Energy Transfer in the Real World: Laser Ablation, Energetic Solids, and Hemeproteins. *J. Opt. Soc. Am. B* **1990**, *7* (8), 1638.

(3) Zel'dovich, Y. B.; Raizer, Y. P. *Physics of Shock Waves and High-Temperature Hydrodynamic Phenomena*, Vol II, Ch.; Academic: New York, 1967.

(4) Dlott, D. D.; Fayer, M. D. Shocked Molecular Solids: Vibrational up Pumping, Defect Hot Spot Formation, and the Onset of Chemistry. *J. Chem. Phys.* **1990**, *92* (6), 3798–3812.

(5) Walker, F. E. Physical Kinetics. *J. Appl. Phys.* **1988**, *63* (11), 5548–5554.

(6) Zerilli, F. J.; Toton, E. T. Shock-Induced Molecular Excitation in Solids. *Phys. Rev. B* **1984**, *29* (10), 5891–5902.

(7) Bardo, R. D. Theoretical Calculations of Rate-Determining Steps for Ignition of Shocked, Condensed Nitromethane. *Int. J. Quantum Chem.* **1986**, *30* (20 S), 455–469.

(8) Millar, D. I. A.; Barry, C.; Marshall, W. G.; Pulham, C. R. Structural

Characterization of Sodium Azide and Sodium Bifluoride at High Pressures. *Zeitschrift fur Krist.* **2014**, *229* (3), 259–275.

(9) Hou, D.; Zhang, F.; Ji, C.; Hannon, T.; Zhu, H.; Wu, J.; Levitas, V. I.; Ma, Y. Phase Transition and Structure of Silver Azide at High Pressure. *J. Appl. Phys.* **2011**, *110* (2).

(10) Simonis, G. J.; Hathaway, C. E. Raman Spectrum and Phase Transition in Sodium Azide. *Phys. Rev. B* **1974**, *10* (10), 4419–4433.

(11) Zhuravlyov, Y. N.; Lisitsyn, V. M. The Gruneisen Parameter for Silver Azide. *Russ. Phys. J.* **2011**, *54* (7), 35–41.

(12) Coffey, C. S.; Toton, E. T. A Microscopic Theory of Compressive Wave-Induced Reactions in Solid Explosives. *J. Chem. Phys.* **1982**, *76* (2), 949–954.

(13) Fox, P. G. The Explosive Sensitivity of the Metal Azides to Impact. *J. Solid State Chem.* **1970**, *2* (4), 491–502.

(14) McNesby, K. L.; Coffey, C. S. Spectroscopic Determination of Impact Sensitivities of Explosives. *J. Phys. Chem. B* **1997**, *101* (16), 3097–3104.

(15) Kim, H.; Dlott, D. D. Theory of Ultrahot Molecular Solids: Vibrational Cooling and Shock-Induced Multiphonon up Pumping in Crystalline Naphthalene. *J. Chem. Phys.* **1990**, *93* (3), 1695–1709.

(16) Hill, J. R.; Chronister, E. L.; Chang, T.; Kim, H.; Postlewaite, J. C.; Dlott, D. D. Vibrational Relaxation and Vibrational Cooling in Low Temperature Molecular Crystals. *J. Chem. Phys.* **1988**, *88* (2), 949–967.

(17) Dlott, D. D. Optical Phonon Dynamics in Molecular Crystals. *Ann. Rev. Phys. Chem.* **1986**, *37*, 157–187.

(18) Hooper, J. Vibrational Energy Transfer in Shocked Molecular Crystals. *J. Chem. Phys.* **2010**, *132* (1), 014507.

(19) Bernstein, J. *Ab Initio* Study of Energy Transfer Rates and Impact Sensitivities of Crystalline Explosives. *J. Chem. Phys.* **2018**, *148* (8), 084502.

(20) McGrane, S. D.; Barber, J.; Quenneville, J. Anharmonic Vibrational Properties of Explosives from Temperature-Dependent Raman. *J. Phys. Chem. A* **2005**, *109* (44), 9919–9927.

(21) Michalchuk, A. A. L.; Fincham, P. T.; Portius, P.; Pulham, C. R.; Morrison, C. A. A Pathway to the Athermal Impact Initiation of Energetic Azides. *J. Phys. Chem. C* **2018**, acs.jpcc.8b05285.

(22) Coffey, C. S. The Localization of Energy and Plastic Deformation in Crystalline Solids during Shock or Impact. *J. Appl. Phys.* **1991**, *70* (8), 4248–4254.

(23) Coffey, C. S. Energy Localization in Rapidly Deforming Crystalline Solids. *Phys. Rev. B* **1985**, *32* (8), 5335–5341.

(24) Manaa, M. R. Shear-Induced Metallization of Triamino-Trinitrobenzene Crystals. *Appl. Phys. Lett.* **2003**, *83* (7), 1352–1354.

(25) Kuklja, M. M.; Aduev, B. P.; Aluker, E. D.; Krasheninin, V. I.; Krechetov, A. G.; Mitrofanov, A. Y. Role of Electronic Excitations in Explosive Decomposition of Solids. *J. Appl. Phys.* **2001**, *89* (7), 4156–4166.

(26) Kuklja, M. M.; Rashkeev, S. N. Shear-Strain-Induced Chemical Reactivity of Layered Molecular Crystals. *Appl. Phys. Lett.* **2007**, *90* (15), 2005–2008.

(27) Grieß, P. On a New Class of Compounds Containing Nitrogen, in Which Hydrogen Is Replaced by Nitrogen. *Philos. Trans. R. Soc. London* **1864**, *13*, 377.

(28) Bowden, F. P.; Williams, H. T. Initiation and Propagation of Explosion in Azides and Fulminates. *Proc. R. Soc. London. Ser. A Math. Phys. Sci.* **1951**, *208* (1093), 176–188.

(29) Tornieporth-Oetting, I. C.; Klapötke, T. M. Covalent Inorganic Azides. *Angew. Chemie Int. Ed. English* **1995**, *34* (5), 511–520.

(30) Fair, H. D.; Walker, R. F. *Energetic Materials 1: Physics and Chemistry of the Inoganic Azides*; Fair, H. D., Walker, R. F., Eds.; Plenum Press: New York, 1977.

(31) Zhang, G.; Weeks, B. L. A Device for Testing Thermal Impact Sensitivity of High Explosives. *Propellants, Explos. Pyrotech.* **2010**, *35* (5), 440–445.

(32) Müller, T. G.; Karau, F.; Schnick, W.; Kraus, F. A New Route to Metal Azides. *Angew. Chemie - Int. Ed.* **2014**, *53* (50), 13695–13697.

(33) Campbell, R.; Konar, S.; Hunter, S.; Pulham, C.; Portius, P. Labile Low-Valent Tin Azides: Syntheses, Structural Characterization, and Thermal Properties. *Inorg. Chem.* **2018**, *57*, 400–411.

(34) Schulz, A.; Villinger, A. Binary Zinc Azides. *Chem. - A Eur. J.* **2016**, *22* (6), 2032–2038.

(35) Martin, W. R.; Ball, D. W. Small Organic Azides as High Energy Materials: Perazidoacetylene, -Ethylene, and -Allene. *ChemistrySelect* **2018**, *3* (25), 7222–7225.

(36) Cartwright, M.; Wilkinson, J. Correlation of Structure and Sensitivity in Inorganic Azides i Effect of Non-Bonded Nitrogen Nitrogen Distances. *Propellants, Explos. Pyrotech.* **2010**, *35* (4), 326–332.

(37) Gray, P.; Waddington, T. . Fundamental Vibration Frequencies and Force Constants in the Azide Ion. *Trans. Faraday Soc.* **1957**, *53*, 901–908.

(38) Meyer, R.; Köhler, J.; Homburg, A. *Explosives*, 6th ed.; Meyer, R., Köhler, J., Homburg, A., Eds.; Wiley-VCH: Weinheim, 2007.

(39) Kamlet, M. J.; Adolph, H. G. The Relationship of Impact Sensitivity with Structure of Organic High Explosives. II. Polynitroaromatic Explosives.

Propellants, Explos. Pyrotech. **1979**, *4* (2), 30–34.

(40) Oxley, J.; Smith, J.; Buco, R.; Huang, J. A Study of Reduced-Sensitivity RDX. *J. Energ. Mater.* **2007**, *25* (3), 141–160.

(41) Johansen, Ø. H.; Kristiansen, J. D.; Gjersøe, R.; Berg, A.; Halvorsen, T.; Smith, K. T.; Nevstad, G. O. RDX and HMX with Reduced Sensitivity towards Shock Initiation-RS-RDX and RS-HMX. *Propellants, Explos. Pyrotech.* **2008**, *33* (1), 20–24.

(42) Marinkas, P. L. A Method of Growing Anhydrous Single Crystals of Barium Azide. *Nature* **1966**, *211*, 1288–1289.

(43) Verneker, V. R. P.; Avrami, L. Explosive Behavior of Barium Azide. *J. Phys. Chem.* **1968**, *72* (3), 778–783.

(44) Avrami, L.; Hutchinson, R. The Sensitivity to Impact and Friction. In *Energetic Materials 2: Technology of the Inorganic Azides*; Fair, H. ., Walker, R. F., Eds.; 1977; pp 111–159.

(45) Shaneyfelt, W. *Complexities of Lead Azide*; 21st DDESB Explosives Safety Seminar, **1984**.

(46) Wohler, L.; Martin, F. *New Fulminates and Azides*; Chemische Berichte, **1917**.

(47) Bresien, J.; Ott, H.; Rosenstengel, K.; Schulz, A.; Thiele, P.; Villinger, A. Binary Polyazides of Zinc. *Eur. J. Inorg. Chem.* **2016**, *2016* (36), 5594–5609.

(48) Yakovleva, G. .; Kurbangalina, R. K.; Stesik, L. N. Detonation Properties of Ammonium Azide. *Combust. Explos. Shock Waves* **1977**, *13*, 405–407.

(49) Denisaev, A. A.; Assovskii, I. G.; Berlin, A. A. A. Study of the Impact Sensitivity of Sodium Azide and Its Mixtures with Water. *Dokl. Phys. Chem.* **2013**, *453* (1), 261–263.

(50) Damse, R. S. Studies on the Decomposition Chemistry of Triaminoguanidine Azide and Guanidine Nitrate. *J. Hazard. Mater.* **2009**, *172* (2–3), 1383–1387.

(51) Evers, J.; Göbel, M.; Krumm, B.; Martin, F.; Medvedyev, S.; Oehlinger, G.; Steemann, F. X.; Troyan, I.; Klapötke, T. M.; Eremets, M. I. Molecular Structure of Hydrazoic Acid with Hydrogen-Bonded Tetramers in Nearly Planar Layers. *J. Am. Chem. Soc.* **2011**, *133* (31), 12100–12105.

(52) Werner, H. J.; Knowles, P. J.; Knizia, G.; Manby, F. R.; Schütz, M. Molpro: A General-Purpose Quantum Chemistry Program Package. *Wiley Interdiscip. Rev. Comput. Mol. Sci.* **2012**, *2* (2), 242–253.

(53) Veryazov, V.; Malmqvist, P. A.; Roos, B. O. How to Select Active Space for Multiconfigurational Quantum Chemistry? *Int. J. Quantum Chem.* **2011**, *111*, 3329–3338.

(54) Clark, S. J.; Segall, M. D.; Pickard, C. J.; Hasnip, P. J.; Probert, M. I. J.; Refson, K.;

Payne, M. C. First Principles Methods Using CASTEP. *Zeitschrift für Krist.* **2005**, *220*, 567–570.

(55) Perdew, J. P.; Burke, K.; Ernzerhof, M. Generalized Gradient Approximation Made Simple. *Phys. Rev. Lett.* **1996**, *77* (18), 3865–3868.

(56) Sabatini, R.; Gorni, T.; De Gironcoli, S. Nonlocal van Der Waals Density Functional Made Simple and Efficient. *Phys. Rev. B - Condens. Matter Mater. Phys.* **2013**, *87* (4), 4–7.

(57) Grimme, S. Semiempirical GGA-Type Density Functional Constructed with a Long-Range Dispersion Correction. *J. Comput. Chem.* **2006**, *27*, 1787–1799.

(58) Tkatchenko, A.; Scheffler, M. Accurate Molecular van Der Waals Interactions from Ground-State Electron Density and Free-Atom Reference Data. *Phys. Rev. Lett.* **2009**, *102* (7), 6–9.

(59) Ramesh Babu, K.; Vaitheeswaran, G. Lattice Dynamics and Electronic Structure of Energetic Solids LiN3and NaN3: A First Principles Study. *Chem. Phys. Lett.* **2013**, *586*, 44–50.

(60) Pack, J. D.; Monkhorst, H. J. Special Points for Brillouin-Zone Integrations. *Phys. Rev. B* **1976**, *13* (12), 5188–5192.

(61) Hinuma, Y.; Pizzi, G.; Kumagai, Y.; Oba, F.; Tanaka, I. Band Structure Diagram Paths Based on Crystallography. *Comput. Mater. Sci.* **2017**, *128*, 140–184.

(62) Bracuti, A. J.; Extine, M. W. 1,2,3-Triaminoguanidinium Azide (TAZ) Structure. *J. Crystallogr. Spectrosc. Res.* **1990**, *20* (1), 31–35.

(63) Dovesi, R.; Orlando, R.; Erba, A.; Zicovich-Wilson, C. M.; Civalleri, B.; Casassa, S.; Maschio, L.; Ferrabone, M.; De La Pierre, M.; D'Arco, P.; et al. CRYSTAL14: A Program for the Ab Initio Investigation of Crystalline Solids. *Int. J. Quantum Chem.* **2014**, *114* (19), 1287–1317.

(64) Krukau, A. V.; Vydrov, O. A.; Izmaylov, A. F.; Scuseria, G. E. Influence of the Exchange Screening Parameter on the Performance of Screened Hybrid Functionals. *J. Chem. Phys.* **2006**, *125* (22).

(65) Peintinger, M. F.; Oliveira, D. V.; Bredow, T. Consistent Gaussian Basis Sets of Triple-Zeta Valence with Polarization Quality for Solid-State Calculations. *J. Comput. Chem.* **2013**, *34* (6), 451–459.

(66) Zagorac, D.; Doll, K.; Schön, J. C.; Jansen, M. Sterically Active Electron Pairs in Lead Sulfide? An Investigation of the Electronic and Vibrational Properties of Pbs in the Transition Region between the Rock Salt and the α-GeTe-Type Modifications. *Chem. - A Eur. J.* **2012**, *18* (35), 10929–10936.

(67) Doll, K.; Pyykkö, P.; Stoll, H. Closed-Shell Interaction in Silver and Gold Chlorides. *J. Chem. Phys.* **1998**, *109* (6), 2339–2345.

(68) Causà, M.; Dovesi, R.; Roetti, C. Pseudopotential Hartree-Fock Study of

Seventeen III-V and IV-IV Semiconductors. *Phys. Rev. B* **1991**, *43* (14), 11937–11943.

(69) Garza, A. J.; Scuseria, G. E. Predicting Band Gaps with Hybrid Density Functionals. **2016**, *7*, 5–10.

(70) Aduev, B. P.; Aluker, É. D.; Belokurov, G. M.; Zakharov, Y. a.; Krechetov, a. G. Explosive Decomposition of Heavy-Metal Azides. *J. Exp. Theor. Phys.* **1999**, *89* (5), 906–915.

(71) Aduev, B. P.; Aluker, E. D.; Kriger, V. G.; Zakharov, Y. A. Study of Silver Azide Explosive Decomposition by Stpectroscopic Methods with High Temporal Resolution. *Solid State Ionics* **1997**, *101–103*, 33–36.

(72) Grechnev, A.; Ahuja, R.; Eriksson, O. Balanced Crystal Orbital Overlap Population - A Tool for Analysing Chemical Bonds in Solids. *J. Phys. Condens. Matter* **2003**, *15* (45), 7751–7761.

(73) Zhu, W.; Xiao, H. First-Principles Band Gap Criterion for Impact Sensitivity of Energetic Crystals: A Review. *Struct. Chem.* **2010**, *21* (3), 657–665.

(74) Droghetti, A.; Rungger, I.; Das Pemmaraju, C.; Sanvito, S. Fundamental Gap of Molecular Crystals via Constrained Density Functional Theory. *Phys. Rev. B* **2016**, *93* (19), 1–8.

(75) Yedukondalu, N.; Ghule, V. D.; Vaitheeswaran, G. Computational Study of Structural, Electronic and Optical Properties of Crystalline NH4N3. **2013**.

(76) Liu, Q. J.; Zeng, W.; Liu, F. S.; Liu, Z. T. First-Principles Study of Hydronitrogen Compounds: Molecular Crystalline NH4N3and N2H5N3. *Comput. Theor. Chem.* **2013**, *1014*, 37–42.

(77) Zhu, W.; Xiao, H. Ab Initio Study of Electronic Structure and Optical Properties of Heavy Metal Azides: TlN3, AgN3 and CuN3. *J. Comput. Chem.* **2007**, *29* (2), 176–184.

(78) Zhu, W.; Xiao, H. First-Principles Study of Structural and Vibrational Properties of Crystalline Silver Azide under High Pressure. *J. Solid State Chem.* **2007**, *180* (12), 3521–3528.

(79) Zhu, W.; Xiao, J.; Xiao, H. Comparative First-Principles Study of Structural and Optical Properties of Alkali Metal Azides. *J. Phys. Chem. B* **2006**, *110* (20), 9856–9862.

(80) Zhu, W.; Xu, X.; Xiao, H. Electronic Structure and Optical Properties of Crystalline Strontium Azide and Barium Azide by Ab Initio Pseudopotential Plane-Wave Calculations. *J. Phys. Chem. Solids* **2007**, *68* (9), 1762–1769.

(81) Zhang, H.; Cheung, F.; Zhao, F.; Cheng, X. Band Gaps and the Possible Effect on Impact Sensitivity for Some Nitro Aromatic Explosive Materials. *Int. J. Quantum Chem.* **2009**, *109*, 1547–1552.

(82) Polak, M.; Gruebele, M.; Saykally, R. . Velocity Modulation Laser Spectroscopy of Negative Ions: The v3 Band of Azide (N3-). *J. Am. Chem. Soc.* **1987**, *109* (10), 2884–2887.

(83) Bryant, J. I. Vibrational Spectrum of Sodium Azide Single Crystals. *J. Chem. Phys.* **1964**, *40* (11), 3195–3203.

(84) Parker, S. F.; Refson, K.; Williams, K. P. J.; Braden, D. a; Hudson, B. S.; Yvon, K. Spectroscopic and Ab Initio Characterization of the [ReH9]2- Ion. *Inorg. Chem.* **2006**, *45* (26), 10951–10957.

(85) Mitchell, P. C.; Parker, S. F.; Ramirez-Cuesta, A. J.; Tomkinson, J. The Theory of Inelastic Neutron Scattering Spectroscopy. In *Vibrational Spectroscopy with Neutrons*; World Scientific, 2005; pp 13–65.

(86) Kirchartz, T.; Rau, U. Decreasing Radiative Recombination Coefficients via an Indirect Band Gap in Lead Halide Perovskites. *J. Phys. Chem. Lett.* **2017**, *8* (6), 1265–1271.

(87) Aduev, B. P.; Aluker, É. D.; Belokurov, G. M.; Drobchik, A. N.; Zakharov, Y. A.; Krechetov, A. G.; Mitrofanov, A. Y. Preexplosion Phenomena in Heavy Metal Azides. *Combust. Explos. Shock Waves* **2000**, *36* (5), 622–632.

(88) Paulatto, L.; Mauri, F.; Lazzeri, M. Anharmonic Properties from a Generalized Third-Order Ab Initio Approach: Theory and Applications to Graphite and Graphene. *Phys. Rev. B - Condens. Matter Mater. Phys.* **2013**, *87* (21), 1–18.

(89) Fried, L. E.; Ruggiero, a J. Energy-Transfer Rates in Primary, Secondary, and Insensitive Explosives. *J. Phys. Chem.* **1994**, *98* (39), 9786–9791.

(90) Ye; Koshi, M. Theoretical Studies of Energy Transfer Rates of Secondary Explosives. *J. Phys. Chem. B* **2006**, *110* (37), 18515–18520.

(91) Aynajian, P. *Electron-Phonon Interaction in Conventional and Unconventional Superconductors*; Springer-Verlag: Berlin, 2010.

(92) Bryant, J. I. Vibrational Spectrum of Barium Azide Single Crystals. *J. Chem. Phys.* **1970**, *52*, 4867.

(93) Dlott, D. D. Multi-Phonon up-Pumpng in Energetic Materials. In *Overview of Recent Research on Energetic Materials*; Shaw, R. W., Brill, T. B., Thompson, D. L., Eds.; World Scientific, 2005; pp 303–333.

(94) Colognesi, D.; Celli, M.; Cilloco, F.; Newport, R. J.; Parker, S. F.; Rossi-Albertini, V.; Sacchetti, F.; Tomkinson, J.; Zoppi, M. TOSCA Neutron Spectrometer: The Final Configuration. *Appl. Phys. A Mater. Sci. Process.* **2002**, *74*, 64–66.

(95) Pinna, R. S.; Rudić, S.; Parker, S. F.; Armstrong, J.; Zanetti, M.; Škoro, G.; Waller, S. P.; Zacek, D.; Smith, C. A.; Capstick, M. J.; et al. The Neutron Guide Upgrade of the TOSCA Spectrometer. *Nucl. Instruments Methods Phys. Res. Sect. A Accel. Spectrometers, Detect. Assoc. Equip.* **2018**, *896*, 68–74.

(96) Arnold, O.; Bilheux, J. C.; Borreguero, J. M.; Buts, A.; Campbell, S. I.; Chapon, L.; Doucet, M.; Draper, N.; Ferraz Leal, R.; Gigg, M. A.; et al. Mantid - Data Analysis and Visualization Package for Neutron Scattering and μ SR Experiments. *Nucl. Instruments Methods Phys. Res. Sect. A Accel. Spectrometers, Detect. Assoc. Equip.* **2014**, *764*, 156–166.

(97) Dymkowski, K.; Parker, S. F.; Fernandez-Alonso, F.; Mukhopadhyay, S. AbINS: The Modern Software for INS Interpretation. *Phys. B Condens. Matter* **2018**, *In Press*, 1–6.

Chapter 4

Vibrational Up-Pumping in Some Molecular Energetic Materials

4.1 Introduction

Many commonly used energetic materials (EM) are composed of organic molecules, with well-known examples including 1,3,5,7-tetranitro-1,3,5,7-tetrazocane (HMX), 2,4,6-trinitrotoluene (TNT) and triaminotrinitrobenzene (TATB). These compounds are typically based on similar structural moieties (explosophores), often -NO_2 functionality, or numerous N-N, N-O or C-N bonds. However, despite these structural similarities, organic EMs exhibit a broad range of impact sensitivities. For example, ϵ-CL-20 (HNIW) initiates with only *ca.* 3 J of impact energy,[1] while TATB requires > 122 J for impact initiation.[2] Particularly striking is the difference in impact sensitivity of TNT and picric acid, whose structures differ only in a single substituent on their aromatic rings. Yet, while TNT initiates at *ca.* 40 J,[3] the initiation of picric acid requires approximately half the energy, *ca.* 22 J.[3] As organic EMs are metal-free, they are particularly promising materials from an environmental perspective. Consequently, there has been considerable interest in developing new organic EMs with a broad range of energetic properties, and large libraries of such molecules now exist. The synthesis of novel organic EMs can require very complex and harsh experimental procedures. With no *a priori* knowledge of the physical properties of the final (or indeed intermediate) products, the process is both expensive and potentially very dangerous.

A number of theoretical approaches have so far been developed in an attempt to rationalise the sensitivity of organic EMs (Chapter 1.3).[4] Briefly, these have included the study of electrostatic potentials,[5,6] bond dissociation energies,[7–10] large-scale empirical fitting[11,12] as well as consideration of static and dynamic band gaps.[9,13,14] These methods have offered rationalisation of the impact sensitivity of organic EMs to varying degrees. However, these models do not typically include a physical underlying mechanism to link a mechanical impact and the subsequent conversion of energy into a chemical reaction. Thus, the reasons for a material displaying a particular impact sensitivity remain elusive.

The concept of vibrational up-pumping has been demonstrated experimentally and theoretically for a range of molecular compounds.[15–17] This has led to scattered analyses of energy transfer rates in molecular EMs based on inelastic neutron scattering spectra,[18,19] or bench-top Raman spectra.[20,21] While these early works did suggest strong correlation between sensitivity and energy transfer rates, the data on which they were based was limited, and the models inconsistent. Most notably, the mechanism of up-pumping (overtone[20] or combination[18,19] pathways) and the target region into which up-pumped energy is considered, differ considerably between these models. Up-pumping phenomena have demonstrated capable of localising energy,[17,22] *i.e.* producing 'hot-spots', and therefore offer a fundamental approach to understanding the impact and shock-induced chemistry of EMs.[17]

The theoretical and experimental techniques required to enhance the fundamental understanding of up-pumping models in solids have only recently become available. A very recent study successfully attempted to correlate zone-centre overtone structure with the impact sensitivity of a selection of organic EMs.[23] Having constructed a more complete picture of these processes from first principles in Chapter 3, it is therefore of interest to further develop and apply the model to a more challenging series of organic systems.

4.2 Aims

Following on from the success of the up-pumping model to predict the relative ordering of impact sensitivity for the azide materials, this chapter aims to extend the model to a series of molecular EMs. In doing so, the work in this chapter seeks to:

- Consider the 'band gap' criterion for a series of organic EMs
- Obtain the full vibrational spectrum for a range of organic EMs
- Further develop the vibrational up-pumping mode of Chapter 3 to more complex, large molecule materials.
- Compare and unify overtone- and combination-based up-pumping approaches.

4.3 Model Systems

Typical organic EMs contain a large number of atoms and, common to molecular materials, crystallise in large, low symmetry unit cells. Molecular materials were selected to ensure calculations were computationally tractable, and to ensure that they spanned a broad range of impact sensitivities and structure types. Many of these materials have been studied extensively, although a breadth of impact sensitivities are still reported for the same compound.[24] This pays testament to the difficultly in recording reproducible impact sensitivity data. Where possible, experimental values of h_{50} were selected – *i.e.* the drop height at which 50% of tests result in initiation (Chapter 2.2.3), and a summary of common literature impact sensitivities is given in Table 4.1.

Table 4.1: Experimental impact sensitivities (IS). Values of h_{50} correspond to the height (cm) from which a 2.5 kg weight is released. The corresponding energy is quoted as E_{50} (*J*). Sensitivities based on unknown testing criteria are labelled as UTC. These may represent h_{50} or the limiting impact value.

Material	Acronym	IS (h_{50}) /cm	IS (E_{50}) /J	IS (J). UTC	Ref.
Triacetonetriperoxide	TATP	--	--	0.3	25
1,1'-azobistetrazole	ABT	--	--	< 1	26
Hexanitrobenzene	HNB	11	2.75	--	27
1,3,5,7-Tetranitro-1,3,5,7-tetrazocane	HMX	32	8	--	1
		29	7.25		2
		26	6.5		2
5,5'-Hydrazinebistetrazole	HBT	--	--	> 30 J	28
1,1-Diamino-2,2-dinitroethene	FOX-7	126	31.5	--	29
Nitrotriazolone	NTO	291	72.75	--	2
Triaminotrinitrobenzene	TATB	490	122.5	--	2

The trend in experimental impact sensitivities adopted in this work, which will be used to assess the output of the computational model, is based on the following literature observations:

1. TATB is widely acknowledged to be insensitive to impact.[4] Most reports state its impact sensitivity to be 'immeasurable'. Only a single source suggests TATB to have a sensitivity of *ca*. 50 J,[24] although no indication for the origin or experimental methodology for this value was reported.
2. NTO is also generally well regarded as a highly insensitive material.[24]
3. Despite discrepancies in the sensitivity value (ranging from *ca.* 20-50 J),[24] it is well accepted that α-FOX-7 is less sensitive than β-HMX.[24]
4. HNB is well known to be a highly sensitive compound, and more sensitive than β-HMX.[29]

The trend used in this work therefore follows as ABT > HNB > HMX > HBT > FOX-7 > NTO ≈ TATB. It is worth noting that ABT sensitivity is not quoted as an h_{50} statistical value; the quoted value may thus be the limiting sensitivity value. Due to the size of the TATP unit cell, it is considered only at the end of this chapter. It is the most sensitive of all the materials explored here.

The unit cell and molecular structure of each material is given in Figure 4.1

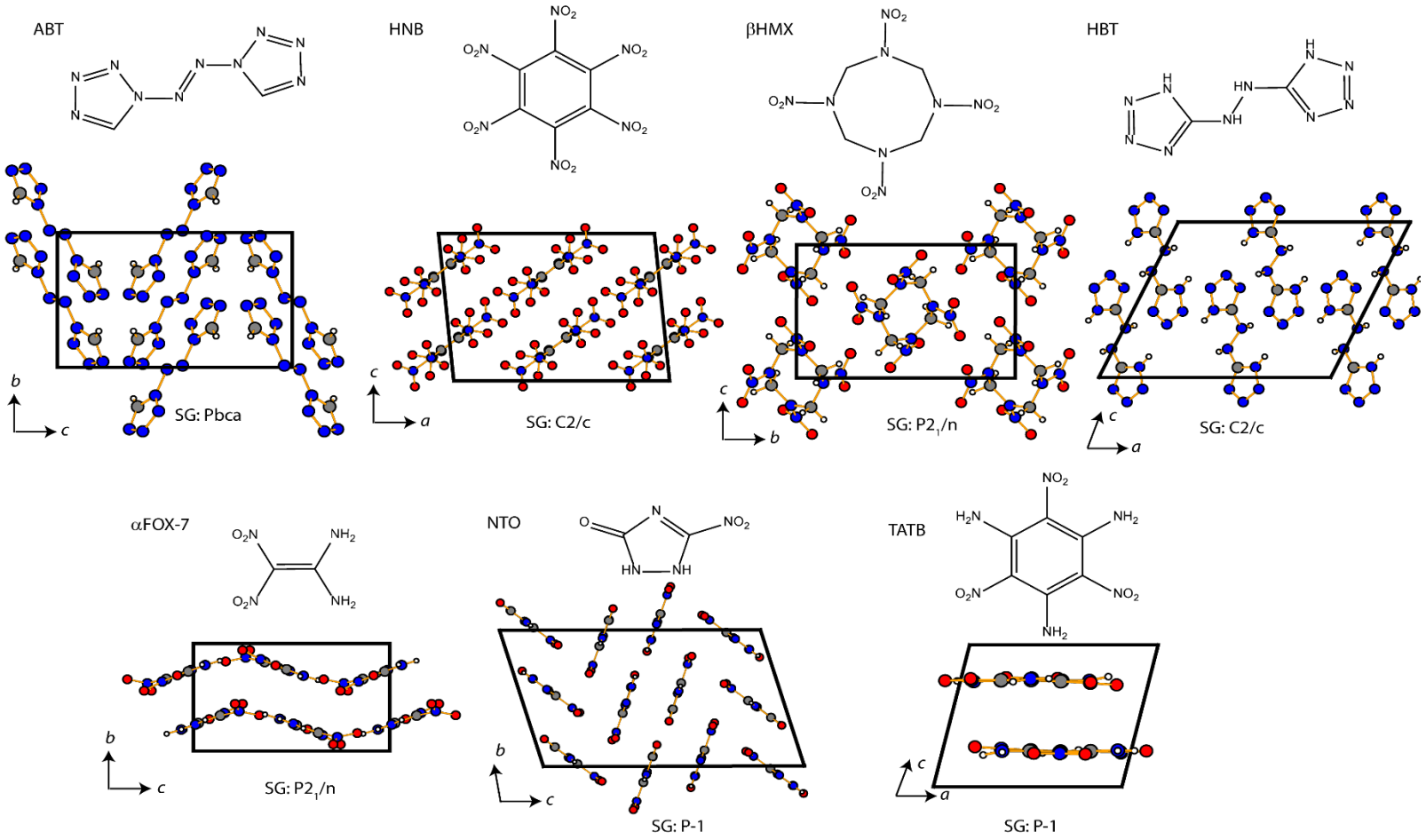

Figure 4.1: Molecular diagrams and crystallographic unit cells for the organic EMs used in this work. The space group (SG) is shown in each case. The structure of TATP is considered independently in Section 4.5.3.4.

4.4 Methods

Sample Preparation.

NTO synthesis. 3-nitro-1,2,3-triazol-5-one (NTO) was prepared by nitration of TO (prepared by Dr. S. Kennedy, School of Chemistry, University of Edinburgh), according to Scheme 4.1.[30] TO (*ca.* 5 g, 60 mmol) was dissolved in excess concentrated nitric acid (70%), and held at 55 ^{o}C for *ca.* 45 minutes. The nitration was quenched in an ice bath, filtered and rinsed in ice water. Purity was verified by X-ray powder diffraction.

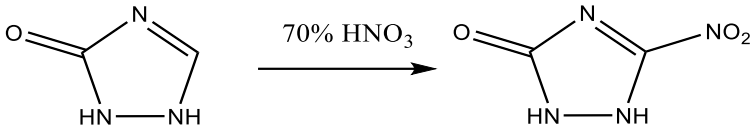

Scheme 4.1: Synthetic approach for the synthesis of NTO.

Synthesis of FOX-7. Preparation of 1,1-diamino-2,2-dinitroethene (DADNE, FOX-7) followed from Scheme 4.2.[30] 2-methyl-4,6-pyrimidinedione (6.0 g, 0.05 mol) was dissolved in concentrated H_2SO_4 (95%, 45 mL), at temperatures < 30 ^{o}C. Concentrated HNO_3 (99%, 20 mL) was subsequently added dropwise, maintaining temperatures < 20 ^{o}C, and the sample stirred for 3 hours. The resulting material was rinsed in concentrated H_2SO_4, added to deionized water (100 mL) and stirred for 2 hours. The resulting product was analysed by ^{1}H and ^{13}C NMR in DMSO, and subsequently by X-ray powder diffraction.

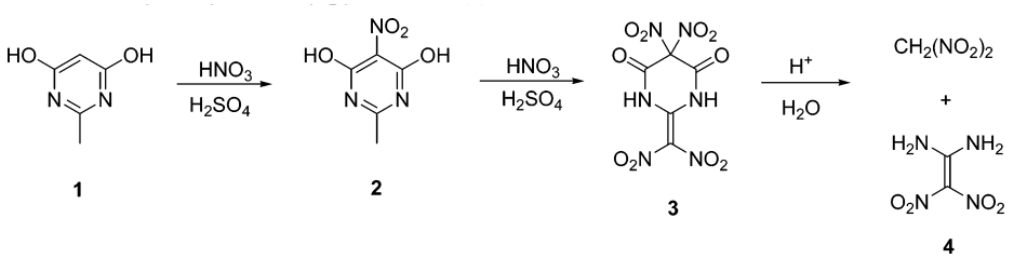

Scheme 4.2: Synthetic approach for preparation of FOX-7.

TATB and β -HMX. Samples of these materials were taken from available stock. β-HMX was provided by the Cavendish Laboratories, University of Cambridge. TATB was synthesised by C. Henderson (School of Chemistry, University of Edinburgh). Samples were used as provided, without further purification.

Condensed Matter Calculations.

The PBE-D2 scheme has been previously demonstrated to work very well for molecular energetic materials.[31–33] It was therefore chosen as a starting point for the calculations presented here. All input structures were taken from the Cambridge Crystallographic Database (CCDC): β-HMX (Ref: OCHTET15[34]), α -FOX-7 (Ref: SEDTUQ03[35]), NTO (Ref: QOYJOD06[36]), HNB (Ref: HNOBEN[37]), ABT (EWEYEL[26]), HBT (TIPZAU[28]), TATB (TATNBZ[38]) and TATP (HMHOCN07[39]). Optimisation was performed using plane wave DFT as implemented in CASTEP v16.[40] The electronic wavefunction was expanded in plane waves to a kinetic energy of 1800 eV for all systems, except HBT (cut-off 1600 eV), and β-HMX, TATB and TATP (cut-off 1300 eV). Forces were converged to $< 5 \times 10^{-4}$ eV/ Å, and stresses to $< 5 \times 10^{-4}$ GPa. The energy change per atom was converged to $< 1 \times 10^{-9}$ eV/atom. The resulting unit cell parameters are given in Table 4.2. In all cases, norm-conserving pseudopotentials were used, as were available within the CASTEP v16 software package. All phonon calculations were based on the primitive unit cells. Phonon calculations were performed using the linear response method to calculate the dynamical matrices on a regular grid of wave vectors, and Fourier interpolated to a fine grid of > 150 points for generation of phonon density of states (DOS, $g(\omega)$). Phonon dispersion curves were generated by Fourier interpolation of the computed dynamical matrices along high symmetry paths as proposed by SeeKPath[41] and labelled by IUPAC convention. For TATP, only the zone-centre phonons were calculated.

Electronic band structures were calculated in CRYSTAL17[42] using localised basis sets, available from the CRYSTAL17 database and selected due to previous success with similar materials and DFT functionals (H- H_pob_TZVP_2012[43]; C- C_m-6-311G(d)_Heyd_2005[44]; N- N_m-6-311G(d)_Heyd_2005[44]; O- O_m-6-311G(2d)_Heyd_2005[44]. To ensure closest reproduction of experimental results, all calculations were performed on the experimental geometries. The band structures were calculated using the HSE06,[44] B3PW91[45] and PBE[46] functionals. For all materials, the tolerances (TOLINTEG) were set at 7 7 7 9 30 (as recommended for use with these basis sets[44]). The electronic structure was sampled across a regular grid of points, with *ca.* 120 points sampled in each material.

Inelastic Neutron Scattering Spectroscopy. All INS spectra were collected using the TOSCA spectrometer at the ISIS Neutron and Muon source.[47,48] Samples (*ca.* 1.5 g) were placed in aluminium sample holders. Samples were cooled to *ca.* 10 K and collected for a total of *ca.* 400 μAh. The sample temperature was subsequently heated in steps of 50 K to a maximum of 200 K for β-HMX and TATB, and 150 K for α-FOX-7. Data were collected at each 50 K interval. Both forward and back-scattered data were summed and corrected for scattering from the sample holder and background. All data processing was done using Mantid.[49] Simulated INS spectra were generated using ABINS,[50] as implemented in Mantid. Only first order quantum events (*i.e.* the fundamentals) are considered in the simulation of INS spectra.

Density of States. All $g(\omega)$ are inherently normalized to $3N$. Consistent with the 'indirect' up-pumping model (*i.e.* where up-pumped energy thermalises across the internal vibrational manifold), the two-phonon density of states, $\Omega^{(2)}$ is normalized by $\int (g(\omega))$. This follows the procedure suggested previously for the treatment of molecular materials.[19,23]

Table 4.2: Optimised unit cell parameters for the molecular EMs studied here using the PBE-D2 functional. The error in total volume is given with respect to the experimental volume. Low temperature data are used where available. Where conventional cells are non-primitive, the primitive cell is also displayed.

		a	*b*	*c*	α	β	γ	*V*	dV/%
ABT^{exp}	*Pbca*	8.352	6.793	11.614	90	90	90	658.962	
ABT^{calc}		8.354	6.789	11.618	90	90	90	658.931	-0.004%
HNB^{exp}	*C2/c*	13.220	9.130	9.680	90	95.500	90	581.490	
HNB^{exp}	*P(C2/c)*	9.046	9.046	9.680	62.280	62.280	60.620	581.492	
HNB^{calc}		9.028	9.028	9.771	62.444	62.444	59.981	582.977	+0.26%
β-HMX^{exp}	*P2$_1$/c*	6.525	11.024	7.362	90	102.642	90	516.675	
β-HMX^{calc}		6.624	11.256	7.373	90	102.222	90	537.299	+4.00%
HBT^{exp}	*C2/c*	12.401	5.513	9.835	90	115.570	90	606.565	
HBT^{exp}	*P(C2/c)*	6.786	6.786	9.835	113.230	113.230	47.940	303.283	
HBT^{calc}		6.706	6.706	9.724	111.837	111.837	49.440	303.075	-0.07%
α-FOX7^{exp}	*P2$_1$/n*	6.934	6.622	11.312	90	90.065	90	519.470	
α-FOX7^{calc}		7.089	6.623	11.440	90	91.273	90	530.898	+2.20%
NTO^{exp}	*P-1*	5.123	10.314	17.998	106.610	97.810	90.130	902.060	
NTO^{calc}		5.159	10.461	17.686	107.247	97.777	90.056	902.450	+0.04%
TATB^{exp}	*P-1*	9.010	9.028	6.812	108.580	91.820	119.970	442.524	
TATB		9.128	9.142	6.767	109.012	92.097	119.936	448.784	+1.41%
TATP^{exp}	*P2$_1$/c*	11.964	14.038	15.595	90	117.270	90	2327.700	
TATP^{calc}		11.913	13.811	15.415	90	117.243	90	2255.047	-3.12%

4.5 Results and Discussion

4.5.1 Electronic Structure

For large systems, the use of high level functionals such as HSE06 are computationally demanding. It has been shown that the hybrid GGA functional B3PW91 is somewhat cheaper, and offers excellent agreement with experimental results for electronic band gap (E_g) prediction across a broad range of inorganic materials.[51,52] It was therefore of interest to consider these two methods for application to molecular materials, and compare to a standard GGA functional, PBE. Only limited experimental data is available for E_g for the materials studied here. Experimental UV-Vis spectra have been documented for β-HMX.[53] While the fundamental band gap (*i.e.* the difference between the ionization potential and electron affinities) is in principles different to the optical band gap (which is stabilized by electron-hole interactions), the discrepancy is often small in solid state materials,[54] and hence the UV-Vis spectra should offer a good indication as to the validity of the calculated E_g values. Furthermore, it should be noted that α-FOX-7 and TATB are both yellow powders, with the former being more strongly coloured. This indicates an optical transition in the region of *ca.* 2.6 eV for both materials.

The values of E_g calculated for the series of molecular energetic compounds are given in Table 4.3 (Note TATP was omitted from this part of the study as the large unit cell renders the band structure calculation intractable). The B3PW91 functional consistently predicts values of E_g that are slightly higher than HSE06 results, ranging from E_g(HSE06)+0.24 eV to E_g(HSE06)+0.32 eV. Hence it appears that on average, the B3PW91 results should be within the same approximate accuracy as the HSE06 results for related systems. As is expected, the PBE calculations return considerably lower E_g values than the higher level functionals. Literature values for PBE-based calculations in Table 4.3 differ only slightly from those calculated here. This is most notable for β-HMX, although literature reports are based on plane-wave basis sets (which contrasts with the localised basis sets used in this work). In all cases, the G_0W_0

calculations found in the literature suggest a larger band gap than calculated by either B3PW91 or HSE06. Given the limited experimental values, and noting the colour of the TATB and FOX-7 materials, it can be inferred that G_0W_0 quasi-particle methods may be overestimating the values of E_g. This has been demonstrated previously for inorganic systems.[51]

As was noted for the azide materials in Chapter 3, there is no visible trend in the band gap values and the reported impact sensitivity of these compounds. Based on the B3PW91 or HSE06 calculations, the predicted sensitivity ordering would be NTO > α-FOX-7 ≈ HNB ≈ TATB > ABT > β-HMX > HBT. This is clearly incorrect when compared to experimental sensitivity ordering. Moreover, the agreement with the experimental ordering worsens if the values from G_0W_0 are considered. As was also observed for the azide materials, there is no evidence of any correlation between sensitivity and a material having a direct or indirect band gap.

Table 4.3: Fundamental electronic band gaps (E_g) in the crystalline molecular energetic materials, arranged in order of decreasing impact sensitivity. All values calculated here are based on a localised basis set. E_g are labelled as direct (D) or indirect (I) band gaps.

Material	*B3PW91*	*PBE*	*HSE06*	*Lit. Calc*	*Lit. Exp.*
ABT	5.0317 (I)	2.9982 (I)	4.7882 (I)	--	--
HNB	3.9433 (I)	2.1040 (I)	3.6887 (D)	--	--
β-HMX	5.4954 (D)	3.6826 (I)	5.2176 (D)	7.21,≠ [a] 4.66 ^[a]	5.32*
HBT	5.9569 (I)	4.2069 (I)	5.6364 (I)	--	--
α-FOX-7	3.9833 (I)	2.4483 (I)	3.6719 (I)	5.1,≠,[b] 2.2,^,[c] 1.9^,[b]	--
NTO	3.5024 (I)	2.1027 (D)	3.1892 (I)	--	--
TATB	3.9824 (I)	2.6334 (I)	3.6599 (I)	4.66,≠ [a] 2.52^[a]	--

≠ G_0W_0 from (a) Ref [55] (b) Ref [56]; ^ PBE from (a) Ref [55] (b) Ref [57] (c) Ref [58]; * From Ref [53] based on UV-Vis spectroscopy.

4.5.2 Vibrational Structure of Some Organic Energetic Materials

Following from the theory presented in Chapter 3, the vibrational structure of the molecular materials was considered. The full phonon dispersion curves

were calculated along the high symmetry lines of the Brillouin zones and are given in Figure 4.2. As expected for molecular materials, it is generally seen that the branch dispersion is relatively small across the Brillouin zone, and almost negligible for the internal vibrational modes.

Slight instabilities are observed in the phonon dispersion curves of both NTO and HNB, with frequencies of the lowest acoustic branch becoming negative at a small set of wave vectors. Unfortunately, no attempts to rectify this were successful. As both compounds are stable, this is unlikely to be indicative of dynamic instability of the structures, but rather more likely to be attributed to a slight numerical error in the calculated structures. However, this is not expected to result in any marked effect on the remaining vibrational structure.

As a means to assess the ability of DFT to model the vibrational structure for these types of compounds, experimental INS spectra for a subset of the test compounds were collected. Calculated phonon dispersion curves were then used to simulated INS spectra for direct comparison.

The simulated INS spectra for the most sensitive compound, β-HMX, Figure 4.3, generally shows good agreement with experiment. The frequencies of the lowest region of the INS spectrum are well reproduced, with the calculated Ω_{max} underestimated by only *ca.* 5 cm^{-1}. There appears to be a *ca.* 20 cm^{-1} systematic underestimation of the vibrational frequencies in the $\omega > 200$ cm^{-1} region of the spectrum. The intensities are not well reproduced for the lowest frequency modes, which suggests some error surrounding the exact structure of the β-HMX phonon modes, or textured powder. In contrast, comparison of the simulated and experimental INS spectra for α-FOX-7, Figure 4.3, shows excellent agreement. While the frequencies are well reproduced based on the zone-centre structure, increased sampling of the Brillouin zone is required to obtain accurate intensities. By 0.08 Å^{-1}, the full INS spectrum is very well reproduced by simulation.

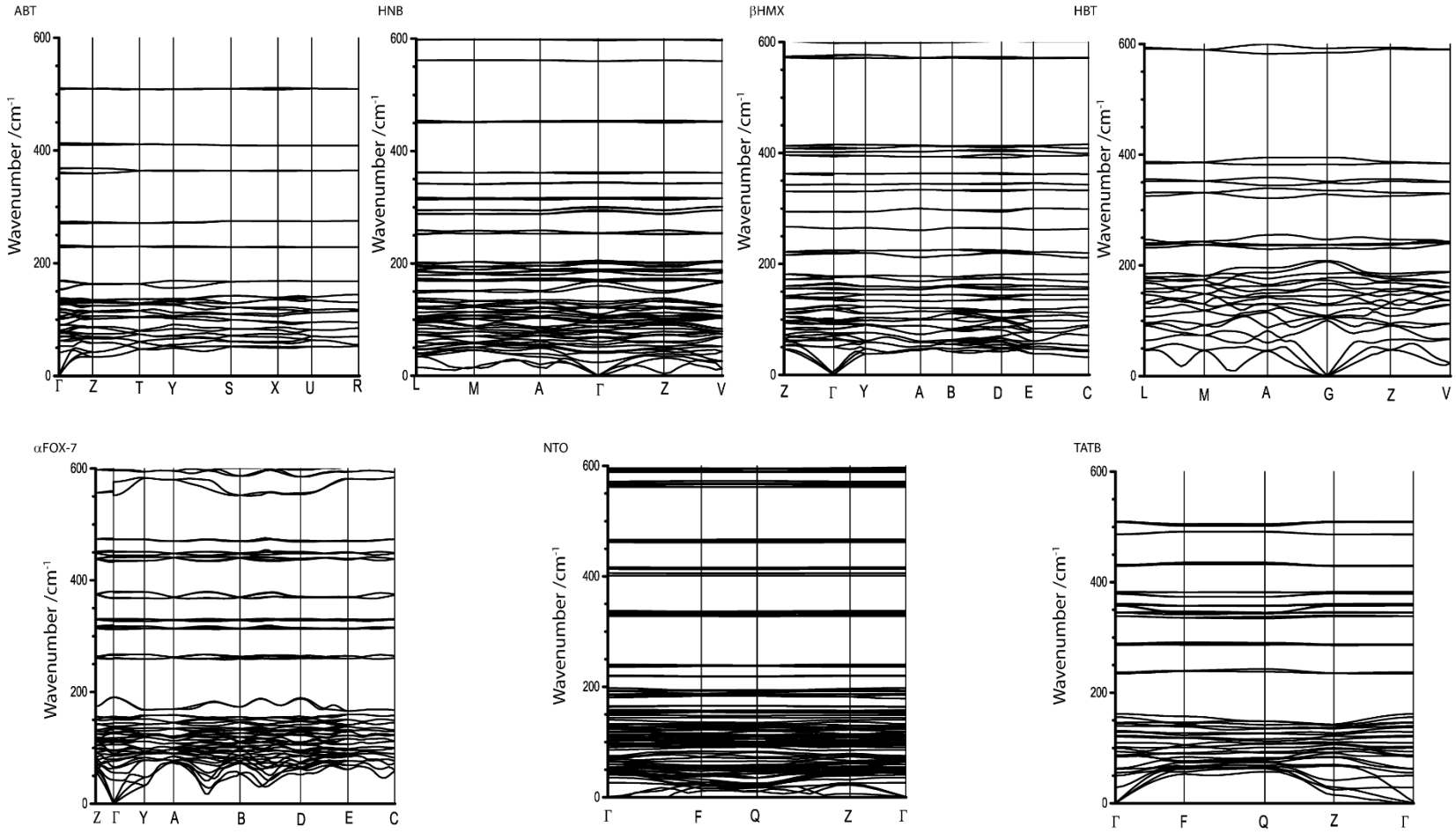

Figure 4.2: Phonon dispersion curves for the molecular EMs discussed in this work. Wavenumber is truncated at 600 cm^{-1} to allow visualisation of the low frequency modes that are important in this work.

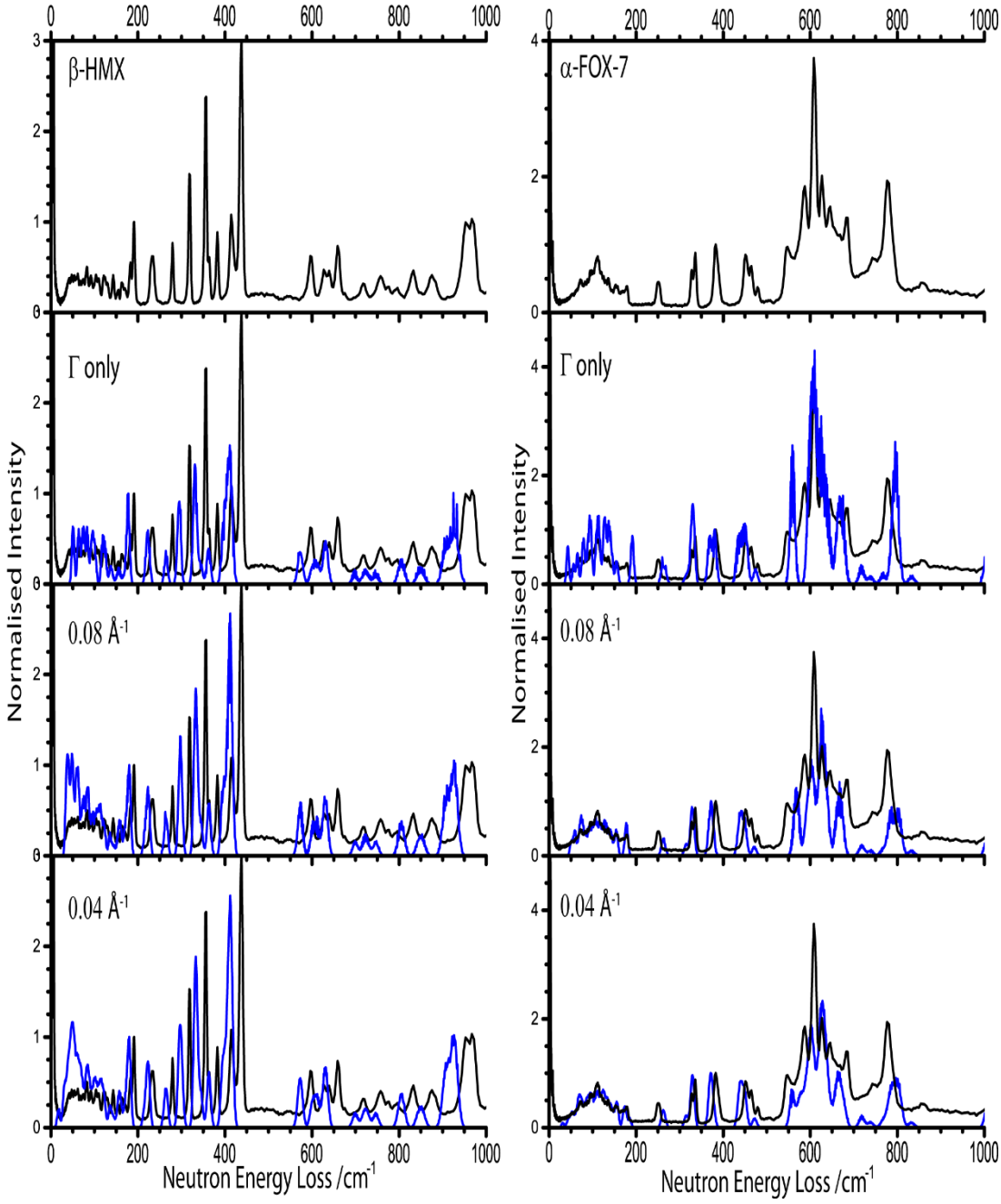

Figure 4.3: Inelastic neutron scattering spectra for β-HMX and α-FOX-7 at 10 K. The experimental pattern (black) is given in comparison to (blue) simulated INS spectra at three different sampling densities of the Brillouin zone. Only the first quantum events are simulated.

For NTO the simulations are an excellent reproduction of the experimental INS spectra, Figure 4.4, despite the small instability (negative frequencies) reported above. Both the intensities and frequencies appear well reproduced across the spectrum, particularly when a dense grid of phonon wave vectors

is used. This strongly suggests that this minor instability has negligible influence on the vibrational structure. The INS spectrum of TATB is also well reproduced, Figure 4.4, but there does appear to be a slight disagreement between the higher frequency vibrational modes at *ca.* 800 cm^{-1}. Internal modes in this region are primarily NH_2 twisting modes. Overall, however, the spectrum is very well reproduced in both frequencies and intensities.

In contrast to the case of α-NaN_3 presented in Chapter 3, INS spectra simulated from zone-centre calculations generally perform well in reproducing both the frequencies and relative intensities observed in the experimental INS spectra of the organic molecular materials. The notable exceptions to this are the lowest frequency lattice modes, which appear to converge to the experimental spectra when the Brillouin zone is sampled at *ca.* 0.04 $Å^{-1}$. Increasing the density of *q*-point sampling for simulation of the INS spectra has negligible effect on frequencies above *ca.* 200 cm^{-1}. These features are presumably due to both the minimal dispersion observed across the Brillouin zone (Figure 4.2), as well as the dominant incoherent scattering of the hydrogen in these materials. Overall, it does appear that the vibrational structure of these molecular materials is well reproduced by the simulations, particularly in the low frequency regions. DFT therefore appears capable of producing an accurate description of not only the zone-centre frequencies, but of the dispersion relationship through the Brillouin zone for these types of materials. The vibrational structures used herein can therefore be taken as representative of the true materials.

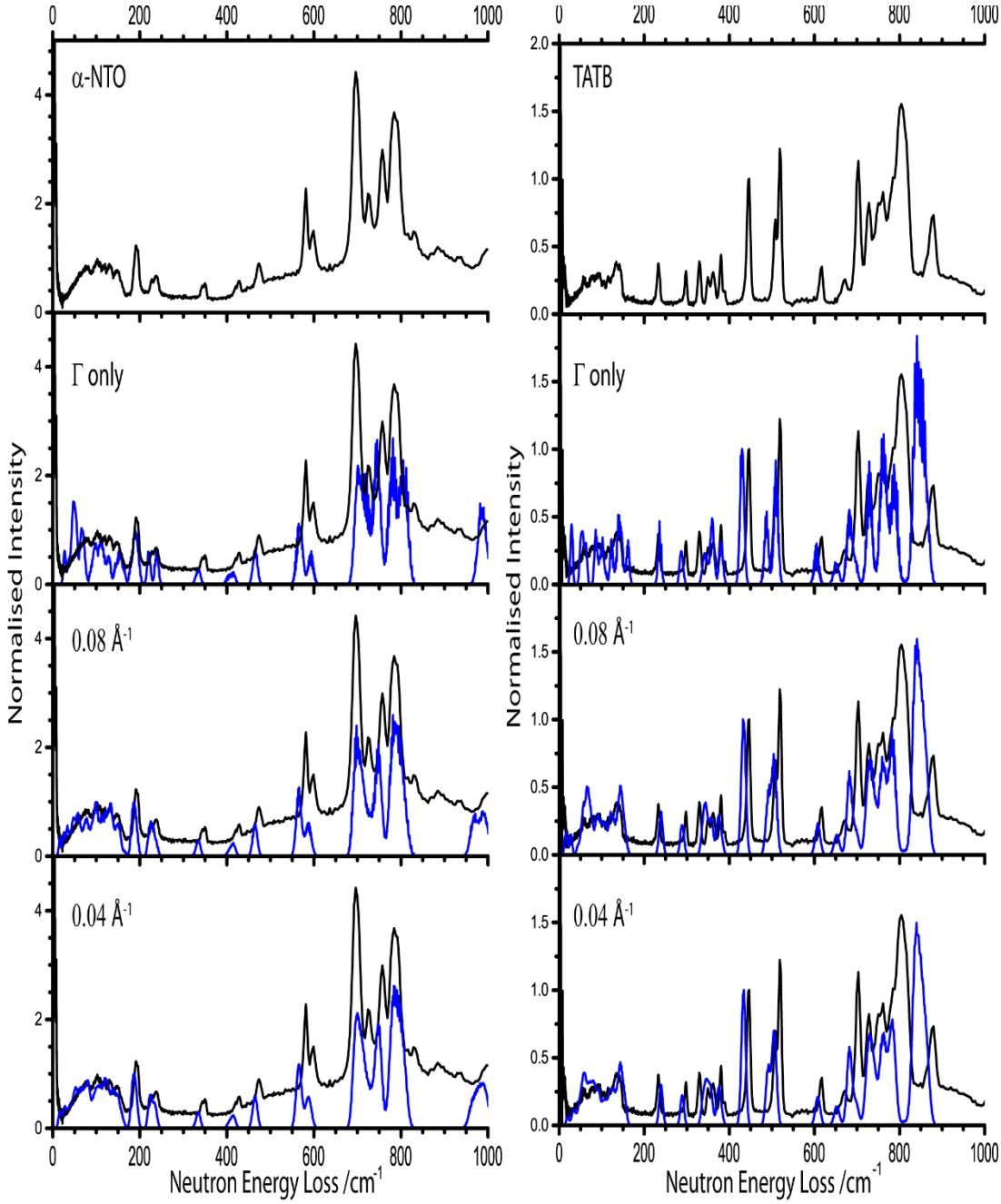

Figure 4.4: Inelastic neutron scattering spectra for NTO and TATB at 10 K. The experimental pattern (black) is given, in comparison to (blue) simulated INS spectra at three different sampling densities of the Brillouin zone. Only the first quantum events are simulated.

4.5.3 Vibrational Up-Pumping in the Molecular Energetic Materials

Prior to considering the vibrational up-pumping in the molecular EMs, it is again necessary to segment the vibrational spectra into sections based on integer values of Ω_{max}. The definition of Ω_{max} stated in Chapter 3 is somewhat less clearly defined when considering the molecular materials. A good example of this is NTO. Across the phonon density of states (DOS, $g(\omega)$) there are clear minima near the top of the phonon region which, when compared to the phonon dispersion curves in Section 4.5.2, do correlate to regions of gaps, albeit small, in phonon density. The non-zero values of $g(\omega)$ result from the applied Gaussian broadening on generation of the DOS. Previous works have suggested that in such cases, the top of the phonon bath should be taken to include (nearly) amalgamated NO_2 rocking modes,[19,20,23] and therefore act as the upper limit of the phonon region. For NO_2 containing compounds, these modes are shown in Table 4.4. However, the DOS and phonon dispersion bands clearly indicate a frequency gap between the top of a semi-continuum and the highest -NO_2 rocking modes at *ca.* 230 cm^{-1}. These highest rocking modes therefore do not fit within the continuum criteria for defining the phonon bath. Where appropriate, consideration is given for Ω_{max} placed in both locations for NTO. Note that the potential Ω_{max} at 170 cm^{-1} indicated by the INS spectra is not considered further as it is lost due to the addition of Gaussian broadening in the calculated spectra, which is added to reflect resonant states.[20,23] This leads to the placement of Ω_{max} as highlighted in Figure 4.5 and reported in Table 4.4.

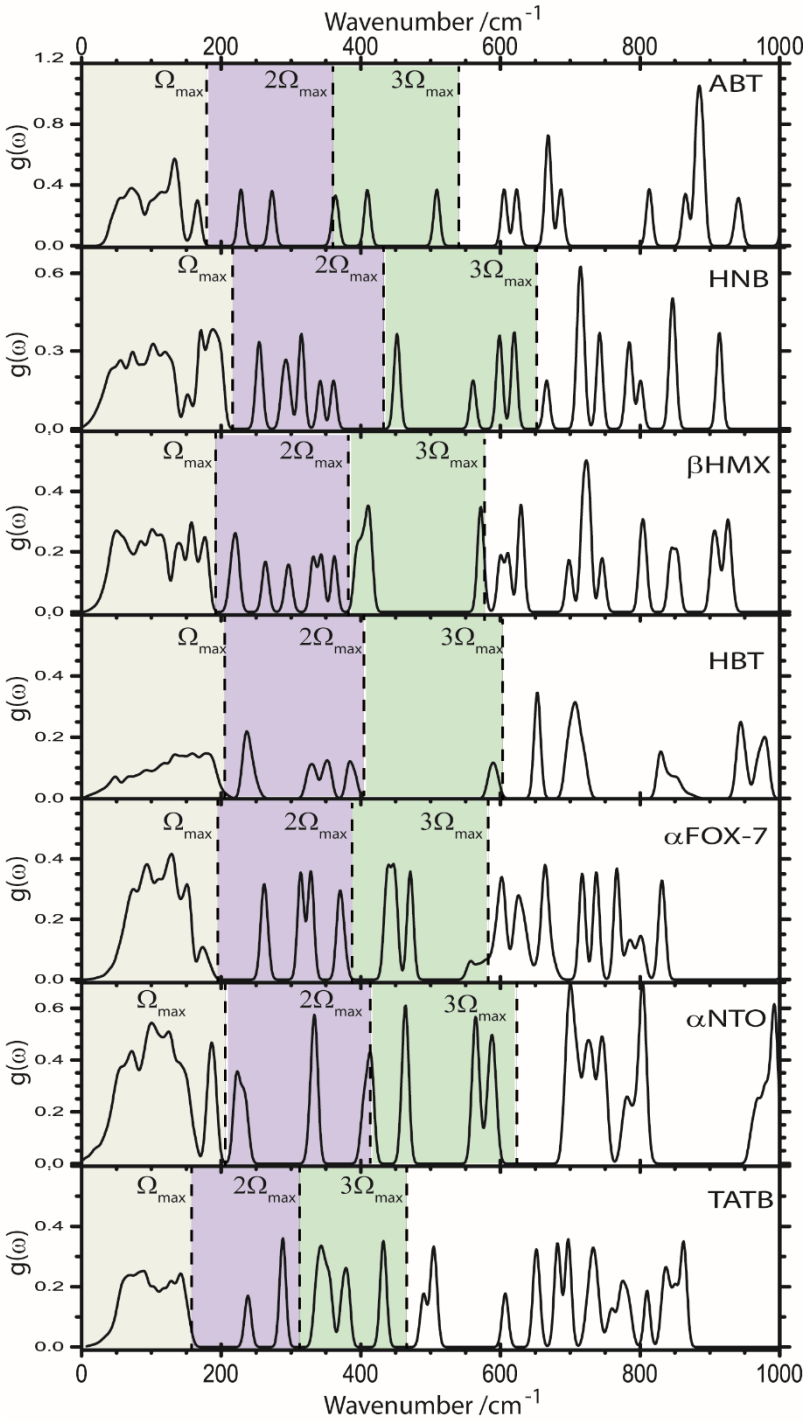

Figure 4.5: Vibrational density of states ($g(\omega)$) for the molecular energetic materials arranged in order of decreasing impact sensitivity. The segments of integer values of Ω_{max} are indicated in each case.

Table 4.4: Vibrational structure (cm^{-1}) of the molecular energetic compounds. The top of the phonon bath Ω_{max}, first doorway mode ω_d, and frequency gap ($\Delta\omega_d = \omega_d - \Omega_{max}$).

	NO_2 rock max	**Ω_{max} (INS)**	**Ω_{max} (CALC)**	**ω_d**	**$\Delta\omega_d$**
ABT	--	--	175	220	45
HNB	200	--	210	245	35
β-HMX	166	195	193	210	15
HBT	--	--	200	225	25
α-FOX-7	155	183	185	255	70
NTO	240	170,202,245	200/240	220 / 325	20/85
TATB	155	155	160	234	74

The decomposition pathways of molecular energetic materials are complex[59,60] and remain largely unknown. Compared to the structurally simpler azide compounds discussed in Chapter 3, it is highly probable that many normal modes are simultaneously required to initiate the decomposition of these large molecules. It is therefore unlikely that a direct up-pumping mechanism (*i.e.* energy localisation into a single vibration, and immediate bond rupture) occurs. Rather, it is more likely that an indirect (or *thermal*)[61] mechanism occurs, whereby the excited molecule reacts at some point following evolution of the highly excited vibrational state.[17] The redistribution of vibrational energy within the internal molecular vibrational manifold is relatively quick, and once energy reaches this manifold it can quickly redistribute. In contrast to the azide systems, the rate determining step is instead taken to be the transfer of energy from the phonon manifold into the internal vibrational manifold.[20,23] This occurs in two steps: (1) population of the doorway modes (*i.e.* modes with $\Omega_{max} < \omega < 2\Omega_{max}$) and (2) population of higher-lying modes.[61]

The concept of the 'target' frequency, ω_T, is therefore no longer meaningful, as there is not a single (or known subset) of vibrational modes into which shock wave energy must be localised to induce a chemical response. Hence, it is no longer appropriate to consider the 'frequency gap' criterion based on $\Delta\omega = \omega_T - \Omega_{max}$. Instead, this simple criterion can be recast as $\Delta\omega = \omega_d - \Omega_{max}$, where ω_d is the first doorway mode. If this assessment is made based on the

full phonon dispersion curves, the resulting sensitivity ordering follows that shown in Figure 4.6. If Ω_{max} for NTO is taken to be 238 cm^{-1} (*i.e.* the top of the -NO_2 rocking modes) only a very weak correlation is observed. The more sensitive compounds tend to have smaller values of $\Delta\omega$ than the less sensitive materials. This trend is more apparent if the energetic materials with explosophoric -NO_2 moieties are instead considered in isolation, and may therefore suggest additional electronic factors may be important in determining sensitivity ordering (red symbols in Figure 4.6). However, while this correlation may be indicative from an initial screening perspective, it is greatly limited beyond a very rough energy classification perspective.

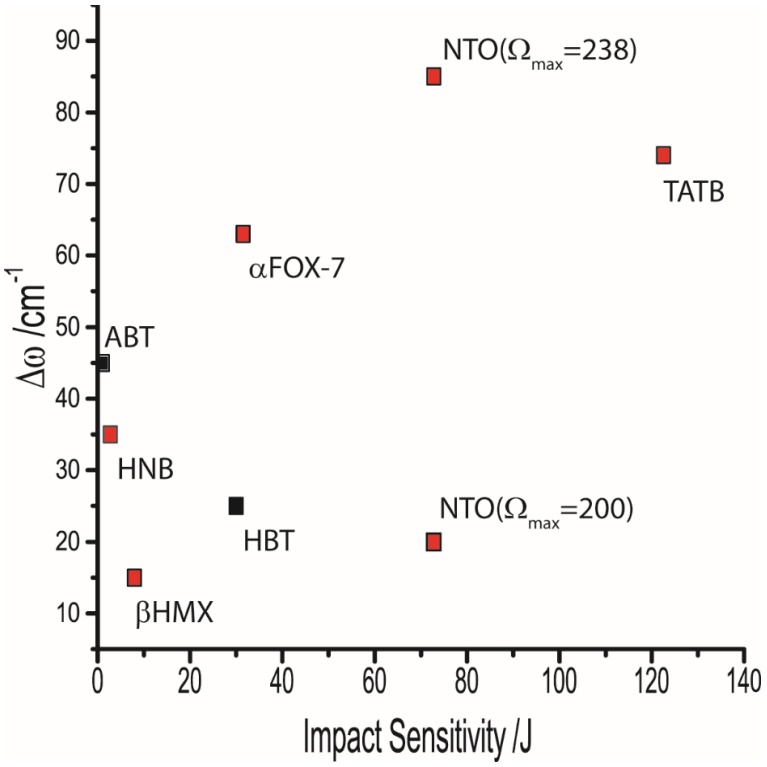

Figure 4.6: Predicted sensitivity order based on the vibrational frequency 'energy gap' criterion, distinguishing between compounds containing -NO_2 groups (red squares) and those that do not (black squares).

Noting that the up-pumping model relies initially on the rate of excitation of the doorway frequencies, an alternative qualitative correlation can be sought between the doorway density and impact sensitivity. If this is instead considered, there does appear to be a good overall correlation with sensitivity,

Figure 4.7. The more sensitive compounds contain a higher density of doorway modes in the range $\Omega_{max} \rightarrow 2\Omega_{max}$, with the less sensitive compounds exhibiting lower densities of states within this region. The notable exception to this rule is ABT. The chemical structure of ABT is considerably different from the remaining compounds studied here, and again it can be suggested that electronic effects dominate in dictating the different sensitivity of this compound.

While this method does not offer high resolution of the sensitivity ordering (that is, that α-FOX-7 is predicted to be more sensitive than β-HMX), it does offer a relatively rapid, qualitative approach to the general classification of these materials once vibrational frequencies have been obtained (by calculation or experimental means).

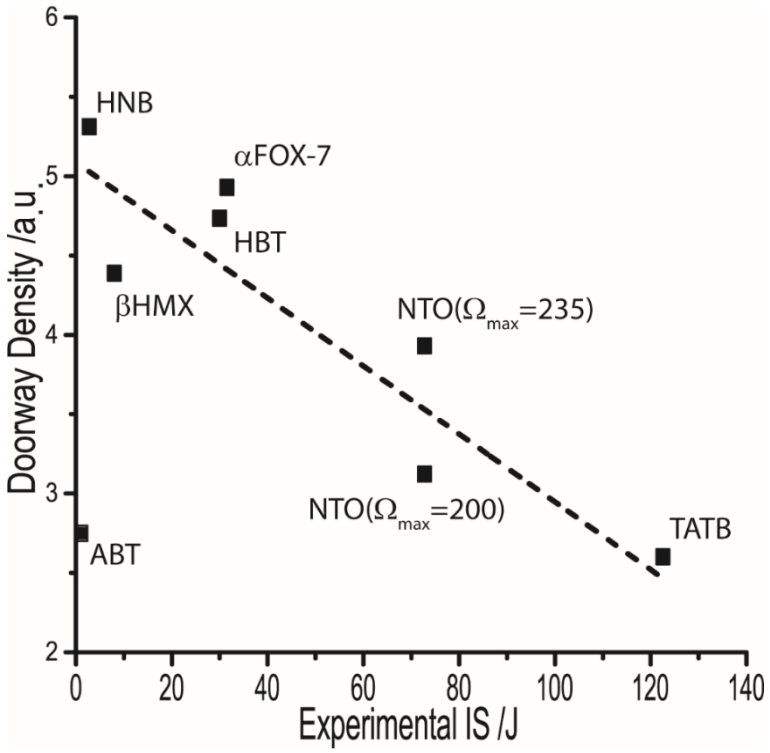

Figure 4.7: Comparison of doorway density of states and experimental impact sensitivities. Doorway densities are normalized by *3N* to account for variations in the normalization of the DOS.

While the qualitative trends suggested above do display some promise in their ordering of the impact sensitivity of these molecular compounds, they do not offer much by means of a physical mechanism. Hence, it is worthwhile

returning to discussion of the up-pumping methodology employed in Chapter 3.

The major difference in the present case, compared to the azide series, is the lack of a well-defined target frequency, ω_T. For the present, ignoring any explicit consideration of temperature, the model in this section makes the following assumptions:

1. Overtone pathways are responsible for the initial transfer of energy.[61] Energy transfer *via* the first overtone is considerably faster than by higher order overtones, and hence the region up to $2\Omega_{max}$ quickly becomes populated. This leads to the definition of the doorway modes as having frequencies, $\Omega_{max} < \omega < 2\Omega_{\max}$.
2. Initial energy transfer that results from overtone up-pumping into the doorway modes can subsequently up-pump *via* combination pathways.
3. It follows from (2) that combination pathways are limited to the excitation of modes below a maximum of $3\Omega_{max}$. That is to say that mode combinations can further populate other, higher frequency doorway modes, or they can populate higher frequency internal modes. Secondary combination pathways, including vibrational cooling, are not considered.
4. The energy up-pumping model is based on the total *number* of available pathways.
5. Overtone pathways lead to initial excitation of the vibrational manifold to a maximum of $2\Omega_{max}$ from the first set of overtones. The second overtone can excite to a maximum of $3\Omega_{max}$ albeit at a slower rate. Higher order processes may occur at even lower rates, but are not competitive. This is due to the rapidly decreasing probability of higher order scattering events.[22]
6. The population of the phonon bath is assumed to remain constant, and the contributions of overtones and combinations are taken as being fully separable: *i.e.* they do not compete. This holds approximately for the initial energy transfer step.[61]

Hence, the total energy transfer into the molecular vibrational region is again dominated by the fastest combination and overtone processes.

Due to the markedly different molecular and crystallographic structures of these materials, the two phonon density of states is recast as:

$$\Omega^{(2)} = \rho(\omega)^{-1} \int d\omega \, \delta(\omega_1 - \omega_2 - \omega_3)$$

Equation 4.1

where $\rho(\omega)$ is the total density of states. This has the effect of normalising the up-pumping contribution by $3N$ and reflects the dissipation of up-pumped energy into the internal vibrational manifold. Furthermore, noting that up-pumped energy is only meaningful if a real vibrational state exists at the resulting energy, $\Omega^{(2)}$ is projected onto $\rho(\omega)$, generating the projected two-phonon density of states, P($\Omega^{(2)}$). As the latter was generated with a Gaussian broadening of 10 cm^{-1}, this process accounts for potential resonance pathways.[20,23]

4.5.3.1 Overtone Pathways

It has been previously suggested that overtone pathways are sufficient to model the relative up-pumping rates in molecular energetic compounds.[20,23] Most recently, based solely on zone-centre vibrational frequencies (*i.e.* not accounting for the varying density of states across the Brillouin zone), Bernstein suggested that Ω_{max} should be placed at 200 cm^{-1} for all molecular compounds, and up-pumping into the region 200-700 cm^{-1} should be considered. Earlier suggestions have imposed the restriction of Ω_{max} at 250 cm^{-1}.[20] The suggestion of a 700 cm^{-1} cap appears to have propagated from early experimental work (which placed a limit at 600 cm^{-1}).[19] However, this experimental work employed this limit artificially, as it was the upper limit of experimental resolution at the time. No alternative explanation has yet been provided for this upper boundary limit. Within the framework of the model proposed in Chapter 3, these previous works exhibit two major flaws:

1. Table 4.4 shows that the limiting value of the phonon bath cannot always be taken to be 200 cm^{-1}. This is particularly notable in cases such as TATB, with a well-defined $\Omega_{\max}$ at 160 cm^{-1}.
2. There is no physical rationale for limiting up-pumping to 700 cm^{-1}, particularly when higher order overtones are considered, as has previously been done.[23] Given the conservation of energy, the maximum overtone contribution from up-pumping should scale as $N\Omega_{max}$, where *N* is the order of the overtone.

At low overtone numbers (*N*) (see Equation 3.7) the arbitrary maximum of 700 cm^{-1} is in fact meaningless. For example, consider the two dominant overtone pathways, *N*=2 and *N*=3. For a system with $\Omega_{max} = 200$ cm^{-1} the maximum overtone frequency is 400 (for *N=2*) or 600 cm^{-1} for (*N=3*). Hence no density will exist above $N\Omega_{max}$ in these cases. Despite these deficiencies, if the criteria set out by Bernstein are followed (Ω_{max} = 200 cm^{-1} overtone vibrational up-pumping and projection onto the 200-700 cm^{-1} region), remarkable correlation is made against experimental impact sensitivity, Figure 4.8. If only the first overtone is considered (*i.e.* the most rapid excitation) there is a seemingly exponential fit between the integrated overtone contributions to $P(\Omega^{(2)})$ as a function of the proposed experimental impact sensitivity. This is to say that $P\left(\Omega^{(2)}\right)$ is higher for more sensitive compounds. This is in particularly excellent agreement if the materials which contain explosophoric -NO_2 groups are considered in isolation (red points on Figure 4.8). As *N* is increased, this correlation holds quite well, with the notable exception of α-FOX-7, Figure 4.8. When the second overtone contributions are considered (*N=3*), the total $P(\Omega^{(2)})$ for α-FOX-7 and β-HMX become nearly equal, with the latter appearing to fall short of the exponential trend. However, consideration of Figure 4.5 for β-HMX (which agrees well with INS data) shows that very little density sits within the region $\omega = 2\Omega_{max} \rightarrow 3\Omega_{max}$. It is therefore not surprising to find that the value of $P(\Omega^{(2)})$ falls as *N* increases.

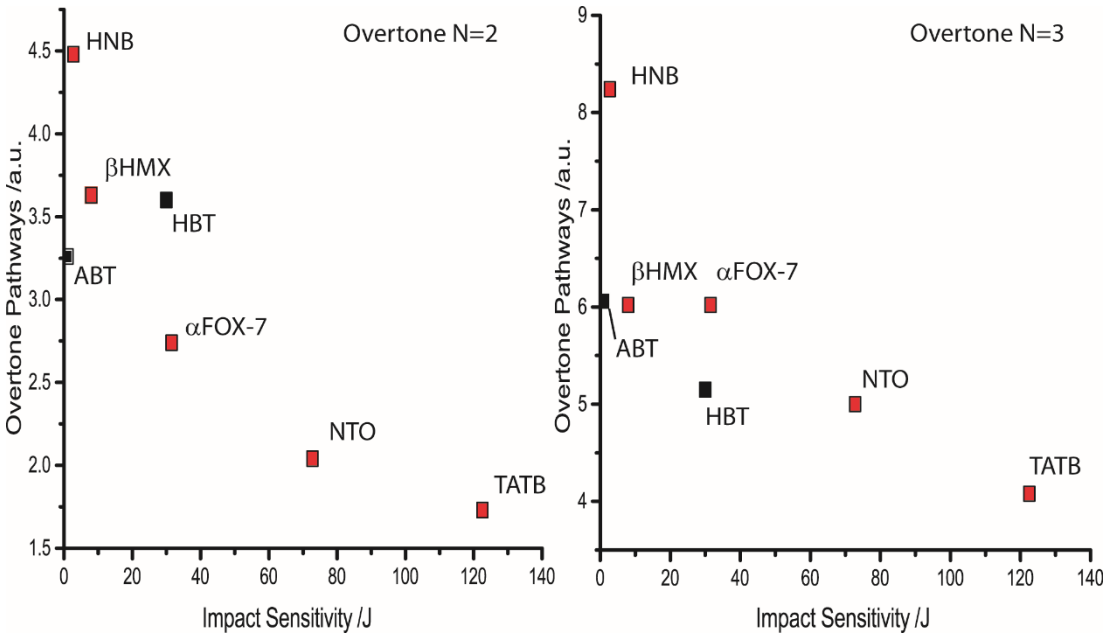

Figure 4.8: Overtone-based prediction of impact sensitivity of molecular energetic materials, P($\Omega^{(2)}$). Data are given for (left) the first overtone, *N=2*, and (right) the second overtone, *N=2+3*. Molecules which contain explosophoric -NO_2 moieties are highlighted in red, those without in black. Up-pumping is considered into the region 200-700 cm^{-1} with Ω_{max} =200 cm^{-1}.

It is worth considering the other two compounds, ABT and HBT. Both compounds are based on the same tetrazole base, and do not contain -NO_2 moieties. Instead, their explosophoric groups are based on N-N bonds. Interestingly, while the values of $\Omega^{(2)}$ do not fall in line with the trend exhibited by the -NO_2 containing compounds, ABT is predicted more sensitive than HBT, consistent with experimental reports. The offset between the two sets of materials presumably reflects the nature of the electronic contribution to dissociation (*i.e.* the dissociation energies).

While it is important to note that higher order overtones are unlikely to contribute to up-pumping due to their lower probabilities, P($\Omega^{(2)}$) was generated up to *N=6,* at which point additional contributions became negligible. Overall, the general trend in predicted sensitivity of the molecular materials holds well as P($\Omega^{(2)}$) is generated from higher overtones, Figure 4.9. Again, the -NO_2 based materials (with the exception of β-HMX) follow a good trend in

$\Omega^{(2)}$ as compared to impact sensitivity. The second structural class of energetic materials, based on N-N explosophores, follow their own trend, but are still in line with experiment.

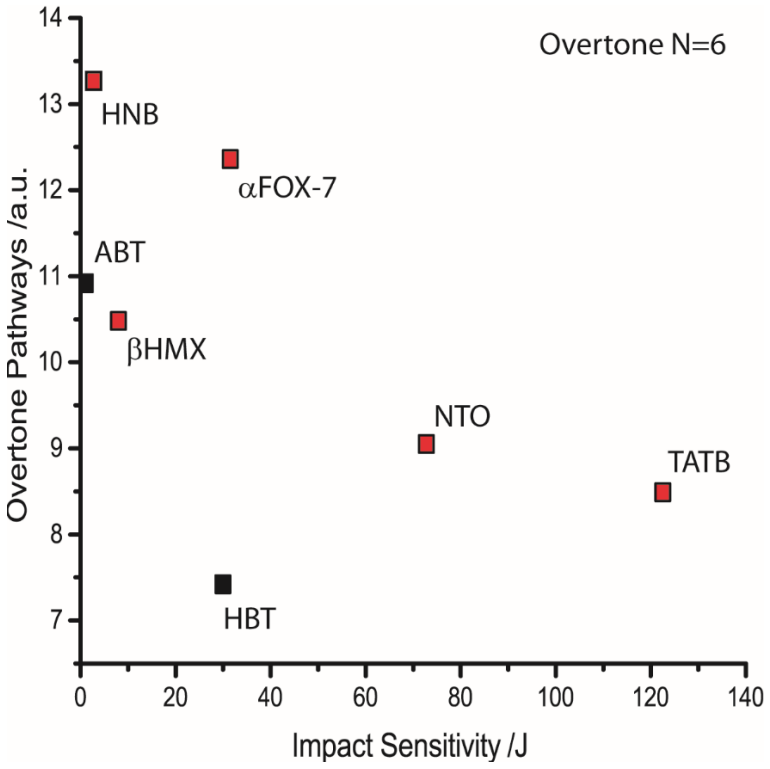

Figure 4.9: Integration of $\Omega^{(2)}$ generated from overtone pathways from *N*=2-6. Materials with explosophoric -NO_2 moieties are highlighted red, those without in black. Up-pumping is considered into the region 200-700 cm^{-1} with Ω_{max} =200 cm^{-1}.

As a final consideration for the overtone pathways, the limits placed on Ω_{max} and the upper end of integration were lifted. The upper limit of integration therefore sits at $N\Omega_{max}$. Upon lifting this restriction, the correlation between impact sensitivity and P($\Omega^{(2)}$) holds until a value of *N*=4, after which point the sensitivity of α-FOX-7 surpasses that of β-HMX, and eventually that of HNB by *N=6*. Hence, this is purely an effect of high order overtones and the result of a markedly higher DOS in the high frequency region of α-FOX-7, (see the DOS

in Figure 4.5). However, it is worth remembering that these scattering processes are highly improbable.

It can therefore be suggested that the seemingly arbitrary upper limit of integration previously suggested (700 cm^{-1}) was in fact a fortunate choice. This limit effectively places the restriction on overtones to *N=3*, with higher order terms contributing a negligible amount, should they be considered (as in the case by Bernstein[23]). If only the first two overtone pathways are considered (as in Chapter 3), and Ω_{max} defined as in Table 4.4, the predicted ordering follows as in Figure 4.10. This is in excellent agreement with experimental sensitivities, noting the two independent sets of materials: -NO_2 (red squares) and N-N (black squares) based.

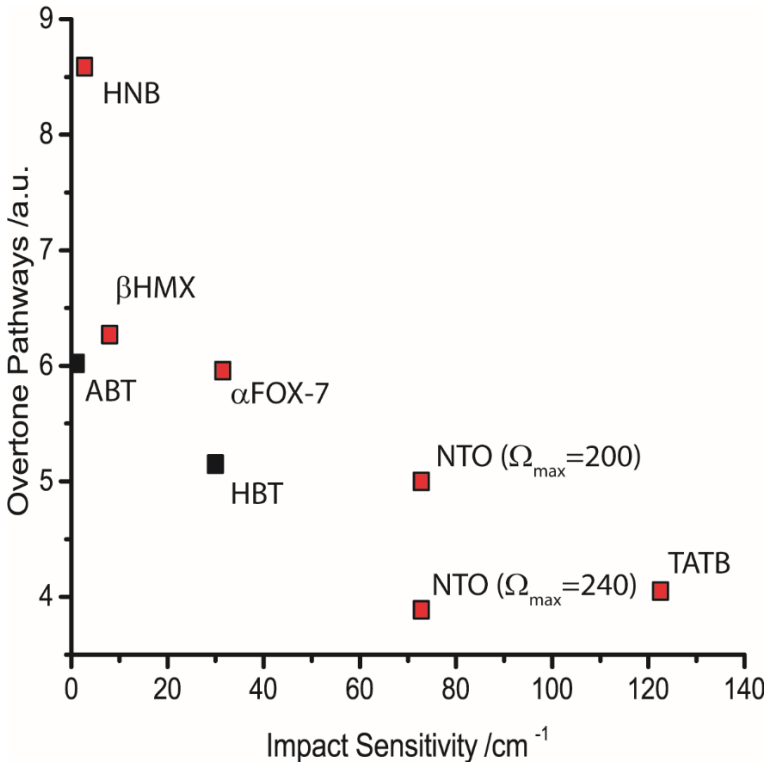

Figure 4.10: Integration of $\Omega^{(2)}$ generated from the overtone pathways for *N=2-3*. The -NO_2 containing materials are highlighted in red, those without in black. No restrictions are placed on Ω_{max} or the upper frequency bound for the doorway modes.

4.5.3.2 Combination Pathways

The initial up-pumping models[62] included consideration of combination pathways, which later formed the base for prediction of impact sensitivity from INS spectra.[19] In the 0 K limit, combination pathways *cannot* contribute until doorway modes have been populated by overtone processes. That said, Kim and Dlott[61] noted that the initial overpopulation of doorway modes (by overtone pathways) is small, and that the subsequent excitation of higher vibrational modes (*i.e.* by combination pathways) follows quickly afterwards (1-2 ps). Hence, it is worth analysing the contributions of combination pathways and their potential to rationalise impact sensitivity.

The combination pathways generated in the absence of temperature are simply taken as the two-phonon density of state, $\Omega^{(2)} = \delta(\omega - \omega_1 - \omega_2)$, with $\omega_1 \neq \omega_2$, in line with Equation 3.5. As discussed in Chapter 3, a restriction is placed on the generation of these curves, such that $\omega_1 < 2\Omega_{max}$ and $\omega_2 < \Omega_{max}$. Hence, the maximum allowed target frequency is $3\Omega_{max}$. This has the effect of ensuring that up-pumping occurs by the addition of at least one mode from the phonon bath, which is initially excited by the impact of the shock wave.

These $\Omega^{(2)}$ curves are generated for the materials studied here, Figure 4.11. As a qualitative rule, $\Omega^{(2)}$ appears to increase earlier and more rapidly for the sensitive compounds of each structure type. For example, the onset of increase is roughly the same between HNB (~ 260 cm^{-1}) and β-HMX (~ 250 cm^{-1}), although the former rises much more rapidly. In contrast, α-FOX-7 has an onset frequency (~ 320 cm^{-1}) approximately 100 cm^{-1} higher than in β-HMX. In general, each successive doorway mode leads to an increase in $\Omega^{(2)}$ that corresponds to the density of states about that doorway mode. Hence, in line with Fermi's Golden Rule, Equation 3.6, a lower onset frequency and more rapid increase in $\Omega^{(2)}$ corresponds to a more rapid transfer of energy into the internal modes. A notable exception to this generalization appears to be NTO, which is based on $\Omega_{max} = 200$ cm^{-1} in Figure 4.11. The rapid onset of $\Omega^{(2)}$ results from the low-lying vibrational band that sits just above Ω_{max}. If NTO is instead recast based on Ω_{max}=240 cm^{-1}, the onset frequency is shifted to

~350 cm^{-1}, Figure 4.11. This further supports previous suggestions to include the -NO_2 rocking motions within the phonon bath.

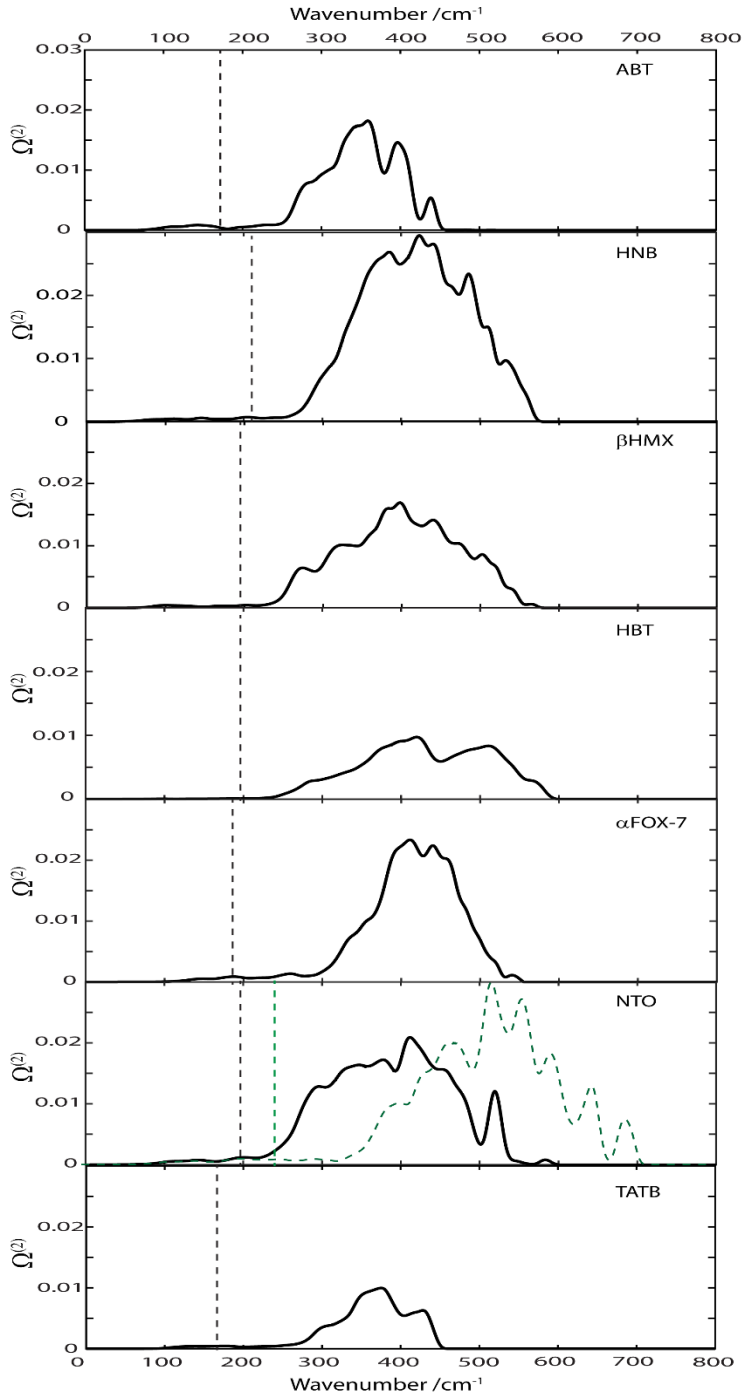

Figure 4.11: $\Omega^{(2)}$ for the molecular energetic materials. $\Omega^{(2)}$ for NTO is given for (black) $\Omega_{max}^{(NTO)} = 200$ cm^{-1} and (green) $\Omega_{max}^{(NTO)} = 240$ cm^{-1}. Plots are generated according to Equation 4.1 and under restriction of $\omega_1 < 2\Omega_{max}$ and $\omega_2 < \Omega_{max}$. Vertical dotted lines indicate Ω_{max}.

Raw integration of $\Omega^{(2)}$ results in largely meaningless quantities, noting that up-pumped energy again only contributes to the excitation of the internal modes if an internal mode exists at a particular frequency. Hence, $\Omega^{(2)}$ are again projected onto the DOS curves, and $P(\Omega^{(2)})$ are generated. An example is given for ABT in Figure 4.12. As is observed for ABT, and indeed holds across the energetic materials, the large majority of $\Omega^{(2)}$ sits between existing vibrational states and can therefore be discarded.

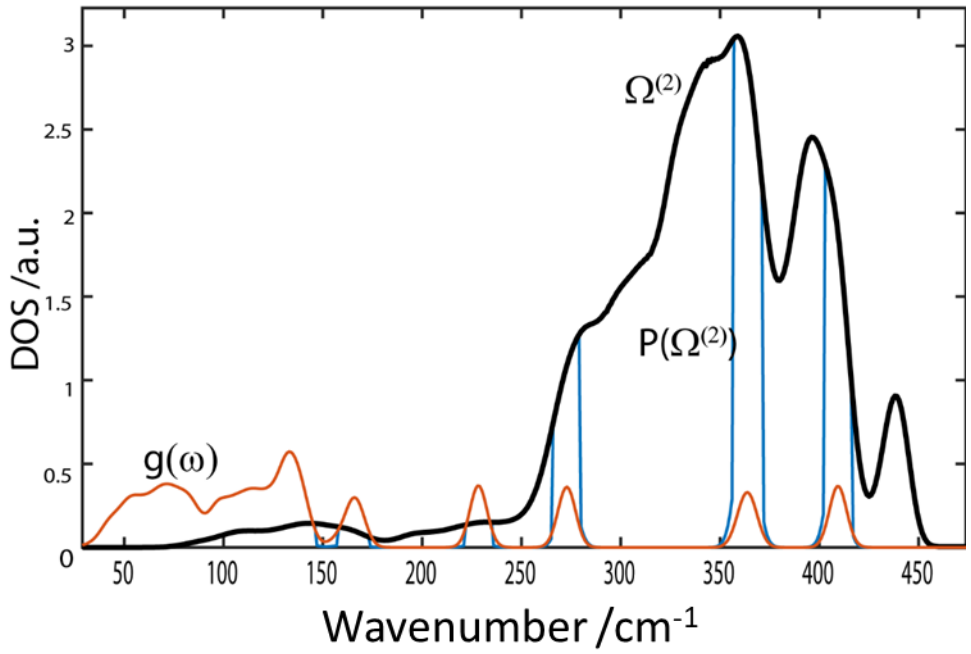

Figure 4.12: The full $\Omega^{(2)}$ for ABT (black), alongside the single phonon DOS g(ω) (orange) and the projection of $\Omega^{(2)}$ onto the DOS, $P(\Omega^{(2)})$ (blue).

With these preparations in mind, it is possible to analyse the combination mode contributions to the energy transfer of the molecular EMs within the 0 K model. In the first instance, this simply corresponds to an integration of the $P(\Omega^{(2)})$ curves generated above.

The integration of P($\Omega^{(2)}$), Figure 4.13, does not reveal as promising a trend as was observed for the azide materials in Chapter 3. There is no exponential decay observed with increasing impact sensitivity, and the integrated values of α-FOX-7 and β-HMX are very similar. In fact, α-FOX-7 is predicted to be slightly more sensitive than β-HMX. This may point towards an error with the assignment of Ω_{max} in the computational model. However, inspection of the INS spectra suggests that the values employed in both cases are accurate, and that no peaks are added or omitted to the region $\Omega_{max} \rightarrow 3\Omega_{max}$ in the simulated spectra for either compound. These therefore appear to be well representative of the systems under the current model.

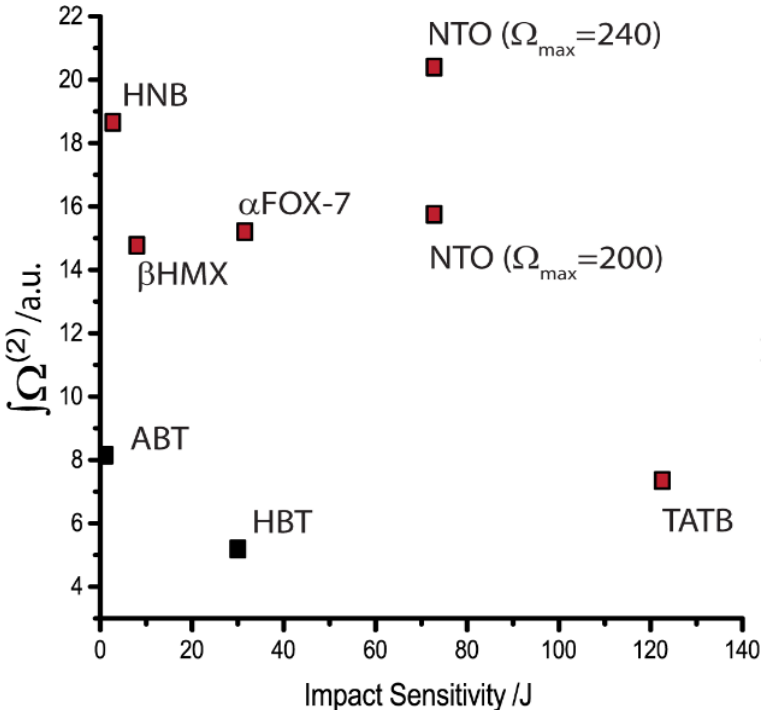

Figure 4.13: Integration of $\Omega^{(2)}$ from combination pathways. Compounds containing -NO_2 explosophores are highlighted in red. Note that $\Omega^{(2)}$ is restricted to a maximum of $3\Omega_{max}$ given the restrictions of $\omega_1 < 2\Omega_{max}$ and $\omega_2 < \Omega_{max}$.

It is generally observed that P($\Omega^{(2)}$) is higher for the sensitive compounds and lower for the insensitive compounds, but the resolution is very poor. The failure of this model is likely due to the complexity of the vibrational structure of the

molecular materials. The number of energy transfer processes that are available within these materials is dependent on the number and density of doorway modes. However, the frequencies of doorway modes differ quite drastically within and between materials, and the present model treats coupling with all of these modes as being equal. While the anharmonic coupling constants may be very similar,[21] the number of scattering pathways available will depend on their relative populations. Hence, doorway modes that sit higher in frequency will contribute fewer pathways if thermal populations are considered. To a large extend, this may explain the inability of these 0 K models to differentiate between β-HMX and α-FOX-7. In the former, the doorway modes tend towards the bottom of the doorway region, while in the latter they tend towards the top. Thus, while a simple counting method appeared sufficient to describe the vibrational up-pumping in the vibrationally 'simple' azide molecules, it appears inadequate to treat the more complex vibrational structure here. Thus $P(\Omega^{(2)})$ alone does not appear sufficient.

4.5.3.3 Two-Layer Combination Pathways

As a first step to develop this model further within the 0 K limit, and attempting to unify previous works, energy transfer is instead explicitly treated as the two-step process that was described above[61], namely:

1. Excitation of the doorway modes by the first overtone, followed by
2. Up-pumping by combination pathways to a maximum of $3\Omega_{max}$

This is done by imposing the populations of the doorway modes that result from the overtone up-pumping calculations in Section 4.5.3 onto $g(\omega)$, and subsequently assessing $P(\Omega^{(2)})$ as before. This is demonstrated in Figure 4.14 for α-FOX-7.

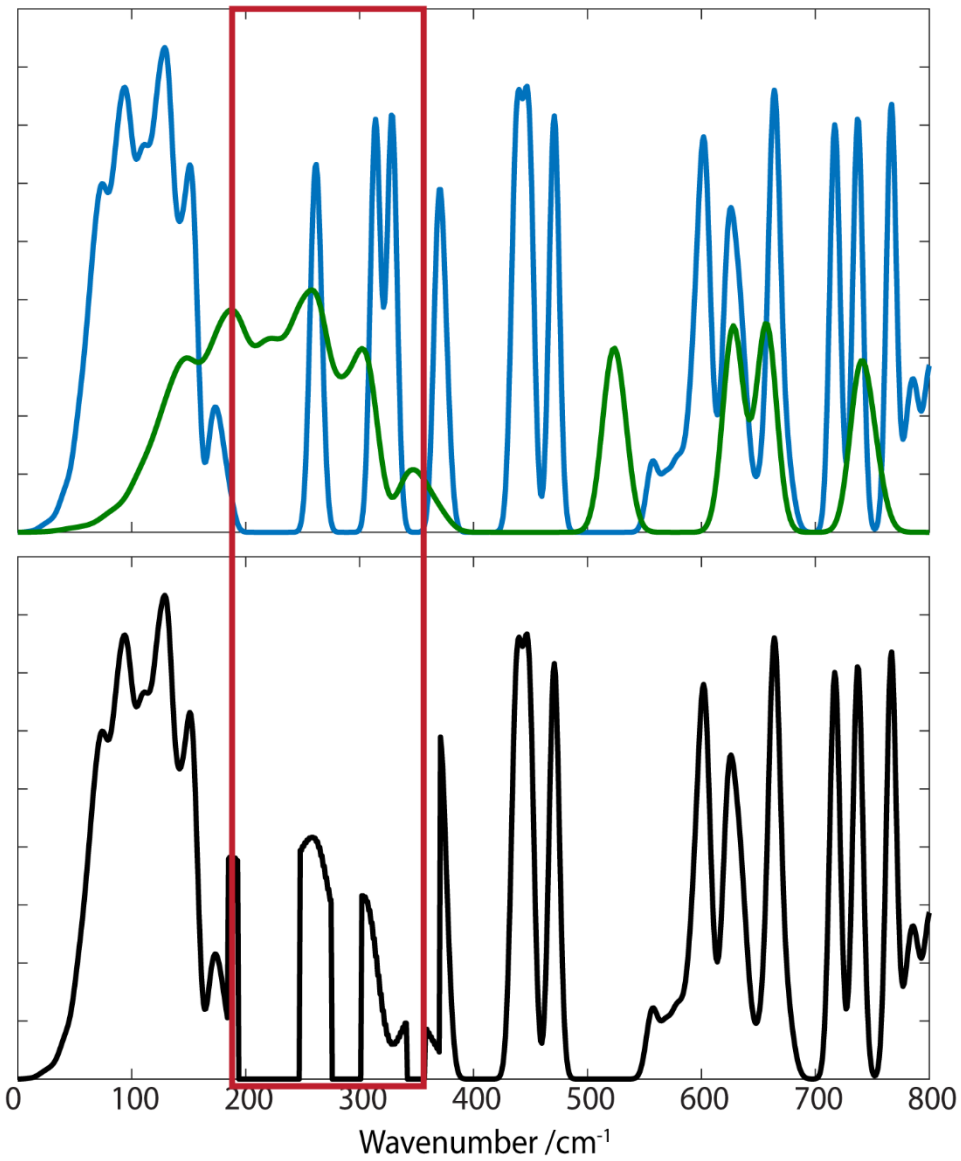

Figure 4.14: Construction of the two-layered approach for vibrational up-pumping for α-FOX-7. (Top) The phonon density of states (blue) is shown, along with the first overtone density of states (green). (Bottom) Recasting the overtone populations onto the phonon density of states in the region $\Omega_{max} < \omega < 2\Omega_{max}$ (highlighted by red box).

If the model (bottom panel, Figure 4.14) is constructed, and the up-pumping contributions re-examined, the predicted trend in sensitivities sits in excellent agreement with experimental results, Figure 4.15. It is assumed here that excitation of *all* modes between $\Omega_{max} \rightarrow 3\Omega_{max}$ (*i.e* the entire internal vibrational manifold) should be considered. The predicted sensitivity ordering

follows as HNB > β-HMX > α-FOX-7 > NTO > TATB across the -NO_2 based energetics, and ABT > HBT for the N-N energetic materials. While the model imposed here is slightly more complex than that required in Chapter 3, it does highlight the need for a more physical basis in understanding the properties of energetic materials with large quantities of doorway modes and complex vibrational structure.

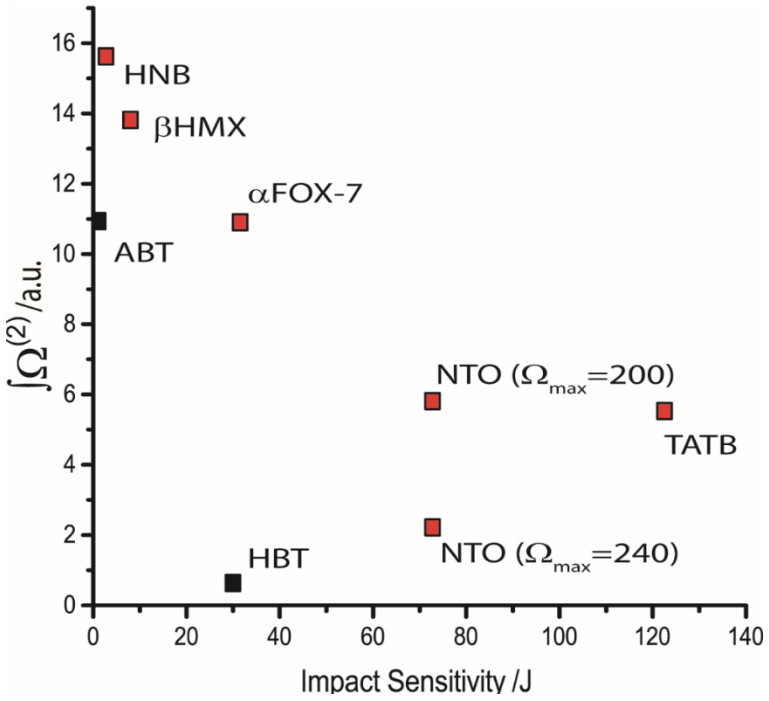

Figure 4.15: Relative up-pumping rates according to the two-layered model. Note that $\Omega^{(2)}$ is restricted to a maximum of $3\,\Omega_{max}$ given the restrictions of $\omega_1 < 2\Omega_{max}$ and $\omega_2 < \Omega_{max}$. Compounds containing -NO_2 explosophores are highlighted in red.

Whilst the ordering proposed in Figure 4.15 shows excellent agreement with experimental impact sensitivities it has been postulated[61,62] that for some materials the main target modes (*e.g.* bond stretching) are confined to the region $2\Omega_{max} < \omega < 3\Omega_{max}$. Without a deeper understanding of the dissociation mechanisms of these energetic materials, it is not possible to say explicitly whether the range $\Omega_{max} < \omega < 3\Omega_{max}$ or $2\Omega_{max} < \omega < 3\Omega_{max}$ should

be considered. However, it is worth highlighting that if the integration from Figure 4.15 is restricted to the upper range, Figure 4.16 is the result. This leads to truly excellent agreement with experimental impact sensitivity ordering, including the positioning of ABT. Now only HBT remains as an outlier. Further information as to which bonds require activation is therefore of great importance in developing this model further.

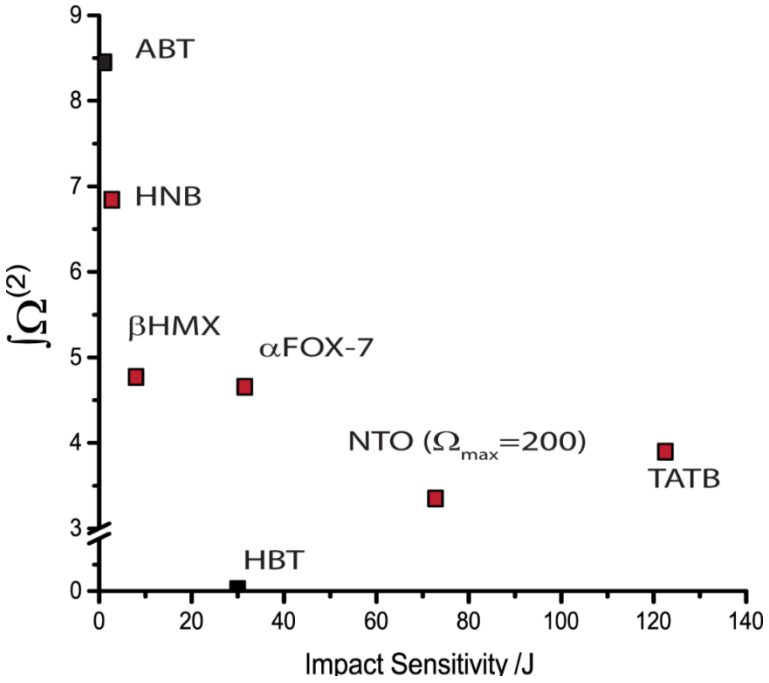

Figure 4.16: Relative up-pumping rates according to the two-layered model. Only the up-pumping contribution to $2\Omega_{max} < \omega < 3\Omega_{max}$ is considered here.

4.5.3.4 Temperature Dependent Up-Pumping

It follows from Section 4.5.3.2 that simple counting of the number of up-pumping pathways is not the best indicator to describe the relative sensitivities of the molecular energetic materials. Instead, it is likely that an understanding of the *rate* of this up-pumping may be more indicative. This will be examined here within the purview of temperature.

It is well known that temperature can have a marked impact on the sensitivities of energetic materials.[63] With variation over relatively small temperature ranges, two mechanisms can be proposed for the effect of temperature on the models presented in this thesis:

1. Induce a change in the phonon bath populations, and
2. Induce a large anisotropic shift in vibrational frequencies

Temperature Effects: Phonon Bath Populations

In the absence of a thorough understanding of the three-phonon scattering probabilities for an arbitrary set of phonons, Dlott[22] noted that the relative rates of energy up-pumping varies with:

$$rate \propto n_p - n_t$$

Equation 4.2

That is, it decreases as the difference between the Bose-Einstein populations of the lower (phonon, n_p) and upper (target, n_t) frequencies narrows. This is analogous to describing the 'heat flow' associated with phonon up-pumping from a vibrationally 'hot' phonon continuum to a vibrationally 'cold' internal vibrational manifold – the closer in 'temperature' the initial and final states, the slower the energy transfer.

With the addition of temperature, a two-stage model is no longer explicitly required. The initial up-pumping of vibrational energy follows the quickest routes, which are presumably the first overtone and combination pathways. These both occur within the first anharmonic approximation. With addition of temperature:

1. The initial contribution from the doorway modes no longer requires population from the overtone pathway, as it rises due to thermally populated states.

2. Combination pathways therefore contribute to scattering across $\omega > 2\Omega_{max}$. At *least* one of the coupling modes must have $\omega < \Omega_{\max}$ – *i.e.* must incorporate the shock temperature (the remaining system is at equilibrium).
3. The rate of up-pumping from the overtone pathways (κ_{OT}) is determined according to[61]

$$\kappa_{OT} = A\Omega^{(2)}[n_p(T) - n_\omega(T)]$$

Equation 4.3

where *A* contains a series of scaling constants as well as the anharmonic coupling constant $V^{(3)}$, $\Omega^{(2)}$ is the two-phonon density of states, and $n_p(T)$ and $n_\omega(T)$ are the Bose-Einstein populations of the phonon and target frequencies, respectively. The coefficient *A* has been suggested to depend on heat capacity and the rate of acoustic propagation in a material. However, as this information is not available for the majority of these materials, this term is assumed to remain constant for all systems.

4. The relative rate of up-pumping from combination pathways (κ_C) is taken to follow[19]

$$\kappa_C = A\,\Omega^{(2)}[n_p(T)n_d(T) - n_\omega(T)]$$

Equation 4.4

with terms defined as above and the addition of $n_d(T)$, the Bose-Einstein population of the doorway mode. This has the effect of scaling the magnitude of up-pumping contributions according to the thermally excited populations of the doorway modes, Figure 4.17.

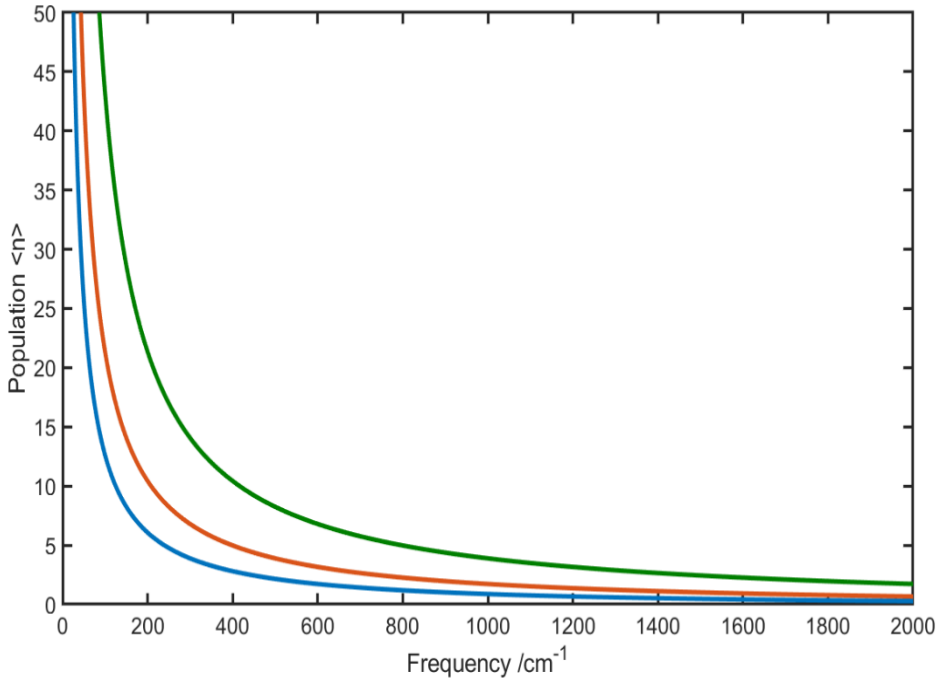

Figure 4.17: Bose-Einstein populations as a function of frequency at (blue) 300 K, (red) 500 K and (green) 1000 K.

Because combination bands can now result from thermally populated states, it is first worth considering the full $\Omega^{(2)}$ curves that are obtained on lifting the restriction of $\omega_1 < 2\Omega_{max}$ (whilst maintaining $\omega_2 < \Omega_{max}$), Figure 4.18. This therefore allows the excited phonon bath to interact with any thermally-populated vibrational mode. In contrast to the phonon density of states, $\Omega^{(2)}$ rarely falls to zero, and only does so when neighbouring frequencies have $\Delta\omega > \Omega_{max}$. Thus, above such regions, rapid redistribution of energy cannot occur within the first anharmonic approximation, and these frequencies can be largely eliminated from a thermal (non-direct) up-pumping model.[22] This is because the thermal up-pumping model requires up-pumped energy to dynamically redistribute into vibrational modes that are responsible for assisting in bond rupture. Therefore the up-pumping is either limited by this point in $\Omega^{(2)}$ or intrinsically by the highest vibrational frequency (*via* generation of P($\Omega^{(2)}$). Across the $\Omega^{(2)}$ for these compounds, none of the sensitive compounds contain regions of $\Omega^{(2)} = 0$. It is worth highlighting that α-FOX-7 does have such a point at *ca.* 1000 cm^{-1}, which corresponds to the large

frequency gap observed in the density of states, Figure 4.5. This feature is promising for segregating the sensitive and insensitive materials. For those compounds that do contain $\Omega^{(2)} = 0$, their values are listed in Table 4.5. These values are important as they set the upper limit for vibrational energy transfer within the first anharmonic approximation.

Table 4.5: Limiting frequencies for the full $\Omega^{(2)}$ for the molecular energetic materials.

	$\boldsymbol{\Omega^{(2)} = 0}$ **/cm^{-1}**
ABT	--
HNB	--
βHMX	--
HBT	600
αFOX-7	1034
NTO	--
TATB	1028

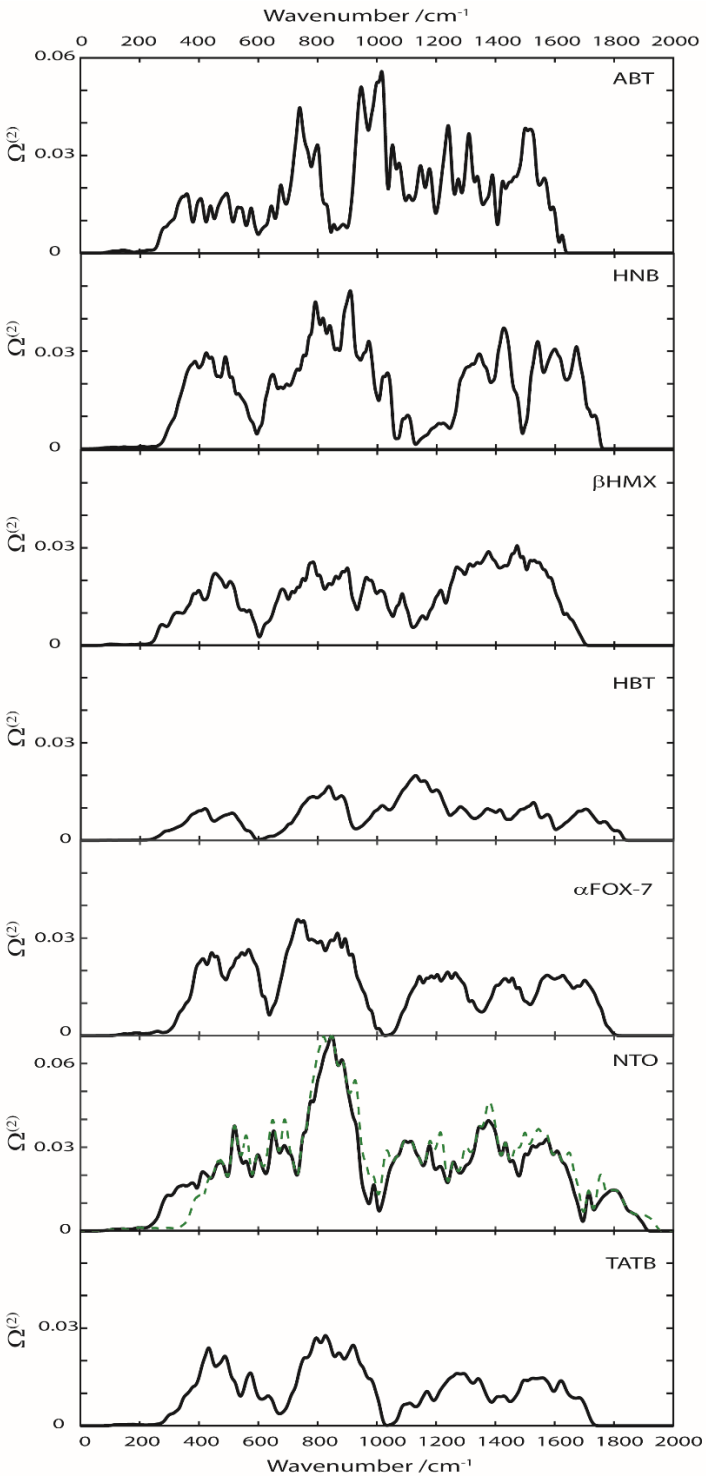

Figure 4.18: Complete temperature independent $\Omega^{(2)}$ for the molecular energetic materials, generated under the single restriction of $\omega_2 < \Omega_{max}$. For NTO, the curves are shown for Ω_{max} of (green) 240 and (black) 200 cm^{-1}. It is encouraging to find that apart from the onset frequency, little changes as a function of Ω_{max}.

It is convenient to begin discussion based only on the combination pathways. This is the result of integrating $P\left(\Omega^{(2)}\right)$, with $\Omega^{(2)}$ generated from a thermally populated $g(\omega)$. If the system is first set at equilibrium temperature, T = 300 K, the predicted order of sensitivities, Figure 4.19, are generally consistent with the pure combination pathway prediction. Note that the absolute values plotted on the Y-axis have markedly increased compared to the earlier T = 0 K models. Thus, only the trends can be compared. However, the resolution between sensitivities of β-HMX and α-FOX-7 improves. Again, the two material types are separated, with up-pumping in the -NO_2 based materials being higher and exhibiting an exponential trend. NTO is unfortunately grossly overestimated using this simple method. Numerically, this results from the high phonon density of states of the NTO phonon bath, as compared to the other materials. This is logical as it reflects the higher heat capacity of the phonon bath, given the larger number of molecules in the primitive cell.

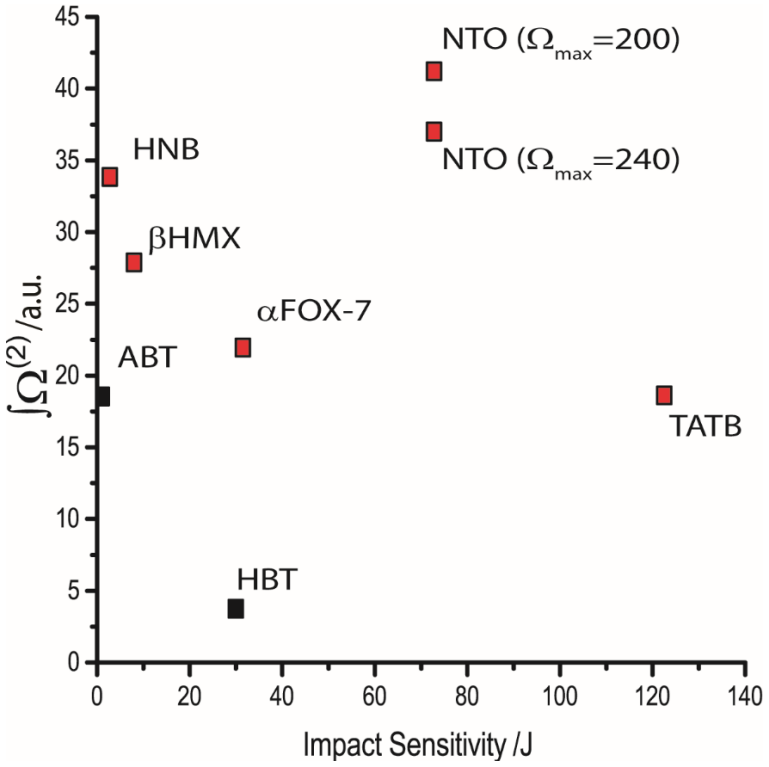

Figure 4.19: Predicted sensitivity based on T = 300 K, based purely on combination pathways (*i.e.* integration of $P\left(\Omega^{(2)}\right)$). $\Omega^{(2)}$ are generated under the restriction $\omega_2 < \Omega_{max}$ and integration restricted by where $\Omega^{(2)} = 0$.

Further development of the model is clearly required to resolve this situation. In the first instance, three physical suggestions can be proposed to account for this:

1. The thermal expansion of the material leads to softening of the phonon bath modes, and hence a decrease in Ω_{max}
2. The bond dissociation energy of NTO is considerably higher than for the more sensitive compounds, and electronic effects become dominant in this compound.
3. A considerably different anharmonic constant occurs for this compound as compared with the others in the test set.

While the two-level model may not explicitly be required, it has been observed that up-pumping rates of overtones greatly exceed those of combination bands, by an order of magnitude in some materials.[61] Hence it is worth re-examining the temperature effects under the construction of the two-level model of Section 4.5.3.3 (*i.e.* population of doorway states by the first overtone, followed by combination mode up-pumping). This is accomplished by first thermally exciting $g(\omega)$ and projecting the first overtone (*i.e. N*=2) onto the doorway frequencies as in Figure 4.14. The remaining $g(\omega)$ remains thermally populated, and the combination pathways (*i.e.* $\Omega^{(2)}$) are calculated, maintaining $\omega_2 < \Omega_{max}$. For the purpose of this discussion, the equilibrium temperature is set at 300 K. Compared to the model built upon thermally populated combination bands alone (*i.e.* Figure 4.19), as well as in comparison to the temperature-independent two-layered model (Figure 4.16), the addition of temperature leads to a remarkable comparison with experimental results, Figure 4.20. All of the sensitive materials exhibit large values of $\Omega^{(2)}$, with the insensitive materials having very low values. In fact, the separation between system types is no longer as obvious. NTO is again an exception, and depends very strongly on the choice of Ω_{max}. If the -NO_2 rocking modes are placed within the phonon bath, $\Omega^{(2)}$ comes in line with other materials in its sensitivity class. However, it falls in line with the highly sensitive compounds if Ω_{max} = 200 cm^{-1} is used. This once again suggests that these modes should be

included in the phonon manifold when present at such low frequencies. For the purpose of the remaining discussion, these rocking modes will therefore be assumed to form part of the amalgamated phonon bath.

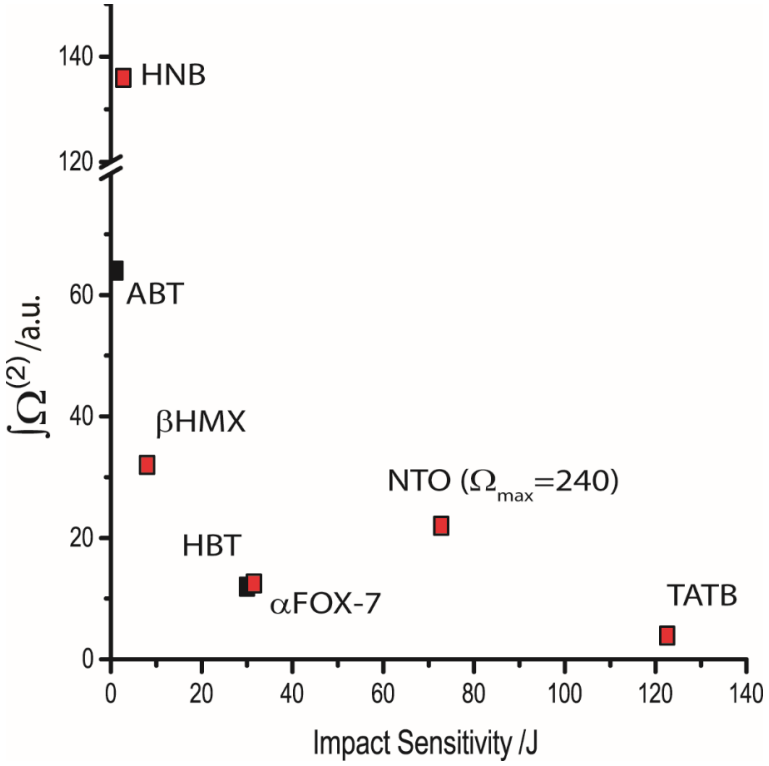

Figure 4.20: Temperature dependent two-layer model to predict impact sensitivity of the molecular EMs. The equilibrium temperature is set at 300 K and integration of $\Omega^{(2)}$ is upper bound by the limiting frequencies given in Table 4.5. Note NTO(Ω_{max}=200) has $\Omega^{(2)}$=120 cm^{-1}. Lifting these integration restrictions lead to only minor increases in the integrations: HBT (+10); α-FOX-7 (+3), TATB (+1). The relative ordering therefore remains unchanged.

Overall, it is remarkable that the simplifications made here reproduce the experimental sensitivity ordering to such an extent. With further investigation into the intricate interplay of electronic factors, as well as the system dependent normalisation coefficients, *A* in Equations 4.3 and 4.4, this model seems promising for understanding the impact sensitivity of organic EMs. As no experimental data were available against which to compare variable temperature predictions, this will not be discussed further here. However, the model does reflect the qualitative trend of decreasing sensitivity of all

compounds as $T \rightarrow 0$ K, and hence convergence of intrinsic material sensitivities.

The addition of temperature effects introduces the ability to investigate *which* modes can become activated upon initial excitation of the lattice. This is done by separating the initial temperatures of the phonon bath modes, T_p, to be different from the remaining modes. In the two-stage construction, this leads to construction of the doorway mode populations based on initial T_p excitation. While limited experimental results are available which provide a thorough study of temperature-dependent sensitivities, it is worth considering a single example briefly. Due to its popularity β-HMX was chosen. In line with experimental reports for organic molecular crystals, a model phonon 'shock' temperature of 2000 K is chosen, Figure 4.21. As can be seen, the relative rates of up-pumping depend strongly on the frequency in question. Generally, the doorway modes with $\Omega_{max} < \omega < 2\Omega_{max}$ are (as expected) most highly excited. Fine-tuning of the model proposed here requires a more fundamental knowledge of which frequencies are in fact responsible for decomposition processes.

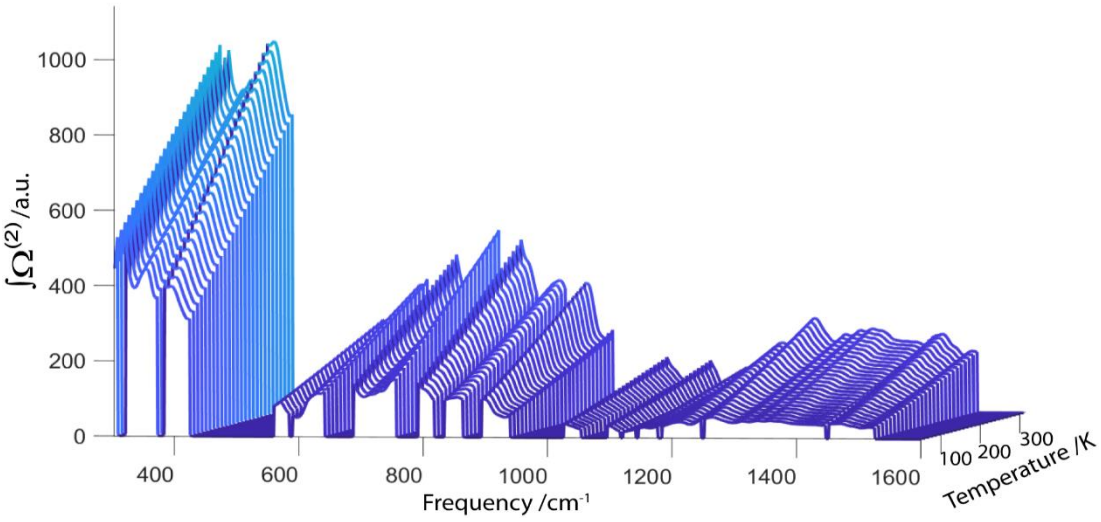

Figure 4.21: Variable temperature P($\Omega^{(2)}$) for β-HMX. The initial excitation temperature for the phonon bath modes (below Ω_{max} = 195 cm^{-1}) is taken to be 2000 K. The temperature of the remaining states is then plotted over the temperature range 10-300K. Note the phonon bath has been omitted from the *x*-axis.

Extending this shock model across different systems requires consideration of the phonon heat capacities, C_{ph}, which can be approximated by assuming within the Einstein model that each phonon mode contributes k_B to the heat capacity at and above ambient conditions. Upon impact with the same energy, U, the total amount of energy transferred to the material as heat depends on the compressibility of the material, Equation 3.1. However, without data on the compressibility of the materials used here, it can be roughly assumed that all of the molecular materials will behave roughly the same. This is generally a good approximation, with available ambient pressure bulk moduli of these materials being very similar (HMX, 14.3 GPa[28];FOX-7, 12.6$\pm$1.4 GPa[29]; TATB, 14.7$\pm$0.8 GPa[30]). It can therefore be assumed that the same proportion of input energy transforms into heat for these materials. Without knowledge of the system-dependent Grüneisen parameters, it is not possible to estimate final bulk equilibrium temperatures. However, for the purpose of the present discussion, it is sufficient to note that the initial phonon excitation depends on

$$\theta_{ph} = q/C_{ph}$$

Equation 4.5

Where θ_{ph} is the phonon quasi-temperature, C_{ph} is the phonon heat capacity and q is the heat added to the system. For an arbitrary input energy, the phonon quasi-temperature therefore decreases with increasing number of phonon bands.

As arbitrary values, an input energy of 21000 cm^{-1} is chosen, and corresponds to the input heat evaluated for a 4 GPa impact on naphthalene (with two molecules in the primitive cell), and a shock phonon quasi-temperature of *ca.* 2000 K.[31] This is arbitrarily assigned to be the phonon quasi-temperature of β-HMX, and the remaining materials scaled accordingly, Figure 4.22. In construction of the two-layered model in this way, the initial excitation of the doorway modes occurs *via* quasi-temperature populations of the phonon bath, and subsequent up-pumping is also performed using a quasi-temperature populated phonon bath. The same procedure is done for a β-HMX phonon quasi-temperature of 1000 K and 3000 K, Figure 4.22. Despite the major

approximations, there is again an excellent agreement observed between the predicted sensitivity ordering, and very similar to that conducted under equilibrium temperature in Figure 4.20. The same exponential trend is observed in all cases and suggests consistency within the model. This model may therefore offer a means to begin to probe the effects of different experimental conditions across a range of materials. Additional data, including accurate heat capacities and compressibility (and associated changes in frequencies), can be added for further refinement of the model.

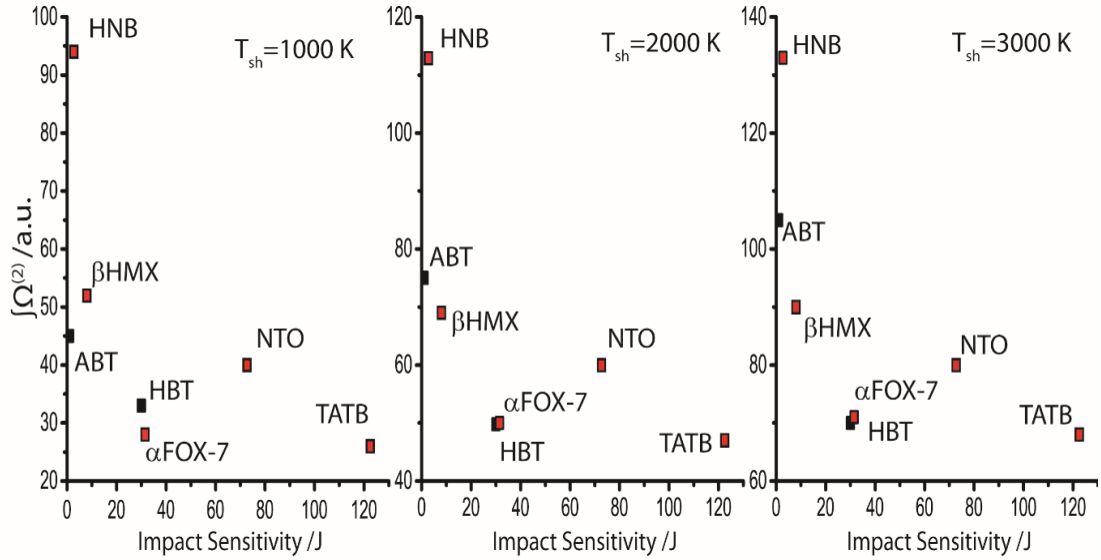

Figure 4.22: Predicting impact sensitivity using the two-layered model at ambient temperature of 300 K. The phonon modes are initially excited to shock temperature T_{sh}. In all cases Ω_{max} for NTO is 240 cm^{-1}. The *y*-axes are comparable and reflect an increase in reactivity with increased shock temperature (and hence stronger impact).

Temperature Effects: Variable Temperature Frequencies

While the introduction of a temperature effect does lead to insight into interesting phenomena, further parameters are clearly required for its development. Most crucially is the validity of the underlying vibrational model that is used in each case. To begin to analyse the underlying vibrational structure, INS spectra were collected across a range of temperatures as

documented in Section 4.4. This offered particular insight into the position of Ω_{max}. Due to time restrictions this was only possible for β-HMX, TATB and α-FOX-7. However, these represent compounds showing a reasonably broad range of structural types (*e.g.* layered, hydrogen bonded, or no directional intermolecular contacts), and therefore offer a good indication of temperature effects on vibrational frequencies in molecular materials in general. An overlay of the INS spectra across the temperatures clearly suggests no notable shift in the vibrational frequencies of the model organic materials at $\omega < 800$ cm^{-1} (*i.e.* within the region of interest for up-pumping calculations), Figures 4.23 and 4.24. Most importantly in terms of the present discussion, the values of Ω_{max}, the relative positions of the major peaks with respect to Ω_{max}, and the number of peaks within the region of interest (< $3\Omega_{max}$) remains unchanged. In β-HMX, Figure 4.23A, Ω_{max} does not shift between 10-200 K, and the largest shift in frequency is just $\pm$3 cm^{-1} on comparing the 200 K and 10 K frequencies. TATB, Figure 4.23B, however, exhibits a *ca.* 15 cm^{-1} decrease in Ω_{max} on heating from 0 to 200 K. The eigenvector of Ω_{max} reveals this mode to be a rocking motion of the molecules, perpendicular to the TATB layers. These layers, stabilised by weak van der Waals interactions, are most susceptible to thermal expansion. It is therefore logical that this mode should soften on increasing temperature. The higher frequency modes in TATB do not shift by more than *ca.* 4-5 cm^{-1} on heating from 10 to 200 K. Thus, overall, this imposes two effects on TATB:

1. The maximum window into which overtone and combination modes can couple in the first instance decreases by $\mathbf{3 \times \Delta\Omega_{max}}$ (*i.e.* the change in $\mathbf{\Omega_{max}}$ observed due to thermal heating/cell volume change). This leads to a change in the upper limit from $\mathbf{3\Omega_{max} \approx 465 \rightarrow 420}$ cm^{-1}, and hence exclusion of the vibrational band at *ca.* 450 cm^{-1}.
2. The rate of up-pumping into these modes will decrease, due to larger energy separations.

A similar effect can be expected for NTO, which is constructed from a similar layering motif, Figure 4.1.

The INS spectra for α-FOX-7, Figure 4.24, show that between 10 – 150 K, there is a change of no more than ± 2 cm^{-1} in the internal modes. For this compound Ω_{max} decreases slightly, from 183 cm^{-1} at 10 K to 180 cm^{-1} at 150K.

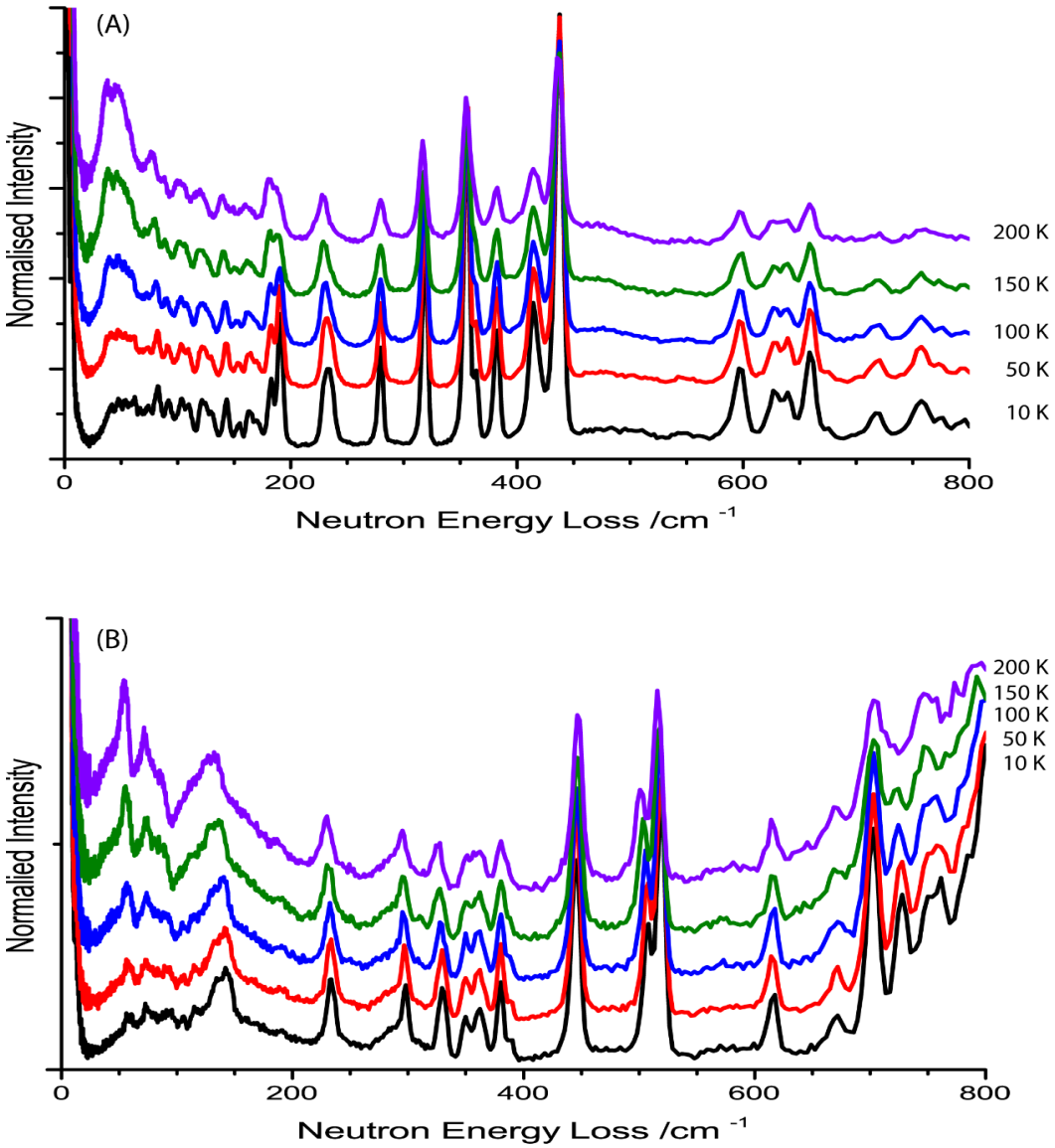

Figure 4.23: Variable temperature INS spectra for (A) β-HMX and (B) TATB from 10 K to 200 K. All spectra have been corrected for sample container contributions and background. The intensities of each system have been normalised to a well-resolved isolated peak (*ca.* 246 cm^{-1} for HMX and *ca.* 446 cm^{-1} for TATB). Note that this does introduce errors in the absolute comparison of intensities across the spectra. The change in intensities across the INS spectra reflects increasing vibrational amplitude (populations) of these vibrational modes in line with Equation 2.47.

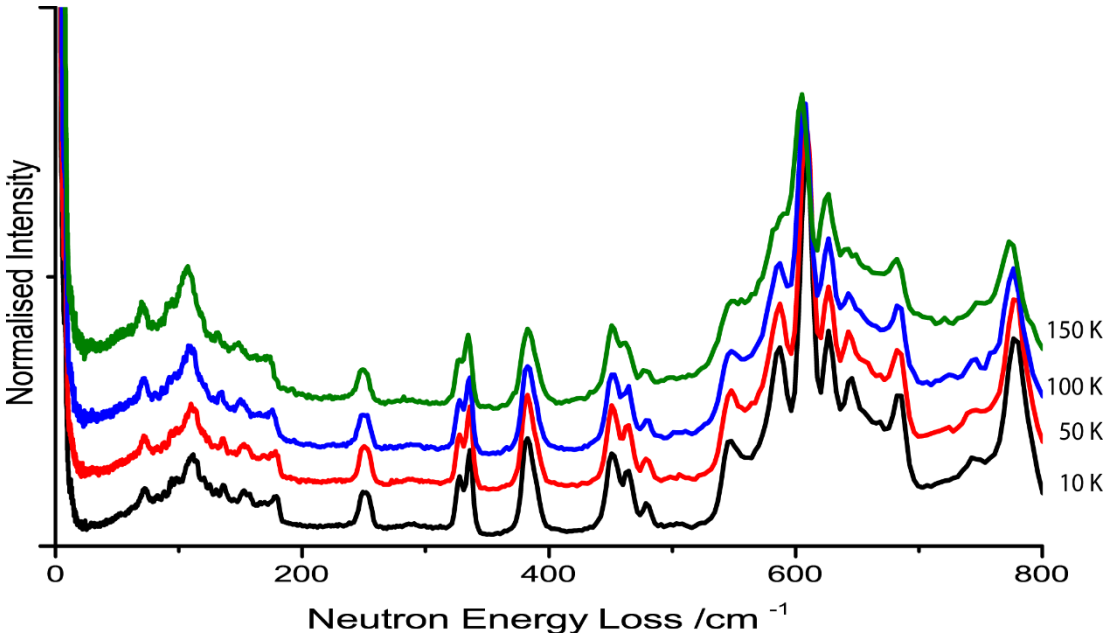

Figure 4.24: Variable temperature INS spectra for α-FOX-7 from 10 K to 150 K. All spectra have been normalised to the peak at *ca.* 385 cm^{-1}.

It therefore appears that over a broad temperature range, there can be expected to be only slight changes in the vibrational structure of these compounds. Hence, the up-pumping model build throughout this chapter can be expected to largely reflect ambient temperature phenomena. The most important factor in considering the up-pumping calculations is the placement of Ω_{max}, which appears to decrease to a notable extent for the layered compounds. This is expected to affect NTO, and may partially indicate the inability of this model to accurately reproduce NTO sensitivity. While this may contribute to the temperature variation in the sensitivity of these compounds, further work is required to fully understand this phenomenon.

4.5.3.5 Up-Pumping from Zone-Centre Frequencies

It is clear from Section 4.5.2 that negligible band dispersion is observed across the Brillouin zone of the molecular energetic materials. As many organic energetic materials are composed of very large molecules in large, low symmetry unit cells, the approach described above is limited by computational resources. Much more tractable, however, is the calculation of zone-centre

vibrational frequencies. It is therefore interesting to determine whether the same trends can be obtained from only the zone-centre vibrational structure.

To investigate this, only two of the above models will be discussed, the overtone pathways as in Figure 4.10, and the two-level combination pathways, Figure 4.20. The zone-centre phonon DOS do not change drastically with respect to those of the full phonon DOS in Figure 4.3. If the most promising overtone-based method is examined (*i.e.* integration across $\Omega_{max} < \omega < 2\Omega_{max}$), Figure 4.25, it is found that no notable changes occur on moving from the full phonon dispersion to zone-centre frequencies. The same is true if the temperature-dependent two-level method is considered, Figure 4.25. The only notable shift is again NTO, whose $\Omega^{(2)}$ appears to increase slightly when only the zone centre is considered.

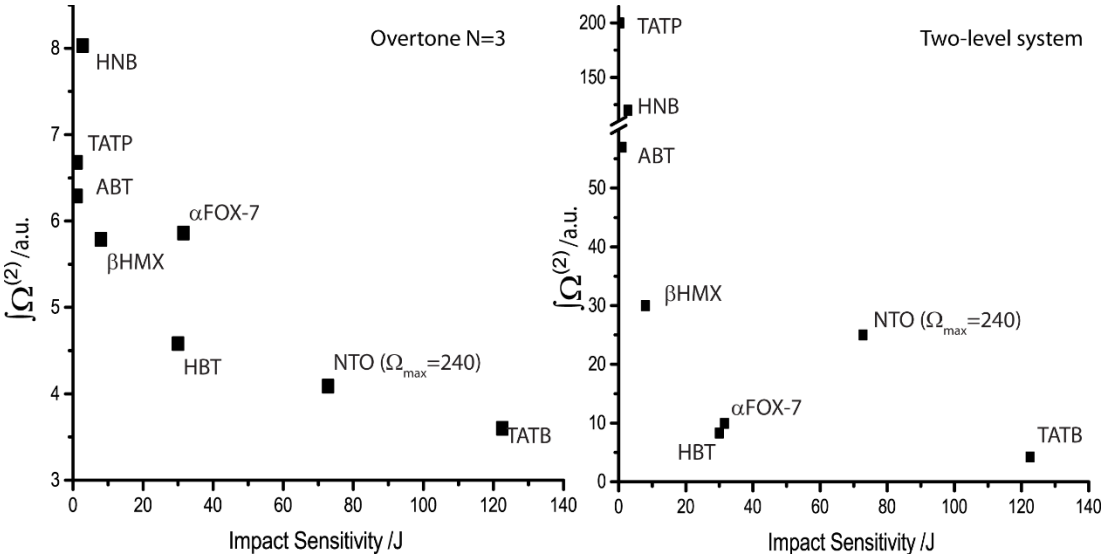

Figure 4.25: Vibrational up-pumping based on zone-centre phonon DOS. (Left) calculation of the temperature independent overtone contribution to *N=3*. (Right) Two-level system with equilibrium temperature 300 K. The addition of temperature in the latter is responsible for the large increase in the *y*-axis.

It is therefore possible to add an additional material to the test set, which was too large for complete phonon dispersion calculations. Triacetonetriperoxide (TATP) is a well-known primary explosive, with impact sensitivity < 1 J.[25] Its structure, phonon DOS and $\Omega^{(2)}$ are given in Figure 4.26. It is very promising to find that this material is well placed as a highly sensitive material in both prediction methods. However, it is best placed as being the most sensitive compound upon addition of a temperature term, Figure 4.25.

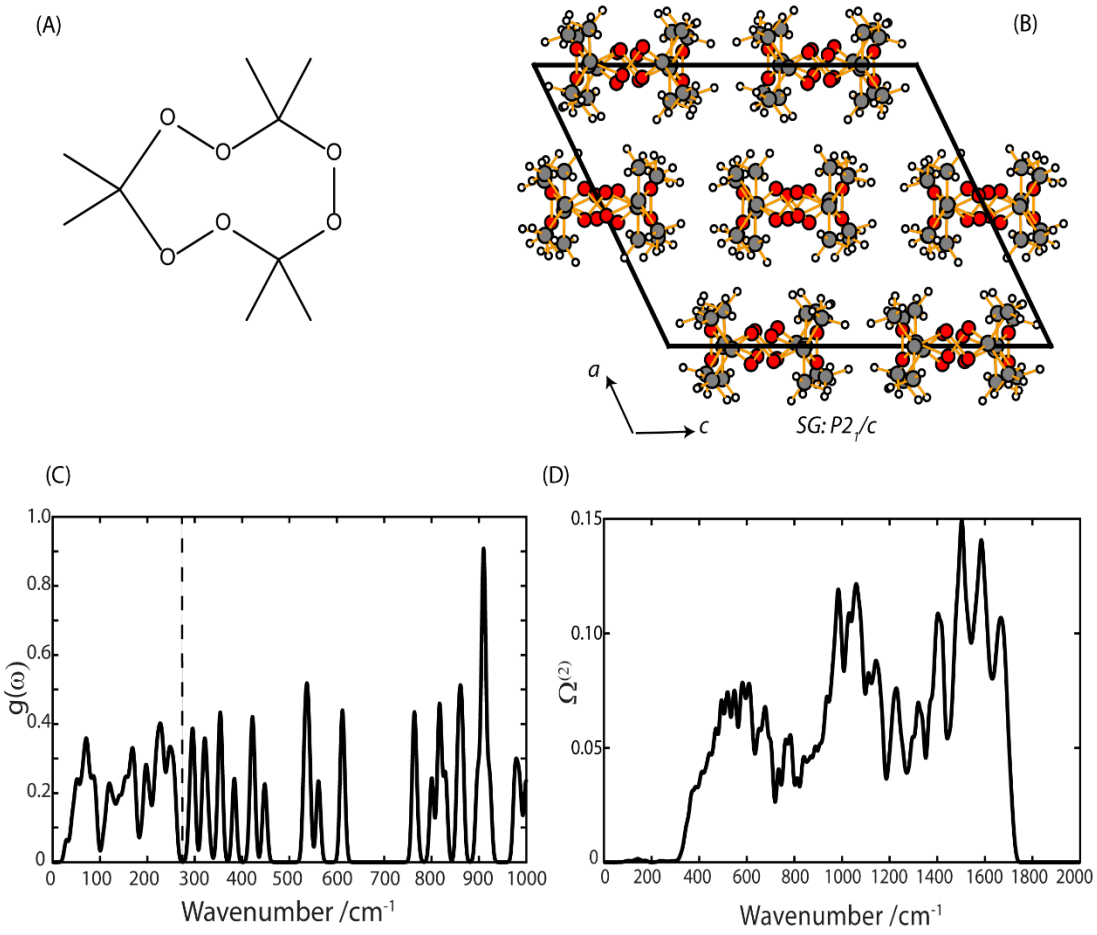

Figure 4.26: (A) Molecular structure of TATP. (B) Crystallographic structure of TATP. (C) Zone-centre $g(\omega)$ for TATP, and (D) $\Omega^{(2)}$, with the restriction that $\omega_2 < \Omega_{max}$.

It follows that, provided the phonon DOS is well reproduced by the zone-center frequencies – *i.e*. that the dispersion curves exhibit negligible dispersion – it may in fact not be necessary to calculate the full vibrational structure. This

opens the door to examining very many organic molecular materials, which may be too large for such expensive calculations. Moreover, it also opens up the possibility of using standard lab-based Raman or terahertz spectrometers, to probe the Brillouin zone-centre modes with sufficient detail to offer insights into impact sensitivity behaviour.

4.6 Conclusions

The organic molecular energetic compounds studied in this chapter span a broad range of both molecular and crystallographic structure types. From highly sensitive compounds like TATP, to highly insensitive compounds such as TATB, the organic EMs exhibit immense diversity in their sensitivity properties. Analysis of the electronic band structure suggests that no correlation exists between the size of the electronic band gap and the sensitivity of these compounds. Hence, the 'band gap criterion' fails across the subset of EMs investigated here.

The full phonon dispersion curves were generated for a series of seven organic EMs: ABT, HNB, β-HMX, HNT, α-FOX-7, NTO and TATB. Comparison of β-HMX, α-FOX-7, NTO and TATB to INS spectra suggest that DFT methods produce excellent agreement with the experimental vibrational structure of these types of materials.

Based on the vibrational up-pumping model, several qualitative correlations could be found. Of the rapid, qualitative approaches, the most promising appears to be simple correlation between the density of doorway modes with the impact sensitivity. Physically, this can be related to the rate with which the initial energy can transfer from the excited phonon bath into the internal vibration manifold. Indeed, if the overtone pathways are considered and projected onto the doorway region, an excellent correlation is observed with impact sensitivity.

Consideration of the combination pathways by means of the two-phonon density of states leads to rather poor correlation with experimental sensitivities. However, this can be largely rectified by implementing a two-layered model. That is, if explicit consideration is given for the initial excitation of the doorway modes by the first overtone, and the combination pathways considered subsequently, then the overall correlation with experiment becomes promising. However, clear deficiencies remain. As a final step, it is found that the distribution of doorway modes (*i.e* clustered at the upper or lower end of the doorway region) requires some consideration for the relative contribution of each doorway mode to up-pumping. This was treated by the addition of a temperature term, populating vibrational states by the Bose-Einstein populations. If this term is considered, the predicted trend in impact sensitivities matches very well with experimental values. Hence, the work in this chapter has developed a fully *ab initio* approach to ranking the impact sensitivity of EMs based on a vibrational up-pumping model. In doing so, the work in this chapter has successfully unified and expanded on competing models that have been reported in the literature.

Reproducing the models based on zone-centre frequency calculations leads to the same conclusions. This is presumably due to the low wave vector dispersion that is exhibited for these materials. Hence, the zone centre frequencies provide a good representation of the total vibrational structure. This opens the door to implementing this model to large molecular materials, such as TATP, for which the task of obtaining complete phonon dispersion curves is simply too large.

It is remarkable to find that this simple mechanism of up-pumping appears to provide a means to predict the relative impact sensitivity of a wide range of structural types. The minor discrepancies that remain are likely due to the intricacies that surround the differences in phonon scattering rates (*i.e.* anharmonic coupling strengths) rates of phonon propagation in these materials, as well as the dissociation energies of the different molecules.

4.7 Suggestions for Further Work

The method presented here has been a first approach at understanding the up-pumping structure in EMs. Foremost, the work presented here includes only seven molecular EMs, and therefore a larger number of systems is a clear direction for additional work. On this subset of organic EMs, the model has proved promising, despite the numerous simplifications and assumptions that have been made. Enhancing this model by reducing the significance of these assumptions is also a clear direction for further work, namely:

- It is clear that these methods perform well at ordering materials with structurally similar explosophoric moieties. However, better understanding of the electronic structure and decomposition pathways is required to compare across different structure types.
- Explicit consideration of anharmonicity constants may prove important in further resolving differences in predicted sensitivities.
- In this model, the phonon bath has been assumed to remain unchanged by up-pumping. This is clearly not a realistic assumption. Further work is required to include this consideration.
- Further investigation is required to unambiguously define the phonon bath region, particularly in cases such as NTO.

The addition of temperature opens the door to very many possibilities within the model presented in this chapter. In particular in its ability to introduce a shock temperature to model the effects of different input energies. However, an impact is associated with compression of the sample, which has been neglected in this work. Explicit consideration for the effect of pressure on the vibrational structure will therefore be a great asset to developing this model further.

4.8 References

(1) Simpson, R. L.; Urtiew, P. A.; Ornellas, D. L.; Moody, G. L.; Scribner, K. J.; Hoffman, D. M. CL-20 Performance Exceeds That of HMX and Its Sensitivity Is Moderate. *Propellants, Explos. Pyrotech.* **1997**, *22*, 249–255.

(2) Storm, C. B.; Stine, J. R.; Kramer, J. F. Sensitivity Relationships in Energetic Materials. In *Chemistry and Physics of Energetic Materials*; Bulusu, S. N., Ed.; Springer, Dordrecht, 1990; pp 605–639.

(3) Kamlet, M. J.; Adolph, H. G. The Relationship of Impact Sensitivity with Structure of Organic High Explosives. II. Polynitroaromatic Explosives. *Propellants, Explos. Pyrotech.* **1979**, *4* (2), 30–34.

(4) Tsyshevsky, R. V.; Sharia, O.; Kuklja, M. M. Molecular Theory of Detonation Initiation: Insight from First Principles Modeling of the Decomposition Mechanisms of Organic Nitro Energetic Materials. *Molecules* **2016**, *21* (236).

(5) Murray, J. S.; Lane, P.; Politzer, P. Relationships between Impact Sensitivities and Molecular Surface Electrostatic Potentials of Nitroaramatic and Nitroheterocyclic Molecules. *Mol. Phys.* **1995**, *85* (1), 1–8.

(6) Zhang, J.; Zhang, Q.; Vo, T. T.; Parrish, D. A.; Shreeve, J. M. Energetic Salts with Stacking and Hydrogen-Bonding Interactions Lead the Way to Future Energetic Materials. *J. Am. Chem. Soc.* **2015**, *137* (4), 1697–1704.

(7) Rice, B. M.; Sahu, S.; Owens, F. J. Density Functional Calculations of Bond Dissociation Energies for NO 2 Scission in Some Nitroaromatic Molecules. *J. Mol. Struct. THEOCHEM* **2002**, *583* (1), 69–72.

(8) Song, X. S.; Cheng, X. L.; Yang, X. D.; He, B. Relationship between the Bond Dissociation Energies and Impact Sensitivities of Some Nitro-Explosives. *Propellants, Explos. Pyrotech.* **2006**, *31* (4), 306–310.

(9) Kuklja, M. M.; Rashkeev, S. N.; Zerilli, F. J. Shear-Strain Induced Decomposition of 1,1-Diamino-2,2-Dinitroethylene. *Appl. Phys. Lett.* **2006**, *89* (7), 071904.

(10) Kuklja, M. M.; Rashkeev, S. N. Shear-Strain-Induced Chemical Reactivity of Layered Molecular Crystals. *Appl. Phys. Lett.* **2007**, *90* (15).

(11) Mathieu, D. Physics-Based Modeling of Chemical Hazards in a Regulatory Framework: Comparison with Quantitative Structure-Property Relationship (QSPR) Methods for Impact Sensitivities. *Ind. Eng. Chem. Res.* **2016**, *55* (27), 7569–7577.

(12) Fayet, G.; Rotureau, P. Development of Simple QSPR Models for the Impact Sensitivity of Nitramines. *J. Loss Prev. Process Ind.* **2014**, *30* (1), 1–8.

(13) Bondarchuk, S. V. Quantification of Impact Sensitivity Based on Solid-State Derived Criteria. *J. Phys. Chem. A* **2018**, *122*, 5455–5463.

(14) Zhu, W.; Xiao, H. First-Principles Band Gap Criterion for Impact Sensitivity of Energetic Crystals: A Review. *Struct. Chem.* **2010**, *21* (3), 657–665.

(15) Chen, S.; Tolbert, W. A.; Dlott, D. D. Direct Measurement of Ultrafast Multiphonon Up-Pumping in High Explosives. *J. Phys. Chem.* **1994**, *98* (32), 7759–7766.

(16) Joshi, K.; Losada, M.; Chaudhuri, S. Intermolecular Energy Transfer Dynamics at a Hot-Spot Interface in RDX Crystals. *J. Phys. Chem. A* **2016**, *120* (4), 477–489.

(17) Dlott, D. D. Multi-Phonon up-Pumpng in Energetic Materials. In *Overview of Recent Research on Energetic Materials*; Shaw, R. W., Brill, T. B., Thompson, D. L., Eds.; World Scientific, 2005; pp 303–333.

(18) Ye; Koshi, M. Theoretical Studies of Energy Transfer Rates of Secondary Explosives. *J. Phys. Chem. B* **2006**, *110* (37), 18515–18520.

(19) Fried, L. E.; Ruggiero, J. Energy-Transfer Rates in Primary, Secondary, and Insensitive Explosives. *J. Phys. Chem.* **1994**, *98* (39), 9786–9791.

(20) McNesby, K. L.; Coffey, C. S. Spectroscopic Determination of Impact Sensitivities of Explosives. *J. Phys. Chem. B* **1997**, *101* (16), 3097–3104.

(21) McGrane, S. D.; Barber, J.; Quenneville, J. Anharmonic Vibrational Properties of Explosives from Temperature-Dependent Raman. *J. Phys. Chem. A* **2005**, *109* (44), 9919–9927.

(22) Dlott, D. D.; Fayer, M. D. Shocked Molecular Solids: Vibrational up Pumping, Defect Hot Spot Formation, and the Onset of Chemistry. *J. Chem. Phys.* **1990**, *92* (6), 3798–3812.

(23) Bernstein, J. *Ab Initio* Study of Energy Transfer Rates and Impact Sensitivities of Crystalline Explosives. *J. Chem. Phys.* **2018**, *148* (8), 084502.

(24) Meyer, R.; Köhler, J.; Homburg, A. *Explosives*, 6th ed.; Meyer, R., Köhler, J., Homburg, A., Eds.; Wiley-VCH: Weinheim, 2007.

(25) Gamage, N. D. H.; Stiasny, B.; Stierstorfer, J.; Martin, P. D.; Klapötke, T. M.; Winter, C. H. Less Sensitive Oxygen-Rich Organic Peroxides Containing Geminal Hydroperoxy Groups. *Chem. Commun.* **2015**, *51* (68), 13298–13300.

(26) Klapötke, T. M.; Piercey, D. G. 1,1′-Azobis(Tetrazole): A Highly Energetic Nitrogen-Rich Compound with a N10 Chain. *Inorg. Chem.* **2011**, *50* (7), 2732–2734.

(27) Wilson, W. S.; Bliss, D. E.; Christian, S. L.; Knight, D. J. *Explosive Properties of Polynitroaromatics*; China Lake, CA, USA, 1990.

(28) Klapötke, T. M.; Sabaté, C. M. 5,5′-Hydrazinebistetrazole: An Oxidation-Stable Nitrogen-Rich Compound and Starting Material for the Synthesis of 5,5′-Azobistetrazolates. *Zeitschrift fur Anorg. und Allg. Chemie* **2007**, *633* (15), 2671–2677.

(29) Rice, B. M.; Hare, J. J. A Quantum Mechanical Investigation of the Relation between Impact Sensitivity and the Charge Distribution in Energetic Molecules. *J. Phys. Chem. A* **2002**, *106* (9), 1770–1783.

(30) Ledgard, J. *The Preparatory Manual of Explosives, Third Edition*, 3rd ed.; Jared Ledgard, 2007.

(31) Hunter, S.; Davidson, A. J.; Morrison, C. A.; Pulham, C. R.; Richardson, P.; Farrow, M. J.; Marshall, W. G.; Lennie, A. R.; Gould, P. J. Combined Experimental and Computational Hydrostatic Compression Study of Crystalline Ammonium Perchlorate. *J. Phys. Chem. C* **2011**, *115* (38), 18782–18788.

(32) Hunter, S.; Sutinen, T.; Parker, S. F.; Morrison, C. A.; Williamson, D. M.; Thompson, S.; Gould, P. J.; Pulham, C. R. Experimental and DFT-D Studies of the Molecular Organic Energetic Material RDX. *J. Phys. Chem. C* **2013**, *117* (16), 8062–8071.

(33) Hunter, S.; Coster, P. L.; Davidson, A. J.; Millar, D. I. A.; Parker, S. F.; Marshall, W. G.; Smith, R. I.; Morrison, C. A.; Pulham, C. R. High-Pressure Experimental and DFT-D Structural Studies of the Energetic Material FOX-7. *J. Phys. Chem. C* **2015**, *119* (5), 2322–2334.

(34) Deschamps, J. R.; Frisch, M.; Parrish, D. Thermal Expansion of HMX. *J. Chem. Crystallogr.* **2011**, *41* (7), 966–970.

(35) Evers, J.; Klapötke, T. M.; Mayer, P.; Oehlinger, G.; Welch, J. α- and β-FOX-7, Polymorphs of a High Energy Density Material, Studied by X-Ray Single Crystal and Powder Investigations in the Temperature Range from 200 to 423 K. *Inorg. Chem.* **2006**, *45* (13), 4996–5007.

(36) Bolotina, N. B.; Hardie, M. J.; Speer Jr, R. L.; Pinkerton, A. A. Energetic Materials: Variable-Temperature Crystal Structures of {γ}- and {\varepsilon}-HNIW Polymorphs. *J. Appl. Crystallogr.* **2004**, *37*, 808–814.

(37) Akopyan, Z. A.; Struchkov, Y. T.; Dashevskii, V. G. Crystal And Molecular Structure of Hexanitrobenzene. *Zh. Strukt. Khim.* **1966**, *7*, 408.

(38) Cady, H. H.; Larson, A. C. The Crystal Structure of 1,3,5-Triamino-2,4,6-Trinitrobenzene. *Acta Crystallogr.* **1965**, *18* (3), 485–496.

(39) Reany, O.; Kapon, M.; Botoshansky, M.; Keinan, E. Rich Polymorphism in Triacetone-Triperoxide. *Cryst. Growth Des.* **2009**, *9* (8), 3661–3670.

(40) Clark, S. J.; Segall, M. D.; Pickard, C. J.; Hasnip, P. J.; Probert, M. I. J.; Refson, K.; Payne, M. C. First Principles Methods Using CASTEP. *Zeitschrift für Krist.* **2005**, *220*, 567–570.

(41) Hinuma, Y.; Pizzi, G.; Kumagai, Y.; Oba, F.; Tanaka, I. Band Structure Diagram Paths Based on Crystallography. *Comput. Mater. Sci.* **2017**, *128*, 140–184.

(42) Dovesi, R.; Orlando, R.; Erba, A.; Zicovich-Wilson, C. M.; Civalleri, B.; Casassa, S.; Maschio, L.; Ferrabone, M.; De La Pierre, M.; D'Arco, P.; et al. CRYSTAL14: A Program for the Ab Initio Investigation of Crystalline Solids. *Int. J. Quantum Chem.* **2014**, *114* (19), 1287–1317.

(43) Peintinger, M. F.; Oliveira, D. V.; Bredow, T. Consistent Gaussian Basis Sets of Triple-Zeta Valence with Polarization Quality for Solid-State Calculations. *J. Comput. Chem.* **2013**, *34* (6), 451–459.

(44) Heyd, J.; Peralta, J. E.; Scuseria, G. E.; Martin, R. L. Energy Band Gaps and Lattice Parameters Evaluated with the Heyd-Scuseria-Ernzerhof Screened Hybrid Functional. *J. Chem. Phys.* **2005**, *123* (17), 174101.

(45) Tran, F.; Blaha, P.; Schwarz, K.; Novák, P. Hybrid Exchange-Correlation Energy Functionals for Strongly Correlated Electrons: Applications to Transition-Metal Monoxides. *Phys. Rev. B - Condens. Matter Mater. Phys.* **2006**, *74* (15), 155108.

(46) Perdew, J. P.; Burke, K.; Ernzerhof, M. Generalized Gradient Approximation Made Simple. *Phys. Rev. Lett.* **1996**, *77* (18), 3865–3868.

(47) Colognesi, D.; Celli, M.; Cilloco, F.; Newport, R. J.; Parker, S. F.; Rossi-Albertini, V.; Sacchetti, F.; Tomkinson, J.; Zoppi, M. TOSCA Neutron Spectrometer: The Final Configuration. *Appl. Phys. A Mater. Sci. Process.* **2002**, *74*, 64–66.

(48) Pinna, R. S.; Rudić, S.; Parker, S. F.; Armstrong, J.; Zanetti, M.; Škoro, G.; Waller, S. P.; Zacek, D.; Smith, C. A.; Capstick, M. J.; et al. The Neutron Guide Upgrade of the TOSCA Spectrometer. *Nucl. Instruments Methods Phys. Res. Sect. A Accel. Spectrometers, Detect. Assoc. Equip.* **2018**, *896*, 68–74.

(49) Arnold, O.; Bilheux, J. C.; Borreguero, J. M.; Buts, A.; Campbell, S. I.; Chapon, L.; Doucet, M.; Draper, N.; Ferraz Leal, R.; Gigg, M. A.; et al. Mantid - Data Analysis and Visualization Package for Neutron Scattering and μ SR Experiments. *Nucl. Instruments Methods Phys. Res. Sect. A Accel. Spectrometers, Detect. Assoc. Equip.* **2014**, *764*, 156–166.

(50) Dymkowski, K.; Parker, S. F.; Fernandez-Alonso, F.; Mukhopadhyay, S. AbINS: The Modern Software for INS Interpretation. *Phys. B Condens. Matter* **2018**, *In Press*, 1–6.

(51) Crowley, J. M.; Tahir-Kheli, J.; Goddard, W. A. Resolution of the Band Gap Prediction Problem for Materials Design. *J. Phys. Chem. Lett.* **2016**, *7* (7), 1198–1203.

(52) Garza, A. J.; Scuseria, G. E. Predicting Band Gaps with Hybrid Density Functionals. **2016**, *7*, 5–10.

(53) Cooper, J. K.; Grant, C. D.; Zhang, J. Z. Experimental and TD-DFT Study of Optical Absorption of Six Explosive Molecules: RDX, HMX, PETN, TNT, TATP, and HMTD. *J. Phys. Chem. A* **2013**, *117* (29), 6043–6051.

(54) Bredas, J.-L. Mind the Gap! *Mater. Horiz.* **2014**, *1* (1), 17–19.

(55) Appalakondaiah, S.; Vaitheeswaran, G.; Lebègue, S. Dispersion Corrected Structural Properties and Quasiparticle Band Gaps of Several Organic Energetic Solids. *J. Phys. Chem. A* **2015**, *119* (24), 6574–6581.

(56) Appalakondaiah, S.; Vaitheeswaran, G.; Lebègue, S. Structural, Vibrational, and Quasiparticle Band Structure of 1,1-Diamino-2,2-Dinitroethelene from Ab Initio Calculations. *J. Chem. Phys.* **2014**, *140* (1).

(57) Hu, A.; Larade, B.; Abou-Rachid, H.; Lussier, L. S.; Guo, H. A First Principles Density Functional Study of Crystalline FOX-7 Chemical Decomposition Process under External Pressure. *Propellants, Explos. Pyrotech.* **2006**, *31* (5), 355–360.

(58) Kuklja, M. M.; Rashkeev, S. N. Shear-Strain-Induced Structural and Electronic Modifications of the Molecular Crystal 1,1-Diamino-2,2-Dinitroethylene: Slip-Plane Flow and Band Gap Relaxation. *Phys. Rev. B - Condens. Matter Mater. Phys.* **2007**, *75* (10), 104111.

(59) Yuan, B.; Yu, Z.; Bernstein, E. R. Initial Decomposition Mechanism for the Energy Release from Electronically Excited Energetic Materials: FOX-7 (1,1-Diamino-2,2-Dinitroethene, C2H4N4O4). *J. Chem. Phys.* **2014**, *140* (7).

(60) Chakraborty, D.; Muller, R. P.; Dasgupta, S.; Goddard, W. A. Mechanism for Unimolecular Decomposition of HMX (1,3,5,7-Tetranitro-1,3,5,7-Tetrazocine), an Ab Initio Study. *J. Phys. Chem. A* **2001**, *105* (8), 1302–1314.

(61) Kim, H.; Dlott, D. D. Theory of Ultrahot Molecular Solids: Vibrational Cooling and Shock-Induced Multiphonon up Pumping in Crystalline Naphthalene. *J. Chem. Phys.* **1990**, *93* (3), 1695–1709.

(62) Coffey, C. S.; Toton, E. T. A Microscopic Theory of Compressive Wave-Induced Reactions in Solid Explosives. *J. Chem. Phys.* **1982**, *76* (2), 949–954.

(63) Zhang, G.; Weeks, B. L. A Device for Testing Thermal Impact Sensitivity of High Explosives. *Propellants, Explos. Pyrotech.* **2010**, *35* (5), 440–445.

Chapter 5

Vibrational Up-Pumping in Polymorphic Materials

5.1 Introduction

Due to the flexibility of molecules and the low directionality of their weak intermolecular interactions, molecules can adopt a variety of packing arrangements upon crystallisation. Hence, the same compound can exist in different crystal forms, or polymorphs. This phenomenon is widespread across molecular materials, with Walter McCrone famously stating that "*every compound has different polymorphic forms and the number of forms known for a given compound is proportional to the time and energy spend in research on that compound*."[1] Different polymorphic forms can be obtained during crystallization, for example by controlling the speed, temperature or pressure under which nucleation occurs.[2,3] Alternatively, polymorphs can interconvert upon heating or application of external pressure.[4,5] Polymorphic forms are known to exhibit drastically different physical properties. This phenomenon has therefore been strongly monitored by the pharmaceutical industry, where polymorphs can exhibit, for example, different solubilities[6] and compressibilities.[7] Hence, a drug composition that is prepared based on one polymorph can behave differently than that based on another polymorphic form.

Energetic materials (EMs) are also highly prone to polymorphism. Some of the most well-known EMs exhibit rich polymorphism. For example, RDX is known to exist in at least two polymorphic forms under ambient conditions, the α- and β-forms, and two additional forms can be obtained under hydrostatic pressures,

γ-RDX at *ca.* 5.2 GPa[8] and δ-RDX at *ca.* 17.8 GPa. A fifth form, ϵ-RDX, has also been identified on simultaneous application of heat and pressure.[9] Other well-known EMs, such as CL-20, TNT, ammonium perchlorate and ammonium nitrate, also exhibit rich polymorphism. As polymorphic transformations often occur when a material is exposed to extremes of temperature and pressure, their occurrence is crucial to understanding the detonation pathways of EMs.

Despite knowledge of their existence, most EM literature does not explicitly consider polymorphic modifications during impact testing. A notable exception is HMX, Figure 5.1. Under ambient conditions HMX exists in the monoclinic β-form. The orthorhombic α-form can be obtained from recrystallisation under elevated temperatures and is stable between 377 and 429 K, and can be recovered to ambient conditions.[10] The δ-form is obtained by heating the β-form, and is stable above 429 K.[11] While highly metastable, the δ-form can be recovered to ambient conditions upon quench cooling.[10] A fourth form, a hydrate (often denoted γ-HMX) is also known to be readily prepared under ambient conditions on rapid recrystallisation of β -HMX from aqueous solutions.[10]

The absolute sensitivity of the δ-form is open to debate, although it is accepted to be considerably more sensitive to impact than the β-form.[12] A thorough analysis of reported sensitivities by Cady and Smith,[10] and subsequent work by Scott,[13] suggests δ -HMX to have a comparable impact sensitivity to pentaerythritol tetranitrate (PETN), the highest sensitivity secondary explosive (*ca.* 3 J)[14] in common use. Other reports have suggested δ-HMX to be as sensitive as lead azide ($<$ 1 J)[15] or other primary explosives.[16] While the exact level to which δ-HMX is more sensitive than the β-form remains uncertain, it is clear that they do exhibit very different sensitivity properties. The available literature therefore suggests the impact sensitivity ordering for HMX as $\delta > \gamma > \alpha > \beta$.[10]

To date, no high-pressure forms of HMX have been structurally characterised. However, some experiments do suggest two potential high-pressure transitions under quasi-hydrostatic conditions.[17,18] A conformational transition

(*i.e.* associated with a small change in the molecular geometry, without a large change in the crystallographic structure) was observed at *ca.* 12 GPa, with an abrupt phase transition observed above 27 GPa. [18]

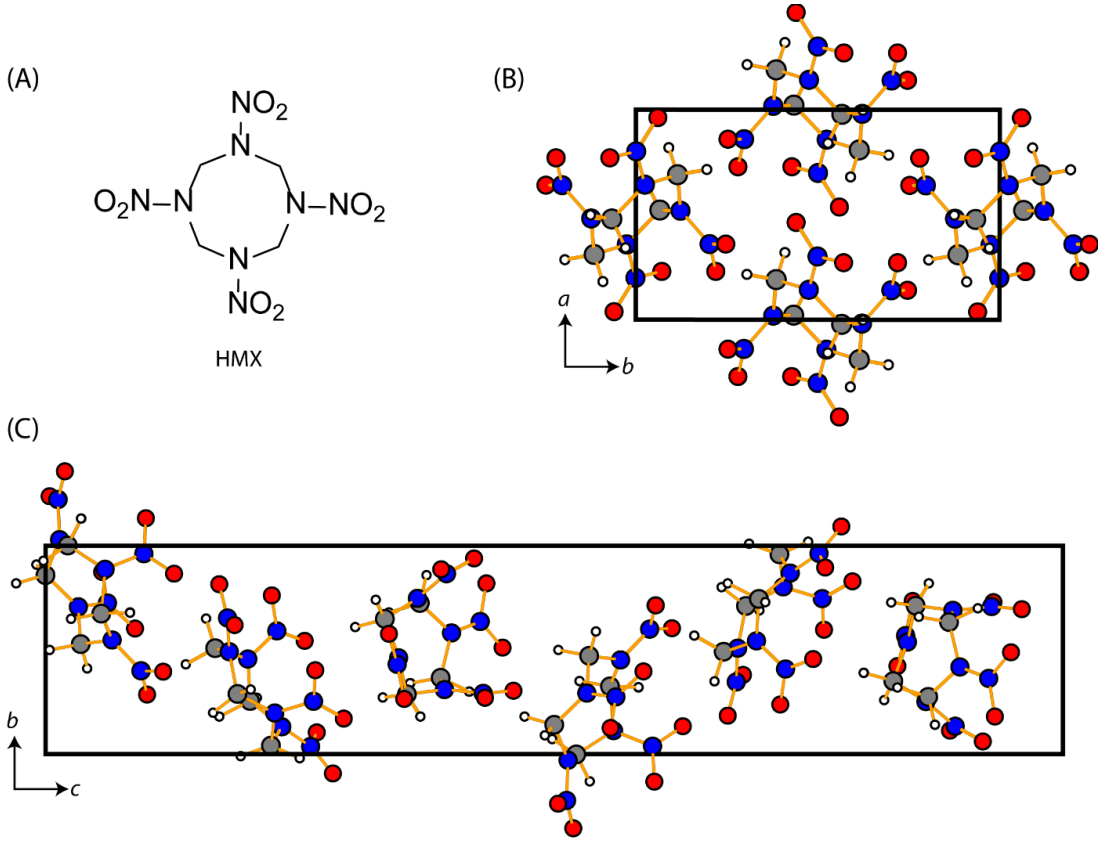

Figure 5.1: Structure of HMX. (A) Schematic representation of the HMX molecule. (B) Crystal structure of β-HMX $P2_1/c$ (CCDC Ref: OCHTET01). (C) Crystal structure of δ-HMX $P6_1$ (CCDC Ref: OCHTET03). Atoms are coloured as (red) oxygen, (blue) nitrogen, (grey) carbon, and (white) hydrogen.

FOX-7 is also well known to be polymorphic. Under ambient conditions, FOX-7 is stable as the monoclinic α-phase. Upon heating, two phase transitions occur, first to β-FOX-7 at 111 °C, and subsequently to γ-FOX-7 at 173 °C.[19] These transitions correspond to an increased layering of the FOX-7 molecules, Figure 5.2. Spectroscopic investigations and thermal analysis have suggested a fourth high-temperature phase (δ-FOX-7) to exist immediately prior to the decomposition temperatures (*i.e.* at T > 230 ºC), although no crystal structure

has yet been obtained. Some reports suggest that the δ-phase is simply a decomposition product of the γ-phase.[20] The application of pressure has also been demonstrated to yield a variety of polymorphic transformations, including formation of two new phases on compression of α-FOX-7 to *ca.* 2 GPa and 5 GPa,[19,21] denoted the α' and ϵ phases, respectively. The latter has been suggested to play a role in the shock-induced processes of FOX-7.[20]

It is generally accepted that energetic materials that adopt layered crystal packing (*e.g.* TATB) display lower sensitivities, although no underlying mechanism for this effect has been deduced. Two common theories include:

1 Increased hydrogen bonding, which forms upon layering, leads to dissipation of energy through the layers[22]
2 Slip planes associated with layered materials[23,24]

Some have also proposed that a higher inter-layer compressibility of layered materials effectively decreases the energy input from an impact. However, in accordance with Equation 3.1, a larger compressibility in fact does quite the opposite, and leads to a larger proportion of the impact energy converting into heat, rather than work. This has the effect of enhancing the direct excitation of the molecules in the system. In line with the theory proposed in Chapter 4, higher compressibility also leads to hardening of vibrational modes and thus enhances up-pumping. Instead, the lower compressibility of hydrogen-bonded layers has instead been proposed to account for the lower sensitivity of layered materials. [22]

The polymorphs of FOX-7 therefore offer an opportunity to test the up-pumping model developed in this thesis, on the effects of how layered structures influence impact sensitivity.

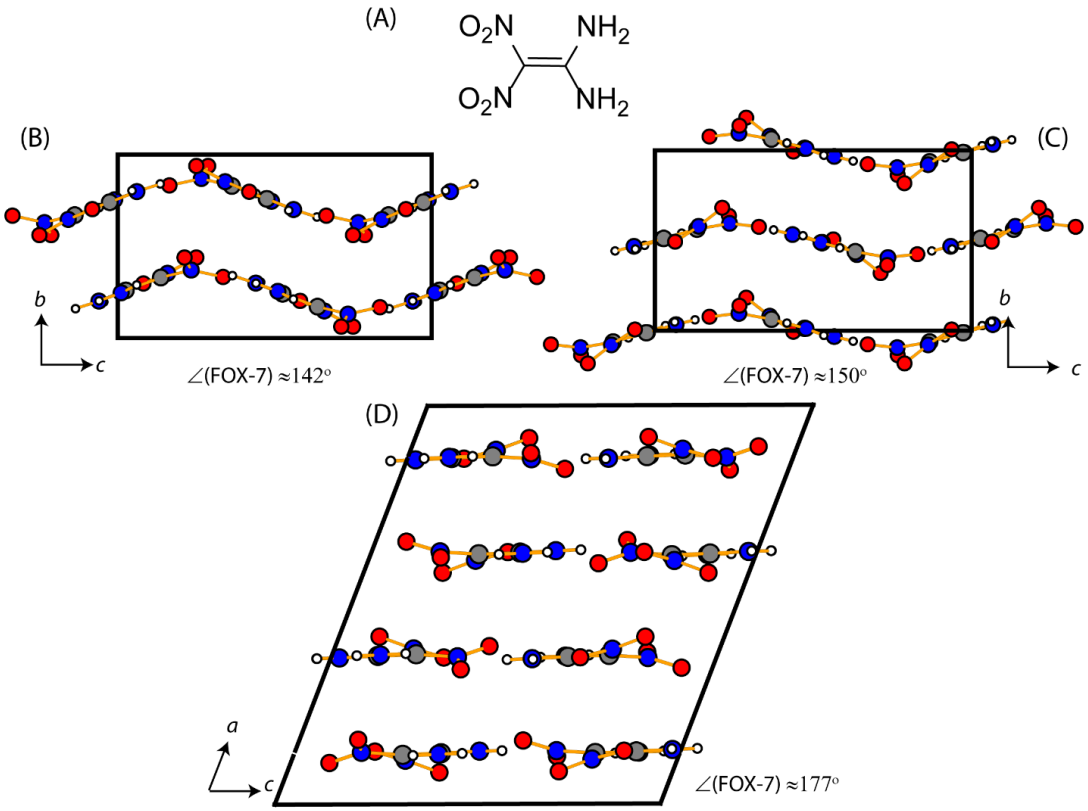

Figure 5.2: Structure of FOX-7. (A) Schematic representation of the FOX-7 molecular structure. (B) Crystal structure of α-FOX-7 $P2_1/n$ (CCDC Ref: SEDTUQ03). (C) Crystal structure of β-FOX-7 $P2_12_12_1$(CCDC Ref: SEDTUQ06). (C) Crystal structure of γ-FOX-7 $P2_1/n$ (From Crawford *et al* [25]). The angle between FOX-7 molecules (∠(FOX-7)) is given in each case. Atoms are coloured as (red) oxygen, (blue) nitrogen, (grey) carbon and (white) hydrogen.

5.2 Aims

The work in this chapter seeks to use the model employed in Chapters 3 and 4 to investigate two polymorphic systems: HMX and FOX-7. The former contains two polymorphs that are well-known to exhibit very different impact sensitivities, while the impact sensitivities of the latter have yet to be experimentally reported. This chapter therefore aims to:

- Determine whether the up-pumping model is sensitive to polymorphic modifications

- Experimentally determine the impact sensitivity of the γ-polymorph of FOX-7
- Explore the effects of increased layering on the sensitivity of energetic materials
- Rationalise the sensitivity of FOX-7 polymorphs based on the up-pumping model.

5.3 Materials

Synthesis of FOX-7. Preparation of 1,1-diamino-2,2-dinitroethene (DADNE, FOX-7) followed from Scheme 5.1.[26] 2-methyl-4,6-pyrimidinedione (6.0 g, 0.05 mol) was dissolved in concentrated H_2SO_4 (95%, 45 mL), at temperatures < 30 ^oC. Concentrated HNO_3 (99%, 20 mL) was subsequently added dropwise maintaining temperatures < 20 ^oC, and the sample stirred for 3 hours. The resulting material was rinsed in concentrated H_2SO_4, added to deionized water (100 mL) and stirred for 2 hours. The resulting product was analysed by ^1H and ^{13}C NMR, and subsequently by X-ray powder diffraction.

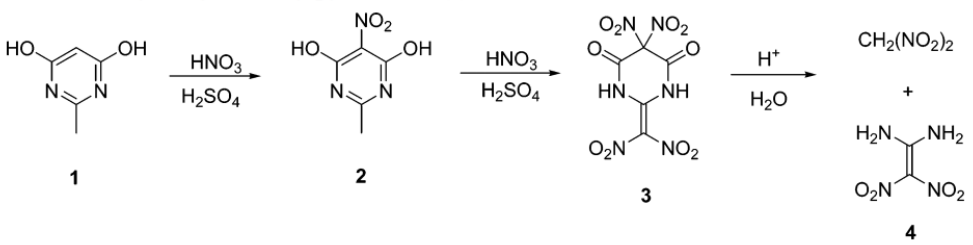

Scheme 5.1: Synthetic approach for preparation of FOX-7.

Preparation of γ-*FOX-7*. The metastable γ-form was prepared by heating the α-form to 180 ^oC for approximately 2 hours, and quench cooling the material to ambient conditions. The phase purity was confirmed by X-ray powder diffraction.

Preparation of δ-*HMX.* A sample of β-HMX was slowly heated in a furnace to 190 ^{o}C,[27] and held at this temperature for *ca.* 12 hours. The sample was quench cooled with an ice bath, and the polymorphic phase verified by X-ray powder diffraction. The sample was stored under an N_2 atmosphere for approximately 1 day prior to INS analysis.

BAM Drop Hammer Testing. BAM fall hammer testing (BFH-12) was conducted at the Cavendish Laboratory, University of Cambridge. A sample of *ca.* 40 mm^3 was placed in an anvil device and sealed between two co-axial steel cylinders. The anvil components were disposed of between each sample test. In this work, the Limiting Energy (1-in-6) go/no-go criterion was used;[28] a 'go' was considered when a flash, audible explosion or discolouration of the sample (black) or scorch marks on the anvil was observed.

X-ray Powder Diffraction. All solid samples were analysed by powder X-ray diffraction using a D2 PHASER diffractometer, with Cu K_α radiation (λ = 1.5406 Å). Data were collected in Bragg-Brentano geometry over the range 2θ = 5-50^0 (*d*-spacing ≈ 1.8-17 Å).

Inelastic Neutron Scattering Spectroscopy. Inelastic neutron scattering spectra were collected on the TOSCA[29,30] spectrometer at the ISIS Neutron and Muon Facility. Samples (*ca.* 1.5 g) were placed in aluminium sample holders. The samples were cooled to *ca.* 10 K and spectra collected for a total of *ca.* 400 μAh. Data from the forward- and backward-scattering detectors were summed and corrected for scattering from the sample container and background. Data processing was performed using the Mantid software.[31] Simulated INS spectra were generated using ABINS[32] as implemented in Mantid.

Condensed Matter Calculations. All condensed matter vibrational calculations were based on experimental crystal structures. Structures for δ -HMX (OCHTET03) and β-FOX-7 (SEDTUQ06) were sourced from the Cambridge Crystallographic Data Centre (CCDC). The input structure for γ-FOX-7 was taken from Crawford *et al.*[25] Data for β-HMX and α-FOX-7 were taken from Chapter 4. All structures were optimised using plane-wave DFT (pw-DFT) as

implemented in CASTEP v16.[33] The GGA functional of Perdew-Burke-Ernzerhof[34] (PBE) was used along with Grimme's D2 dispersion correction scheme,[35] PBE-D2. This scheme has previously been demonstrated to perform well for these materials.[21,36] The electronic wavefunction was expanded in plane waves to a kinetic energy cut-off of 1800 eV (α-FOX-7), 1300 eV (β-HMX, δ-HMX and β-FOX-7) and 950 eV (γ-FOX-7). All forces were converged to $< 5 \times 10^{-4}$ eV/Å and stresses to $< 5 \times 10^{-4}$ GPa. γ-FOX-7 was converged to less stringent parameters, forces $< 1 \times 10^{-3}$ eV/ Å and stresses to $< 1 \times 10^{-3}$ GPA. The energy change per atom was accepted after convergence $< 5 \times 10^{-9}$ eV/atom for all cases except γ-FOX-7, for which a convergence was accepted $< 1 \times 10^{-8}$ eV/atom. The electronic structure was sampled on a *k*-point Monkhorst-Pack[37] (MP) grid with spacing no more than 0.05 $Å^{-1}$. Norm-conserving pseudopotentials were used throughout. Optimised geometries are summarized in Table 5.1.

Table 5.1: Optimisation Parameters for the HMX and FOX-7 materials investigated here.

	a	b	c	α	β	γ	V	ΔV
β-HMX^{exp}	6.525	11.024	7.362	90	102.642	90	516.675	+4.00%
β-HMX^{calc}	6.624	11.256	7.373	90	102.222	90	537.299	
δ-HMX^{exp}	7.711	7.711	32.553	90	90	120	1676.270	+0.57%
δ-HMX^{calc}	7.670	7.670	33.091	90	90	120	1685.860	
α-FOX-7^{exp}	6.934	6.622	11.312	90	90.065	90	519.470	+2.20%
α-FOX-7^{calc}	7.089	6.623	11.440	90	91.273	90	530.898	
β-FOX-7^{exp}	6.974	6.635	11.648	90	90	90	538.943	+1.12%
β-FOX-7^{calc}	7.093	6.495	11.830	90	90	90	544.967	
γ-FOX-7^{exp}	13.354	6.895	12.050	90	111.102	90	1035.110	+5.02%
γ-FOX-7^{calc}	13.565	7.084	12.224	90	112.247	90	1087.170	

Phonon calculations were performed using the linear response method as implemented in CASTEP v16 at either the Γ-point or sampled across the Brillouin zone on a regular grid of wave vectors and subsequently Fourier interpolated onto a finer grid. Electronic band structures were calculated using localized basis sets (H- H_pob_TZVP_2012[38]; C- C_m-6-311G(d)_Heyd_2005[39]; N- N_m-6-311G(d)_Heyd_2005[39]; O- O_m-6-311G(2d)_Heyd_2005[39]) within the CRYSTAL17 code,[40] based on

experimental structures. Band structures were generated using the HSE06,[39] B3PW91[41] and PBE[34] functionals. Electronic structure was calculated across no less than 120 *k*-points, evenly spaced across an MP grid. The wavefunction was accepted after the absolute change in SCF cycle energies was < 10^{-8}. For all materials, the tolerances (TOLINTEG) were set at 7 7 7 9 30 (as recommended for use with these basis sets[39]).

5.4 Results and Discussion

5.4.1 Polymorphism of HMX

5.4.1.1 Electronic Structure of HMX Polymorphs

The calculated band gaps for both β- and δ-HMX were found to be approximately the same, with the δ-form exhibiting a slightly larger band gap than the β-form, Table 5.2. Furthermore, δ-HMX exhibits an indirect band gap for all three functionals, while two of the three functionals suggest that β-HMX has a direct band gap. Any correlation to the 'band gap criterion'[42] (*i.e.* that the more sensitive material has the smaller band gap) therefore does not hold when considering these two polymorphs of HMX.

With no notable electronic differences in the solid state, it is therefore worth considering a vibrational basis to rationalise the sensitivity differences.

Table 5.2: Band gaps for δ-HMX as compared to those for β-HMX. Band gaps are indicated as direct (D) or indirect (I).

	B3PW91	PBE	HSE06
β-HMX	5.4954 (D)	3.6826 (I)	5.2176 (D)
δ-HMX	5.7422 (I)	3.7011 (I)	5.4745 (I)

5.4.1.2 Vibrational Structure of HMX Polymorphs

The primitive unit cell of δ-HMX is considerably larger than that of β-HMX, and it was therefore not possible to obtain a full phonon dispersion curve for the former. However, as demonstrated in Section 4.5.3.5, for the materials which exhibit negligible dispersion, the zone-centre frequencies are sufficient for consideration of the vibrational up-pumping model. Given the low dispersion of the β-polymorph (see Chapter 4.5.2), it is reasonable to expect a similar character in the δ-form.

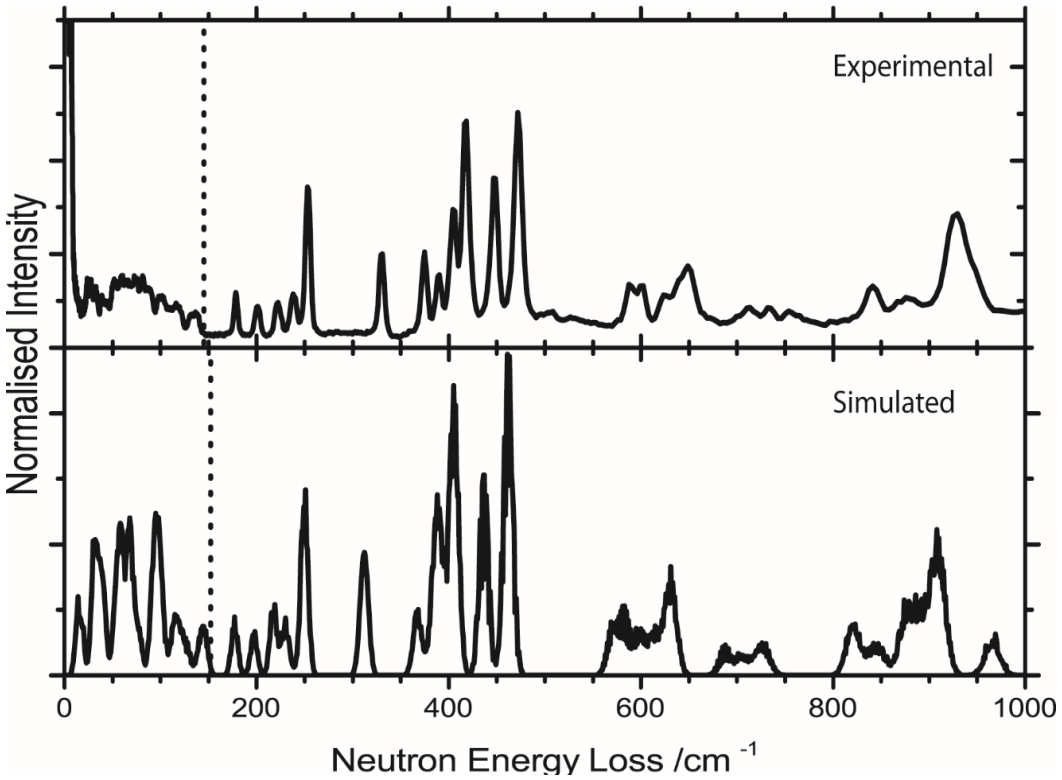

Figure 5.3: Inelastic neutron scattering spectra of δ-HMX at *ca.* 10 K. (Top) The experimental pattern and (Bottom) simulated patterns are given. The latter is generated from Γ-point frequencies only. The vertical dotted line indicates Ω_{max} in each case.

The zone-centre vibrational structure for δ-HMX was therefore calculated, and compared to experimental INS data, Figure 5.3. There is generally very good agreement between the simulated and experimental frequencies. The value of Ω_{max} sits only *ca.* 5 cm^{-1} lower in the experimental pattern as compared to the simulated pattern, with the close comparison suggesting little band dispersion exists at the top of the phonon bath. The frequencies are very well reproduced

across the INS spectrum, underestimated by only 2-3% across most modes, Table 5.3. A notable exception is M_5, which is underestimated by *ca.* 6% in the simulated pattern. This corresponds to the deformation modes of the HMX ring, and suggests that PBE-D2 may struggle in reproducing some internal modes of these materials, which is also apparent when the higher frequency modes with $\omega > 1000$ cm^{-1} are considered. This was also noted in Chapters 3 and 4 for the internal frequencies of other materials. Overall, however, it appears that the model used is in general a good reproduction of the experimental vibrational structure for δ-HMX.

Table 5.3: Comparison of simulated (Γ-point only) and experimental INS frequencies for well-resolved peaks. The difference is given as a percentage over the experimental value.

	INS	Calc.	Δω /%
Ω_{max}	178	177	-0.56%
M_1	201	198	-1.49%
M_2	222	218	-1.80%
M_3	238	230	-3.48%
M_4	253	250	-1.19%
M_5	331	312	-5.74%
M_6	374	367	-1.87%
M_7	390	382	-2.05%
M_8	404	388	-3.96%
M_9	418	405	-3.01%
M_{10}	448	436	-2.68%
M_{11}	471	461	-2.12%
M_{12}	587	561	-4.43%
M_{13}	649	631	-2.77%
M_{14}	710	688	-3.10%
M_{15}	735	703	-4.35%
M_{16}	753	730	-3.05%
M_{17}	837	820	-2.03%
M_{18}	924	908	-1.73%
M_{19}	1026	970	-5.46%

The phonon density of states, $g(\omega)$, and two-phonon density of states, $\Omega^{(2)} = \delta(\omega - \omega_1 - \omega_2)$, are given in Figure 5.4, under the restriction $\omega_2 < \Omega_{max}$. The value of Ω_{max} is placed at 160 cm^{-1} in δ-HMX, which agrees well with both the theory and INS spectra. Based on analysis of the $g(\omega)$, an alternative would be to place it at 260 cm^{-1}, above the ring deformation modes that span the region $160 < \omega < 260$ cm^{-1}. However, no evidence exists to suggest this is a more appropriate placement of Ω_{max}, and the former will subsequently be used.

While Ω_{max} is found to be lower for δ-HMX (160 cm^{-1}) than in the β-form (195 cm^{-1}), the doorway region ($\Omega_{max} < \omega < 2\Omega_{max}$) is notably denser in the former (7.1 vs 4.4 states per atom). Hence it can already be suggested that the δ-form will be more readily excited by vibrational up-pumping. Furthermore, the onset of $\Omega^{(2)}$ occurs approximately 50 cm^{-1} earlier in δ-HMX, and grows much more rapidly than for β-HMX. Qualitatively, all of these factors suggest the δ-form to be more sensitive according to the up-pumping model.

To compare the two polymorphs, vibrational up-pumping was considered in line with the two most promising models from Chapter 4, but now applied to Γ-point data only: (1) the contribution of the first two overtones to the region $\Omega_{max} \rightarrow 3\Omega_{max}$, and (2) the two-level model under an equilibrium temperature of 300 K. Note that as in Chapter 4, the lack of a specific target frequency requires consideration of an 'indirect' phonon up-conversion mechanism.[43] Hence up-pumped values are normalised by $\int g(\omega)$.

In the first model, the two lowest order overtones (*i.e.* the fastest coupling pathways) are generated, Figure 5.5, and their projection onto $g(\omega)$ are considered, *i.e.* $P(g(\omega))$, which is then normalized by $\int g(\omega)$. As only the first two overtones are included, this restricts the upper value for integration to $3\Omega_{max}$, with the resulting $\int P(g(\omega))$ for δ-HMX (~6.62 a.u.) > β-HMX (~5.85 a.u.). Thus the overtone up-pumping model suggests more pathways exist for the δ-form. As such δ-HMX is therefore predicted to be more sensitive to impact than the β-form, and ranks the sensitivities as HNB > δ-HMX ≈ TATP > ABT > β-HMX according to Figure 4.25.

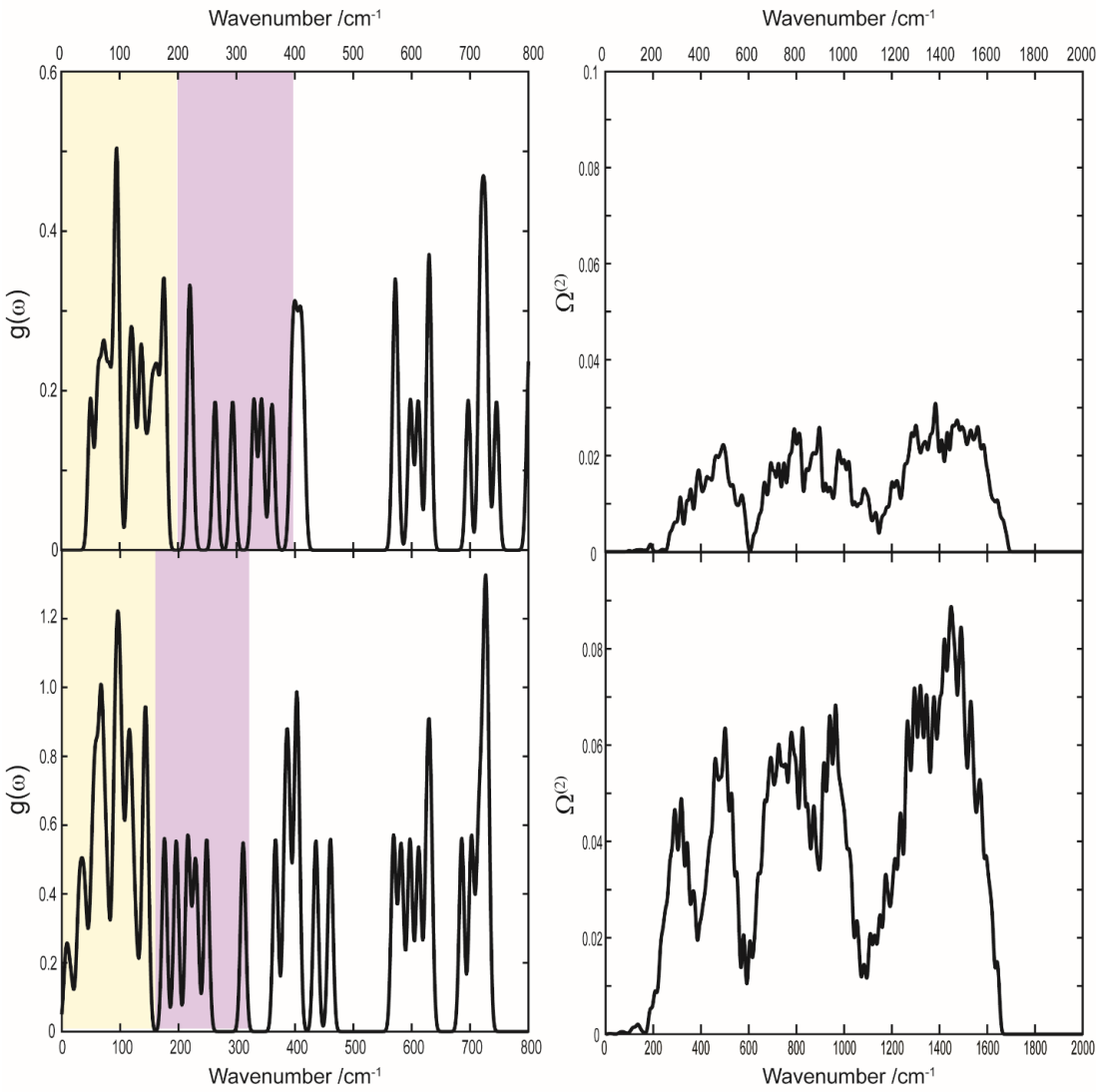

Figure 5.4: Comparison of the vibrational structure of two HMX polymorphs. (Top) $g(\omega)$ and $\Omega^{(2)}$ for β-HMX, and (bottom) $g(\omega)$ and $\Omega^{(2)}$ for δ-HMX. $0 \rightarrow \Omega_{max}$ and $\Omega_{max} \rightarrow 2\Omega_{max}$ are identified in $g(\omega)$ by yellow and purple, respectively. Note that $\Omega^{(2)}$ have been normalised by $\int g(\omega)$ to account for a different number of atoms (and hence vibrational modes) in the unit cell according to the indirect up-pumping mechanism.

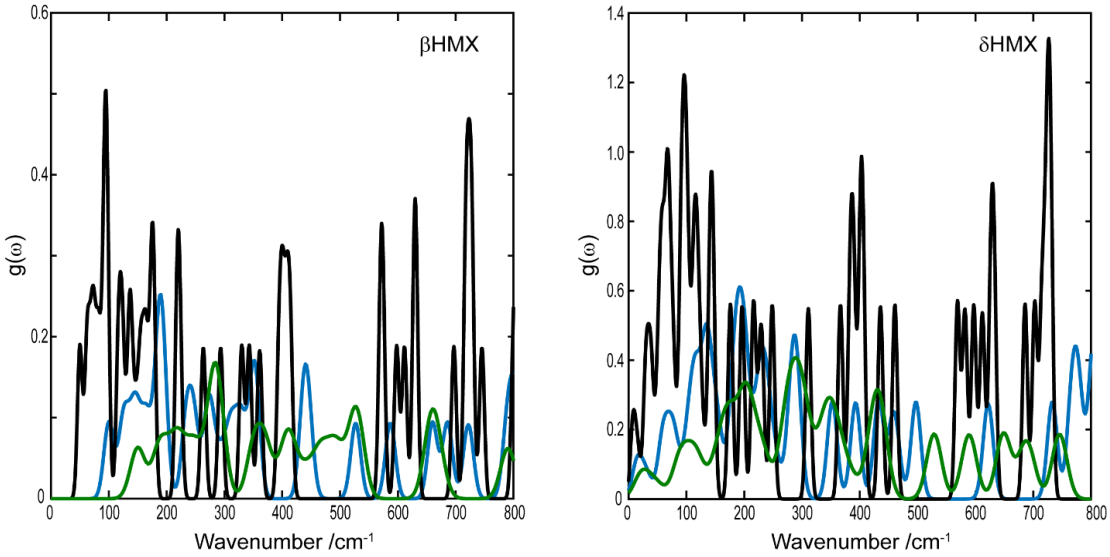

Figure 5.5: Overtone contributions to vibrational up-pumping in HMX polymorphs. The overtones are shown for (blue) $N = 2$ and (green) $N = 3$, and overlain by $g(\omega)$ (black).

Within the two-layer model, the populations from the first overtone (with T = 300 K) are projected onto the doorway region, and up-pumped with the underlying phonon modes *via* combination pathways. As $\Omega^{(2)}$ (see Figure 5.4) does not drop to zero < 1800 cm^{-1} for either polymorph, up-pumping contributions to $\omega < 1800$ cm^{-1} are considered for both. This results in $\int \Omega^{(2)}$ for δ-HMX (~200 a.u.) > β-HMX (~32 a.u.), which again reproduces the experimental observation that δ-HMX is more sensitive than the β-form. For the two-layer model the sensitivity ordering is TATP ≈ δ-HMX > HNB > ABT > β-HMX according to Figure 4.25, which does appear to place δ-HMX somewhat higher in sensitivity than expected experimentally. However, it clearly places it in line with the other highly impact-sensitive compounds.

To summarise, it is clear that both up-pumping models predict that the δ-form should be notably more sensitive to impact than the β-form, consistent with experimental reports. Thus, while this is a limited test set, it does suggest that the vibrational up-pumping model is sensitive not only to different molecular materials, but also to different crystallographic forms of the same energetic molecule.

5.4.2 Polymorphism of FOX-7

Having demonstrated the ability of the up-pumping model to distinguish between different polymorphic forms of HMX, the three temperature-related FOX-7 polymorphs were considered next.

5.4.2.1 Experimental Impact Sensitivity

Samples of both α- and γ-FOX-7 were subjected to impact sensitivity testing using the BAM fall-hammer with 'go/no-go' criteria. A sample of α-FOX-7 was first subjected to testing, Table 5.4, with an impact sensitivity of *ca.* 8 J according to the 1/6 Limiting Impact sensitivity criteria. This is clearly more sensitive than is reported based on the h_{50} statistics (E_{50} ≈ 24-30 J)[44]. The 1/6 method indicates the lower end of the sensitivity sigmoidal curve shown in Chapter 2, and hence is always lower than the h_{50} value. Moreover, it is known that FOX-7 sensitivity increases with decreasing particle size, with a limiting value of *ca.* 10-11 J having been reported in literature.[44]

Table 5.4: BAM impact sensitivity results for α-FOX-7. A 'go' is indicated as ✓ and 'no-go' by ×.

			Trial Number					
Mass /kg	**Height /cm**	**Energy /J**	**1**	**2**	**3**	**4**	**5**	**6**
5	22.4	11.20	✓					
	17.8	8.90	✓					
1	89.1	8.91	×	×	×	×	×	✓
	79.4	7.94	×	✓				
	70.8	7.08	×	×	×	×	×	×

A sample of α-FOX-7 was subsequently heated to convert it to γ-FOX-7. The α → γ phase transition is a single-crystal to single-crystal transformation.[25] Hence, the particle size distribution can be taken to be the same across the two polymorphic forms, on the basis that no reconstructive phase transition occurs. When this sample was subjected to BAM hammer testing, the impact sensitivity was found to be the same to within the experimental error of the measurement, Table 5.5. This was unexpected given the extreme insensitivity

of other layered compounds,[45] including those based on the same energetic material.[46]

Table 5.5: BAM impact sensitivity results for γ-FOX-7. A 'go' is indicated as ✓ and 'no-go' by ×.

			Trial Number					
Mass /kg	**Height /cm**	**Energy /J**	**1**	**2**	**3**	**4**	**5**	**6**
5	31.6	15.80	✓					
	28.2	14.10	✓					
	25.1	12.55	✓					
	22.4	11.20	✓					
	20	10.00	×	×	✓			
1	89.1	8.91	×	✓				
	79.4	7.94	×	×	×	×	×	×

Powder samples that did not initiate on impact were therefore analysed by X-ray powder diffraction (XRPD), Figure 5.6. It was surprising to find that all of the material that had been subjected to BAM hammer testing had converted to the α-form, while the material that had not, remained as the γ-form for a period of at least three days (under ambient conditions) following the experiments, Figure 5.6. This suggests that upon impact, there is a γ → α phase transition, which is presumably responsible for the similarities between the impact sensitivity of the layered and non-layered polymorphs. Further work is required to determine the cause of this transition: pressure, shear, temperature or their combination. This demonstrates a clear deficiency in the applications of BAM hammer testing to the study of polymorphic materials. Upon impact, phase transitions may be possible. Thus, the material which is actually analysed during an experiment may not be the intended material and can therefore lead to potentially erroneous reports and conclusions. Without a clear method to determine the sensitivity of the γ-polymorph experimentally, the three phases of FOX-7 were therefore analysed in the framework of the vibrational up-pumping models developed in this thesis.

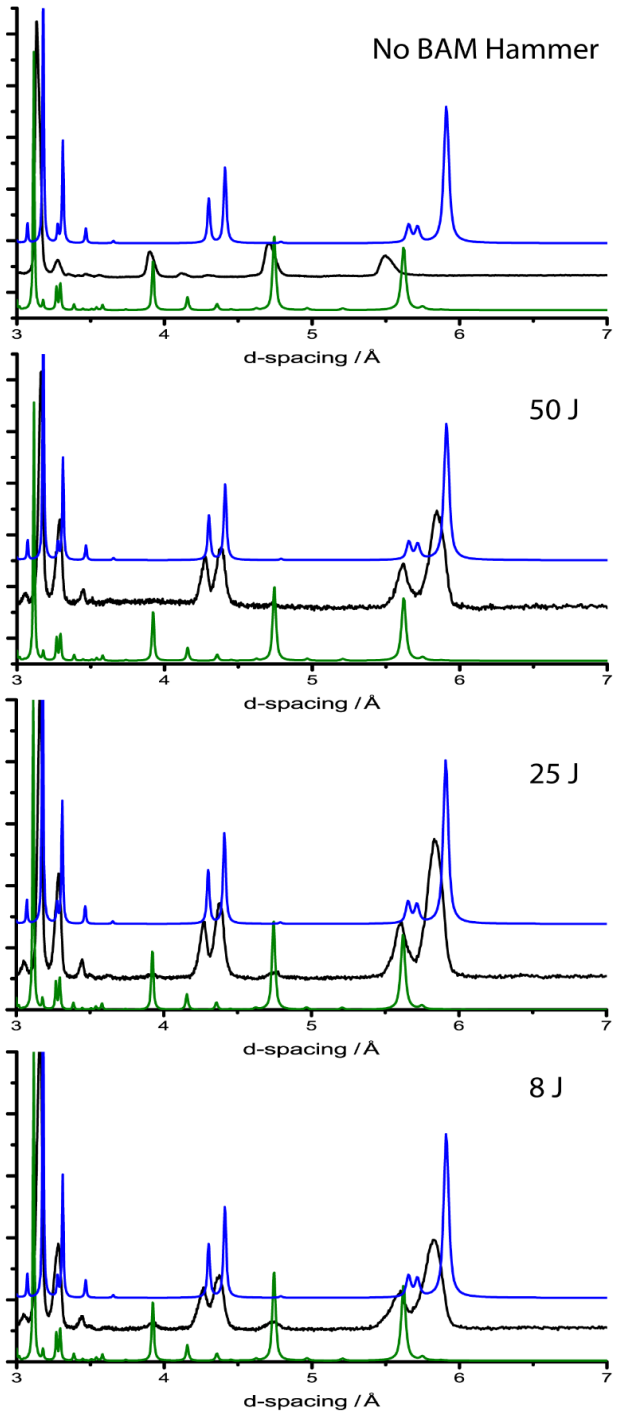

Figure 5.6: XRPD profiles for FOX-7 before and after BAM hammer treatment. Experimental patterns (black) are compared to simulated (blue) α-FOX-7 and (green) γ-FOX-7 in all cases. Note a small offset in the position of the experimental peak of γ-FOX-7 at $d \approx 5.5$ Å, which corresponds to the crystallographic (0 0 2) plane. This offset is due to minor misalignment of the diffractometer and sample geometry.

5.4.2.2 Electronic Structure

Despite the failings of the 'band gap' criterion across the series of molecular energetic compounds in Section 4.5.1, it was nevertheless worthwhile considering this effect for the polymorphic forms of FOX-7. The electronic structure of the three polymorphs of FOX-7 were therefore calculated using the same three functionals as in Section 4.5.1 and 5.4.1.1. and are summarised in Table 5.6. There does appear to be a very slight increase in the band gap as the material becomes increasingly layered.

Table 5.6: Band gap values for the three polymorphs of FOX-7. Band gaps are labelled as direct (D) or indirect (I) in each case.

Material	*B3PW91*	*PBE*	*HSE06*
α-FOX-7	*3.9833 (I)*	*2.4483 (I)*	*3.6719 (I)*
β-FOX-7	*4.2252 (I)*	*2.6643 (I)*	*3.9169 (I)*
γ-FOX-7	*4.2462 (I)*	*2.5866 (D)*	*3.9430 (I)*

5.4.2.3 Vibrational Up-Pumping in FOX-7 Polymorphs

Note that the phonon dispersion curve for γ-FOX-7 was calculated by Ms S Piggott (Master's student, EaStCHEM School of Chemistry, University of Edinburgh).

It is hence worth considering the sensitivity of the polymorphs within the up-pumping models of impact sensitivity that have been built in Chapters 3 and 4. The phonon dispersion curves and associated density of states for all three polymorphs of FOX-7 are given in Figure 5.7. Note the imaginary frequency associated with the two lowest acoustic branches at *q*-point B (-0.5 0 0). This vector runs perpendicular to the FOX-7 planes. As γ-FOX-7 is highly metastable, further work is required to determine the validity of this result, although it is not expected to have any notable consequence on the following discussion. As the FOX-7 layers become increasingly planar, the energy gap between Ω_{max} and the doorway mode region increases, with Ω_{max} found at 185 cm^{-1}, 170 cm^{-1} and 160 cm^{-1} for the α-, β- and γ-polymorphs, respectively.

This decrease in Ω_{max} is due to softening of the NO_2 rocking modes that are polarized perpendicular to the FOX-7 planes and therefore soften upon layering. Within the framework of vibrational up-pumping, this has the effect of reducing the density of the doorway manifold, $\Omega_{max} < \omega < 2\Omega_{max}$ (see Figure 5.8) and hence greatly reducing the number of potential up-pumping pathways. Indeed, the doorway density decreases in the sequence α-FOX-7 (~4.67 states per atom) > β-FOX-7 (~4.20 states per atom) > γ-FOX-7 (~2.52 states per atom).

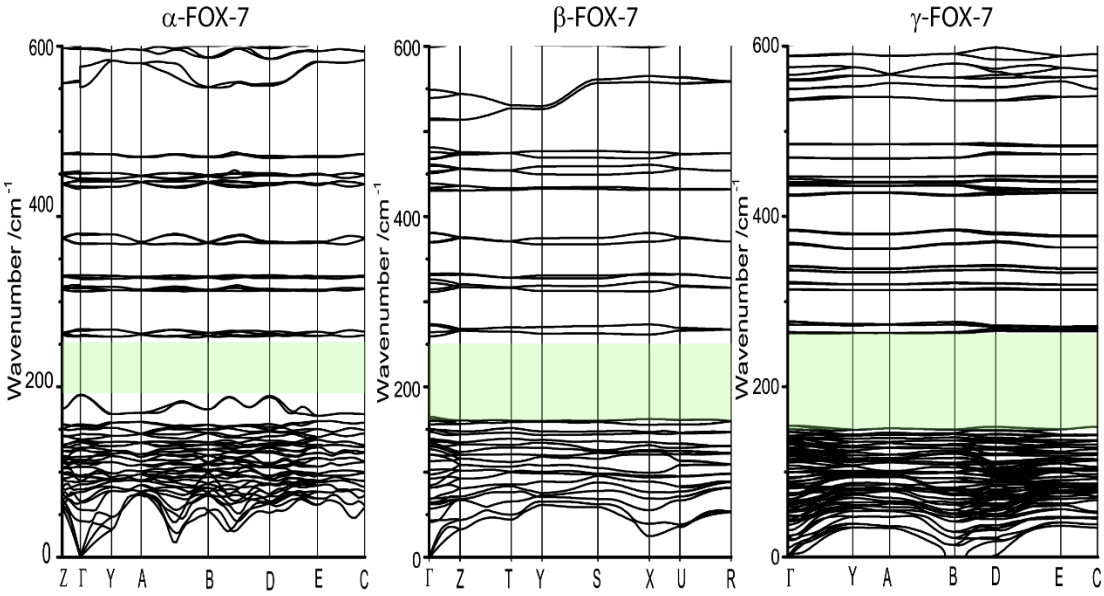

Figure 5.7: Phonon dispersion curves for three polymorphs of FOX-7. The gap between the phonon bath and doorway modes is highlighted with a green box.

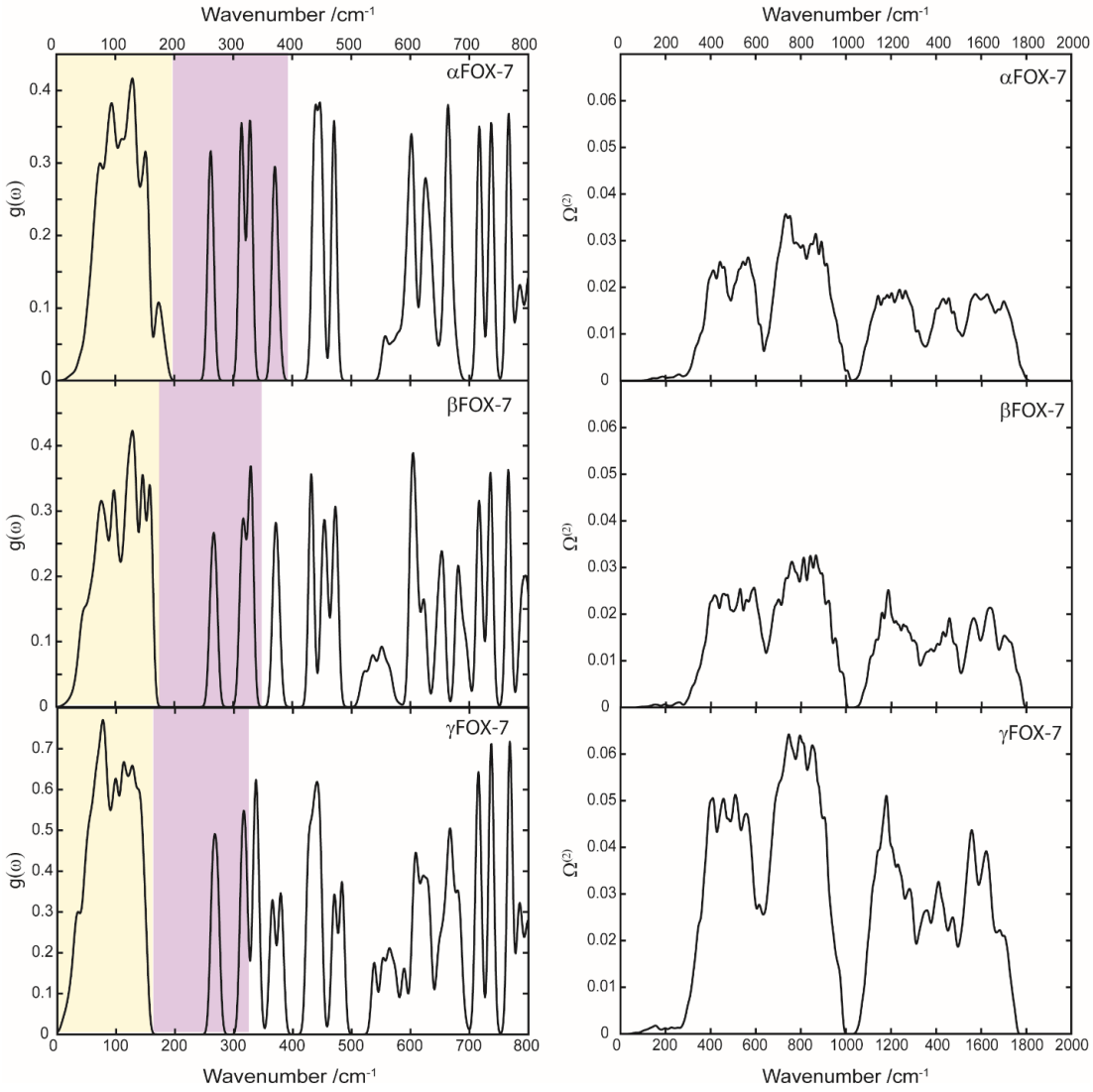

Figure 5.8: Comparison of (left) $g(\omega)$ and (right) $\Omega^{(2)}$ for the three polymorphs of FOX-7. The phonon bath and doorway mode regions in $g(\omega)$ are indicated in yellow and purple, respectively. Note that $\Omega^{(2)}$ have been normalized by $\int g(\omega)$ to account for a different number of atoms (and hence vibrational modes) in the unit cell according to the indirect up-pumping mechanism.

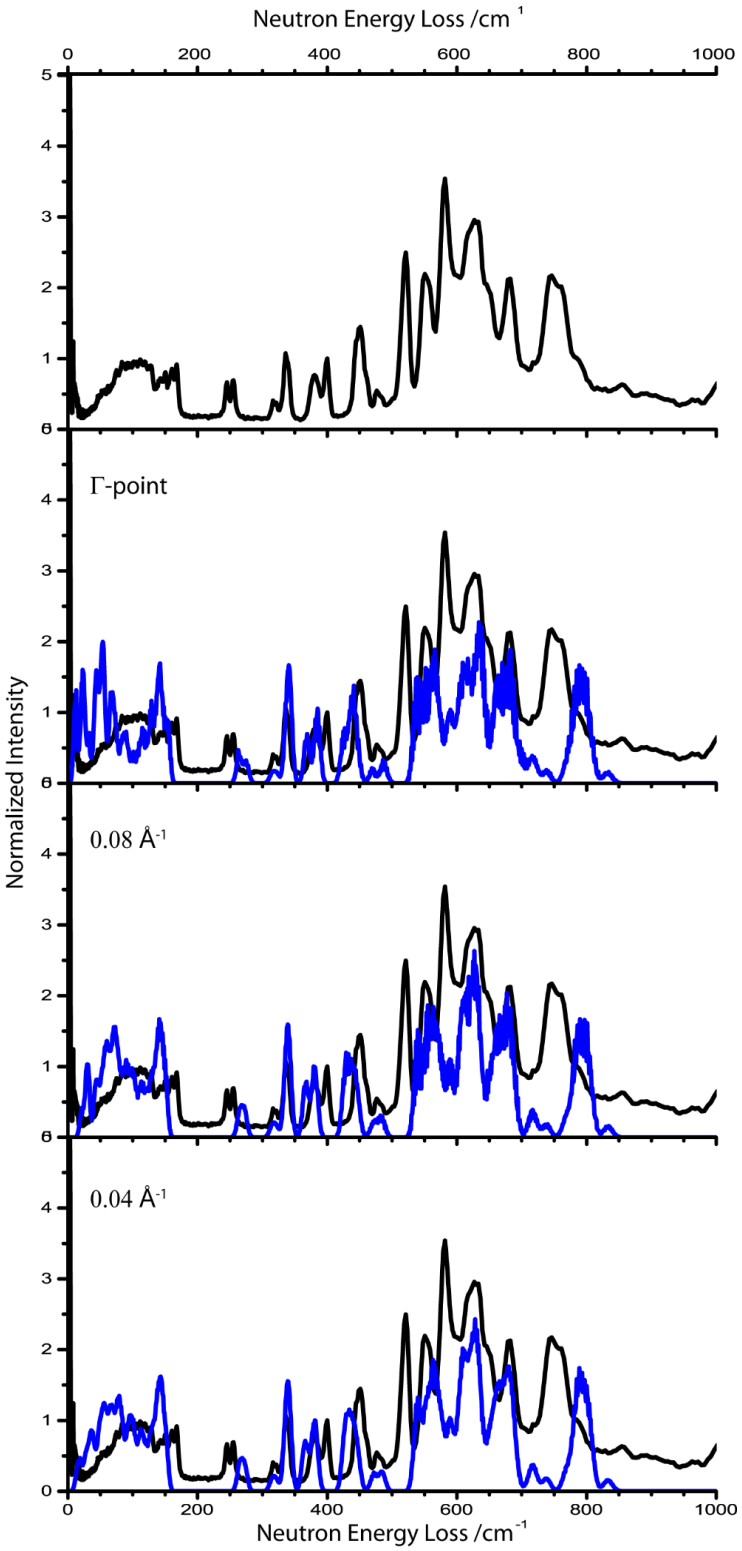

Figure 5.9: INS spectrum (10 K) for γ-FOX-7. The (black) experimental spectrum is given alongside the (blue) simulated spectra using increasing densities of wave vectors for the phonon calculations. Note that only first order quantum events are simulated.

While it was not possible to isolate the β-form, the γ-form could be quench cooled, and analysed by INS spectroscopy, Figure 5.9. The calculated vibrational structure for γ-FOX-7 yields a simulated INS spectrum that generally agrees well with the experimental spectrum. The most notable difference is the underestimation of Ω_{max} in the simulated spectrum (Ω_{max} is 160 cm^{-1} from simulation, and 171 cm^{-1} from INS). While this is likely to have some consequence on the calculation of the up-pumping model, it is important to note that the experimental Ω_{max} is still approximately 20 cm^{-1} lower than the experimental Ω_{max} value for α-FOX-7 presented in Chapter 4. The remainder of the INS spectra exhibit the same expected features, with discrepancies in the calculated frequencies < 6%. While this does suggest some difficulty with reproducing the vibrational structure of γ-FOX-7, it is overall representative of the experimental frequencies and is therefore carried forward for data processing in the up-pumping model.

As described for the HMX polymorphs, the FOX-7 polymorphs were analysed within the framework of the two most successful models of Chapter 4. This first required generation of $g(\omega)$ (for this system, sampling could be obtained from across the Brillouin zone) and $\Omega^{(2)}$ for the three polymorphs, Figures 5.8, respectively. Across all three polymorphs, $\Omega^{(2)}$adopts a very similar structure. The onset wavenumber is approximately 270 cm^{-1} in each case, which reflects the generally similar structure of the doorway modes. Furthermore, all three polymorphs exhibit $\Omega^{(2)} = 0$ just above 1000 cm^{-1}, and feature the same groupings of density. With very similar vibrational structures, it follows that the main difference in understanding the up-pumping between these polymorphs will be Ω_{max} and the relative rates at which energy can up-pump into these nearly identical structures.

If the three FOX-7 polymorphs are analysed first using the overtone-based model, built on the first two overtones, Figure 5.10, the relative sensitivity ordering that was determined by doorway density is recovered: α-FOX-7 ≈ β-FOX-7 > γ-FOX-7, with the overtone up-pumped density equal to ~ 6.0, ~ 6.1 and ~ 4.9, respectively. This places the two FOX-7 polymorphs that exhibit

herringbone packing at approximately the same sensitivity, with the layered γ-form predicted to have a lower sensitivity.

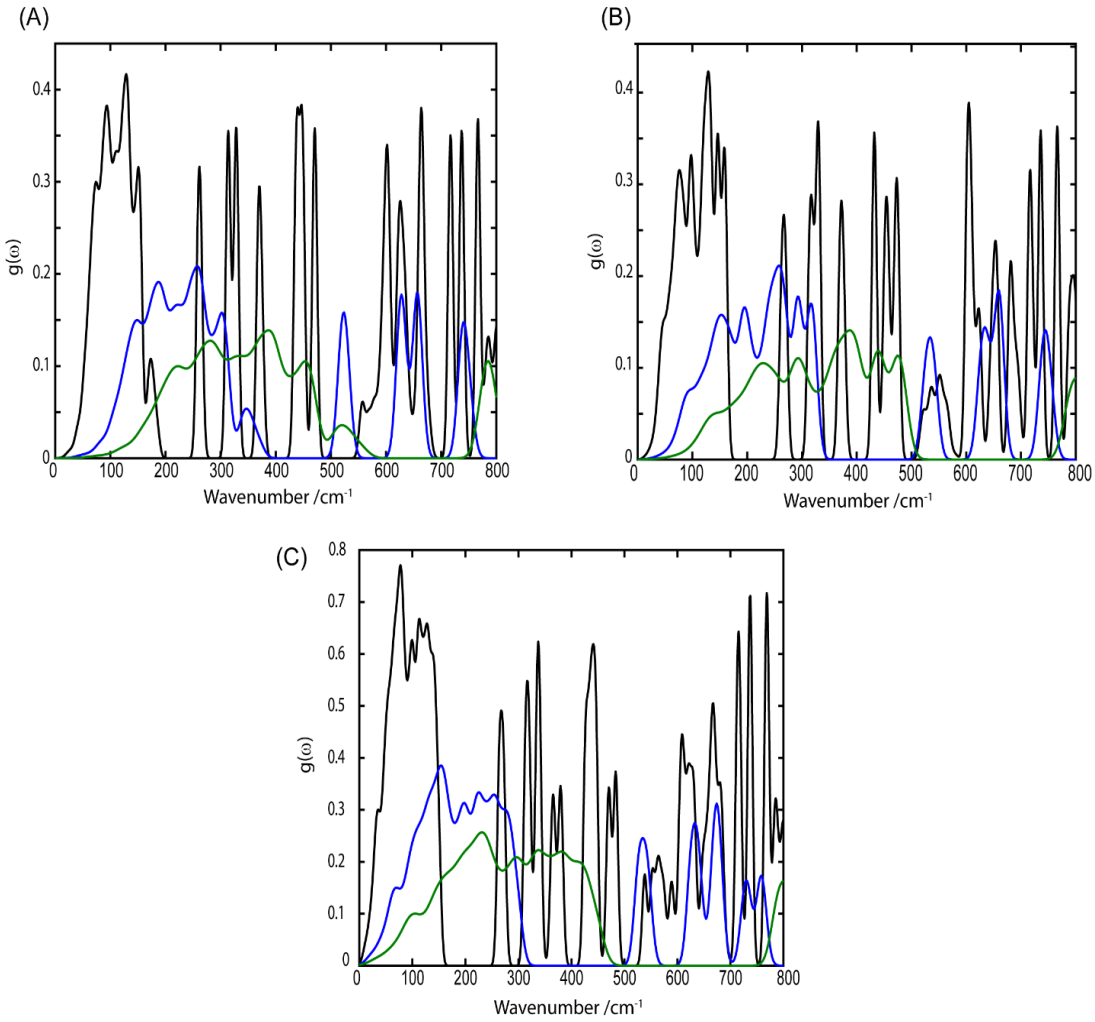

Figure 5.10: Overtone contributions to vibrational up-pumping in FOX-7 polymorphs. The overtones are shown for (blue) $N = 2$ and (green) $N = 3$, and overlain by $g(\omega)$ (black). Plots are shown for (A) α-FOX-7, (B) β-FOX-7 and (c) γ-FOX-7.

It is finally worth considering the three FOX-7 polymorphs using the two-layered model, and an equilibrium temperature of 300 K. Despite the projection of the overtone pathways onto the doorway modes leading to considerably fewer doorway contributions for γ-FOX-7, Figure 5.8, the larger number of populated modes available in the phonon bath for this polymorph greatly reduces this effect. According to discussions in Chapter 4, all three polymorphs exhibit $\Omega^{(2)} = 0$ at approximately 1000 cm^{-1} (Figure 5.8). Hence, this is taken

to be the upper limit for integration in the two-layered model. The values of $\int \Omega^{(2)}$ for the three polymorphs are found to be 14.5, 12.6 and 12.2 a.u. for the α-, β- and γ-polymorphs, respectively. The results of Chapter 4 (Figure 4.20) suggest that this corresponds to a sizeable difference in predicted sensitivity between the α- and γ-forms, with the latter being less sensitive.

Both the overtone and the two-layered models therefore suggest that flattening the crystal layers of an energetic compound should decrease the impact sensitivity. The models point towards the sensitivity decrease being purely the result of a decrease in Ω_{max}, given that the remaining $g(\omega)$ are largely unchanged, Figure 5.8. Hence, a new mechanism for the decreased sensitivity of layered materials is therefore proposed based on the decreased ability of these materials to up-pump vibrational energy. Without a larger dataset it is not yet possible to correlate the change in predicted impact sensitivity to an absolute change in initiation energy. However, based on the datasets in Chapter 4, it is predicted that γ-FOX-7 should be notably less sensitive than the α-form. Thus this model suggests a major deficiency in the current experimental approach to studying impact sensitivity of polymorphic materials. Furthermore, this demonstrates the importance of considering mechanically-induced structural transformations that may occur immediately before, or during, initiation events.

5.5 Conclusions

Polymorphism is very prevalent amongst energetic materials, and can lead to drastic changes in a material's sensitivity to impact. Most notable are the δ- and β-polymorphs of HMX. The former has been reported to be as sensitive to impact as a primary explosive material, while the latter exhibits much lower sensitivity to impact. Application of the up-pumping model was able to reproduce these experimental findings and assessed δ-HMX as being a highly sensitive material. This therefore demonstrates that the up-pumping model is

sensitive to polymorphic modifications. It was therefore applied to a second polymorphic energetic material, FOX-7.

Under ambient conditions, FOX-7 exists in the α-form, which adopts a herringbone-type structure. When heated, these layers flatten, and are nearly flat in the γ-form. This form was recovered to ambient conditions and its impact sensitivity measured using a BAM fall hammer. This suggested that the layered γ-form had the same impact sensitivity as the α-form, despite the general principle that layered materials are insensitive. X-ray powder diffraction, however, revealed that the γ-form undergoes transformation to the α-form on impact, and hence it is not known which polymorphic phase was in fact tested. The mechanism for this impact-induced transformation is not yet known, and may be the result of pressure, temperature or their combination. The up-pumping model was therefore applied to the FOX-7 polymorphs. Both the overtone-based model and the temperature-dependent two-layered model suggested that the layered γ-form should be notably less sensitive than the α-form. It is suggested that the reduction in sensitivity is the result of a decrease in Ω_{max} (an observation noted in both the INS spectra and simulated phonon density of states plots) that results from the increased layering. This reduction in Ω_{max} is observed across all layered materials studied thus far. Hence, a new structurally-based mechanism for the decreased sensitivity of layered materials has been proposed.

Due to the $\gamma \rightarrow \alpha$ transition, BAM hammer testing appears incapable of directly measuring the impact sensitivity of the γ-form. Current experimental approaches are inadequate for the investigation of polymorphic materials. Furthermore, this transition demonstrates the importance of considering structural transformations during the initiation process of EMs, and the ability of the up-pumping model to assist in the interpretation of experimental results.

5.6 Suggestions for Further Work

It is clear from this chapter that the up-pumping models can be applied to polymorphic series. However, the sample size used here is limited. It is therefore of great interest to extend this work to a broader set of polymorphic materials. To do this, it will be necessary to conduct experimental investigations on the sensitivity of polymorphic materials, many of which have yet to be thoroughly analysed.

A more detailed analysis of the impact-induced polymorphism of γ-FOX-7 can also be suggested, with the aim of identifying the mechanism for the $\gamma \rightarrow \alpha$ transition. This can be done by monitoring the material during impact by spectroscopic or X-ray techniques. Understanding this transformation may be critical to fully rationalise the transformation that was observed in this work. Additionally, it will be worth considering the role of the ϵ-form (which forms when FOX-7 is exposed to pressure[21]) in this transformation, and its impact sensitivity relative to the α- and γ-forms.

Furthermore, it is apparent that a deeper correlation between the predicted impact sensitivity and experimental values must be sought. This can only be obtained by expanding the set of compounds studied using these models. However, this also requires accurate capture of the experimental impact sensitivities of EMs, which can prove difficult in many cases.

5.7 References

(1) McCrone, W. C. Polymorphism. In *Polymorphism in Physics and Chemistry of the Organic Solid State*; Fox, D., Labes, M. M., Weissenberg, A. A., Eds.; Interscience: New York, 1965; p 726.

(2) Fabbiani, F. P. A.; Pulham, C. R. High-Pressure Studies of Pharmaceutical Compounds and Energetic Materials. *Chem. Soc. Rev.* **2006**, *35* (10), 932–942.

(3) Bernstein, J. *Polymorphism in Molecular Crystals*; Claredon Press, OUP, 2002.

(4) Bishop, M. M.; Chellappa, R. S.; Liu, Z.; Preston, D. N.; Sandstrom, M. M.; Dattelbaum, D. M.; Vohra, Y. K.; Velisavljevic, N. High Pressure-Temperature Polymorphism of 1,1-

Diamino-2,2-Dinitroethylene. *J. Phys. Conf. Ser.* **2014**, *500* (5), 052005.

(5) Boldyreva, E. V. Non-Ambient Conditions in the Investigation and Manufacturing of Drug Forms. *Curr. Pharm. Des.* **2016**, *22*, 1–20.

(6) Pudipeddi, M.; Serajuddin, A. T. M. Trends in Solubility of Polymorphs. *J. Pharm. Sci.* **2005**, *94* (5), 929–939.

(7) Joiris, E.; Di Martino, P.; Berneron, C.; Guyot-Hermann, A.-M.; Guyot, J.-C. Compressive Behaviour of Orthorhombic Paracetamol. *Pharm. Res.* **1998**, *15* (7), 1122–1130.

(8) Davidson, A. J.; Oswald, I. D. H.; Francis, D. J.; Lennie, A. R.; Marshall, W. G.; Millar, D. I. A.; Pulham, C. R.; Warren, J. E.; Cumming, A. S. Explosives under Pressure—the Crystal Structure of γ-RDX as Determined by High-Pressure X-Ray and Neutron Diffraction. *CrystEngComm* **2008**, *10* (2), 162–165.

(9) Millar, D. I. A.; Oswald, I. D. H.; Barry, C.; Francis, D. J.; Marshall, W. G.; Pulham, C. R.; Cumming, A. S. Pressure-Cooking of Explosives—the Crystal Structure of ε-RDX as Determined by X-Ray and Neutron Diffraction. *Chem. Commun.* **2010**, *46* (31), 5662–5664.

(10) Howard, C.; Smith, L. . Studies on the Polymorphs of HMX. *Los Alamos* **1961**.

(11) Soni, P.; Sarkar, C.; Tewari, R.; Sharma, T. D. HMX Polymorphs: Gamma to Beta Phase Transformation. *J. Energ. Mater.* **2011**, *29* (3), 261–279.

(12) Asay, B. W.; Henson, B. F.; Smilowitz, L. B.; Dickson, P. M. On the Difference in Impact Sensitivity of Beta and Delta Hmx. *J. Energ. Mater.* **2003**, *21* (4), 223–235.

(13) Scott, P. D. *Impact Sensitivity Testing*; Los Alamos, 1998.

(14) Rice, B. M.; Hare, J. J. A Quantum Mechanical Investigation of the Relation between Impact Sensitivity and the Charge Distribution in Energetic Molecules. *J. Phys. Chem. A* **2002**, *106* (9), 1770–1783.

(15) Matyáš, R.; Pachman, J. *Primary Explosives*; Springer-Verlag: Berlin, 2013.

(16) Herrmann, M.; Engel, W.; Eisenreich, N. Thermal Expansion, Transitions, Sensitivities and Burning Rates of HMX. *Propellants, Explos. Pyrotech.* **1992**, *17*, 190–195.

(17) Yoo, C. S.; Cynn, H. Equation of State, Phase Transition, Decomposition of β-HMX (Octahydro-1,3,5,7-Tetranitro-1,3,5,7-Tetrazocine) at High Pressures. *J. Chem. Phys.* **1999**, *111* (22), 10229–10235.

(18) Gump, J. C.; Stoltz, C. A.; Mason, B. P.; Freedman, B. G.; Ball, J. R.; Peiris, S. M. Equations of State of 2,6-Diamino-3,5-Dinitropyrazine-1-Oxide. *J. Appl. Phys.* **2011**, *110* (7), 3–10.

(19) Bishop, M. M.; Velisavljevic, N.; Chellappa, R.; Vohra, Y. K. High Pressure–Temperature Phase Diagram of 1,1-Diamino-2,2-Dinitroethylene (FOX-7). *J. Phys. Chem. A* **2015**, *119* (37), 9739–9747.

(20) Dreger, Z. A.; Tao, Y.; Gupta, Y. M. Phase Diagram and Decomposition of 1,1-Diamino-2,2-Dinitroethene Single Crystals at High Pressures and Temperatures. *J. Phys. Chem. C* **2016**, *120* (20), 11092–11098.

(21) Hunter, S.; Coster, P. L.; Davidson, A. J.; Millar, D. I. A.; Parker, S. F.; Marshall, W. G.; Smith, R. I.; Morrison, C. A.; Pulham, C. R. High-Pressure Experimental and DFT-D Structural Studies of the Energetic Material FOX-7. *J. Phys. Chem. C* **2015**, *119* (5), 2322–2334.

(22) Politzer, P.; Murray, J. S. Energetic Materials (Part2. Detonation, Combustion). **2003**.

(23) Zhang, J.; Mitchell, L. A.; Parrish, D. A.; Shreeve, J. M. Enforced Layer-by-Layer Stacking of Energetic Salts towards High-Performance Insensitive Energetic Materials. *J. Am. Chem. Soc.* **2015**, *137* (33), 10532–10535.

(24) Kuklja, M. M.; Rashkeev, S. N.; Zerilli, F. J. Shear-Strain Induced Decomposition of 1,1-Diamino-2,2-Dinitroethylene. *Appl. Phys. Lett.* **2006**, *89* (7), 071904.

(25) Crawford, M. J.; Evers, J.; Göbel, M.; Klapötke, T. M.; Mayer, P.; Oehlinger, G.; Welch, J. M. G-FOX-7: Structure of a High Energy Density Material Immediately Prior to Decomposition. *Propellants, Explos. Pyrotech.* **2007**, *32* (6), 478–495.

(26) Ledgard, J. *The Preparatory Manual of Explosives, Third Edition*, 3rd ed.; Jared Ledgard, 2007.

(27) Weese, R. K.; Burnham, A. K. Coefficient of Thermal Expansion of the Beta and Delta Polymorphs of HMX. *Propellants, Explos. Pyrotech.* **2005**, *5* (5), 344–350.

(28) NATO. *Classification Procedures, Test Methods and Criteria Relating to Explosives of Class 1*; 2009.

(29) Colognesi, D.; Celli, M.; Cilloco, F.; Newport, R. J.; Parker, S. F.; Rossi-Albertini, V.; Sacchetti, F.; Tomkinson, J.; Zoppi, M. TOSCA Neutron Spectrometer: The Final Configuration. *Appl. Phys. A Mater. Sci. Process.* **2002**, *74*, 64–66.

(30) Parker, S. F.; Fernandez-Alonso, F.; Ramirez-Cuesta, A. J.; Tomkinson, J.; Rudic, S.; Pinna, R. S.; Gorini, G.; Fernández Castañon, J. Recent and Future Developments on TOSCA at ISIS. *J. Phys. Conf. Ser.* **2014**, *554* (1), 012003.

(31) Arnold, O.; Bilheux, J. C.; Borreguero, J. M.; Buts, A.; Campbell, S. I.; Chapon, L.; Doucet, M.; Draper, N.; Ferraz Leal, R.; Gigg, M. A.; et al. Mantid - Data Analysis and Visualization Package for Neutron Scattering and μ SR Experiments. *Nucl. Instruments Methods Phys. Res. Sect. A Accel. Spectrometers, Detect. Assoc. Equip.* **2014**, *764*, 156–166.

(32) Dymkowski, K.; Parker, S. F.; Fernandez-Alonso, F.; Mukhopadhyay, S. AbINS: The Modern Software for INS Interpretation. *Phys. B Condens. Matter* **2018**, *In Press*, 1–6.

(33) Clark, S. J.; Segall, M. D.; Pickard, C. J.; Hasnip, P. J.; Probert, M. I. J.; Refson, K.; Payne, M. C. First Principles Methods Using CASTEP. *Zeitschrift für Krist.* **2005**, *220*, 567–570.

(34) Perdew, J. P.; Burke, K.; Ernzerhof, M. Generalized Gradient Approximation Made Simple. *Phys. Rev. Lett.* **1996**, *77* (18), 3865–3868.

(35) Grimme, S. Semiempirical GGA-Type Density Functional Constructed with a Long-Range Dispersion Correction. *J. Comput. Chem.* **2006**, *27*, 1787–1799.

(36) Hunter, S.; Sutinen, T.; Parker, S. F.; Morrison, C. A.; Williamson, D. M.; Thompson, S.; Gould, P. J.; Pulham, C. R. Experimental and DFT-D Studies of the Molecular Organic Energetic Material RDX. *J. Phys. Chem. C* **2013**, *117* (16), 8062–8071.

(37) Pack, J. D.; Monkhorst, H. J. Special Points for Brillouin-Zone Integrations. *Phys. Rev. B* **1976**, *13* (12), 5188–5192.

(38) Peintinger, M. F.; Oliveira, D. V.; Bredow, T. Consistent Gaussian Basis Sets of Triple-Zeta Valence with Polarization Quality for Solid-State Calculations. *J. Comput. Chem.* **2013**, *34* (6), 451–459.

(39) Heyd, J.; Peralta, J. E.; Scuseria, G. E.; Martin, R. L. Energy Band Gaps and Lattice Parameters Evaluated with the Heyd-Scuseria-Ernzerhof Screened Hybrid Functional. *J. Chem. Phys.* **2005**, *123* (17), 174101.

(40) Dovesi, R.; Orlando, R.; Erba, A.; Zicovich-Wilson, C. M.; Civalleri, B.; Casassa, S.; Maschio, L.; Ferrabone, M.; De La Pierre, M.; D'Arco, P.; et al. CRYSTAL14: A Program for the Ab Initio Investigation of Crystalline Solids. *Int. J. Quantum Chem.* **2014**, *114* (19), 1287–1317.

(41) Tran, F.; Blaha, P.; Schwarz, K.; Novák, P. Hybrid Exchange-Correlation Energy Functionals for Strongly Correlated Electrons: Applications to Transition-Metal Monoxides. *Phys. Rev. B - Condens. Matter Mater. Phys.* **2006**, *74* (15), 155108.

(42) Zhu, W.; Xiao, H. First-Principles Band Gap Criterion for Impact Sensitivity of Energetic Crystals: A Review. *Struct. Chem.* **2010**, *21* (3), 657–665.

(43) Dlott, D. D. Multi-Phonon up-Pumpng in Energetic Materials. In *Overview of Recent Research on Energetic Materials*; Shaw, R. W., Brill, T. B., Thompson, D. L., Eds.; World Scientific, 2005; pp 303–333.

(44) Trzciński, W. A.; Belaada, A. 1,1-Diamino-2,2-Dinitroethane (DADNE,FOX-7) - Properties and Formulations. **2016**, *13* (2), 527–544.

(45) Storm, C. B.; Stine, J. R.; Kramer, J. F. Sensitivity Relationships in Energetic Materials. In *Chemistry and Physics of Energetic Materials*; Bulusu, S. N., Ed.; Springer, Dordrecht, 1990; pp 605–639.

(46) Kennedy, S. R.; Pulham, C. R. Co-Crystallization of Energetic Materials. In *Co-crystals: Preparation, Characterization and Applications*; Aakeröy, C. B., Sinha, A. S., Eds.; Royal Society of Chemistry: Cambridge, UK, 2018; pp 231–266.

Chapter 6

General Conclusions and Future Directions

6.1 General Conclusions

The work in this thesis has explored the development and application of a model to predict the relative impact sensitivity of a range of EMs. This model is based on the concept of vibrational up-pumping, which was developed to rationalise the localisation (and hence intensification) of energy resulting from mechanical perturbation of a solid. In contrast to previous attempts, the model in this thesis is based purely on *ab initio* input. Hence, this work provides a new approach to *predict* relative impact sensitivities of EMs.

A model was first constructed for a series of nine azide-based EMs, selected for investigation on the basis of their diverse structural types and range of experimental impact sensitivities. Based on literature reports, the relative sensitivities of these compounds should follow the order: NaN_3 ≈ TAGZ (triaminoguanidinium azide) ≈ NH_4N_3 < LiN_3 < $Ba(N_3)_2$< AgN_3 < $Sn(N_3)_2$, with the exact position of HN_3 and $Zn(N_3)_2$ within this order being unknown, except that they are sensitive to impact. Due to the simplicity of the N_3^- explosophore, it was possible to investigate these systems within the framework of a 'direct' up-pumping mechanism. Hence, the vibrational normal coordinates of the explosophore were followed and its electronic structure was monitored. It was found that the bending modes ($\delta\theta_{NNN}$) led to crossing of the ground-state (S_0) and first triplet-state (T_1) potential energy surfaces (PES). Dissociation of the N-N bond of N_3^- is favourable for the T_1 PES, and hence $\delta\theta_{NNN}$ is suggested

as the target vibrational mode. This was confirmed in the solid state by monitoring the evolution of the electronic band structure as a function of the normal coordinates associated with crystalline NaN_3. Based on *ab initio* phonon dispersion curves, the vibrational up-pumping into the target mode within each system was considered. In line with previous consideration of the up-pumping model, the overtone and combination pathway contributions were isolated. Using only the overtone contributions (which is the method proposed in previous work[1,2]), the sensitivity ordering was not well reproduced. While the prediction does generally place the insensitive compounds at lower sensitivity than the sensitive compounds, a number of notable exceptions occurred. This was largely rectified by consideration of the combination contributions (the method applied in other previous work[3–5]), although there are again notable exceptions. It was found that only by considering *both* mechanisms could the sensitivity ordering be reproduced.

An up-pumping model was subsequently considered for a series of molecular energetic materials: 1,1'-azobistetrazole (ABT), hexanitrobenzene (HNB), 1,3,5,7-tetranitro-1,3,5,7-tetrazocane (HMX), 5,5'-hydrazinebistetrazole, 1,1-Diamino-2,2-dinitroethene (FOX-7), nitrotriazolone (NTO), and triaminotrinitrobenzene (TATB). However, due to the complexity associated with dissociation of these molecules, no target vibrational mode could be identified. Instead, the sensitivity of these materials was explored within the framework of an 'indirect' (or thermal) vibrational up-pumping mechanism. The calculated vibrational spectra for a subset of the materials (α-FOX-7, NTO, TATB and β-HMX) were verified by comparison to inelastic neutron scattering spectra. A number of models were explored based on *ab initio* calculation of the full phonon dispersion curves and are summarised in Table 6.1. The first two models listed in Table 6.1 can be assessed purely from spectroscopic data. This may prove useful for rapid screening of newly synthesised materials.

Table 6.1: Summary of the up-pumping models considered for the treatment of the organic EMs in Chapter 4.

Model	Concept	Performance Remarks
Vibrational frequency gap	Correlation of the gap in vibrational frequencies between the top of the phonon bath (Ω_{max}) and the first doorway mode.	Broad classification of EMs as 'sensitive' or 'insensitive'. Fails to predict sensitivity ordering within each classification. (Figure 4.6)
Doorway mode density	Correlate the density of doorway mode states against impact sensitivity	Good agreement with relative sensitivity ordering. Minor mis-ordering. (Figure 4.7)
Overtone Excitation	Correlate overtone up-pumping and projection onto doorway modes.	Most successful based on *N*=2,3 (*i.e*. two fastest) overtones (Figure 4.10). Excellent agreement with experiment across structurally similar compounds.
Combination Excitation	Correlate combination up-pumping of all frequencies < $3\Omega_{max}$.	Very poor. No notable correlation (Figure 4.13)
Two-layer Model	Explicitly consider the two stages of up-pumping: (1) overtone population and projection onto doorway frequencies, and (2) combination up-pumping of PDOS resulting from step (1).	Good correlation across structurally similar compounds (Figure 4.15). Excellent correlation if up-pumping is restricted to $2\Omega_{max} \rightarrow 3\Omega_{max}$ (Figure 4.16)
Two-layer Model + T	The *two-layer model* considering all up-pumping based on thermally-populated vibrational bands.	Excellent correlation across all EMs investigated (Figure 4.20).

Unlike with the azide-based materials, consideration of the combination pathways performed very poorly at predicting the impact sensitivity ordering for these materials. Instead, the sensitivity of these EMs appears to correlate best with the structure of the doorway region, since:

(1) overtone up-pumping of the doorway region performed well on its own;
(2) The two-layered approach led to significant improvements over the pure combination-based model.

While the model based on the overtone up-pumping of the doorway frequencies (the model chosen by Bernstein[2] and Coffey[1]) performed well, the most successful model was that based on the temperature-dependent construction of the two-layered model. The difference between the performance of the temperature-independent and temperature-dependent two-layer models demonstrates the importance of considering more closely the *rate* rather than purely the *number* of up-pumping pathways. This new two-layered model is constructed from a mixture of the two independent models that have previously been proposed in the literature, and therefore represents the first unified approach to predicting the relative impact sensitivities of EMs.

The largest barrier to the successful application of this model is the simulation of the full phonon dispersion curves, particularly for large organic EMs. It was promising to find that (due to low vibrational dispersion) the same trends were observed when only the zone-centre vibrational frequencies were used for the input. Hence it was possible to add TATP (a highly sensitive material) to the model. Applying both the overtone up-pumping model and the temperature-dependent two-layer model, TATP was successfully identified as being the most sensitive compound in the test set.

In the final chapter of this thesis, the up-pumping model was tested on two HMX polymorphs: δ- and β-HMX. The δ-form is well known to be more sensitive to impact than the β-form. The calculated vibrational structure of δ-HMX was verified by comparison to inelastic neutron scattering spectroscopy. Consideration of the overtone up-pumping (third model, Table 6.1) and the

temperature-dependent, two-layer model both suggested that the δ-form should be considerably more sensitive than the β-polymorph. This clearly demonstrated that the up-pumping models are sensitive not only to different molecules, but also to the crystal structure. The series of temperature-related FOX-7 polymorphs (α-, β- and γ-FOX-7) were therefore explored. As the structure becomes increasingly layered ($\alpha < \beta < \gamma$) this series offered an opportunity to explore why layered materials appear less sensitive than non-layered materials. BAM fall hammer testing of γ-FOX-7 suggested that it exhibited the same impact sensitivity as α-FOX-7. However, X-ray powder diffraction measurements showed that upon impact the γ-form transformed to the α-form, and hence the impact sensitivity of the former could not be directly measured. The full phonon-dispersion curves for the three polymorphs of FOX-7 showed that the maximum frequency of the phonon bath (Ω_{max}) decreased with increased layering. The flat, low frequency Ω_{max} is shared by TATB (the other insensitive layered material studied here). This appeared to be responsible for the decrease in predicted impact sensitivity of the FOX-7 polymorphs in the sequence $\alpha > \beta > \gamma$, according to both the overtone up-pumping and temperature-dependent two-layer models. Thus, the vibrational up-pumping model offers a new mechanism to rationalise the decreased sensitivity of layered materials.

With both datasets based on the 'indirect' up-pumping mechanism, it is possible to consider the trends of both Chapters 4 and 5 together. This is done based on the two most successful models (see Figure 6.1): the overtone up-pumping model (Model 3 in Table 6.1) and the temperature-dependent two-layer model. Both models reveal a clear trend between experimental impact sensitivity and that predicted by the up-pumping contributions. In both cases, the highly sensitive compounds exhibit considerably larger up-pumping values than the low sensitivity materials. The δ-form of HMX is predicted to have an impact sensitivity similar to TATP in both models, and γ-FOX-7 is predicted as being slightly more sensitive than TATB in both models. Overall, these models offer a remarkable correlation between experimental impact sensitivity and predicted sensitivity, across a broad range of EMs and explosophores.

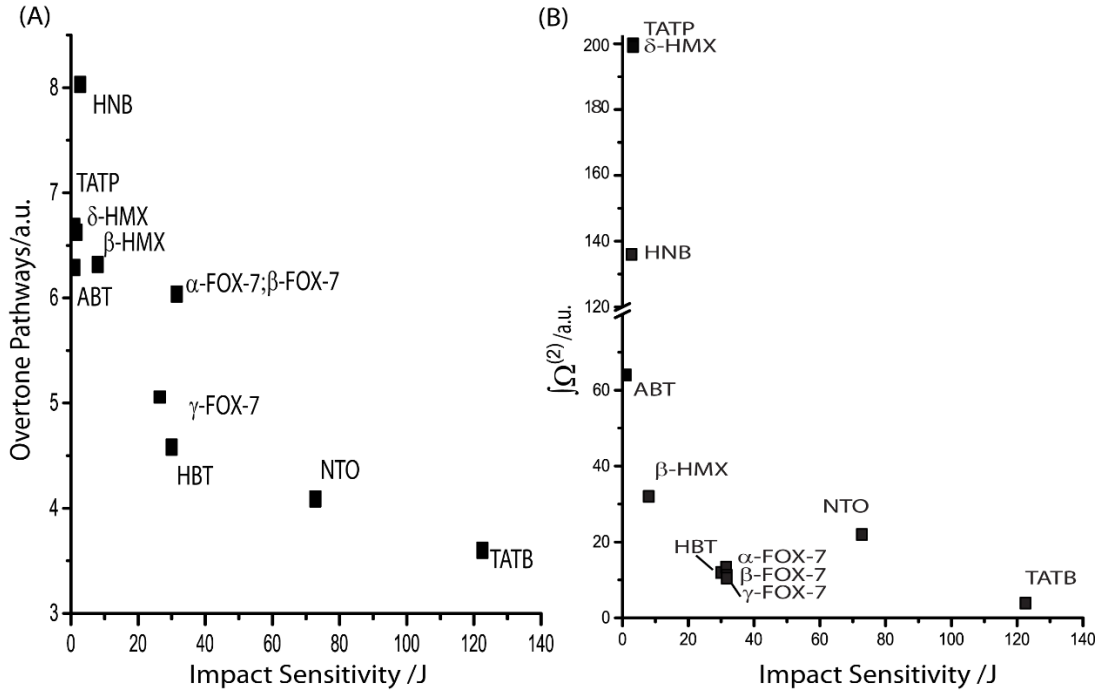

Figure 6.1: Final predicted sensitivity order for the molecular energetic materials. Note that in all cases, complete phonon dispersion curves are used, except for TATP and δ-HMX, for which Γ-point density of states are used. (A) Impact sensitivity based on the overtone up-pumping model (Model 3 in Table 6.1). (B) Impact sensitivity based on the temperature-dependent two-layer model (T = 300 K). The difference in *y*-axis scale results from the number of up-pumping pathways considered in each case, and the addition of temperature in (B).

However, there do remain some minor discrepancies in the model, particularly for the most sensitive compounds. Furthermore, some differences also exist between the overtone and two-layered predictions. The relative ordering of TATP, δ-HMX and HNB changes between the overtone and two-layered approach, as shown in Figure 6.1. Noting that TATP is experimentally more sensitive than HNB[6,7] it can be suggested that the two-layered approach is more successful. The two-layered approach also performs better for the ordering of β-HMX with respect to the FOX-7 systems. ABT is consistently predicted to be less sensitive than HNB. However, the nature of the experimentally reported sensitivity for ABT[8] is not known and may therefore

represent the limiting impact energy. In this case, the ordering of ABT would not be anomalous.

In summary, the work in this thesis has demonstrated that a vibrational up-pumping model, based *solely* on *ab initio* input, can predict the relative sensitivity of EMs across a range of materials and explosophores. Within the direct vibrational up-pumping model (based on a target frequency) used for the azide materials, a combination of both literature models was required to obtain a successful prediction of impact sensitivity, hence unifying the literature discrepancy. Description of the more complex organic EMs required development of a variety of new models within the framework of an indirect up-pumping mechanism. Of these models, the newly developed temperature-dependent two-layered approach appears to be the most successful. This model comprises aspects of both up-pumping models previously described in the literature and successfully unifies them into a highly successful approach. This two layered model proved capable of successfully ordering the impact sensitivity of a range of materials, as well as of polymorphic systems.

6.2 Future Directions

The individual challenges associated with further development of the up-pumping model presented in this thesis are presented in each chapter. In these closing remarks, it is instead worth considering some of the 'real-world' applications and new research directions to which this thesis may lead.

There is currently considerable effort being devoted to the development of new EMs. While the aim is always to develop EMs with enhanced performance, it is no longer sufficient to consider performance in isolation. New constraints are now in place, with particular emphasis on the development of insensitive munitions (IMs). The development of IMs, however, is particularly challenging as there remains no fundamental insight into what physical or chemical parameters define sensitivity. Thus, current methods in EM research require

(often lengthy) synthesis of new EMs and experimental testing of their sensitivity properties. However, without *a priori* insight into the physical properties of a new EM, its synthesis is not only a financial risk, but is accompanied by potentially serious risks to health and safety.

Modern quantum chemical methods are able to correctly predict molecular and crystalline structure, vibrational and thermodynamic properties, interaction energies, amongst a plethora of other properties. Typically, these calculations run over the period of days to weeks, can be run in parallel, and are comparatively cheap as an alternative to experiment. Thus, if a method were known that was capable of predicting sensitivity properties, one could in principle design an IM *in silico*, with a full assessment of its sensitivity properties, without ever needing to set foot in the laboratory until a promising candidate was found.

The vibrational up-pumping model developed in this thesis is one such model. It was demonstrated to be capable of predicting the relative sensitivity ordering of a broad range of EMs based on knowledge of the crystal structure. In its current form, this model makes it possible to predict the sensitivity of materials which may be difficult to obtain in large quantities. High-pressure phases are of particular note. During a detonation, immense pressures are experienced at the shock front, which are well above the pressures typically required to induce structural phase transitions in organic EMs.[9–11] The reactivity of a material to mechanical perturbation may therefore change during detonation. Thus, understanding the relative sensitivity of pressure-related polymorphs may prove crucial for understanding the detonation properties of polymorphic EMs. An excellent example of this is RDX, which undergoes numerous high-pressure phase transitions.[11–13] In other cases, new polymorphic forms may crystallise under pressure,[14] and thus it may not be possible to easily prepare large quantities for testing. The model developed in this thesis can therefore be applied to predict the sensitivity of a new phase, and make judgement as to whether purification of this phase should be pursued further. Alternatively, polymorphic phases may appear as non-isolable impurities within a powder. If

this impurity acts to sensitise the mixture (*e.g.* δ-HMX impurities in β-HMX samples[15]) additional work must be done to remove it. Hence, the up-pumping model offers a means to new validation methods for material composition. Finally, as demonstrated in this thesis, the experimental impact sensitivity testing of polymorphic materials can prove very challenging, and perhaps impossible in some cases. The up-pumping model can therefore be used in parallel with experimental results to assist in their interpretation.

A particularly promising application of the model developed in this thesis is in parallel with crystal structure prediction. It is now possible to predict the potential crystal structures of complex organic molecules to a good degree of accuracy.[16] The combination of crystal structure prediction with sensitivity prediction truly offers the way to a new paradigm in EM research. New molecules could be completely designed *in silico*, their crystal structures predicted, and the up-pumping model applied to generate a list of sensitivities. In doing so, the work in this thesis would open the door to a complete restructuring of the way EM research is performed. As further developments are made on the up-pumping model (*e.g*. inclusion of electronic effects, vibrational response to pressure, defects, etc.), its performance will surely improve. As it does, the reality of making *in silico* EM design a reality becomes closer.

6.3 References

(1) McNesby, K. L.; Coffey, C. S. Spectroscopic Determination of Impact Sensitivities of Explosives. *J. Phys. Chem. B* **1997**, *101* (16), 3097–3104.

(2) Bernstein, J. *Ab Initio* Study of Energy Transfer Rates and Impact Sensitivities of Crystalline Explosives. *J. Chem. Phys.* **2018**, *148* (8), 084502.

(3) Ye; Koshi, M. Theoretical Studies of Energy Transfer Rates of Secondary Explosives. *J. Phys. Chem. B* **2006**, *110* (37), 18515–18520.

(4) Ye, S.; Tonokura, K.; Koshi, M. Energy Transfer Rates and Impact Sensitivities of Crystalline Explosives. *Combust. Flame* **2003**, *132* (1–2), 240–246.

(5) Fried, L. E.; Ruggiero, a J. Energy-Transfer Rates in Primary, Secondary, and Insensitive Explosives. *J. Phys. Chem.* **1994**, *98* (39), 9786–9791.

(6) Storm, C. B.; Stine, J. R.; Kramer, J. F. Sensitivity Relationships in Energetic Materials. In *Chemistry and Physics of Energetic Materials*; Bulusu, S. N., Ed.; Springer, Dordrecht, 1990; pp 605–639.

(7) Gamage, N. D. H.; Stiasny, B.; Stierstorfer, J.; Martin, P. D.; Klapötke, T. M.; Winter, C. H. Less Sensitive Oxygen-Rich Organic Peroxides Containing Geminal Hydroperoxy Groups. *Chem. Commun.* **2015**, *51* (68), 13298–13300.

(8) Klapötke, T. M.; Piercey, D. G. 1,1′-Azobis(Tetrazole): A Highly Energetic Nitrogen-Rich Compound with a N10 Chain. *Inorg. Chem.* **2011**, *50* (7), 2732–2734.

(9) Klapötke, T. M. *Chemistry of High-Energy Materials*, 2nd ed.; Klapötke, T. M., Ed.; De Gruyter: Berlin, 2012.

(10) Millar, D. I. A.; Maynard-Casely, H. .; Kleppe, A. .; Marshall, W. G.; Pulham, C. .; Cumming, A. . Putting the Squeeze on Energetic Materials - Structural Characterisation of High-Pressure Phase of CL-20. *CrystEngComm* **2010**, *12*, 2524–2527.

(11) Millar, D. I. A.; Oswald, I. D. H.; Barry, C.; Francis, D. J.; Marshall, W. G.; Pulham, C. R.; Cumming, A. S. Pressure-Cooking of Explosives—the Crystal Structure of ε-RDX as Determined by X-Ray and Neutron Diffraction. *Chem. Commun.* **2010**, *46* (31), 5662–5664.

(12) Davidson, A. J.; Oswald, I. D. H.; Francis, D. J.; Lennie, A. R.; Marshall, W. G.; Millar, D. I. A.; Pulham, C. R.; Warren, J. E.; Cumming, A. S. Explosives under Pressure—the Crystal Structure of γ-RDX as Determined by High-Pressure X-Ray and Neutron Diffraction. *CrystEngComm* **2008**, *10* (2), 162–165.

(13) Millar, D. I. A.; Oswald, I. D. H.; Francis, D. J.; Marshall, W. G.; Pulham, C. R.; Cumming, A. S. The Crystal Structure of Beta-RDX-an Elusive Form of an Explosive Revealed. *Chem. Commun.* **2009**, No. 5, 562–564.

(14) Fabbiani, F. P. A.; Pulham, C. R. High-Pressure Studies of Pharmaceutical Compounds and Energetic Materials. *Chem. Soc. Rev.* **2006**, *35* (10), 932–942.

(15) Achuthan, C. P.; Jose, C. . Studies on HMX Polymorphism. *Propellants, Explos. Pyrotech.* **1990**, *275*, 271–275.

(16) Price, S. L. Predicting Crystal Structures of Organic Compounds. *Chem. Soc. Rev.* **2014**, *43* (7), 2098–2111.

Appendix A

Publications

In This Thesis

Published

1. Michalchuk, A.A.L., Fincham, P.T., Portius, P., Pulham, C.R., and Morrison, C.A., A Pathway to the Athermal Impact Initiation of Energetic Azides, *J Phys. Chem. C.* **2018,** 122(34), 19395-19408

2. Michalchuk, A.A.L. Rudic, S., Pulham, C.R., and Morrison, C.A., Vibrationally Induced Metallisation of the Energetic Azide α-NaN3, *Phys Chem Chem Phys*, **2018** , 20, 29061-29069

In Preparation

3. Michalchuk, A.A.L., Piggott, S., Rudic, S., Pulham, C.R., and Morrison, C.A. Impact Sensitivity of Polymorphic Energetic Materials: The Curious Case of FOX-7. In preparation

4. Michalchuk, A.A.L., Triestman, M., Rudic, S., Pulham, C.R. and Morrison, C.A, Vibrational up-pumping in molecular energetic materials. In preparation

5. Michalchuk, A.A.L., Rudic, S., Pulham, C.R. and Morrison, C.A. Predicting Impact Sensitivity from Inelastic Neutron Scattering Spectroscopy. In preparation

Not In This Thesis

Published

1. Michalchuk, A.A.L., Tumanov, I.A., Boldyreva, E.V., Complexities of Mechanochemistry, Elucidation of Processes Occurring in Mechanical Activators *via* Implementation of a Simple Organic System, *CrystEngComm*, **2013** 15, 6403. **Hot Article**
2. Michalchuk, A.A.L., Tumanov, I.A., Drebushchak, V.A. and Boldyreva, E.V., Advances in elucidating mechanochemical complexities *via* implementation of a simple organic system, *Faraday Disucss*, **2014**, 170, 311

3. Bell, N.G.A., Michalchuk, A.A.L., Blackburn, J.W., Graham, M.C., and Uhrin, D., Isotope-filtered 4D NMR spectroscopy for structure determination of humic substances, *Angew. Chem. Int. Ed.*, **2015**, 54, 8382
4. Tumanov, I.A., Michalchuk, A.A.L., Politov, A.A, Boldyreva, E.V., and Boldyrev V.V., Inadvertent liquid assisted grinding: a key to 'dry' organic mechano-co-crystallisation? CrystEngComm, **2017** 19, 2830
5. Tumanov, I.A., Michalchuk, A.A.L., Politov, A.A., Boldyreva, E.V., and Boldyrev, V.V, Inhibition of organic mechanochemical synthesis by water vapor, *Doklady Chem.*, **2017** 472.
6. Michalchuk, A.A.L., Tumanov, I.A., Konar, S. Kimber, S.A.J., Pulham, C.R. and Boldyreva, E.V. Challenges of Mechanochemistry: Is In Situ Real‐Time Quantitative Phase Analysis Always Reliable? A Case Study of Organic Salt Formation, *Adv. Sci*., **2017,** 4, 1700132

7. Bouvart, N., Palix, R.-M., Arkhipov, S.A., Tumanov, I.A., Michalchuk, A.A.L., and Boldyreva, E.V. Polymorphism of chlorpropamide on liquid assisted mechanical treatment: choice of liquid and type of mechanical treatment matter, *CrystEngComm*, **2018,** 20, 1797
8. Michalchuk, A.A.L., Hope, K.S., Kennedy, S.R., Blanco, M.V., Boldyreva E.V. and Pulham, C.R., Ball-free mechanochemistry: In situ real time monitoring of pharmaceutical co-crystal formation by resonant acoustic mixing, *Chem. Commun.* ***2018***, 54, 4033.
9. Michalchuk, A.A.L., Tumanov, I.A., and Boldyreva, E.V. The effect of ball mass on the mechanochemical transformation of a single-component organic system: anhydrous caffeine, *J. Mat. Sci*, **2018,** 53 (19), 13380-13389.
10. Zakharov, B.A., Michalchuk, A.A.L., Morrison, C.A. and Boldyreva, E.V. Anisotropic Lattice softening near the structural phase transition in the thermosalient crystal 1,2,4,5-tetrabromobenzene, *Phys Chem Chem Phys*, **2018,** 20, 8523 **Hot Article**
11. Tantardini, C. and Michalchuk, A.A.L. Dess-martin periodinane: The reactivity of a λ5-iodane catalyst explained by topological analysis *Int. J. Quantum Chem.* ***2019,*** *Accepted.*

In Preparation

1. Konar, S, Michalchuk, A.A.L., Sen, N., Bull, C., Morrison, C.A., Pulham, C.R. *High pressure neutron diffraction and DFT-D study of TNT polymorphs.* In preparation

Appendix B

Conferences and Courses

Year 1

This year was dedicated to training under the EPSRC Doctoral Training Centre in Innovative Manufacturing in Continuous Manufacturing and Crystallisation. Training included 11 training weeks from Oct 2014 – May 2015 distributed across the centre partner institutions.

Conferences

1. MechChem, July 2015. Montpelier, France. **Poster Presentation**: '*To beat or not to beat. The role of impact frequency on mechanochemical transformations*'

Workshops

1. Resodyn Technical Exchange. Aug 2015. Butte, Montana, USA.

Courses (University of Edinburgh)

1. Electronic Structure Theory and Classical Simulation Methods
2. Computational Modelling of Materials
3. Computer-Aided Drug Design

Year 2

Conferences

1. Hot Topics in Solid State Chemistry: All Russian (with international participants) Conference. Novosibirsk, Russian Federation. October 2015. **Oral Presentation**: '*In situ real time monitoring of mechanochemical transformations'*
2. International Research Conference on Expanding Frontiers of RNA Chemistry and Biology, Novosibirsk, Russian Federation. Nov 2016. **Oral Presentation**: *'Mechanochemical methods for organic systems'*

3. 31st European Crystallographic Conference. Basel, Switzerland. Aug. 2016. **Oral Presentation** *(on behalf of E Boldyreva): 'Crystallography in Education'*
4. 31st European Crystallographic Conference. Basel, Switzerland. Aug. 2016. **Poster Presentation**: *'In situ real-time monitoring of mechanochemical salt formation'*

Workshops

1. ISIS Neutron Training Course, 12-21 Apr 2016

Year 3

Conferences

1. Crystal Forms, University of Bologna, Italy. 4-6 June 2017
2. 24th IUCr, Aug 2017. Hyderabad, India. **Poster Presentation**: 'The Big Bang Theory. Towards Predicting Impact Sensitivity of Energetic Materials'

Year 4

Conferences

1. 49th Conference of the Fraunhofer ICT. June 2018. **Oral Presentation**: '*The Big Bang Theory. Towards Predicting Impact Sensitivity of Energetic Materials*'